The University of Sheffield

Investigation of Novel Hybrid Excited Permanent Magnet Machines

Shun Cai

A thesis submitted for the degree of Doctor of Philosophy

Department of Electronic and Electrical Engineering
The University of Sheffield
Mappin Street, Sheffield, S1 3JD, UK

April 2020

Abstract

Hybrid excited (HE) machines, with the synergy of high torque density of permanent magnet (PM) excitation and controllable flux of wound field (WF) excitation, have been perceived as a promising candidate for electric and hybrid electric vehicle (EV/HEV) application. Since an additional source of excitation, i.e. DC excitation, is introduced in the HE machine, flux-weakening control strategies are more flexible. With the utilization of stationary field winding (FW), the mechanical contact of brushes and slip rings can be eliminated to improve the system reliability. Furthermore, when the field and armature windings are located in the same slot, the integrated winding technique can be employed to obtain DC coil free HE machines to solve spatial conflicts.

In this thesis, two HE machines with stationary PM and FW are proposed firstly. The stator possesses a compact structure with non-overlapped field and armature windings, and the salient rotor is robust similar to that of the switched reluctance machine. Since all the excitations are located in the stationary part, thermal management is much easier. It is revealed that the torque/power-speed envelopes of the proposed HE machines are extended with the utilization of both field and *d*-axis currents. Furthermore, a third HE machine with stationary FW and consequent-pole PM rotor is developed by utilization of the harmonic rich MMFs in the non-overlapped armature winding. The proposed HE machine exhibits comparable torque density with the conventional surface-mounted PM machine, but the operation range is extended significantly. Moreover, various interior PM rotor configurations can be extended to retain the magnets and utilize the flux-concentrating effect. By employing dual-electric-port inverter to supply a biased AC excitation, the field winding can be eliminated to further enhance the efficiency. All the electromagnetic performances of the proposed machines are investigated by finite element (FE) analyses and validated by experiments.

Finally, the proposed HE machines are optimized and compared with a commercialized interior PM machine to demonstrate the feasible operation in EV/HEV. Although the torque density and overall efficiency are reduced slightly compared with the pure PM machine without field excitation, the maximum power in the flux-weakening region is improved in the HE machines with the regulation of additional DC excitation. Moreover, the proposed HE machines exhibit enhanced fault-tolerant capability at high-speed operation with a controllable magnetic field.

Acknowledgements

The author would like to express his most sincere gratitude to his supervisor, Prof. Z. Q. Zhu, for his invaluable suggestion, support, and encouragement throughout the Ph.D. study. Great thanks are also due to all members of the Electrical Machines and Drives Research Group, at the University of Sheffield, for their assistance and helpful discussions.

The author also wishes to acknowledge Valeo Electrical Systems in France for their sponsorship, particularly Dr. J. C. Mipo and Dr. S. Personnaz for their technical discussion and assistance.

Finally, grateful thanks are due to the author's family and friends for their love and support.

Contents

Nomenclature

B_{g_DC}	Field winding excited air-gap flux density	T
B_{g_PM}	Permanent magnet excited air-gap flux density	T
B_r	Permanent magnet remanence	T
d_{so}	Stator outer diameter	mm
e_A	Phase back electromotive force	V
e_{DC}	Field winding excited phase back electromotive force	V
e_{PM}	Permanent magnet excited phase back electromotive force	V
f_{DC}	Field winding excited magnetomotive force	AT
f_{PM}	Permanent magnet excited magnetomotive force	AT
H_c	Permanent magnet coercivity	kA/m
h_{PM}	Permanent magnet height	mm
h_{rib}	Iron bridge thickness	mm
h_y	Stator yoke thickness	mm
i_{ac}	Armature winding current	A
i_d	*D*-axis current	A
i_{dc}	Field winding current	A
i_q	*Q*-axis current	A
J_{dc}	Field winding current density	A/mm^2
k_{fw}	Flux weakening factor	-
k_p	Winding packing factor	-
L_{aa}	Self-inductance of phase A	mH
L_d	*D*-axis inductance	mH
l_g	Air-gap length	mm
L_q	*Q*-axis inductance	mH

l_{st}	Stack length	mm
M_{ab}	Mutual inductance between phase A and B	mH
M_{df}	Mutual inductance between field winding and d-axis armature winding	mWb
M_{qf}	Mutual inductance between field winding and q-axis armature winding	mWb
N_{ac}	Number of turns per armature coil	-
N_{dc}	Number of turns per field coil	-
N_r	Rotor pole number	-
N_s	Stator slot number	-
p_{ac}	Armature winding copper loss	W
p_r	Rotor pole number	-
R_p	Armature winding resistance per phase	Ω
R_{PM}	Permanent magnet reluctance	/H
r_{ri}	Rotor inner radius	mm
R_{rib}	Iron bridge reluctance	/H
r_{si}	Stator inner radius	mm
r_{so}	Stator outer radius	mm
S_c	Single slot area	mm^2
w_t	Stator tooth width	mm
Λ_r	Air-gap permeance accounting for rotor slots	H/mm^2
Λ_s	Air-gap permeance accounting for stator slots	H/mm^2
Ω_r	Mechanical rotating speed	rad/s
δ_{DC}	Average torque regulation ratio	-
ϕ_g	Air-gap flux	mWb
γ_{DC}	Back-EMF regulation ratio	-
γ_{sp}	Split ratio	-

φ_v	Phase for the v^{th} harmonic flux linkage	rad
v	Harmonic order	-
θ_e	Rotor electrical position	rad
θ_m	Rotor mechanical position	rad
θ_{rp}	Rotor pole arc	^{o}
θ_{sp}	Stator pole arc	^{o}
ρ_{Cu}	Copper electrical resistivity	Ωm
ω_e	Electrical rotating speed	rad/s
ψ_A	Phase flux linkage	mWb
ψ_d	*D*-axis flux linkage	mWb
ψ_{DC}	Field winding excited flux linkage	mWb
ψ_{PM}	Permanent magnet flux linkage	mWb
ψ_q	*Q*-axis flux linkage	mWb

Abbreviation

2D	Two dimensional
2IPM	Double layer interior permanent magnet
3D	Three dimensional
CPSR	Constant power speed region
DSHE	Doubly salient hybrid excited
DSPM	Doubly salient permanent magnet
EMF	Electromotive force
EV	Electric vehicle
FE	Finite element
FEM	Finite element method
FPM	Frozen permeability method
FRPM	Flux reversal permanent magnet
FSNW	Fractional slot non-overlapped winding
FSPM	Flux switching permanent magnet
FW	Field winding
GA	Genetic algorithm
HE	Hybrid excited
HEM	Hybrid excited machine
HEV	Hybrid electric vehicle
IPM	Interior permanent magnet
IPMM	Interior permanent magnet machine
LCM	Least common multiplier
MEA	More electric aircraft
MMF	Magnetomotive force

MTPA	Maximum torque per ampere
NEDC	New European drive cycle
PM	Permanent magnet
RMS	Root mean square
SMC	Soft magnetic composite
SPM	Surface mounted permanent magnet
SRM	Switched reluctance machine
SSPM	Stator slot permanent magnet
UCGF	Uncontrolled generator fault
UIPM	U-shaped interior permanent magnet
UMF	Unbalanced magnetic force
VFRM	Variable flux reluctance machine
VIPM	V-shaped interior permanent magnet
WF	Wound field

Chapter 1

General Introduction

Due to significant environmental concerns, electric vehicles and hybrid electric vehicles (EVs/HEVs) are increasingly being developed and commercialized [ZHU07] [CHA07]. Electrical machines are a key technology for EV/HEV, and the main requirements of machines for EV/HEV include [ZHU07] [CHA07] [BIA16]:

- High torque density and high power density;
- High overload capability;
- Extensive flux-weakening region;
- High efficiency over the whole operating region;
- High reliability and fault tolerant capability;
- Low cost and low acoustic noise.

Permanent magnet (PM) machines, especially equipped with high-energy product rare-earth PM material, exhibit high torque density as well as high efficiency, and have been perceived as good candidates for EV/HEV, e.g. Toyota PRIUS, Nissan LEAF, BMW I3, etc. [KAM06] [SAT11] [WIL15]. However, the magnetic field of PM machines is constant, and a flux-weakening current component is required to operate at high speed. Consequently, the efficiency at high speed is degraded and uncontrolled overvoltage fault may damage the power inverter [SOO02] [RAM11].

An alternative solution is to develop hybrid excited electrical machine, with synergies of PM machine and wound field (WF) machine. The introduction of field winding can help to regulate the magnetic field and the output capability according to working condition, which is beneficial for the EV/HEV with variable speed requirements. Compared with the conventional PM machines, an extra flexibility can be utilized to adjust the flux linkage by the field excitation current. Consequently, higher torque at low speed and wider operating speed range, as well as high efficiency over a wide operating region can be obtained by employing appropriate control strategies [WAN12a] [GIE12].

Various HE machine topologies have been reviewed in the previous publications [ZHA05] [ZHU08a] [OWE11] [HUA14] [AMA09] [AMA11] [HLI13] [WAN17a]. This chapter

emphasizes on the origination of the HE machines, either to enhance the torque density of WF machine or improve the flux weakening performance of stator/rotor PM machine.

This chapter reviews various hybrid excited (HE) machines from the perspective of location of PM and field winding (FW), series/parallel connection of PM and FW excited magnetic fields, and 2D/3D magnetic fields, respectively, to demonstrate the possibility to achieve hybridization from existing PM/WF machine and further enhance the electromagnetic performance for variable speed requirement of EV/HEV. The advantages as well as drawbacks of each category are analyzed. Since an additional control degree, i.e. DC excitation, is introduced in the HE machine, the flux weakening control strategies are more complex. The flux weakening performance as well as efficiency are compared with different control strategies. Then, the potential to mitigate the risk of uncontrolled overvoltage fault at high speed operation is highlighted by controlling the field excitation. Since additional FW is usually required for HE machines compared with pure PM excitation, the spatial confliction inevitably results in electromagnetic performance reduction. The technique to integrate the field and armature windings with open-winding drive circuit is introduced, and novel HE machines without FW are summarized. Finally, the research outlines and major contributions of this thesis are summarized. This chapter is based on a paper presented on EVER 2019 [ZHU19b] and a paper published on CES TEMS [ZHU19c].

1.1 Permanent Magnet Synchronous Machines

Firstly, the non-hybrid excited machine topologies with pure PM excitation are introduced in this section.

1.1.1 Rotor PM Machines

The rotor PM machine topologies are popular and have been widely investigated [ZHU07] [CHA08]. According to the locations of PMs in the rotor, they can further be classified as surface mounted PM (SPM), surface inset PM (Inset-PM), radial magnetized interior PM (radial IPM), and tangential interior PM (tangential IPM), as shown in Fig. 1.1.

For the SPM machine shown in Fig. 1.1 (a), the PMs are simply mounted on the rotor surface. Since the permeability of the PMs is similar to that of the air-gap, the equivalent air-gap length is large. The significant effective air-gap length results in a low inductance and limited armature reaction. Moreover, since the PMs are exposed in the air-gap, the demagnetization withstanding capability may be sacrificed. As the reluctance of PMs is close

to that of air, the *d*- and *q*-axis inductances are similar, resulting in a negligible reluctance torque.

For the Inset-PM machine shown in Fig. 1.1 (b), the PMs are inset in the rotor surface. Since the PMs are also exposed in the air-gap, the inset-PM machine also potentially suffers the demagnetization problem. Meanwhile, the iron besides the PMs may cause flux leakage. However, since the permeability of iron is significantly larger than the PM, the *q*-axis inductance is increased compared with SPM machine. Subsequently, the armature reaction effect is more significant, and reluctance torque can be produced due to the difference between *d*- and *q*-axis inductances.

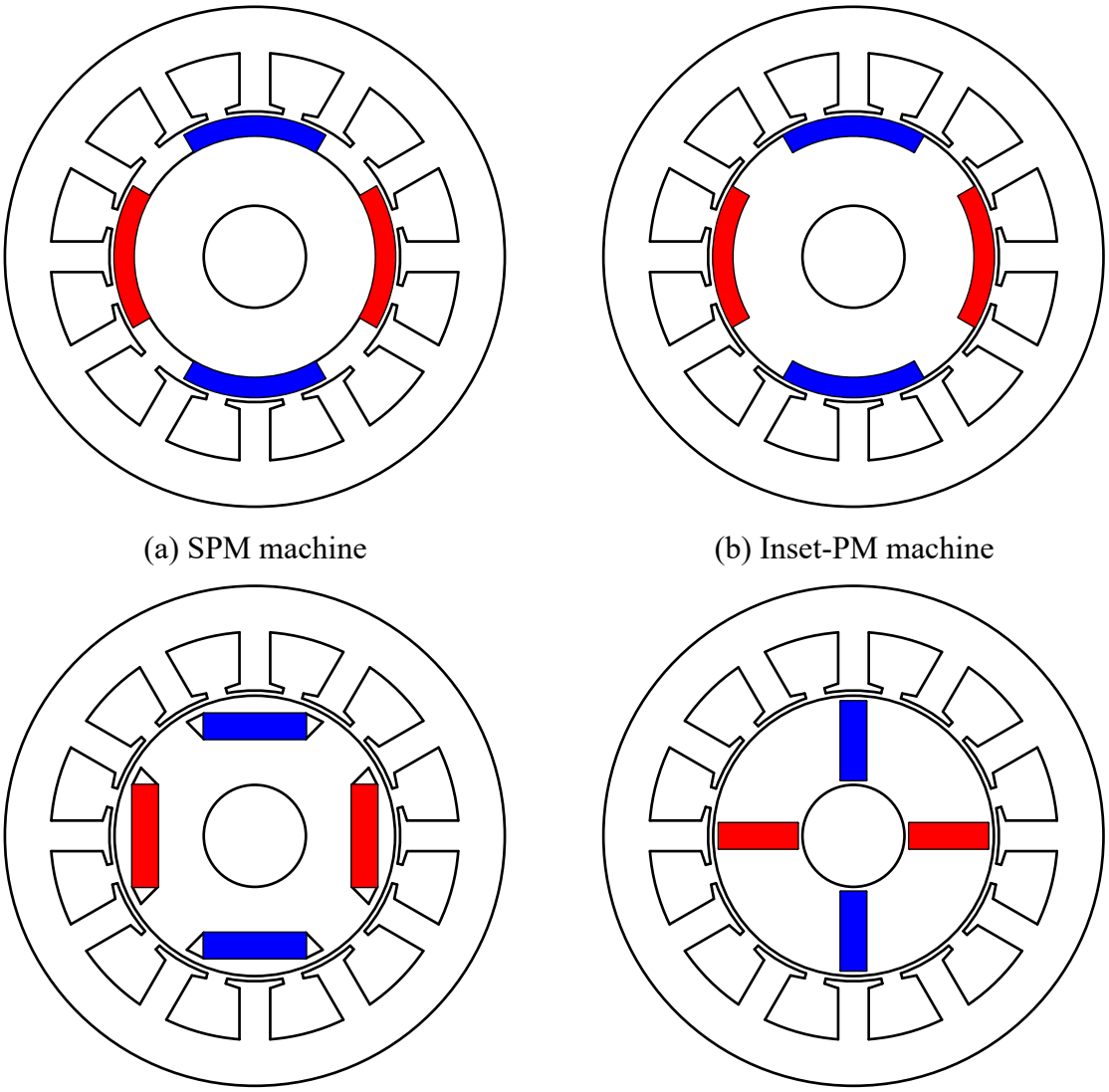

(a) SPM machine (b) Inset-PM machine

(c) Radial IPM machine (d) Tangential IPM machine

Fig. 1.1. Rotor PM machines.

For the radial IPM machine shown in Fig. 1.1 (c), the radial magnetized PMs are interior buried in the rotor. Since the PMs are mechanically and magnetically shielded by the rotor core, the demagnetization withstanding capability is enhanced. However, the iron bridge to connect the rotor core potentially results in flux leakage and should be designed as the trade-off between mechanical stress and electromagnetic performance. Since the permeability of iron is large, the equivalent air-gap length is small and the armature reaction is significant. Moreover, the difference between *d*- and *q*-axis inductances can be observed and reluctance torque can be utilized in the IPM machine.

For the tangential IPM machine shown in Fig. 1.1 (d), the tangential magnetized PMs are interior buried in the rotor. Similar with the radial IPM machine, the tangential IPM machine also possesses enhanced demagnetization withstanding capability, reluctance torque utilization and flux leakage in the iron bridge. Moreover, the air-gap of one-pole is excited by two pieces of magnets in parallel, and flux-concentrating effect can be utilized.

According to the above analyses, the advantages and limitations of different rotor PM machines shown in Fig. 1.1 can be summarized in Table 1.1.

Table 1.1 Comparison of different rotor PM machines

	SPM	Inset-PM	Radial IPM	Tangential IPM
Effective air-gap length	Large	Small	Small	Small
Armature reaction	Small	Large	Large	Large
Demagnetization withstanding	Poor	Poor	Good	Good
Flux leakage	Small	Medium	Large	Large
Reluctance torque	Negligible	Yes	Yes	Yes
Flux-focusing	No	No	No	Yes

1.1.2 Stator PM Machines

The stator PM machine topologies are with stationary PMs and generally salient rotor [CHE11a] [ZHU11a]. They mainly utilize PM aligned torque with negligible reluctance torque. According to the location of stationary PMs, the stator PM machines can be classified into stator yoke PM, i.e. doubly salient PM (DSPM) machine in Fig. 1.2 (a) [LIA95], stator tooth tip PM, i.e. flux reversal PM (FRPM) machine in Fig. 1.2 (b) [DEO97], stator teeth sandwiched

PM, i.e. flux switching PM (FSPM) machine in Fig. 1.2 (c) [HOA97], and stator slot PM (SSPM) machine in Fig. 1.2 (d) [AFI16].

For the DSPM machine shown in Fig. 1.2 (a), one stator unit is composed by three stator teeth sandwiched by two pieces of PMs. Overall, the PM consumption is small and the flux linkage in single coil is unipolar. Moreover, the medium tooth wound coil has different flux linkage with the other two counterparts and asymmetric phase back-EMF is produced.

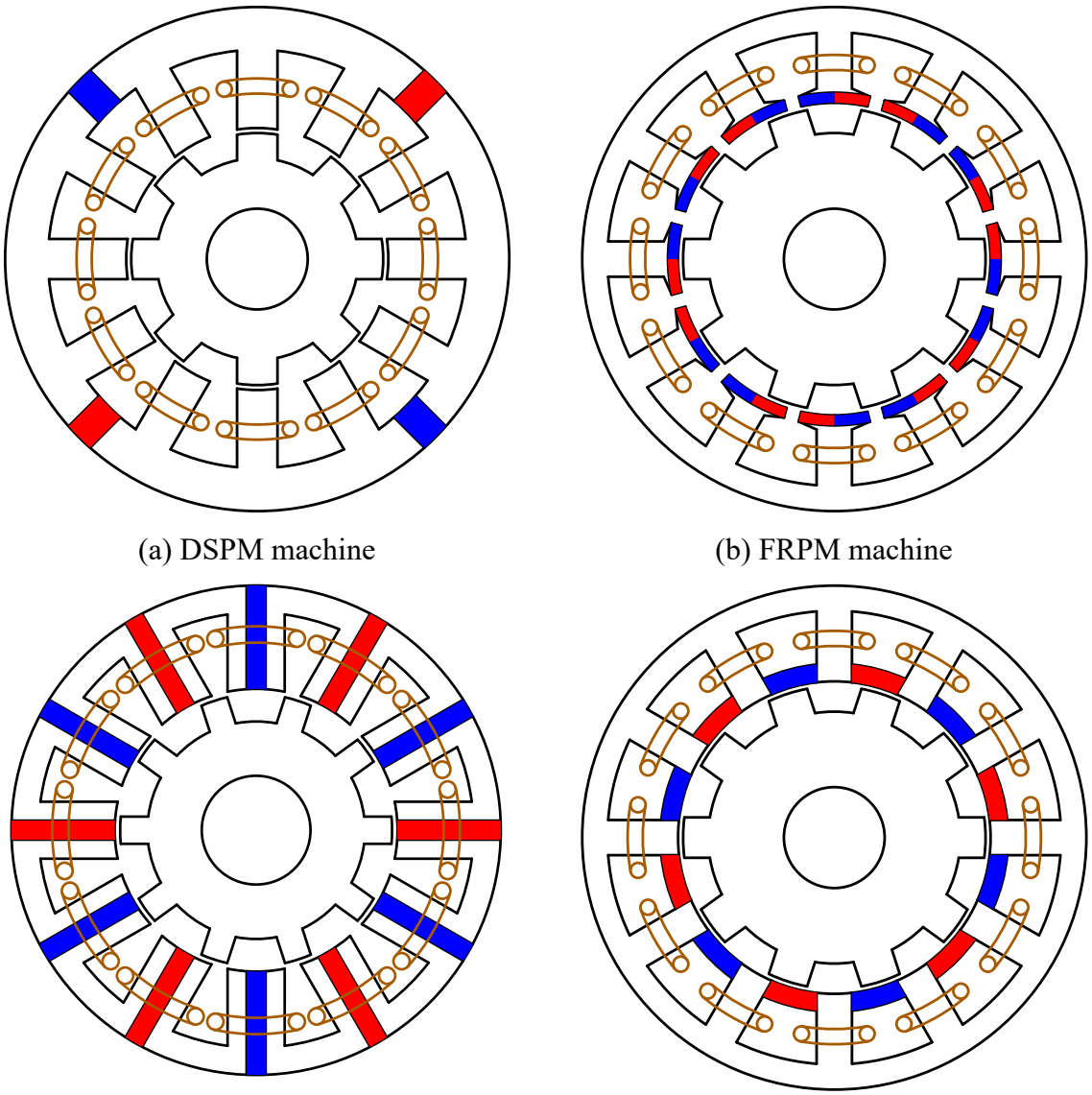

(a) DSPM machine (b) FRPM machine

(c) FSPM machine (d) SSPM machine

Fig. 1.2. Stator PM machines.

For the FRPM machine shown in Fig. 1.2 (b), a pair of magnets are mounted on the surface of stator tooth tips. Since the permeability of PM is similar with air-gap, the thickness of PMs increases the effective air-gap length. Therefore, there exists a trade-off for the thickness of PMs and the PM consumption is medium. The PMs exposed in the air-gap potentially suffer

from irreversible demagnetization. Moreover, the single coil flux linkage polarity alters as the salient rotor moves from one piece of PM to the adjacent one. Although the single coil flux linkage is bipolar, there is no flux focusing effect.

For the FSPM machine shown in Fig. 1.2 (c), the PMs are sandwiched by the stator teeth and the PM consumption is significant. As the salient rotor moves from one side of PM to the other side, the polarity of single coil changes. Therefore, the flux linkage as well as back-EMF of single coil are bipolar. Moreover, flux-focusing effect can be observed in the FSPM by two adjacent pieces of PMs. Overall, the torque density of the FSPM is high and comparable with the IPM machine [CAO12a].

For the SSPM machine shown in Fig. 1.2 (d), the tangentially magnetized PMs are located in the stator slots. Flux-concentrating effect is utilized by the adjacent two pieces of magnets. As the rotor moves from the stator tooth aligned position to the unaligned position, the single coil flux linkage changes from maximum value to minimum value. Subsequently, the flux linkage and back-EMF of single coil is unipolar.

According to the above analyses, the advantages and limitations of different rotor PM machines shown in Fig. 1.2 can be summarized in Table 1.2.

Table 1.2 Comparison of different stator PM machines

	DSPM	FRPM	FSPM	SSPM
PM location	Stator yoke	Stator tooth tip	Sandwiched by stator teeth	Stator slot
PM consumption	Small	Medium	Large	Medium
Flux focusing	No	No	Yes	Yes
Flux linkage	Unipolar	Bipolar	Bipolar	Unipolar
Three phase back-EMF	Asymmetric	Symmetrical	Symmetrical	Symmetrical
Reluctance torque	Negligible	Negligible	Negligible	Negligible
Torque density	Low	Medium	High	Low

1.2 Hybrid Excited Machine Topologies

Based on the discussed PMSM topologies, the hybrid excitation can be achieved by attaching FW for flux regulation. The HE machine topologies can be classified in Fig. 1.3 according to the location of PM and FW. The detailed topologies will be introduced as follows.

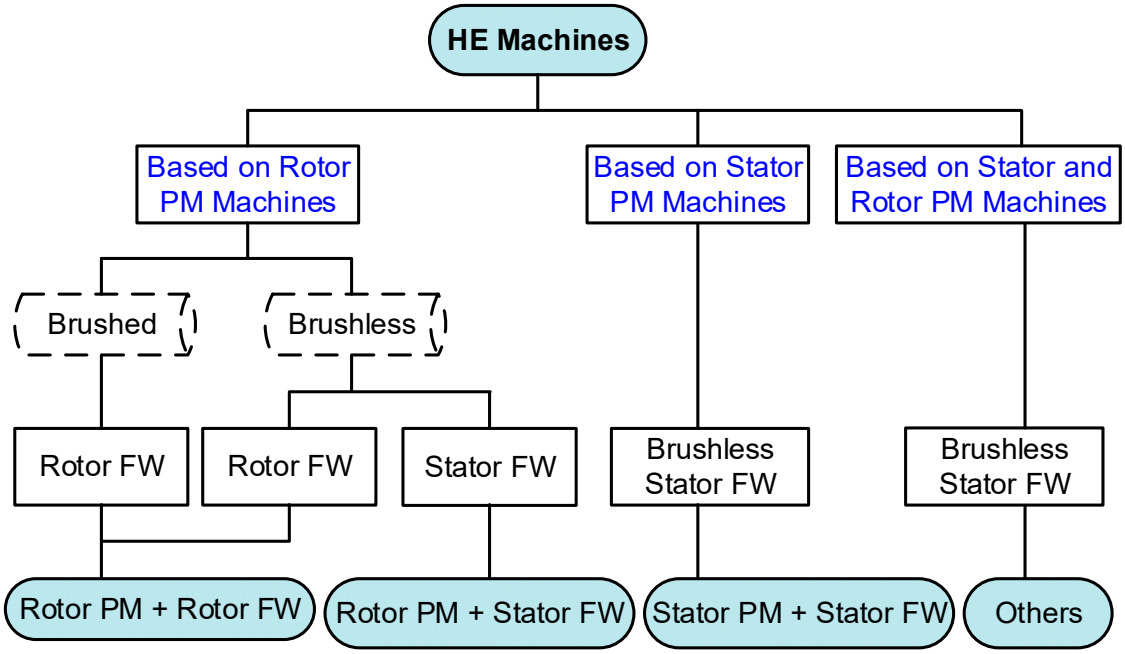

Fig. 1.3. Classification of HE machines.

1.2.1 HE Machines with Rotor PM and FW

Based on the classical rotor surface-mounted PM (SPM) machines, HE machines can be obtained by attaching the field winding in the rotor PM pole directly, as shown in Fig. 1.4 (a) with all pole PMs [HEN94a] [FOD07] [LIN14] and Fig. 1.4 (b) with consequent pole PMs [AKE00], respectively. The machine topology can be perceived as the integration of a rotor SPM machine and a rotor WF machine. Since the flux path of FW passes through the PM, the reluctance is significant and the flux regulation capability is limited.

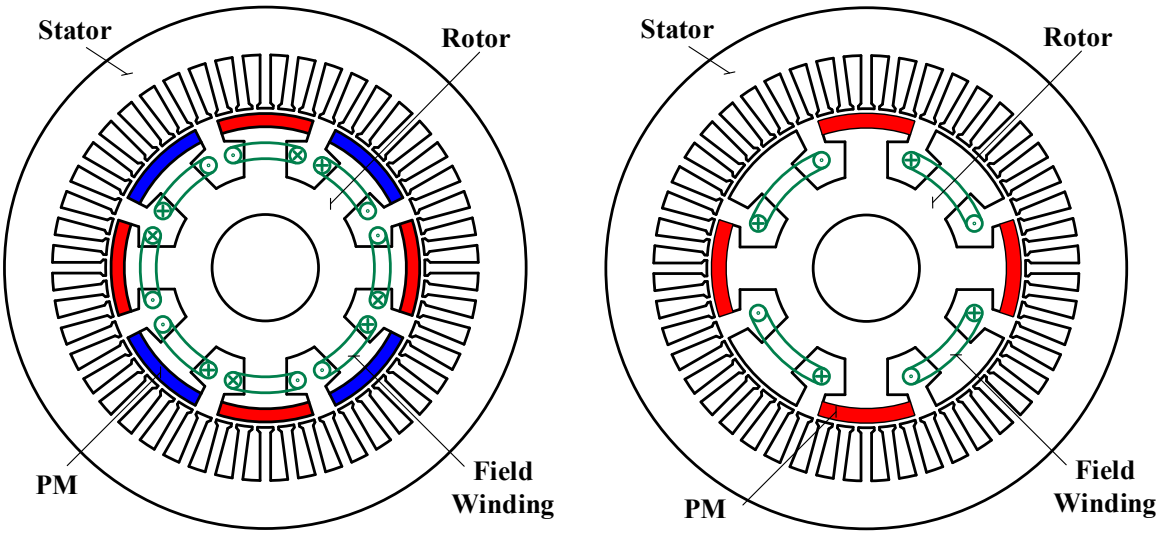

(a) All pole PMs [HEN94a] [FOD07] (b) Consequent pole PMs [AKE00]

Fig. 1.4. HE machines with rotor surface mounted PM.

An alternate topology is to allocate the field winding and PM in different poles, as shown in Fig. 1.5 [LUO00]. As a result, the flux regulation capability and demagnetization withstanding capability are enhanced.

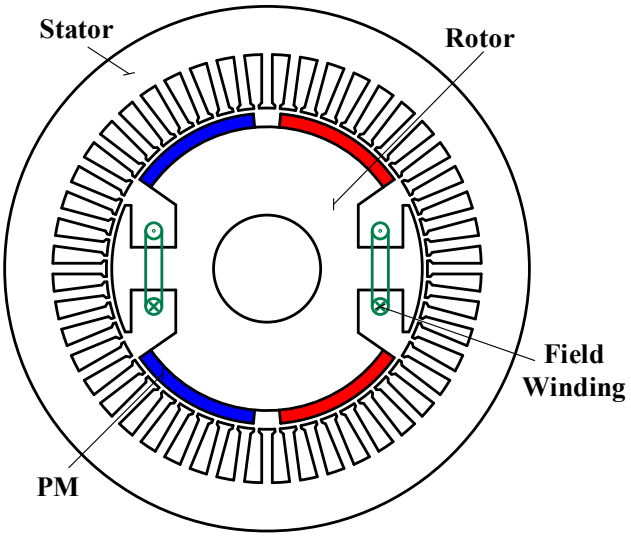

Fig. 1.5. HE machine with field winding and PM in different rotor poles [LUO00].

Besides, HE machines with rotor radial and tangential interior PMs are shown in Fig. 1.6 (a) and (b), respectively. The machine configurations in Fig. 1.4 (b) and Fig. 1.6 (a) are similar, but the iron bridge in the IPM machine provides additional flux path for FW. Therefore, the risk of irreversible demagnetization is reduced although the flux regulation capability is still limited by the saturated iron bridge.

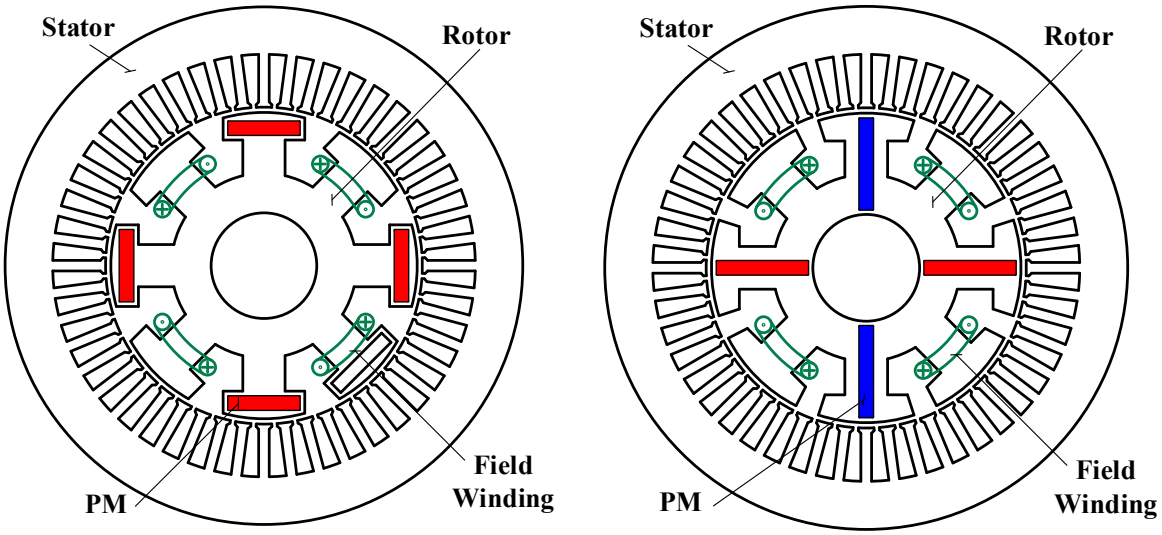

(a) Radial magnetized PM. (b) Tangential magnetized PM.

Fig. 1.6. HE machines with rotor interior PM [AKE00].

Moreover, circumferentially magnetized PMs can be added in the rotor slots of the rotor WF machine, as shown in Fig. 1.7 [FUK08a] [YAM11] [HWA18] [HUA16a]. The PM flux is short circuited in the rotor, and therefore, negligible cogging torque and back-EMF are produced at open-circuit. With field winding excitation, the PM flux can counteract the FW flux in rotor and alleviate magnetic saturation. It is revealed that the torque density as well as efficiency can be enhanced with the assistance of PMs.

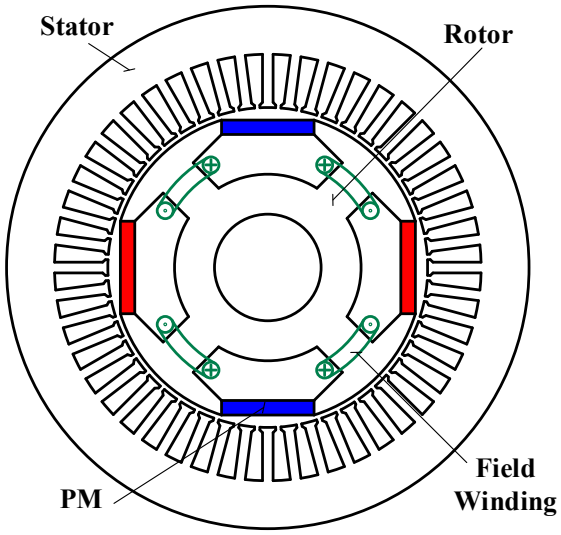

Fig. 1.7. HE machine with PMs in the rotor slots of field winding [FUK08a] [YAM11] [HWA18] [HUA16a].

In [SYV98] and [NAO01], a HE machine is developed by combining the rotor PM machine and the rotor WF machine directly, as shown in Fig. 1.8. The proposed machine consists of a single stator whereas the PM rotor and the WF rotor are connected by the same shaft. The flux paths of PM excitation and field winding excitation are separated inherently and parallel hybridization with wide flux regulation range is achieved. However, additional gap between two rotors is inevitably introduced by the end-winding of field coil.

It should be noted that brushes and slip rings are required to feed DC excitation to the rotary component for the HE machine topologies in Fig. 1.4 - Fig. 1.8. The mechanical contact reduces the system reliability while increasing the cost of maintenance.

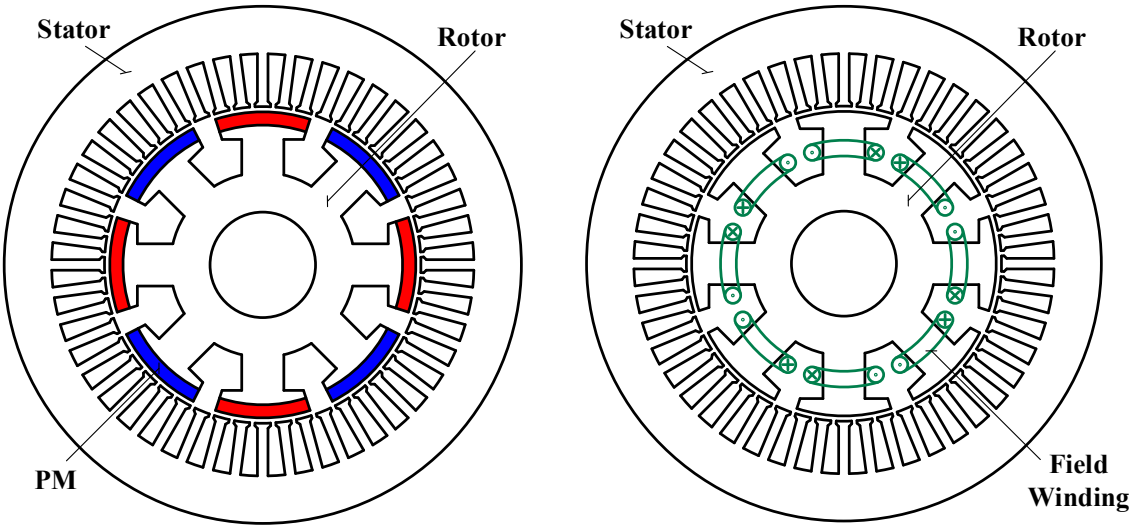

(a) PM machine. (b) WF machine.

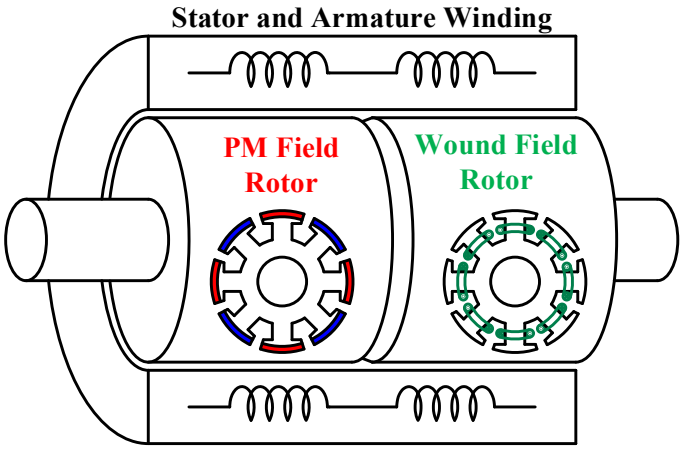

(c) HE configuration with the combination of two parts.

Fig. 1.8. HE machine with the combination of two rotors [SYV98] [NAO01].

To remove the slip rings and brushes, a brushless rotor WF HE machine is proposed in Fig. 1.9 [ALI16] [HUS18] [YAO15] [JAW16] [ALI15a] [HUS17]. The stator accommodates armature winding, whereas the rotor is located with field and harmonic windings. An additional rectifier is attached in the rotor to supply DC to field winding through harmonic winding, and therefore, mechanical contact of brushes with slip rings is saved. The HE machines with all PM rotor poles and consequent PM poles are presented in Figs. 1.9 (a) and (b), respectively. The introduction of rotor PMs can improve the torque density and especially enhance the starting performance. In order to produce current in the rotor harmonic winding, various techniques have been proposed, e.g. single phase third harmonic current injection [YAO15] [JAW16], dual inverter to feed unequal amplitude of current [ALI15a], single inverter to feed the unequal turns of armature winding [HUS17], as shown in Fig. 1.9 (c).

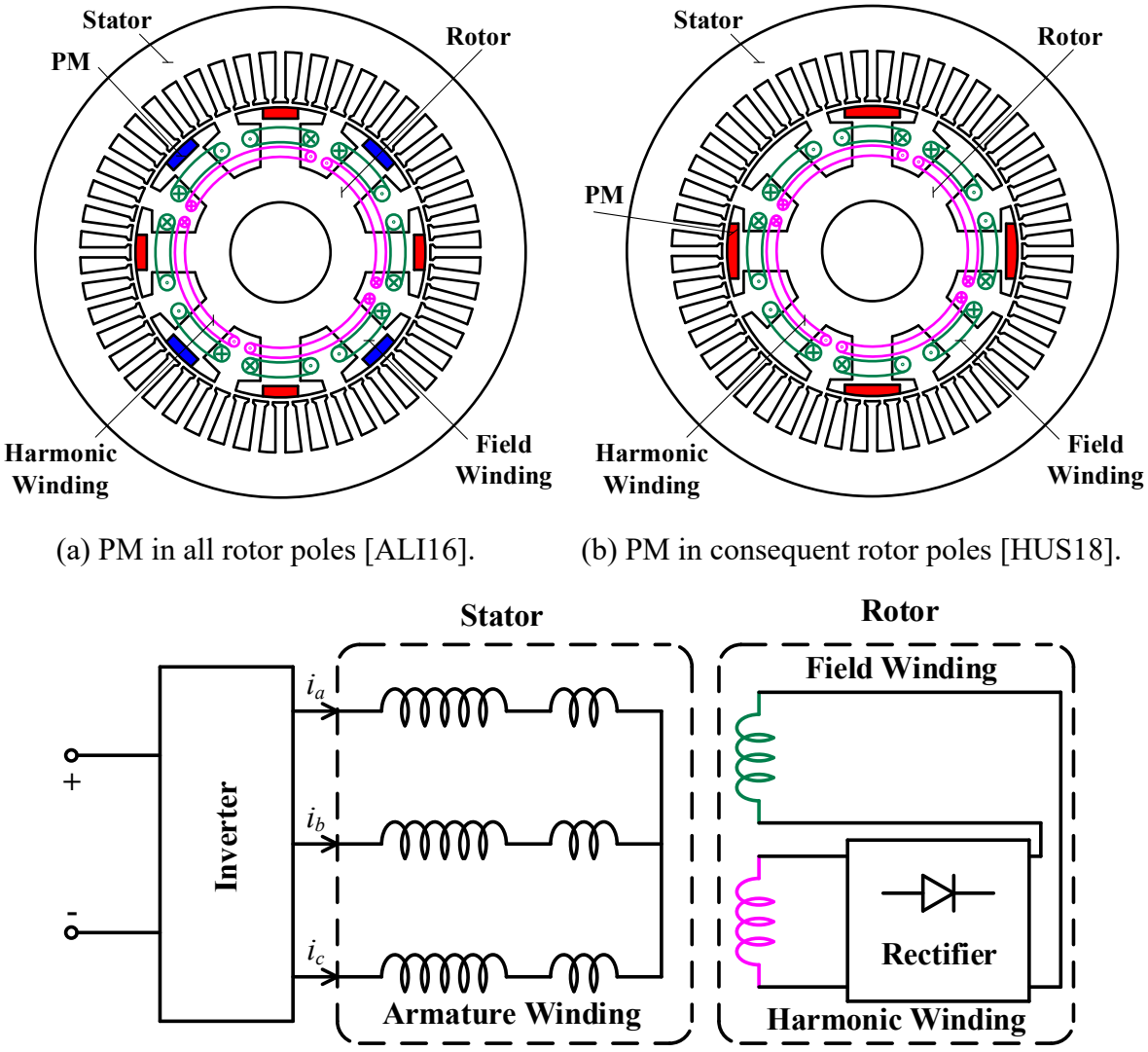

(a) PM in all rotor poles [ALI16]. (b) PM in consequent rotor poles [HUS18].

(c) Single inverter to feed to unequal turns of armature winding [HUS17].

Fig. 1.9. Brushless rotor WF HE machines.

Overall, the HE machines discussed in Fig. 1.4 - Fig. 1.9 can be perceived as the hybridization of a rotor SPM or IPM machine with a WF machine. Therefore, the machine topologies are generally simple with controllable magnetic field. However, brushes and slip rings are required to feed DC excitation to rotary part. Although brushless structure can be achieved in Fig. 1.9, both the machine topology and the drive circuit become complicated. Moreover, the rotor spatial confliction of PM and FW restricts the torque density as well as flux regulation capability. In summary, the advantages and limitations of the HE machines with rotor PM and field winding are summarized in Table 1.3.

Table 1.3 Advantages and limitations of HE machines with rotor PM and FW

	Advantages	Limitations
Brushed FW	✓ Controllable flux with FW ✓ Overall simple structure except brushes and slip rings	• Requirement for brushes and slip rings • Rotor spatial confliction of PM and FW
Brushless FW	✓ Controllable flux with FW ✓ Elimination of brushes and slip rings	• Complicated machine topology • Rotor spatial confliction of PM, field and harmonic windings

1.2.2 HE Machines with Rotor PM and Stator FW

Another solution to eliminate the sliding contacts is to locate the field winding in the stationary parts, whilst PMs are still on the rotor. In [MCC87] [SPO89] [TAP03], a consequent pole rotor PM HE machine with toroidal field winding is investigated, as shown in Fig. 1.10 (a). The PM flux path circulates from PM north pole to PM south pole, whereas the FW flux path passes from one iron pole to another iron pole with reduced reluctance. Both the PM and FW excited magnetic fields have 3D flux path and the synthesized magnetic field can be regulated by the field current. Compared with the conventional rotor PM machine, a solid stator yoke core is attached outside the stator laminated core and the rotor core should also be solid iron to allow for both radial and axial fluxes.

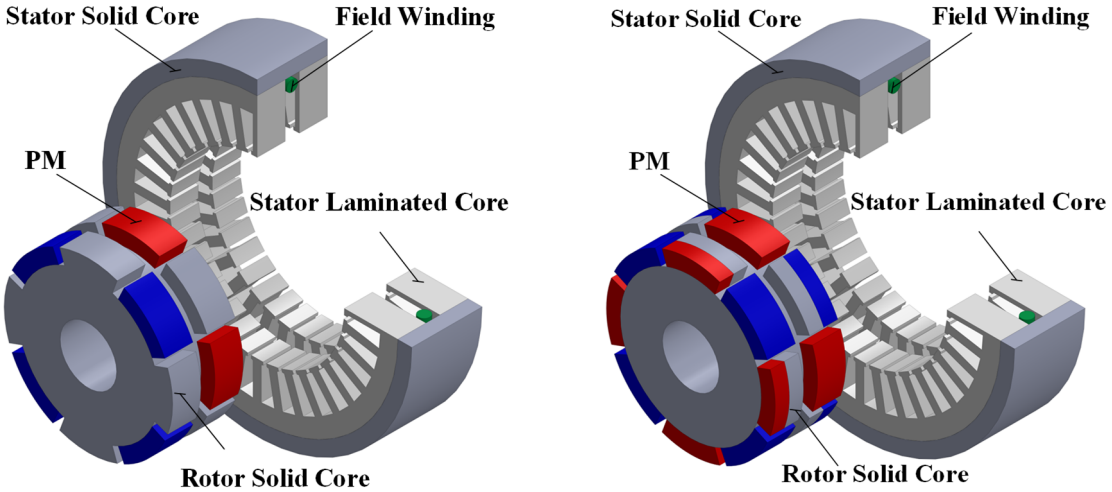

(a) Consequent pole rotor with equal PM pole and iron pole [MCC87] [SPO89] [TAP03].

(b) Consequent pole rotor with enlarged axial PM pole [WAN05].

Fig. 1.10. Consequent pole HE machines with toroidal field winding.

To further enhance the HE machine performances, some improvements have been made in [AYD02] [WAN05] [YAN08] [LI17]. In [AYD02], this concept is utilized in the axial flux PM machine to achieve hybridization. In [WAN05], the proportion of PM to iron pole is enlarged to reduce the voltage regulation and improve the power density, as shown in Fig. 1.10 (b). In order to reduce the field winding length as well as copper loss, the toroidal field winding is moved to inner stator in [YAN08]. In [LI17], the toroidal field winding is further employed for consequent pole Vernier machine to achieve hybrid excitation.

Besides, in [VID05a] [VID05b] [HLI08] [NED11], homopolar and bipolar HE machines are proposed based on the spoke type IPM machine by introducing toroidal field windings in the end plate, as shown in Fig. 1.11. The PM flux path is radial, whereas the FW excited magnetic field has both radial and axial flux paths. Therefore, additional solid stator yoke core, solid end plate as well as solid rotor core are required to allow for 3D magnetic flux path. The two field windings of the homopolar HE machine are of opposite direction, whereas those of the bipolar HE machine are of the same direction. In [ZHA08] [HAN11] [LIU17a], an improved topology with inner stator to accommodate the field winding is proposed, which is beneficial to shorten the toroidal field winding length.

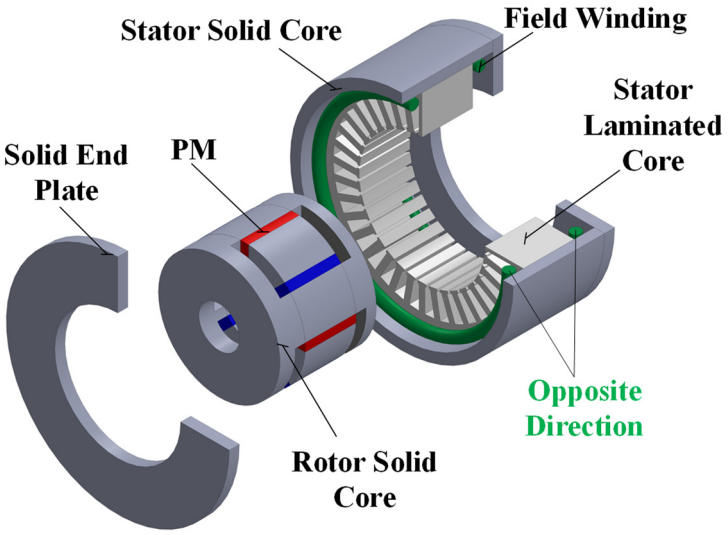

(a) Homopolar HE machine with field windings at two edges of opposite direction.

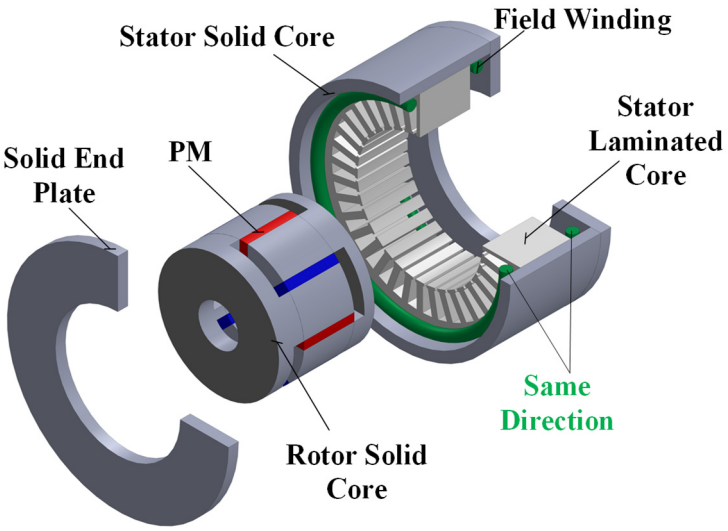

(b) Bipolar HE machine with field windings at two edges of the same directions.

Fig. 1.11. Homopolar and bipolar HE machines with toroidal field winding [VID05a] [VID05b] [HLI08] [NED11].

Besides, HE machines can be developed by introducing PMs in WF claw pole machines to reduce flux leakage and further improve the performance. The toroidal field winding can be wound around the inner stator [CHA96] [CHA97] or the rotor [HEN94b] [ISH96], as shown in Figs. 1.12 (a) and (b), respectively. For the inner stator topology, brushes and slip rings to feed DC excitation can be removed. However, additional air-gap between the inner stationary holder and the rotor is inevitably introduced, which decreases the machine performance. In [REB11] and [REB14], PMs are further introduced both in the rotor and the stator to improve the performance, whereas the machine configuration becomes complex, as shown in Fig. 1.12 (c). Moreover, the hybrid excitation can be achieved by combining dual stator PM machine with WF claw pole machine [LIU07] [LIU09], as illustrated in Fig. 1.12 (d).

It is worth noticing that the brushless claw pole HE machine in Fig. 1.12 (a) and the bipolar HE machine in Fig. 1.11 (b) share similar machine topology and operating principle. The differences can be observed as the spoke type IPM is evolved into claw slot PM, and the field winding is moved from the outer stator to the inner stator.

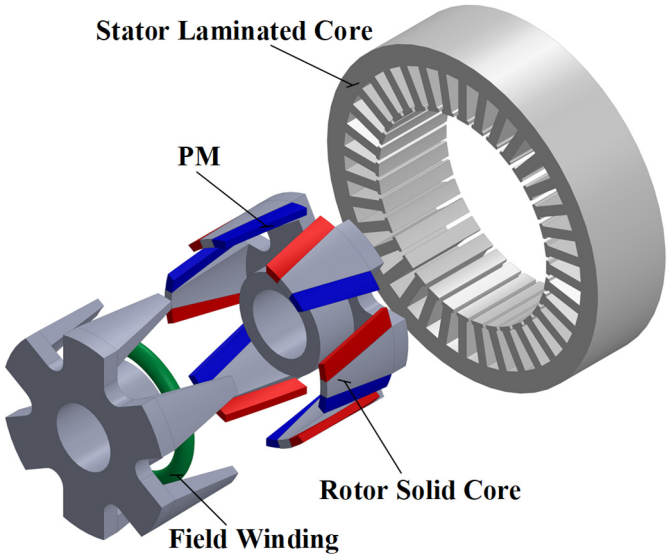

(a) Brushless structure with inner stator accommodating toroidal field winding [CHA96] [CHA97]

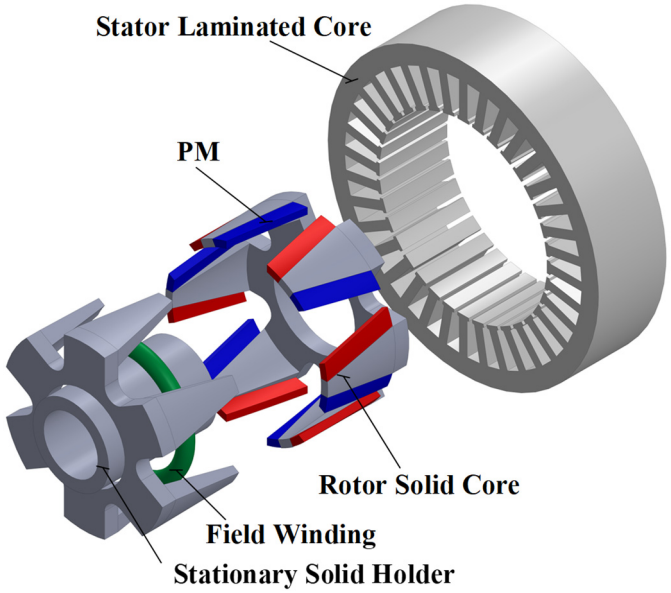

(b) Brushes and slip rings required with rotor accommodating toroidal field winding [HEN94b] [ISH96]

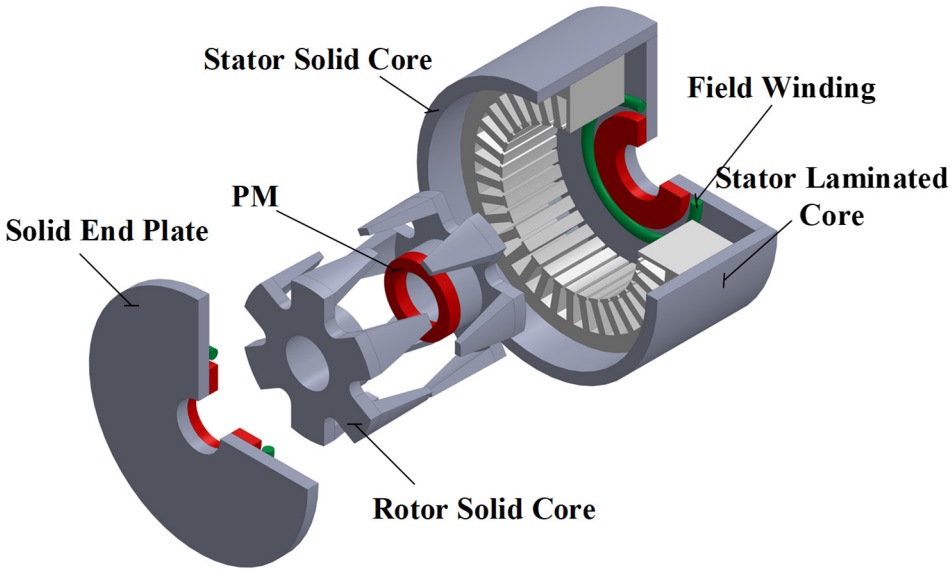

(c) Brushless structure with field winding in stationary end plate [REB11] [REB14]

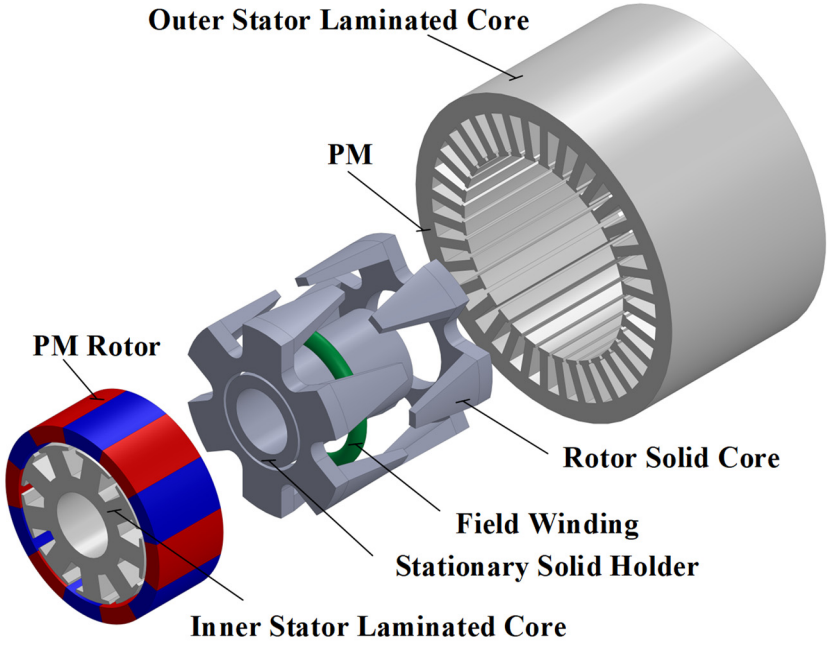

(d) Combination of dual stator PM machine with WF claw pole machine [LIU07] [LIU09]

Fig. 1.12. Claw pole HE machines with PM between rotor claws.

Another HE stepper machine is shown in Fig. 1.13 [KOS05] [KOS10]. The PM is sandwiched by two reluctance rotors with a half rotor pole pitch shift and the toroidal field winding is located at the stationary end plate. Since the magnetic field is controllable and the rotor is robust, the HE stepper machine is suitable for high speed application.

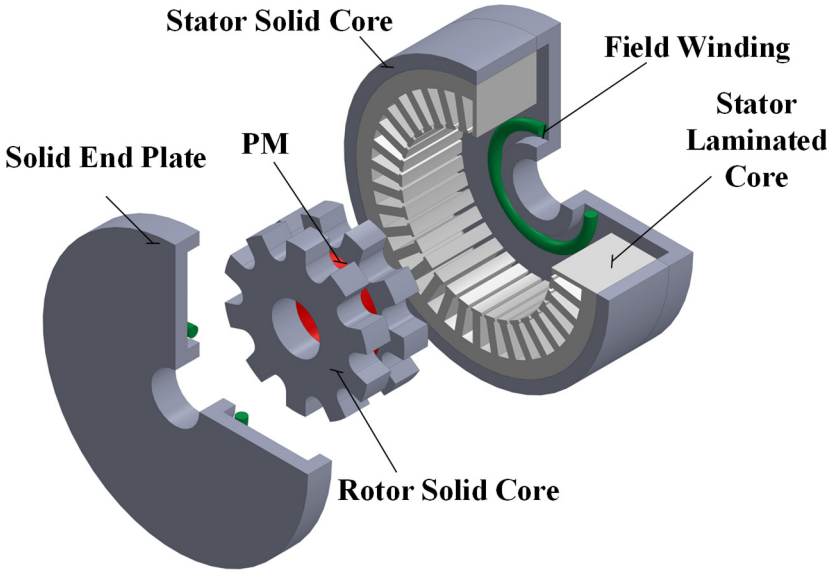

Fig. 1.13. HE stepper machine [KOS05] [KOS10].

In summary, the HE machines discussed in Fig. 1.10 - Fig. 1.13 can be perceived as the introduction of a stationary toroidal field winding to the rotor PM machines. Therefore, the brushes and slip rings can be removed and mechanical contract problem is solved. Moreover, the flux path of FW bypasses the PM and the demagnetization issue becomes less severe compared with flux weakening with *d*-axis current directly. Nevertheless, both radial and axial fluxes exist in the PM and FW excited magnetic fields. Therefore, soft magnetic composite (SMC) or solid material is required to allow for the 3D magnetic field, making the manufacturing and assembling complicated. The summary of advantages and limitations of HE machines with rotor PM and stator FW are listed in Table 1.4.

Table 1.4 Advantages and limitations of HE machines with rotor PM and stator FW

	Advantages	Limitations
HE machines with rotor PM and stator FW	✓ Controllable flux with FW ✓ Elimination of brushes and slip rings	• Complicated machine topology • 3D flux path with both radial and axial magnetic fields • Requirement for SMC or solid core

1.2.3 HE Machines with Stator PM and FW

Besides developing from the rotor PM machines, HE machine configurations can be achieved by attaching field coils in stator PM machines. The sliding contacts are eliminated, and the machine possesses good heat management since all the excitations are stationary.

Generally, all the stator PM machines presented in Fig. 1.2 can be developed for hybridization as follows.

Based on the conventional doubly salient PM machine, hybrid excitation can be obtained in Fig. 1.14. In Fig. 1.14 (a), a field winding is attached in series with PM excitation [LI95]. The doubly salient HE machine is further improved to adopt PM in stator yoke to reduce the PM usage in Fig. 1.14 (b) [CHA02]. However, the flux path of field winding passes through PM, which restricts the flux regulation capability and may potentially cause irreversible demagnetization. In [CHA03], an additional air-gap is introduced in the field winding path to achieve parallel hybridization as shown in Fig. 1.14 (c). Moreover, the iron bridge is introduced in [ZHU05] [ZHU06] to avoid irreversible demagnetization as shown in Fig. 1.14 (d). Similar concept is employed in the outer rotor HE machine in [LIU10a]. However, the magnetic field regulation is still limited since the magnetic bridge is saturated by PM flux. In [CHE08] and [ZHA12], PM poles are replaced with field winding poles, as illustrated in Fig. 1.14 (e) to achieve a wide flux regulation range. In [CHE14], the flux regulation capability of the HE doubly salient machines are compared. It is revealed that the series HE machine in Figs. 1.14 (a) (b) has the lowest flux regulation ratio whereas the parallel HE machine in Fig. 1.14 (e) possesses the best controllable flux capability.

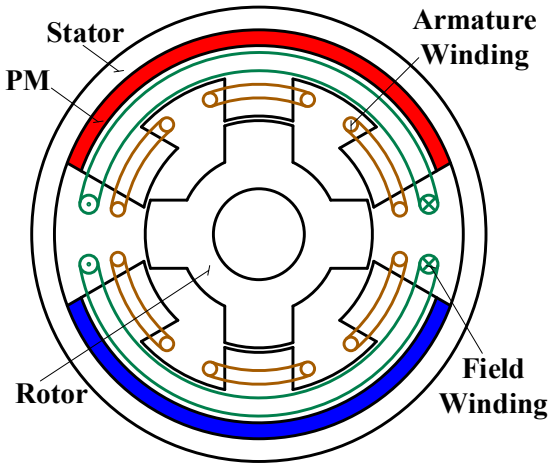

(a) Original series hybridization [LI95]

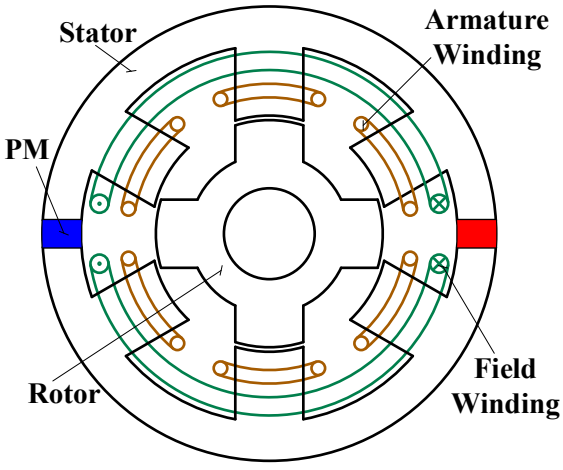

(b) PM moved to the stator yoke [CHA02]

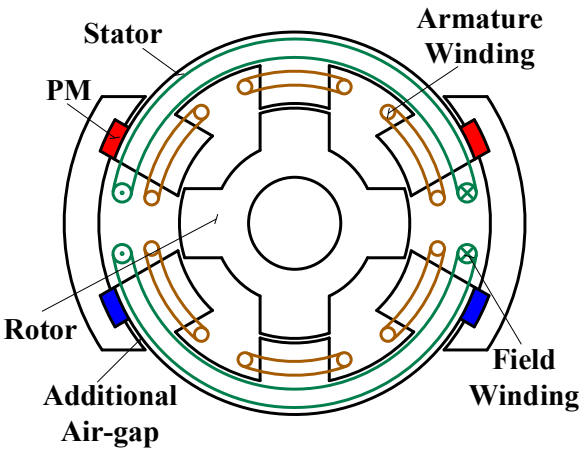

(c) Parallel hybridization with additional air-gap [CHA03]

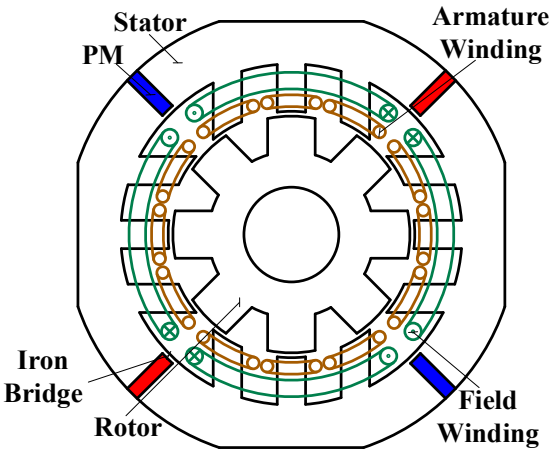

(d) Parallel hybridization with iron bridge [ZHU05] [ZHU06]

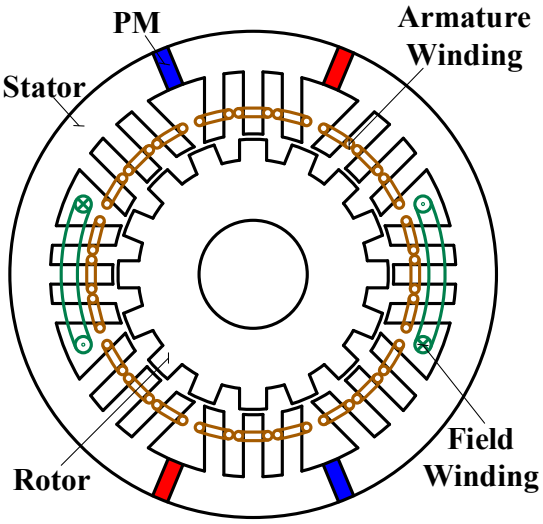

(e) Parallel hybridization by replacing PM poles with field winding poles [CHE08] [ZHA12]

Fig. 1.14. Doubly salient HE machines.

Besides, other HE machines with stator yoke PMs are presented in Figs. 1.15 (a) and (b), with field winding coil pitch of 1 [XU16] and 2 [HE18], respectively. Compared with the conventional doubly salient machines in Fig. 1.14, the three phase back-EMFs of the HE machines in Fig. 1.15 are the same due to symmetrical structure. Similarly, iron bridge is attached not only to connect the stator segment, but also to avoid flux lines of field winding passing through PM.

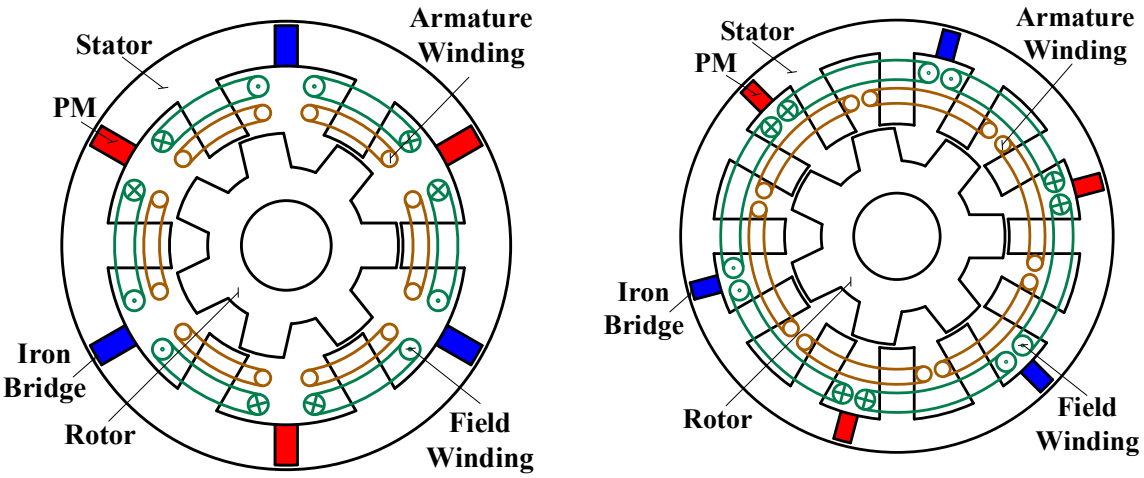

(a) Field winding coil pitch of 1 [XU16] (b) Field winding coil pitch of 2 [HE18]

Fig. 1.15. Other HE machines having PMs on stator yoke.

In Fig. 1.16, the HE machines developed from the flux reversal PM machine are presented. In [GAO18] and [JIA16], PMs are located at the edge and center of the stator tooth, respectively, whereas the field winding is placed in the stator slots as shown in Figs. 1.16 (a) and (b). Moreover, consequent pole machines with PMs alternately located at the tooth center is proposed in [JIA17b], as shown in Fig. 1.16 (c). The magnetic field of the FW is in parallel with PMs, which can ensure the flux regulation capability.

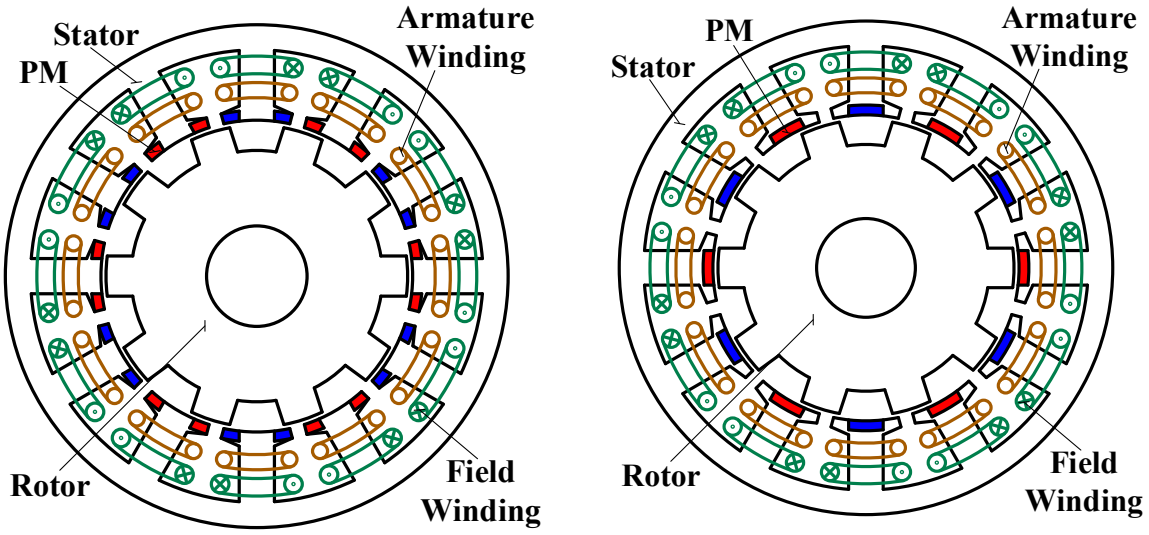

(a) PM sandwiching iron pole [GAO18] (b) Iron pole sandwiching PM [JIA16]

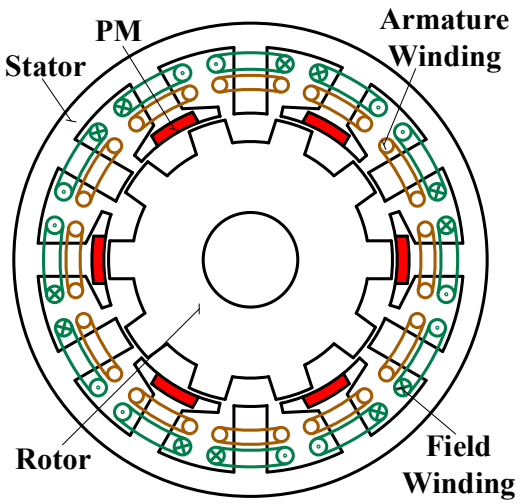

(c) Consequent pole with PMs alternately sandwiched by iron pole [JIA17b]

Fig. 1.16. Flux reversal HE machines.

Flux switching PM machines utilize the flux-concentrating effect of circumferentially magnetized PMs, and possess comparable torque density as IPM machines [FAS14]. Therefore, the HE machines developed based on flux switching PM machines are most widely investigated, as shown in Figs. 1.17-1.19.

In Fig. 1.17 (a), the flux switching HE machine is achieved by attaching additional stator yoke for FW flux path [HOA07]. However, the stator outer diameter is enlarged compared with the conventional flux switching PM machine. In Fig. 1.17 (b), a part of PM is replaced by FW to achieve hybrid excitation [HUA09]. The location, polarity, and flux regulation mechanism of the FW have been investigated in [OWE09] [ZHA15a] [HUA15], as shown in Fig. 1. 17 (c) and (d). It is revealed that the HE machine with inner and outer FW of the same polarity exhibits better flux regulation capability.

To avoid the flux lines of FW passing through the PM and achieve a parallel hybridization, an iron bridge has been introduced in Fig. 1.17 (e) [OWE10]. In fact, the flux switching HE machines in Figs. 1.17 (a) and (e) share similar operating principle and topology, whereas the difference can be perceived as the thickness of iron bridge. Moreover, PM pole-pair and FW pole-pair can be allocated alternately to achieve parallel hybridization in Fig. 1.17 (f) [OWE09]. In [CHE11b], a novel E-core stator is proposed for the flux switching HE machine, as shown in Fig. 1.17 (g). Similarly, it is extended to an axial flux E-core HE flux switching machine in [ZHA16]. In Fig. 1.17 (h), a field winding is introduced in the stator slots of a conventional flux switching PM machine [GAU14]. However, only flux weakening can be achieved via magnetic saturation.

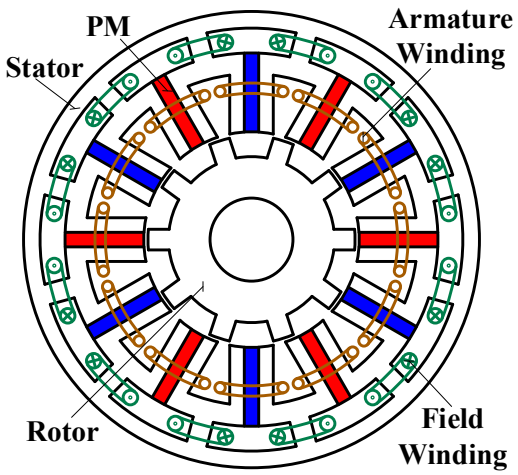

(a) HE machine with additional stator yoke and field winding [HOA07]

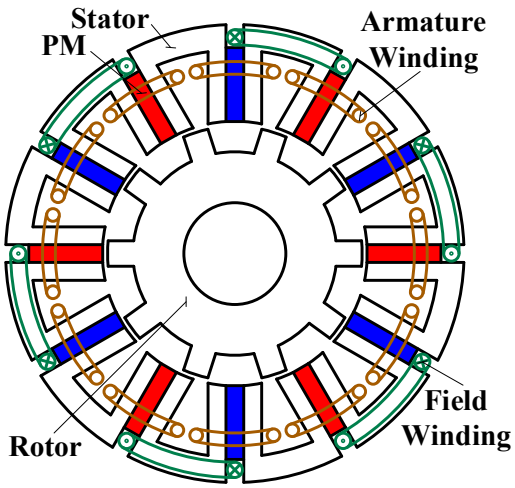

(b) HE machine with FW replacing part of PM [HUA09]

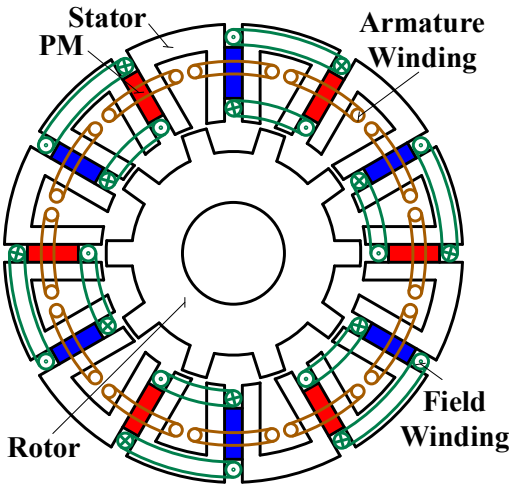

(c) HE machine with outer and inner FW of opposite direction [OWE07]

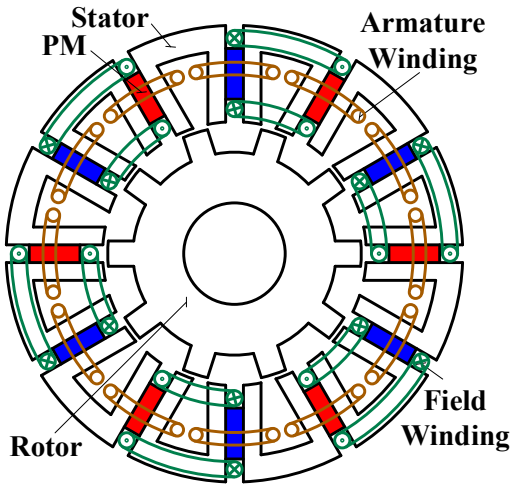

(d) HE machine with outer and inner FW of the same direction [ZHA15a]

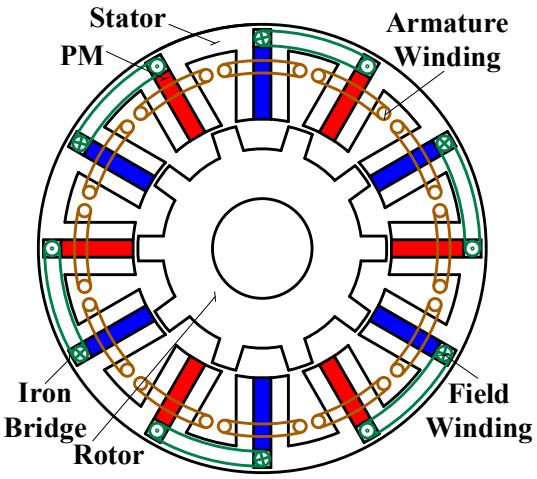

(e) HE machine with iron bridge [OWE10]

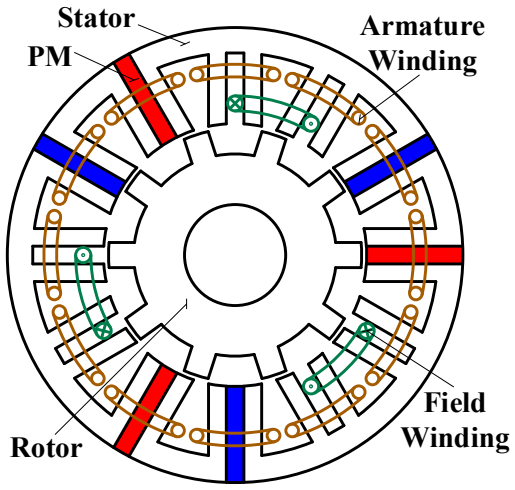

(f) HE machine with PM pole-pair and FW pole-pair locating alternately [OWE09]

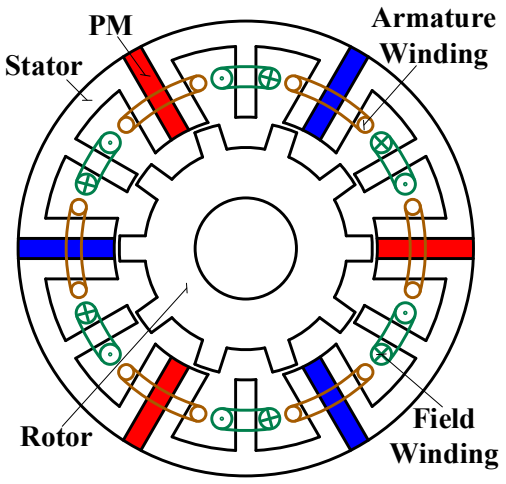

(g) HE machine with E-core segment [CHE11b]

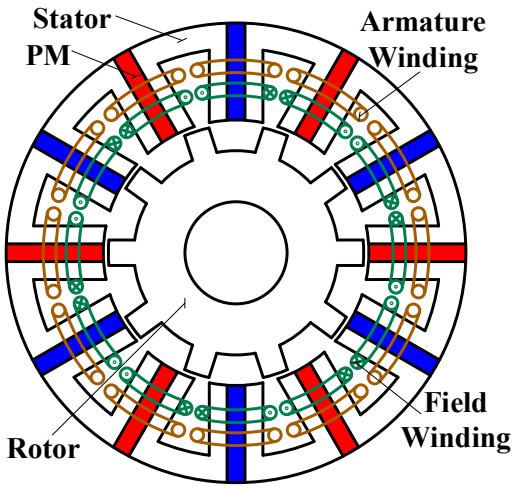

(h) HE machine with by adding field winding in stator slots [GAU14]

Fig. 1.17. Flux switching HE machines.

In Fig. 1.18, the two-part flux switching HE machine is proposed by combining a flux switching PM machine and a flux switching WF machine directly [LIU14a]. The stators are split into a PM field stator and a WF stator, as shown in Figs. 1.18 (a) and (b), respectively. The HE structure inherently possesses parallel hybridization and a wide flux regulation range.

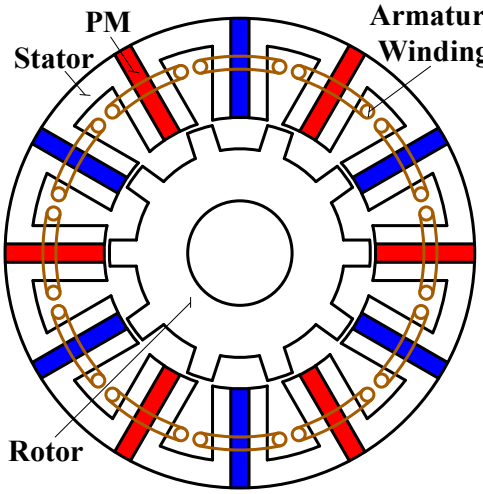

(a) Flux switching PM machine

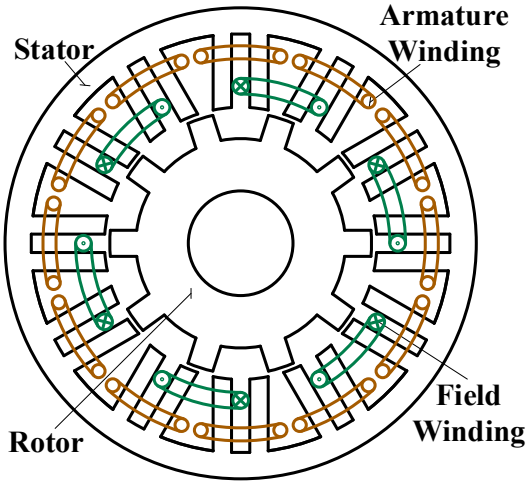

(b) Flux switching WF machine

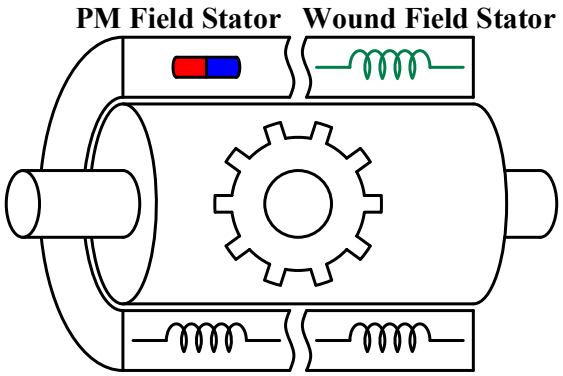

(c) HE machine with the combination of PM field stator and WF stator

Fig. 1.18. HE flux switching machine with the combination of two stators [LIU14a].

In Fig. 1.19, HE flux switching machines with a segmental rotor have been discussed [ALI15b]. Field winding can be wound on the PM poles directly in Fig. 1.19 (a) or wound alternately with PM poles in Fig. 1.19 (b). The machine shown in Fig. 1.19 (a) is series hybridization, whereas parallel hybridization and better flux regulation capability can be obtained in Fig. 1.19 (b).

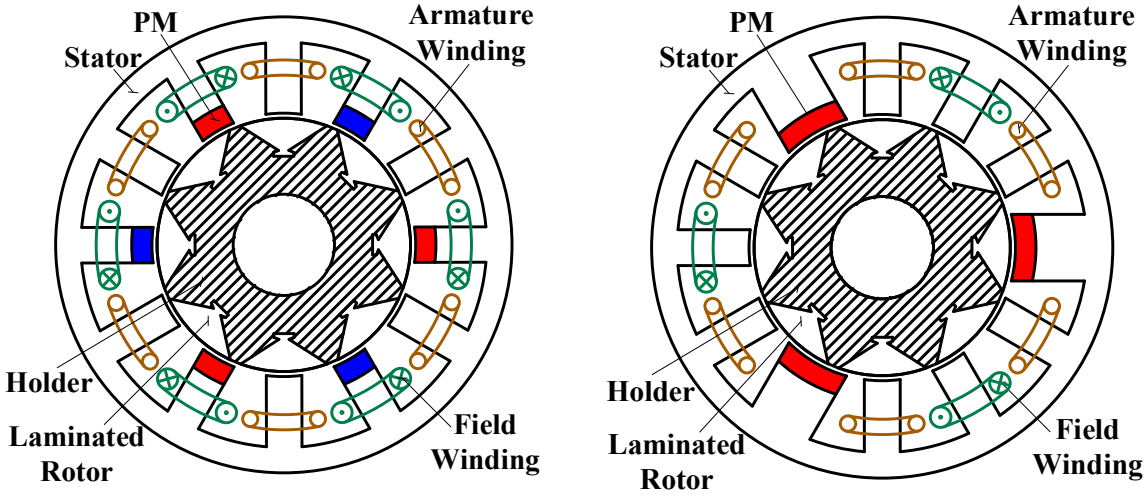

(a) PM and field winding in the same pole (b) PM and field winding in alternate pole

Fig. 1.19. HE flux switching machines with segmental rotor [ALI15b].

Besides locating PMs in the stator yoke, stator tooth tip, stator tooth center, the HE machines with stator slot PM are shown in Figs. 1.20 (a) and (b) [AFI15] [ZHE19]. The PM flux is short-circuited in stator at open-circuit, and the HE machine potentially exhibits high speed fault tolerant capability. When field winding is excited, PM flux is pushed to link with air-gap, and the field excitation can regulate the magnetic field effectively. Furthermore,

different stator/rotor pole combinations and overlapping windings are introduced for the HE stator slot PM machine [ZHU18].

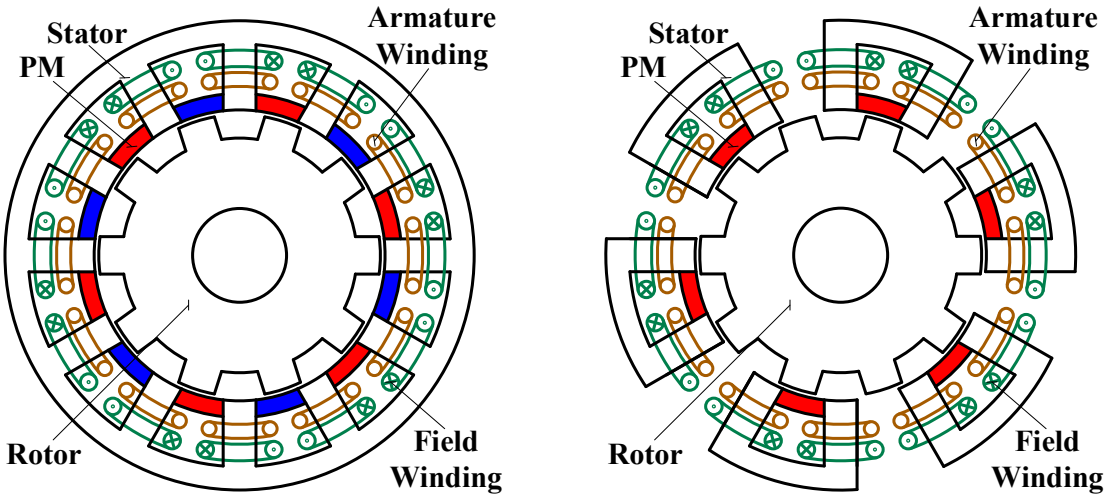

(a) Stator slot HE machine [AFI15] (b) Modular stator HE machine [ZHE19]

Fig. 1.20. HE machine having PMs in stator slots.

Although the HE machines with both stator PM and FW exhibit good heat management, the stator is crowded with PM, field winding and armature winding. To solve the spatial confliction, HE machines with partitioned stator have been proposed in Fig. 1.21 [HUA16b] [JIA17a] [HUA17a] [WU17] [HUA16c] [HUA16d] [HUA18a]. HE machines with inner stator to accommodate field winding, PM, and both field winding and PM are shown in Figs. 1.21 (a)-(c), respectively [HUA16b] [JIA17a] [HUA17a]. In [WU17], the PM is further moved from the inner stator yoke to the inner stator tooth tip to reduce the iron bridge flux leakage, as shown in Fig. 1.21 (d). Besides, the field winding poles can be employed to replace the PM South poles or a pair of PM poles as shown in Figs. 1.21 (e) and (f), respectively [HUA16c] [HUA16d]. It should be noted that PMs and field winding are in series hybridization in Fig. 1.21 (e) and parallel hybridization in Fig. 1.21 (f). Furthermore, circumferentially magnetized PMs can be allocated in the inner stator slots of field winding to alleviate the magnetic saturation and enhance flux regulation capability in Fig. 1.21 (g) [HUA18a].

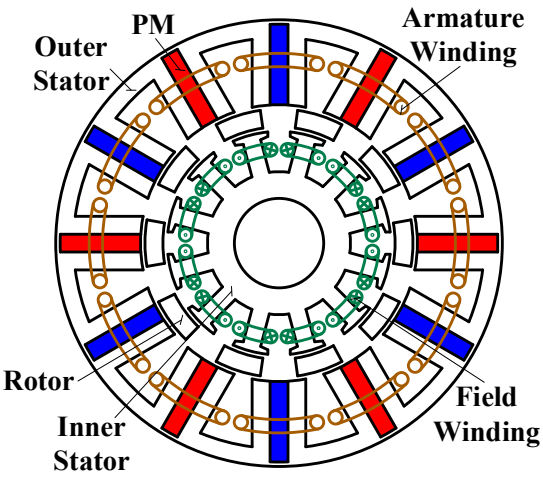

(a) Inner stator accommodates field winding [HUA16b]

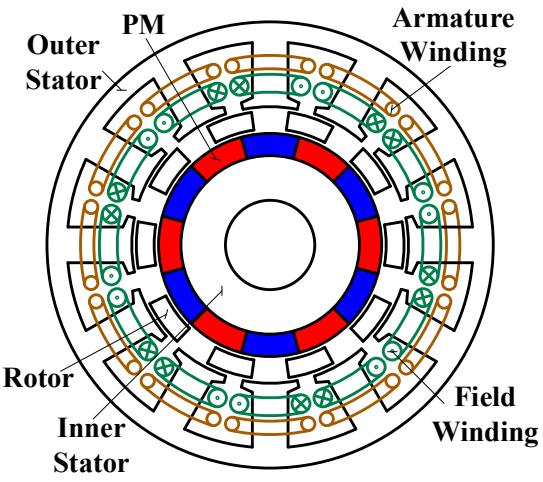

(b) Inner stator accommodates PMs [JIA17a]

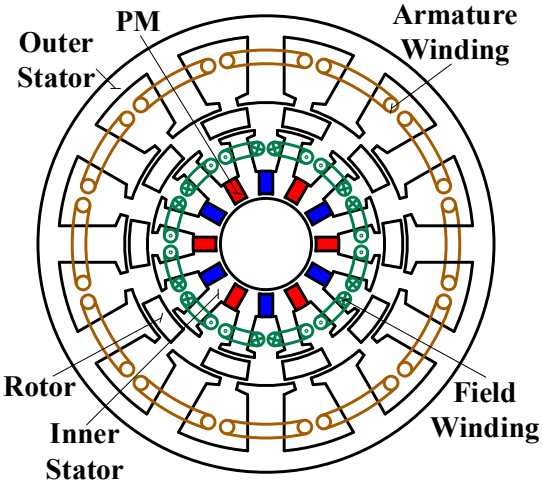

(c) Inner stator accommodates both field winding and PMs [HUA17a]

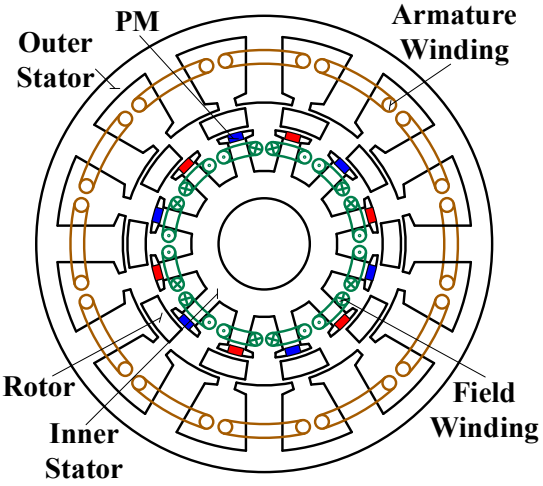

(d) PMs moved to inner stator tooth tip [WU17]

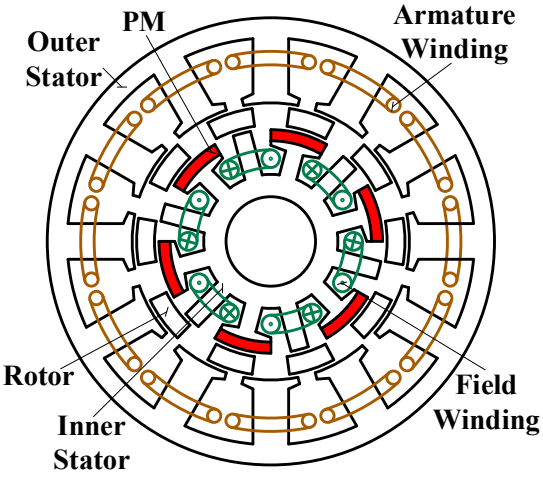

(e) Field winding poles replacing PM South poles [HUA16c]

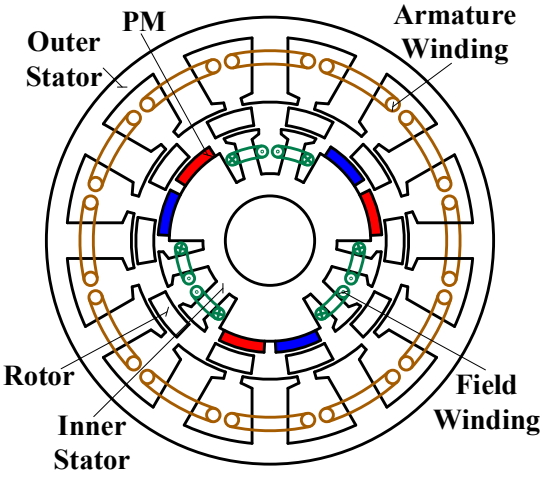

(f) Field winding poles replacing pairs of PM poles [HUA16d]

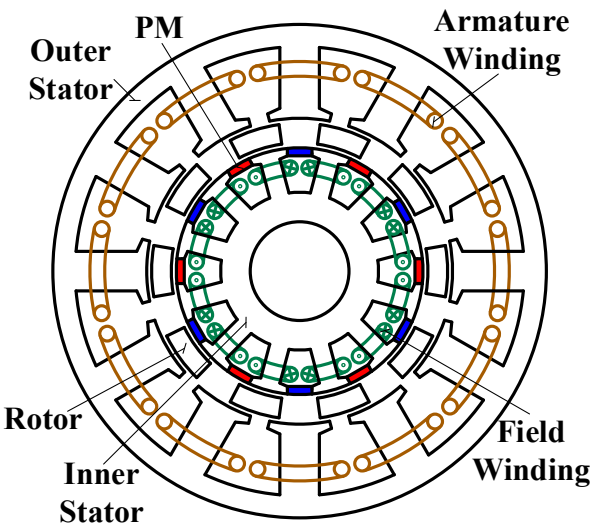

(g) PMs in the inner stator slots of field winding [HUA18a]

Fig. 1.21. HE machines having partitioned stators.

To conclude, the HE machines discussed in Figs. 1.14 - 1.21 can be perceived as the combination of a stator PM machine with a stator WF machine. The machine structure is generally simple without brushes and slip rings. All the excitations are located in the stator and the heat management is efficient. However, the stator spatial confliction problem exists with the PM, field winding and armature winding. Although partition stator concept has been utilized in Fig. 1.21, the segmental rotor requires mechanical connection, making the manufacturing and assembling complex. In conclusion, the advantages and limitations of the HE machines with stator PM and FW are summarized in Table 1.5.

Table 1.5 Advantages and limitations of HE machines with stator PM and FW

	Advantages	Limitations
HE machines with stator PM and FW	✓ Controllable flux with FW ✓ Overall simple structure ✓ Elimination of brushes and slip rings	• Stator spatial confliction of PM, field and armature windings (can be solved by partitioned stator) • Partitioned stator HE machines suffer from mechanical fragile rotor

1.2.4 Others

Moreover, Vernier machine with stator and rotor PM has been widely investigated due to high torque density. HE machines based on stator and rotor PM Vernier machines are presented in Fig. 1.22 [WAN17b] [ZHA18]. PMs are located in stator tooth tip and rotor surface with

consequent pole, whereas the field winding is placed in the stator slots. Series hybridization and parallel hybridization are presented in Figs. 1.22 (a) and (b), respectively.

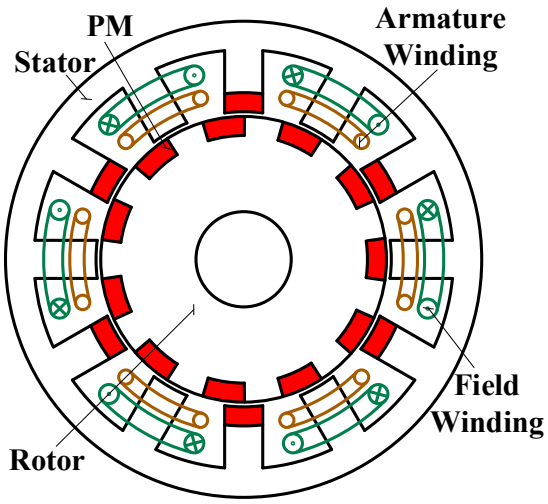

(a) Series hybridization of field winding and stator PMs [WAN17b]

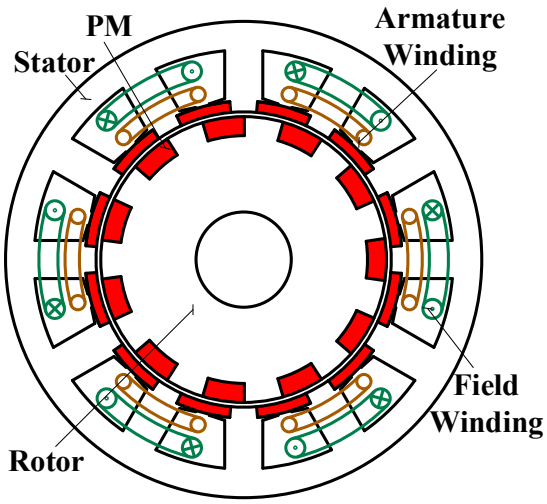

(b) Parallel hybridization of field winding and stator PMs [ZHA18]

Fig. 1.22. HE machines based on Vernier PM machines.

According to the above discussion, the characteristics of the various HE machines can be summarized in Table 1.6. Although various HE machines have been proposed and investigated, the limitations still exist for each classification.

Table 1.6 Comparison of various HE machines

	Rotor PM and FW	Rotor PM and Stator FW	Stator PM and FW
Machine Structure	Overall simple except brushes and slip rings	Complex	Simple
Brushes and Slip Rings	Generally required	No	No
Spatial Confliction	Crowded rotor	No	Crowded stator
Flux Path	2D	3D	2D
SMC or Solid Core	No	Yes	No

1.3 Series and Parallel Hybridization

According to the connection of PM and FW excited magnetic fields, HE machines can be classified as series hybridization and parallel hybridization. If the flux lines of FW pass through

PM, series hybrid excitation is achieved. In this section, the series and parallel hybridization characteristic of the above HE machines will be analyzed.

1.3.1 Series Hybridization

In the series HE machines, the PM and FW excitations share the same flux path, and the FW is simply wound around the PM pole. The series HE machines have been developed from the rotor SPM machine (Fig. 1.4 [HEN94a] [FOD07] [LIN14]), the stator doubly salient PM machine (Figs. 1.14 (a) and (b) [LI95] [CHA02]), the flux switching PM machine (Figs. 1.17 (b), (c) and (d) [HUA09] [OWE09] [ZHA15a], Fig. 1.19 (a) [ALI15b]), the partitioned stator PM machine (Figs. 1.21 (b) and (e) [JIA17a] [HUA16c]), and the Vernier machine (Fig. 1.22 (a) [WAN17b]) by replacing a part of PM with FW, or adding FW around the PM.

The series HE machines generally possess simple structure with the combination of PM and FW excitations. However, the FW flux path is of significant reluctance and the flux regulation capability is limited. Moreover, the flux lines of FW excitation passing through the PM may potentially cause irreversible demagnetization.

1.3.2 Parallel Hybridization

Compared with series HE machine, the flux path of FW excitation in the parallel HE machine bypasses the PM. Therefore, the flux regulation capability can be enhanced and the risk of demagnetization is reduced. The parallel HE machine discussed above can be summarized as follows.

Type I: Iron bridge to provide additional flux path for FW excitation. This concept has been utilized in the IPM HE machine (Fig. 1.6 [AKE00]), the doubly salient HE machine (Fig. 1.14 (c) [ZHU05] [ZHU06]), the flux switching HE machine (Figs. 1.17 (a) and (e) [HOA07] [OWE10]), the partitioned stator HE machine (Figs. 1.21 (a) and (c) [HUA16b] [HUA17a]). However, since the iron bridge is saturated by the PM flux, the reluctance of FW flux path is still large and the flux regulation ratio is restricted.

Type II: One pole consisting of PM and FW excitations parallel. This classification of HE machine contains the SPM HE machine (Fig. 1.9 [ALI16] [HUS18] [YAO15] [JAW16] [ALI15a] [HUS17]), the IPM HE machine (Fig. 1.6 (b) [AKE00]), the flux reversal HE machine (Fig. 1.16 [GAO18] [JIA16] [JIA17b]), the partitioned stator HE machine (Fig. 1.21 (d) [WU17]), and the Vernier HE machine (Fig. 1.22 (b) [ZHA18]). Obviously, the PM should

be located at the stator or rotor tooth tip, and otherwise, the PM flux short-circuits from the FW flux path as Type I.

Type III: Two-part parallel HE machine by combining a PM machine and a WF machine axially. The two-part rotor PM HE machine discussed in Fig. 1.8 [SYV98] [NAO01] shares the same stator, whereas the two-part flux switching HE machine discussed in Fig. 1.18 [LIU14a] shares the same rotor. Moreover, the two-part HE machine can consist of both different stators and rotors. In [GEN15] [WU18], the rotor PM machine is combined with a doubly salient WF machine to achieve parallel hybridization. It should be noted an additional axial gap is introduced due to end-winding of field coils, and the axial length is increased inevitably.

Type IV: PM pole-pairs and FW pole-pairs alternately allocated. This concept has been employed in the SPM HE machine (Fig. 1.5 [LUO00]), the doubly salient HE machine (Fig. 1.14 (d) [CHE08] [ZHA12]), the flux switching HE machine (Fig. 1.17 (f) [OWE09], Fig. 1.19 (b) [ALI15b]), and the partitioned stator HE machine (Fig. 1.21 (f) [HUA16d]).

Type VI: Slot PM HE machine with tangential magnetized PM. This classification includes the rotor slot PM HE machine (Fig. 1.7 [FUK08a] [YAM11] [HWA18] [HUA16a]), the stator slot PM HE machine (Fig. 1.20 [AFI15] [ZHE19] [ZHU18]), the partitioned stator slot PM HE machine (Fig. 1.21 (g) [HUA18a]), and the claw pole slot PM HE machine (Fig. 1.12 [CHA96] [CHA97] [HEN94b] [ISH96]). Since the PM flux is short-circuited without field excitation, the slot PM HE machines exhibit high fault tolerant capability.

Type V: Toroidal FW with additional flux path. In Figs. 1.10-1.14, a stationary toroidal field winding is added for the rotor PM machine to regulate magnetic field [MCC87] [SPO89] [TAP03] [AYD02] [WAN05] [YAN08] [LI17] [VID05a] [VID05b] [HLI08] [NED11] [ZHA08] [HAN11] [LIU17a] [CHA96] [CHA97] [HEN94b] [ISH96] [REB11] [REB14] [KOS05] [KOS10]. The FW excitation has both radial and axial fluxes, and consequently, SMC or solid stator and rotor cores are required to allow for 3D flux. The benefit of this classification is better spatial utilization with separate PM and FW flux paths. However, the machine configuration is complex and manufacturing can be expensive.

Although the flux path of FW excitation bypasses the PM in the above topologies, the HE machine with iron bridge (Type I) possesses a lower flux regulation capability due to saturated iron bridge. Therefore, the HE machine with iron bridge can be classified as the third type beside series and parallel hybridizations [WAN12b].

According to the above discussion, the characteristics of the series and parallel hybridization can be summarized in Table 1.7. Although series HE machines generally have simpler structure, the flux regulation capability and demagnetization withstanding capability are limited. Therefore, the parallel HE machines are more popular considering electromagnetic performance.

Table 1.7 Comparison of series/parallel hybridization

	Series Hybridization	Parallel Hybridization
Machine structure	Generally simple	More complex
Flux regulation capability	Limited	Good
Demagnetization withstanding capability	Limited	Good

1.4 2D and 3D Magnetic Fields

According to the magnetic fields of PM and FW excitations, HE machines can also be classified into 2D and 3D HE machines. If the PM and FW excitations have both radial and axial fluxes, it is called as a 3D HE machine.

1.4.1 2D Magnetic Field

2D HE machine can be achieved by attaching a rotary FW to the rotor PM machines (Figs. 1.4-1.9 [HEN94a] [FOD07] [LIN14] [AKE00] [LUO00] [FUK08a] [YAM11] [HWA18] [HUA16a] [SYV98] [NAO01] [ALI16] [HUS18] [YAO15] [JAW16] [ALI15a] [HUS17]), or a stationary FW to the stator PM machines (Figs. 1.14-1.22 [LI95] [CHA02] [CHA03] [ZHU05] [ZHU06] [LIU10a] [CHE08] [ZHA12] [CHE14] [XU16] [HE18] [GAO18] [JIA16] [JIA17b] [FAS14] [HOA07] [HUA09] [OWE09] [ZHA15a] [HUA15] [OWE10] [CHE11b] [ZHA16] [GAU14] [LIU14a] [ALI15b] [AFI15] [ZHE19] [ZHU18] [HUA16b] [JIA17a] [HUA17a] [WU17] [HUA16c] [HUA16d] [HUA18a] [WAN17b] [ZHA18]). The hybridization can be either in series or parallel, as illustrated in section 1.3.

Overall, the machine structure is simple for designing, optimizing, manufacturing, and assembling. However, since the PM and FW excitations are located in the same component (stator or rotor), the spatial confliction inevitably results in limited torque density as well as flux regulation capability.

1.4.2 3D Magnetic Field

Compared with 2D HE machine, the 3D magnetic field structure is more complex. As shown in Figs. 1.10-1.13 [MCC87] [SPO89] [TAP03] [AYD02] [WAN05] [YAN08] [LI17] [VID05a] [VID05b] [HLI08] [NED11] [ZHA08] [HAN11] [LIU17a] [CHA96] [CHA97] [HEN94b] [ISH96] [REB11] [REB14] [KOS05] [KOS10], the HE machines with rotor PM and toroidal field winding have both radial and axial fluxes. The field excitation has separate axial flux path with PM excitation, and therefore, this classification of HE machine is generally parallel hybrid with a wide flux regulation range.

Since the toroidal field winding is located at the end or center of stator core, the spatial utilization is improved. However, SMC or solid material stator and rotor cores are required for both radial and axial fluxes, making the manufacturing and assembling complex.

According to the above discussion, the characteristics of HE machines with 2D/3D magnetic fields can be summarized in Table 1.8. Although the HE machines with 3D magnetic field solve the spatial confliction of co-existence of PM and field winding, the machine topologies are complex, making the designing, manufacturing and assembling complicated. Therefore, the HE machines with 2D magnetic field are generally more popular.

Table 1.8 Comparison of HE machines with 2D/3D magnetic fields

	2D Magnetic Field	3D Magnetic Field
Machine structure	Simple	Complex
Field winding	Axial winding	Toroidal winding
SMC or solid core	No	Yes
Spatial confliction	Yes	No

1.5 Control of Hybrid Excited Machines

1.5.1 Typical Flux Regulation Performance

In the previous sections, various HE machine topologies have been overviewed, and the benefits as well as drawbacks are demonstrated. In this section, a typical flux switching HE machine, shown in Fig. 1.17 (a), is chosen to illustrate the basic flux regulation of hybrid excitation.

The open-circuit field distribution of the HE machine is illustrated in Fig. 1.23. The FW and PM excitations are in parallel, and the field excitation can regulate the flux density effectively. Fig. 1.24 shows the flux linkage variation with field excitation current density. It

can be observed that the field excitation can control the magnetic field as well as the flux linkage. Without PM excitation, i.e. B_r=0, the effect of positive and negative DC excitation is symmetrical. With the increase of PM remanence, the flux regulation ratio is reduced due to magnetic saturation. Overall, the DC current can regulate the flux linkage, and consequently the output capability according to the EV/HEV requirements effectively. At low speed operation, positive DC excitation can be employed to improve the starting torque. At high speed operation, negative DC excitation can be injected to weaken the magnetic field.

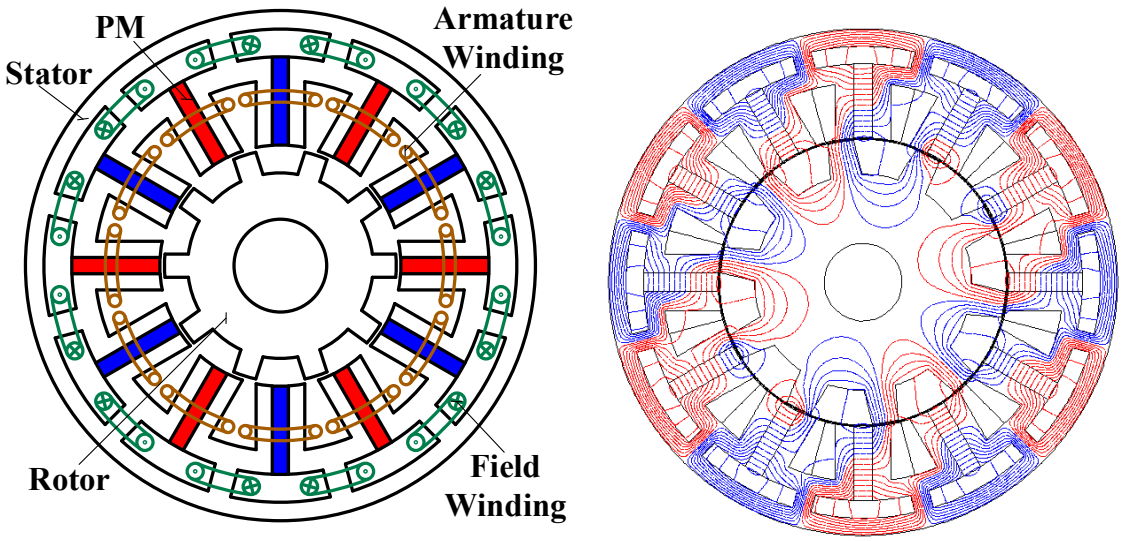

Fig. 1.23. Field distribution of flux switching HE machine.

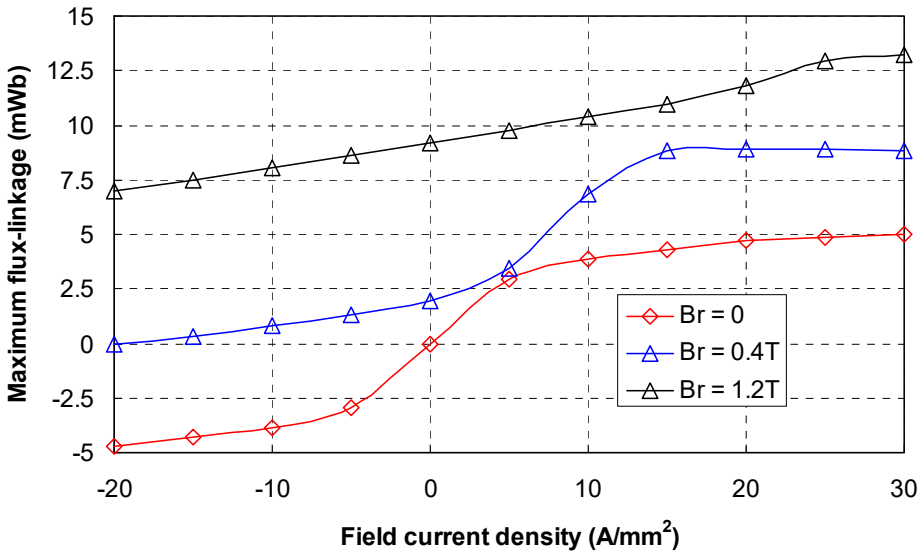

Fig. 1.24. Flux linkage variation with field excitation for the flux switching HE machine.

1.5.2 Flux Weakening Control Strategies

An important issue for EV/HEV is wide constant power speed region (CPSR) and potential to operate at deep flux weakening region [SOO02] [REF05]. Different from conventional PM machines, both the field excitation current and the *d*-axis current can be utilized to adjust the magnetic field in the HE machines, which provides more flexible control parameters for flux-weakening operation [CHU15]. It has been revealed that better flux weakening performance can be expected for HE machine compared with conventional PM machine in [ZHA15b]. In [KEF10], a novel flux weakening control strategy is discussed for the HE machine by utilizing double excitations to enhance the flux weakening performance.

Therefore, three control strategies can be employed during flux weakening control, i.e. (1) utilization of field excitation current only, (2) utilization of armature current only, and (3) utilization of both field and armature current, as listed in Table 1.9.

Table 1.9 Flux weakening control strategies for HE machines

	Method I	Method II	Method III
i_{dc}	Varying	Constant	Varying
i_d	Constant	Varying	Varying
i_q	Varying	Varying	Varying

In [POT19], the three flux weakening control strategies are conducted on a stator slot PM HE machine shown in Fig. 1.20 (a). The measured torque, power and efficiency map with three flux weakening strategies are compared in Fig. 1.25. The efficiency is relatively low due to the experiments on a small motor with only 90mm outer diameter and 25mm axial length and thus the mechanical loss is a major portion. However, the improvement of efficiency with different control methods can still be identified. At constant torque region, all three methods can achieve the same output torque due to the same flux-enhancing field excitation currents. In the flux weakening region, the torque of Method-I deteriorates significantly, and the operating speed range is also limited by weakening field excitation current only. Based on the utilization of the optimal field excitation and *d*-axis armature currents, Method-III can obtain a wider speed region compared with Method-I and achieve higher efficiency in the flux weakening region compared to Method-II.

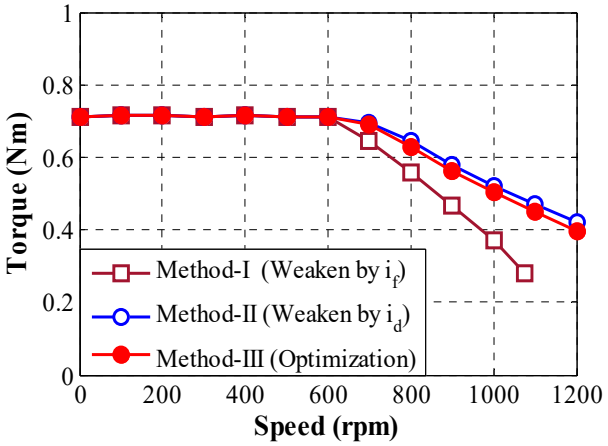

(a) Torque-speed envelope

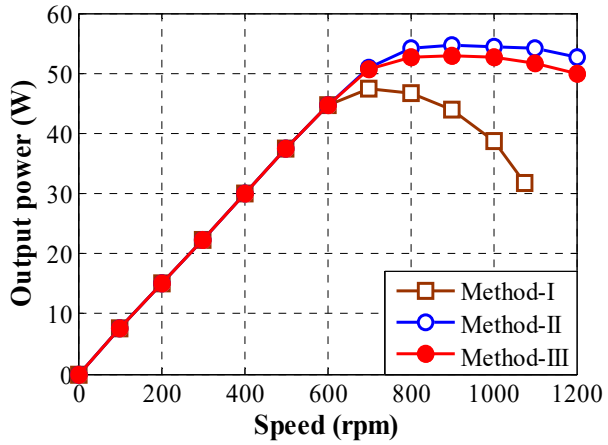

(b) Power-speed envelope

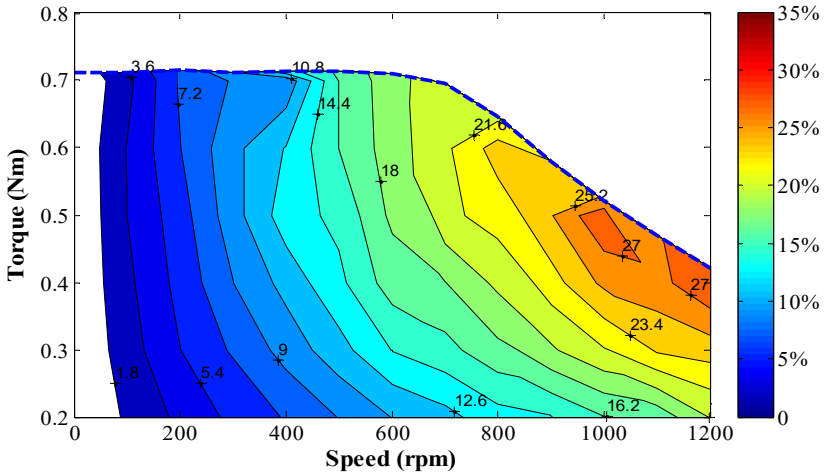

(c) Efficiency map by regulating *d*-axis current only with constant maximum field excitation (Method II)

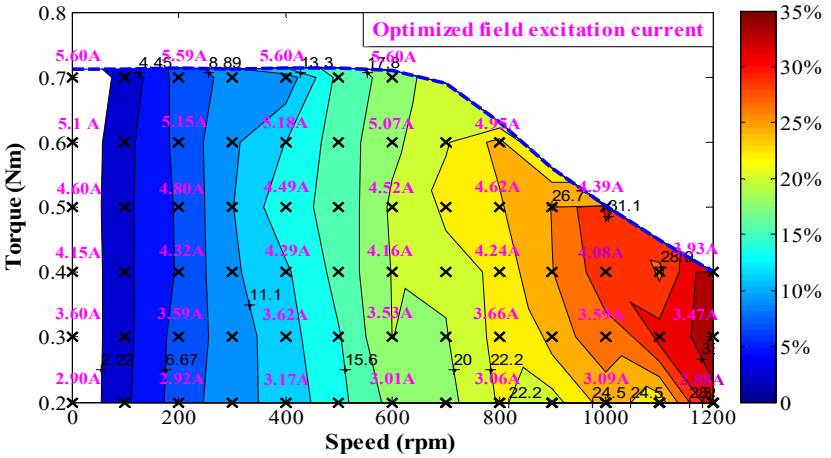

(d) Efficiency map by regulating both field and *d*-axis currents (Method III)

Fig. 1.25. Measured torque, power, and efficiency maps with different flux weakening strategies [POT19].

Moreover, a self-optimization method of field current based on variable step size search theory is proposed in [WAN13]. In [SHI07], the minimum copper loss and maximum torque control strategies under flux weakening region are investigated. In [DIN19], an optimized maximum torque per copper loss control strategy is investigated for HE machine. In [LIU19], an improved control strategy for maximum output power is presented with the consideration of winding resistance and magnetic saturation.

1.5.3 Uncontrolled Generator Fault Mitigation

The PM machines have been popular due to high torque density and efficiency. However, some parasitic effect exists in the PM machines inevitably, such as cogging torque and potential uncontrolled overvoltage fault at high speed operation. Recently, the slot PM HE machines have been investigated and are shown to exhibit high fault tolerant capability. The slot PM HE machine can be classified into the rotor slot PM HE machine (Fig. 1.7 [FUK08a] [YAM11] [HWA18] [HUA16a]), the stator slot PM HE machine (the single stator in Fig. 1.20 [AFI15] [ZHE19] [ZHU18] and the partitioned stator in Fig. 1.21 (g) [HUA18a]), and the claw pole slot PM HE machine (Figs. 1.12 (a) and (b) [CHA96] [CHA97] [HEN94b] [ISH96]). All the slot PM HE machines share similar operating principle and characteristic.

The stator slot PM HE machine in Fig. 1.20 (a) is taken as an example, and the flux paths with/without field excitation are illustrated in Fig. 1.26. Without field excitation, the PM flux is short-circuited in the stator and hardly link with the rotor. When the field current is employed, the PM flux is pushed to link with the rotor and air-gap flux density is produced. As salient

rotor moves, the flux variation will produce back-EMF in the armature winding. Fig. 1.27 shows the open-circuit back-EMF with different DC excitations for the stator slot PM HE machine. The back-EMF is almost 0 without DC excitation and the amplitude can be regulated by the field current, verifying the theoretical analysis.

Compared with the stator WF machine, the introduction of PM alleviates the magnetic saturation and further improves the torque density. Compared with other PM machine, the PM flux hardly links with rotor without DC excitation, and the cogging torque is negligible. Furthermore, the open-circuit back-EMF caused by PM only is almost 0. Therefore, the slot PM HE machines exhibit high fault tolerant capability considering high speed operation (see next sub-section), which is critical for EV/HEV.

(a) Without field excitation (b) With field excitation

Fig. 1.26. Schematic of PM and DC flux paths for stator slot PM HE machine at open-circuit.

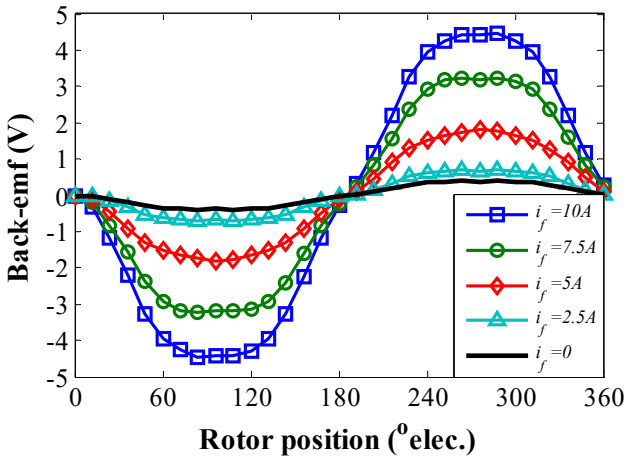

Fig. 1.27. Open-circuit back-EMF corresponding to the DC excitation current for the stator slot PM HE machine.

For the EV/HEV with high requirements of safe operation and fault tolerance in extreme environments, reliability of the machine system must be considered [WEL04] [LIU10b]. Among the various machine fault types, the uncontrolled generator fault (UCGF) at high speed is one of the most serious faults that could damage the drive system [JAH99] [LIA05]. It occurs

when the gating control signals of the inverter switches are suddenly removed during operation. This damage can be more severe for the PM machines since the magnetic field is hard to regulate and the back-EMF can be several times higher than the rated supply voltage at high speed.

In order to extend the operating region within the current and voltage limits, flux-weakening control is demanded for PM machines [SOO02] [REF05]. Should the flux-weakening control signals unexpectedly disappear during high speed operation, the winding with high back-EMF would instantaneously become a large voltage source and deliver regenerated current back to the DC-link through the free-wheeling diodes of the inverter switches, as shown in Fig. 1.28. If the DC-link capacitor cannot absorb the abruptly regenerative energy, both the capacitor and inverter switches may be damaged as the result of overvoltage. Therefore, a trade-off between healthy operating performance and fault tolerance capability is required during optimization for PM machines [PEL11].

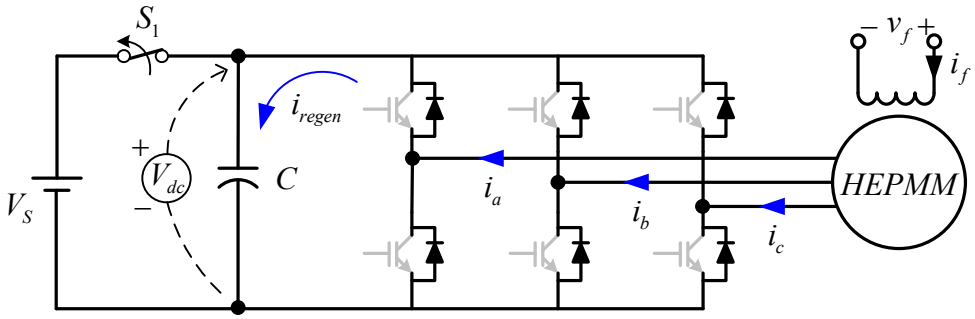

Fig. 1.28. Uncontrolled generator fault due to the remove of gate signals.

For HE machines with the combination of PM and FW magnetic fields, the magnetic field can still be weakened by field excitation at the UCGF. In [ZHU19a], a field excitation control strategy with fault protection is proposed as shown in Fig. 1.29. In normal operation, the maximum flux-enhancing field excitation current is employed to achieve the highest torque. When the UCGF occurs, the DC-link capacitor is rapidly charged by the regenerated current. Therefore, the DC-link voltage can be measured as the detection of UCGF, and consequently the field excitation current can be diminished to protect the inverter from overvoltage damage.

The UCGF experiment is conducted on a stator slot PM HE machine shown in Fig. 1.20 (a) in [ZHU19a] and the test results are presented in Fig. 1.30. The field current is maximized to achieve high output capability at healthy operation. When the UCGF occurs, the DC-link capacitor is rapidly charged, which potentially damages the inverter. However, the overvoltage

problem in the DC-link capacitor can be eliminated by removing the field excitation. The regenerated current as well as power storage in capacitor can be sharply reduced to zero by controlling DC excitation, which is beneficial to protect the capacitors and inverter switches.

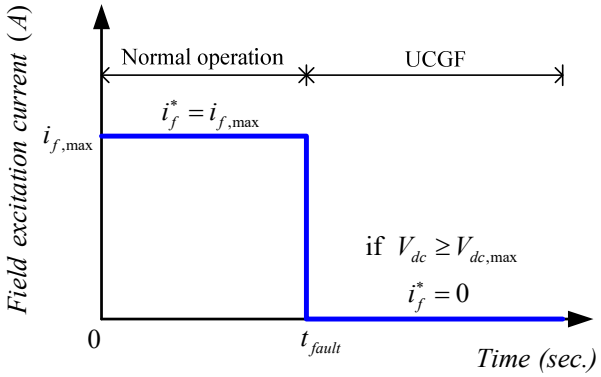

Fig. 1.29. Field excitation control strategy with fault protection [ZHU19a].

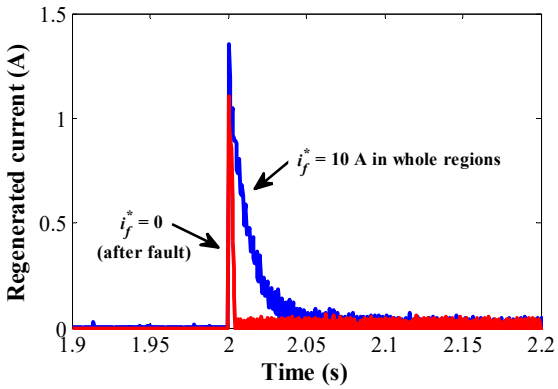

(a) Regenerated current

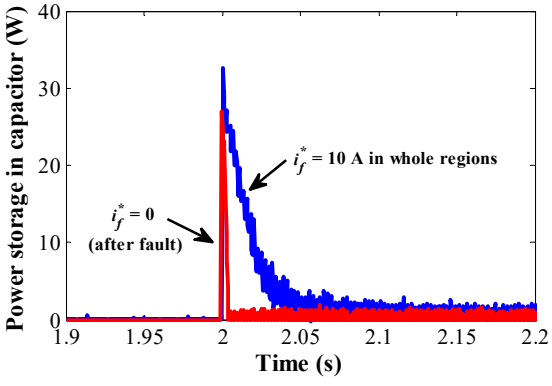

(b) Measured power storage in capacitor

Fig. 1.30. Measured regenerated current and power storage in capacitor of the proposed fault protection method (i_{dc}= 0) compared to the method that utilising the maximum field excitation current in whole regions (i_{dc}= 10 A) [ZHU19a].

1.5.4 Integrated Hybrid Excitation with Open-Winding

Since the HE machine contains PM, field and armature windings, the spatial confliction inevitably restricts the torque density as well as flux regulation capability. In [ZHU16], the field and armature windings are integrated with open-winding inverter shown in Fig. 1.31. Different from conventional machines, the neutral point of three-phase armature winding is released. The terminals of each phase winding are connected to two inverters at the same time, so that zero-sequence, i.e. DC excitation, can flow in the winding. Since the field winding is removed with open-winding, it is DC coil free in the integrated HE machine [WAN19].

Besides, the conductor area for DC and AC excitation is enlarged with integrated winding, and consequently, the copper loss can be reduced, and the operating range can be extended. Furthermore, Fig. 1.32 shows the measured operating envelopes with separate as well as integrated DC and AC winding. The operating range is extended, and efficiency is improved due to the reduction of winding resistance. Moreover, the voltage utilization ratio is increased with open-winding drive circuit, which is beneficial to the low voltage battery supplied EV/HEV.

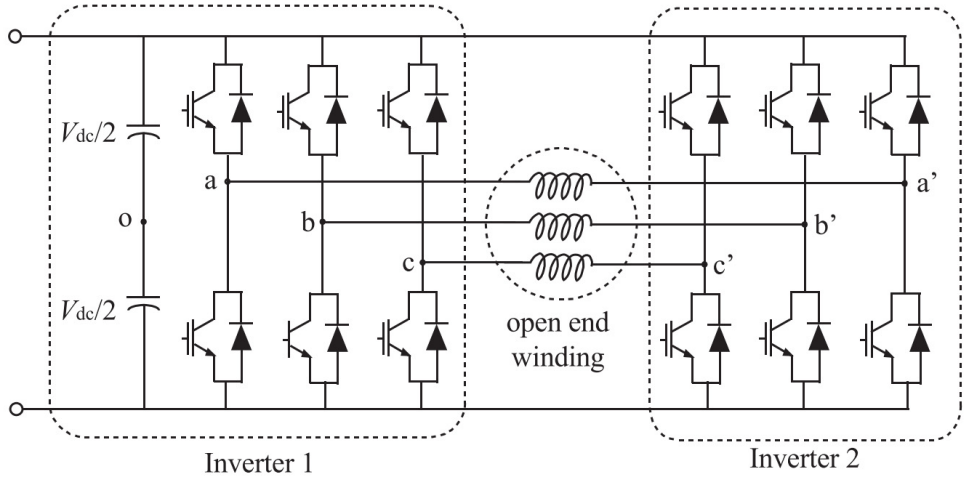

Fig. 1.31. Open-winding inverter with single voltage source.

The concept to integrate field and armature winding using open-winding technique is firstly introduced in the variable flux reluctance machine in [ZHU16]. Then, it is further extended to the flux reversal HE machine (Figs. 1.33 (a) and (b) [JIA16] [JIA17b]), Vernier HE machine (Fig. 1.33 (c) [WAN17c]), and flux modulated HE machine (Fig. 1.33 (d) [JIA17a]). In fact, the integrated field and armature winding technique is suitable for all the HE machines with DC and AC coils in the same slots to further enhance the performances.

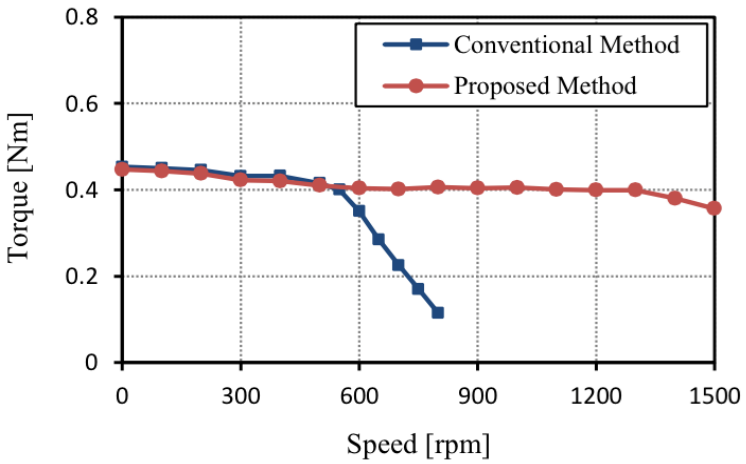

(a) Torque-speed curves

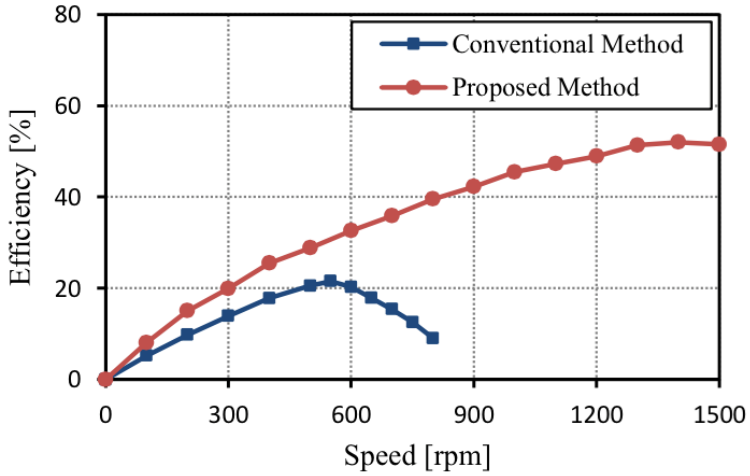

(b) Efficiency-speed curves

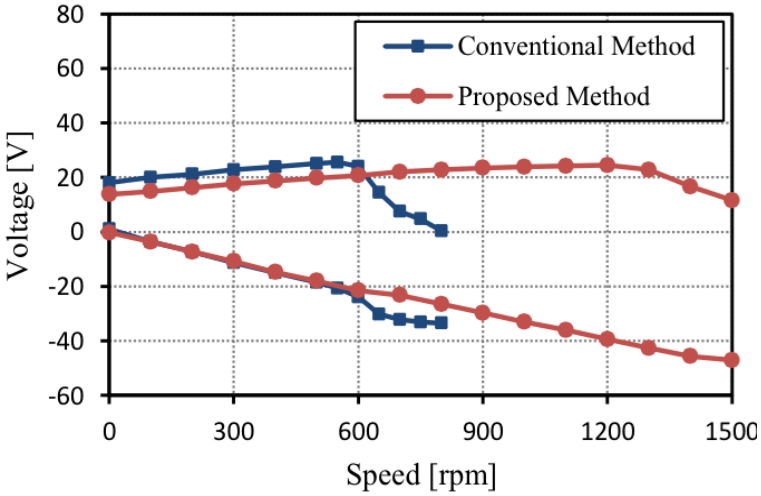

(c) Voltage-speed curves

Fig. 1.32. Measured operating envelopes with separate field and armature winding (conventional method) as well as integrated field and armature winding (proposed method with open-winding technique) [ZHU16].

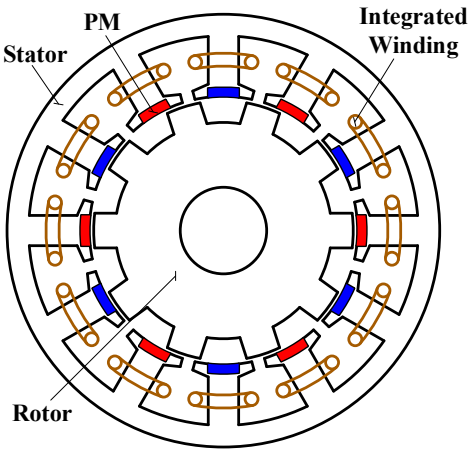

(a) Flux reversal machine [JIA16]

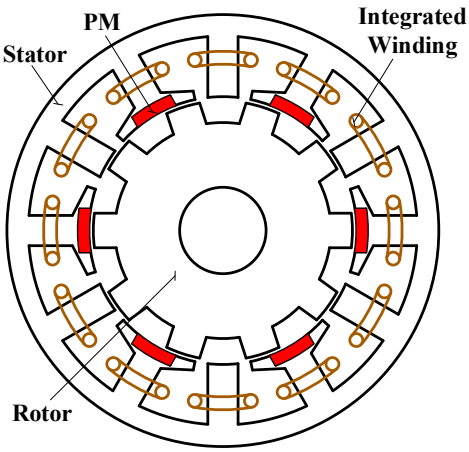

(b) Flux reversal machine with consequent pole stator PM [JIA17b]

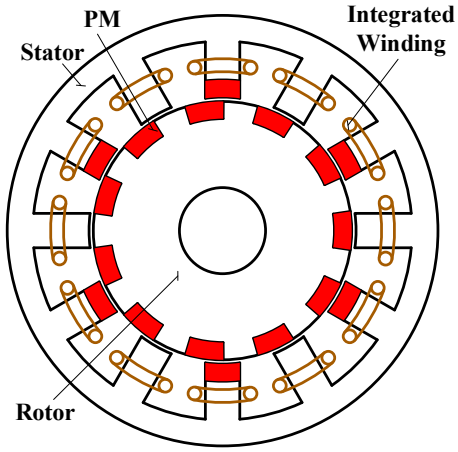

(c) Vernier machine with both stator and rotor PMs [WAN17c]

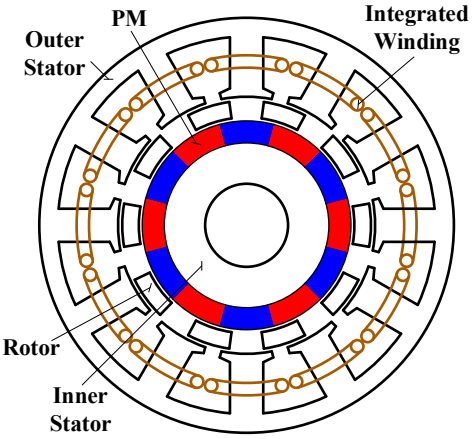

(d) Flux modulation machine [JIA17a]

Fig. 1.33. HE machines with integrated field/armature winding.

1.6 Research Outline and Major Contributions

1.6.1 Research Outline

The introduction in this chapter is mainly concerned with various HE machines, including the machine topologies and control strategies. Then, the merits as well as challenges are identified and compared with pure PM or FW excitation. Based on the existing HE machine topologies, some novel HE machines are further proposed and investigated in this thesis. The proposed HE machines are optimized in comparison with commercialized IPMM to demonstrate the benefits and limitations. The research structure and methodologies of the thesis are summarized in Fig. 1.34. The major HE machine (HEM) topologies proposed and investigated in this thesis are presented in Fig. 1.35.

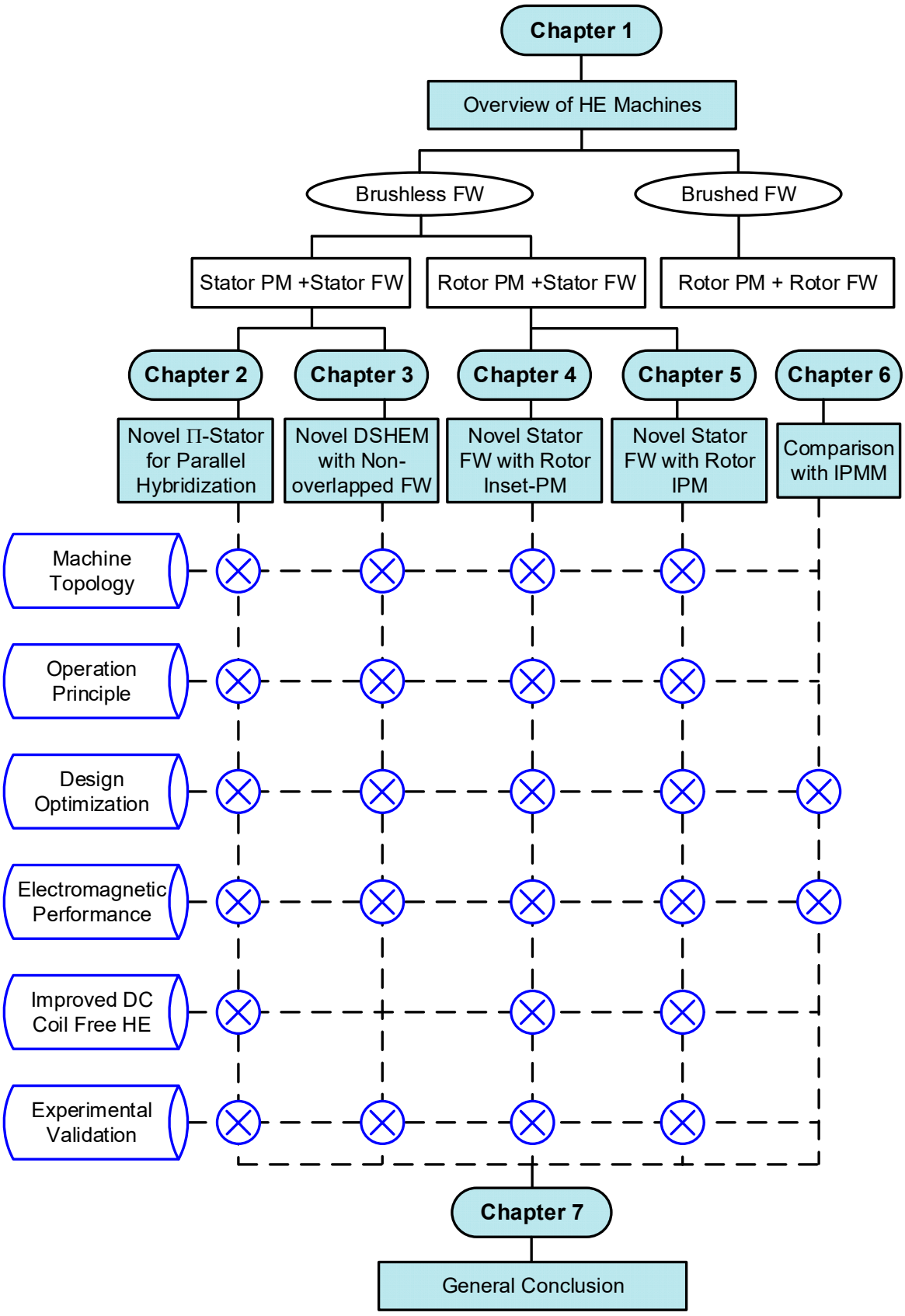

Fig. 1.34. Illustration of the research scope in this thesis.

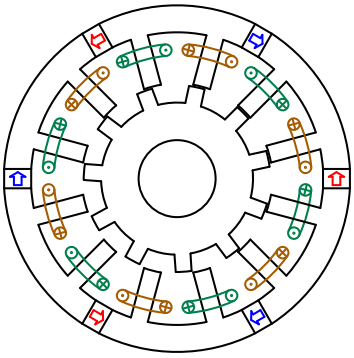

(a) HEM with parallel flux path, Chapter 2

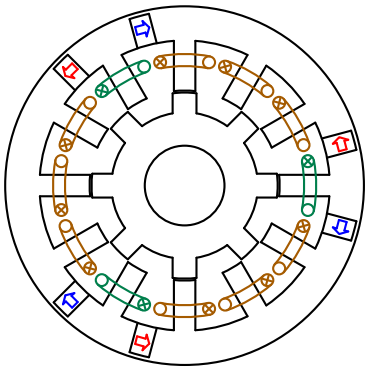

(b) DSHEM with non-overlapped field winding, Chapter 3

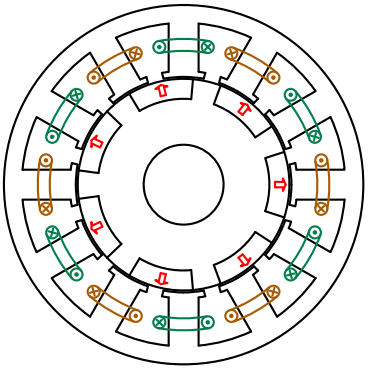

(c) HEM with consequent-pole SPM rotor, Chapter 4

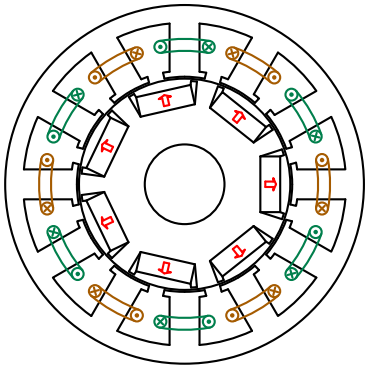

(d) HEM with consequent-pole IPM rotor, Chapter 5

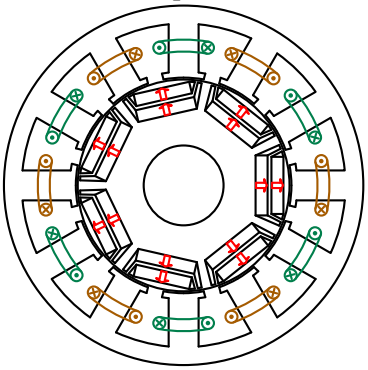

(e) HEM with consequent-pole 2IPM rotor, Chapter 5

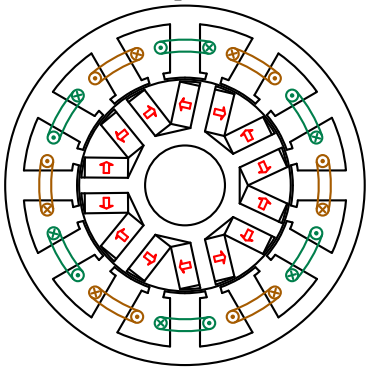

(f) HEM with consequent-pole VIPM rotor, Chapter 5

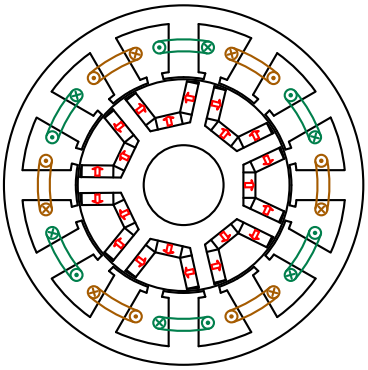

(g) HEM with consequent-pole UIPM rotor, Chapter 5

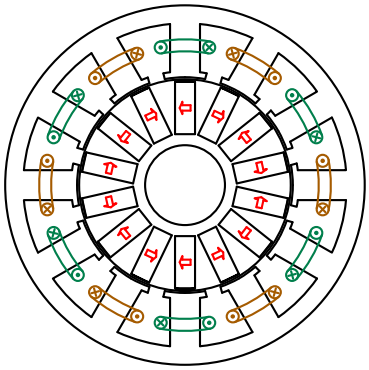

(h) HEM with consequent-pole spoke-PM rotor, Chapter 5

Fig. 1.35. Configurations of the proposed HEMs in this thesis (Red and blue arrow components indicate PMs, brown and green lines indicate field and armature windings).

The contents of the subsequent chapters can be summarized as follows:

Chapter 2

This chapter proposes a novel HE machine with Π-shape segment stator core to enhance the flux regulation capability. The machine topology and operation principle are introduced in detail from the perspective of PM and FW flux paths. Based on the 2D FE calculation, the proposed machine is optimized and compared with an existing HE counterpart. Furthermore, open-winding technique is employed to eliminate the field winding and reduce the copper loss. Finally, a prototype is fabricated to validate the FE predictions.

Chapter 3

This chapter proposes a novel doubly salient HE machine with non-overlapped field winding based on the conventional doubly salient PM machine. The machine topology and operation principles are illustrated firstly. Then, the effect of iron bridge on the hybridization of PM and FW excitations is derived from a simplified magnetic circuit model and verified by the FE simulation. The electromagnetic performances of the proposed HE machine are investigated with the 2D FE calculation and validated by the experiment.

Chapter 4

This chapter proposes a novel HE machine with stator non-overlapped FW and rotor consequent-pole PM. The machine topology and operation principle are introduced based on the interaction between the PM and FW excited magnetic fields with the armature winding function. Then, the electromagnetic performances are investigated with 2D FE calculation, and compared with the conventional SPM machines. Finally, the prototype is fabricated and tested to validate the analyses.

Chapter 5

This chapter extends the HE machine in chapter 4 to various rotor configurations to retain the PM and utilize flux-concentrating effect. The operation principles with different rotor configurations are discussed from the PM and FW flux paths. The HE machines with different rotor topologies are optimized under the same constraint and compared with 2D FE calculation. The field winding can be eliminated with open-winding and the DC coil free HE machines are introduced. Finally, the prototypes with different rotor topologies are fabricated and tested to verify the FE simulation.

Chapter 6

This chapter compares the proposed HE machines in chapters 2, 3, 4, 5 with the pure PM and WF machines. A commercialized rotor IPM machine, Toyota Prius 2010, is selected as the benchmark. The various HE machines are optimized under the same constraint of Toyota Prius 2010 with genetic algorithm based global optimization. Then the electromagnetic performances of the HE machines are compared with the IPM machine with 2D FE simulation comprehensively.

Chapter 7

This chapter is a general conclusion based on the work of this thesis and includes the potential future work in this research field.

1.6.2 Major Contributions and Publications Resulted from This Research

The major contributions of the thesis can be summarized as follows:

1. A novel HE machine with separated PM and FW flux paths is proposed in chapter 2. The parallel PM and FW excitations are beneficial to the flux regulation, fault tolerant, and demagnetization withstanding capability [CAI19a].
2. A novel doubly salient HE machine with non-overlapped field winding is proposed based on the conventional doubly salient PM machine. The proposed machine inherits the compact structure of doubly salient machine, and the field winding facilitates the field regulation [CAI20a].
3. A novel HE machine with stator non-overlapped FW and rotor consequent-pole PM is proposed. The abundant harmonics in the magnetomotive force (MMF) of non-overlapped winding are utilized to regulate the magnetic field through field modulation [CAI20b].
4. The concept of HE machine with stator non-overlapped FW and rotor consequent-pole PM is extended to various IPM rotor configuration to retain the PMs and achieve flux-concentrating effect [CAI19b].
5. Open-winding technique proposed in [ZHU16] is employed in the HE machine to eliminate the field winding, and novel DC coil free HE machines with reduced copper loss can be achieved [CAI19a] [CAI20a] [CAI20b].

Publications resulted from this research are listed as follows:

[CAI19a] S. Cai, Z. Q. Zhu, J. Mipo and S. Personnaz, "A novel parallel hybrid excited machine with enhanced flux regulation capability," *IEEE Trans. Energy Convers.*, vol. 34, no. 4, pp. 1938-1949, Dec. 2019.

[CAI19b] S. Cai, Z. Q. Zhu, S. Mallampalli, J. Mipo and S. Personnaz, "Comparative analysis of novel fractional slot non-overlapping winding hybrid excited machines having different consequent pole rotor topologies," *2019 IEEE Energy Conversion Congress and Exposition (ECCE)*, Baltimore, MD, USA, 2019, pp. 6508-6515. Extended and submitted to *IEEE Trans. Industry Application.*

[CAI20a] S. Cai, Z. Q. Zhu, C. Wang, J. C. Mipo and S. Personnaz, "A novel fractional slot non-overlapping winding hybrid excited machine with consequent-pole PM rotor," *IEEE Trans. Energy Convers.*, accepted.

[CAI20b] S. Cai, Z. Q. Zhu, J. C. Mipo, and S. Personnaz, "Investigation of novel doubly salient hybrid excited machine with non-overlapped field winding," *IEEE Trans. Energy Convers.,* submitted.

[ZHU19a] Z. Q. Zhu and S. Cai, "Overview of hybrid excited machines for electric vehicles," *Keynote Speech at 2019 Eleventh International Conference on Ecological Vehicles and Renewable Energies (EVER)*, Monte Carlo, 2019.

[ZHU19b] Z. Q. Zhu and S. Cai, "Hybrid excited permanent magnet machines for electric and hybrid electric vehicles," in *CES Transactions on Electrical Machines and Systems*, vol. 3, no. 3, pp. 233-247, Sept. 2019.

CHAPTER 2

A Novel Parallel Hybrid Excited Machine with Enhanced Flux Regulation Capability

This chapter presents a novel parallel hybrid excited (HE) machine with wide flux regulation range. The flux paths of PM and field winding are separated to avoid irreversible demagnetization and achieve improved flux regulation capability. Since the field winding and armature winding are located in the same stator slots, a dual-electric-port inverter can be employed to feed biased AC excitation in one set of winding and solve the spatial confliction of conventional hybrid excited machine. Finite element method (FEM) is utilized to analyze the electromagnetic performances of the proposed HE machine, in comparison with the original HE machine. It is revealed that the proposed HE machine exhibits lower PM excited back-EMF, which is beneficial to high speed fault tolerant operation, whereas the torque density can be higher with flux enhancing, albeit with reduced PM usage. Finally, a prototype is manufactured and tested to validate the FE predictions. This chapter is based on a published paper [CAI19a] and extends the analyses.

2.1 Introduction

Due to high cost and potential supply shortage of rare earth permanent magnet (PM), less or no PM machines are being reconsidered in recent years [BOL14] [LEE15]. Stator wound field synchronous machines have been perceived as promising candidates owing to robust rotor structure, good heat management, less potential demagnetization, elimination of brushes and slip rings [BAN06] [TAN12]. Therefore, numerous machine topologies have been developed such as doubly fed doubly salient machine [FAN06a], stator wound field Vernier machine [YU18], stator wound field flux-switching machine [CHE10] [ZUL10], variable flux reluctance machine (VFRM) [LIU13] [FUK08b].

Compared with the counterparts, VFRMs have the distinct merits of short non-overlapping field and armature windings, as shown in Fig. 2.1 (a). Moreover, the field winding and the armature winding can be combined with an open-winding inverter, in which winding resistance as well as copper loss can be reduced [ZHU16]. However, the torque density of VFRMs is relatively small compared with PM machines and low power factor can be another fatal problem [JIA15] [ZHU15].

To maintain the benefit of flexible magnetic field regulation and improve the torque density, PMs have been attached to assist the performance and hybrid excited (HE) machines are widely investigated. Hybrid excited (HE) machines can be classified as series hybridization and parallel hybridization according to the connection of PM and DC excited magnetic fields [AMA09] [OWE11]. In the series HE machines, the flux generated by field coils passes through PMs, otherwise parallel hybridization is obtained. Although the series HE machines generally have simpler structure, the flux regulation capability is limited and irreversible demagnetization should be considered [KAM12]. Therefore, parallel hybridization is more popular especially considering extension for flux weakening region [TAP03] [HUA16d].

In [AFI15], stator slot PMs with circumferential magnetization are introduced to reduce the magnetic saturation. The hybrid excited machines have negligible PM excited back-EMF, which is beneficial to eliminate the uncontrolled generator fault at high speed operation [JAH99] [ZHU19a]. Besides, the introduction of PMs can alleviate the magnetic saturation and enhance torque density. In [GAO18], PMs with radial magnetization are added in the tooth tip to enhance the magnetic field. Since field winding provides an extra degree to adjust the magnetic field, the power density at flux-weakening region is improved. In [XU16], a hybrid excited machine with stator yoke PMs is proposed, as shown in Fig. 2.1 (b). The stator PMs can enhance the magnetic field and improve the output capability. To avoid field winding flux passing through PMs, additional magnetic bridge by PMs are attached. For the HE machines developed in [AFI15] [GAO18] [XU16], the PMs are added in the flux path of DC excitation to enhance the magnetic field. Therefore, the operating principle and winding configuration, including field winding and armature winding are the same as VFRMs [HUA17b].

To further improve the flux regulation capability, this chapter proposes a novel parallel hybrid excited machine, as shown in Fig. 2.1 (c). The doubly salient PM machine with the same stator core has been reported in [DU18]. In [HE18], the field coils are introduced whereas the flux regulation range is still limited due to the large reluctance in field excitation flux path. In this chapter, the PM and field winding flux paths are separated to achieve parallel hybridization and wide flux regulation region. The machine adopts modular stator segment technique, which facilitates manufacturing and transportation [LI14]. Meanwhile, field winding and armature winding can be integrated to obtain a DC coil free HE machine and solve stator space confliction, as shown in Fig. 2.1 (d). It should be noted that the end-winding length can be slightly increased by merging two coils into single-layer winding. The increased end-winding length results in longer axial length and additional copper losses. Therefore, the selection of

separate and integrated field/armature winding techniques should be determined with the consideration of all the above aspects.

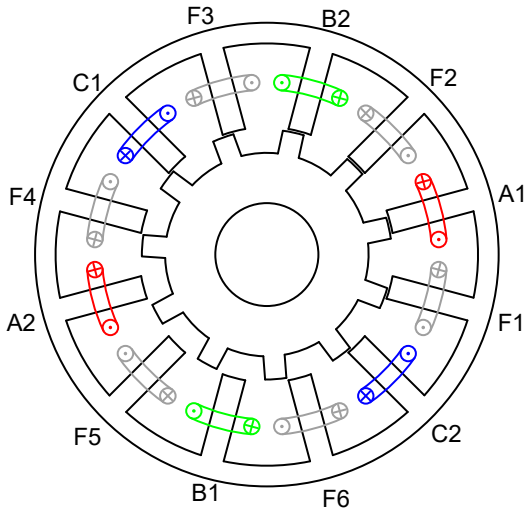

(a) VFRM [LIU13]

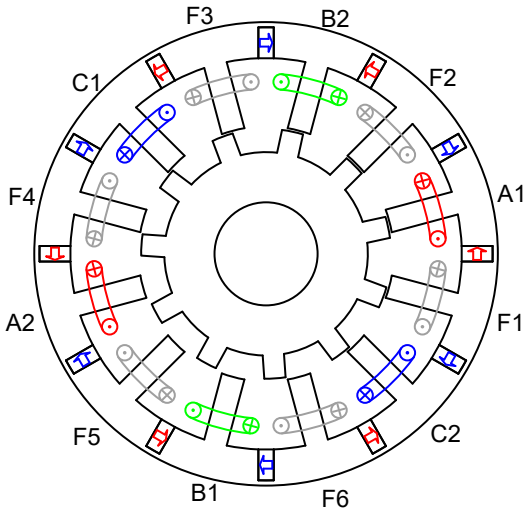

(b) HE doubly salient machine with stator yoke PMs [XU16]

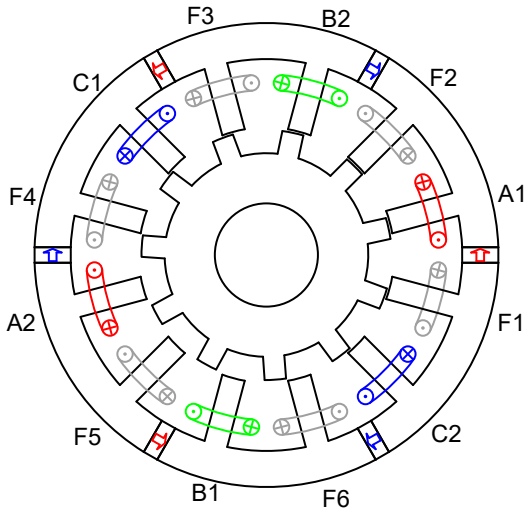

(c) Proposed parallel HE machine with separate field and armature windings

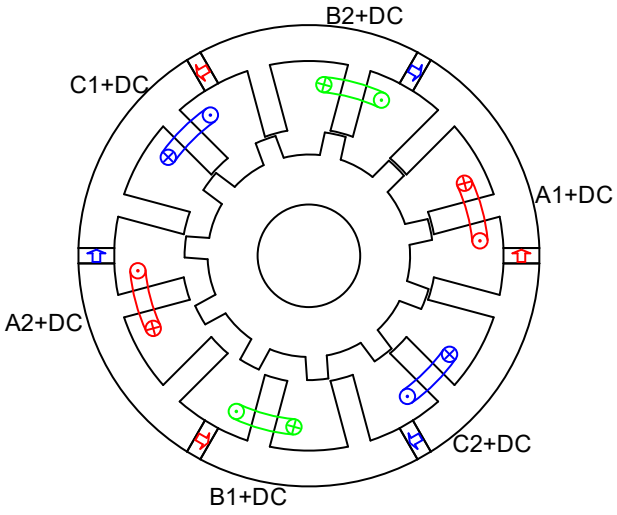

(d) Proposed parallel HE machine with integrated field and armature winding

Fig. 2.1. Cross-sections of 12/11 stator/rotor-pole VFRM and HE machines.

This chapter is organized as follows. In section 2.2, the machine topology and operating principle without field excitation are introduced. Then, in section 2.3, the flux regulation mechanism is discussed in comparison with that of the original HE machine shown in Fig. 2.1 (b). In section 2.4, different stator and rotor pole number combinations are extended and the condition to eliminate the even order harmonics in the back-EMF is illustrated. Further in section 2.5, the machine optimization and the influence of iron bridge are presented. In section

2.6, the electromagnetic performances are comprehensively compared with the original model. Furthermore, the flux regulation capability and torque density for integrated field and armature winding are investigated in section 2.7. Finally, a prototype is manufactured and tested to validate the analyses and FE predictions in section 2.8.

2.2 Machine Topology and Operating Principle

2.2.1 Machine Topology

The cross-section of the proposed 12/11 stator/rotor poles parallel HE machine is illustrated in Fig. 2.1 (c). The stator core comprises laminated Π-shape segment, sandwiched by circumferentially magnetized PM of alternate polarity. The rotor is salient and robust without excitations. The field and armature coils are wound around the Π-shape segment tooth alternately, with each segment carrying one field coil and one armature coil. Therefore, pre-wound segment process can be utilized to simplify the assembling and improve the winding packing factor. Since all the excitations are located in the stationary part, the heat management is easy and effective [CHE11a].

Compared with the HE doubly salient machine shown in Fig. 2.1 (b), the stator laminated segment is modified from T-shape to Π-shape. Besides, the PM pieces are reduced to half, which facilitates assembling process and reduces the material cost [BAR14]. For the original HE doubly salient machine, magnetic bridges are attached to increase the flux regulation ratio, which connect the adjacent stator segments entirely. The ribs can be eliminated in the proposed machine topology since it exhibits parallel hybridization inherently. Therefore, the proposed machine shares the benefits of modular stator technique. As the PMs are merely attached to assist the magnetic field of DC coils, the winding configuration of the original HE machine is the same as the VFRM shown in Figs. 2.1 (a) and (b). However, the winding connections of the proposed HE machine, both field coils and armature coils, are changed.

2.2.2 Winding Configuration

Similar to the torque production of doubly salient machine, the proposed HE machine operates on the flux linkage variation caused by the rotation of salient rotor. As the salient rotor rotates one rotor pole pitch, the electromagnetic field alternates one period. Therefore, the relationship between the electrical position and mechanical position can be deduced as

$$\theta_e = N_r \theta_m \tag{2.1}$$

where θ_e and θ_m are the electrical position and mechanical position, respectively, and N_r represents the number of rotor poles.

The field coils of adjacent segment are of opposite polarity, in accordance with PM polarity. Therefore, the field winding allocation is different from that of VFRM and the original HE machine, as shown in Fig. 2.1.

Besides, due to the fact that each stator segment carries one armature coil, the electrical angle between two armature coils can be expressed as (2.2), where N_s is the number of stator teeth.

$$\alpha_c = \frac{2\pi}{N_s/2} \times N_r \tag{2.2}$$

Therefore, the coil position and corresponding EMF phasor of 12/11 stator/rotor poles proposed HE machine can be illustrated in Fig. 2.2. The superscript of coil *n*' denotes the opposite direction accounting for the alternate magnetization of PMs. The rotor pole number is chosen to be close to stator pole number to ensure parallel hybridization and flux regulation ratio. According to the coil EMF phasor region, the three phase armature winding can be connected as shown in Fig. 2.1 (c). It is worth emphasizing that unbalanced magnetic force (UMF) exists with given stator and rotor pole number combination due to odd number of rotor pole. Other stator and rotor pole number combinations with potential elimination of UMF will be discussed in section 2.4.

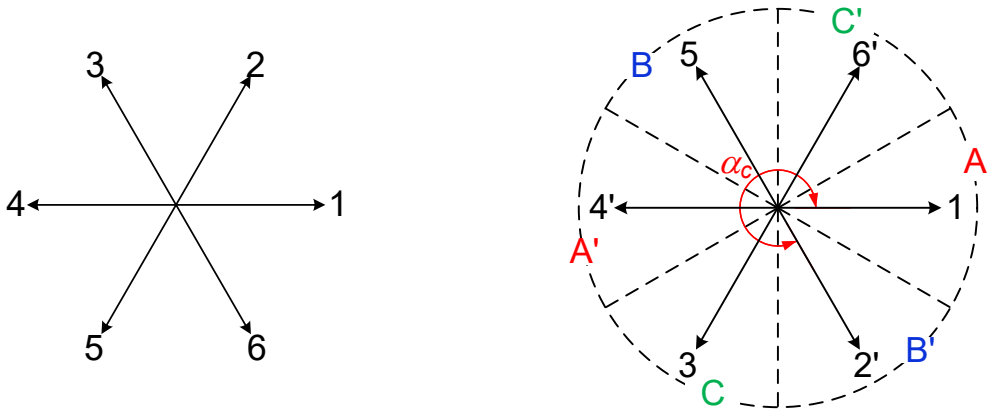

(a) Coil mechanical position (b) Coil EMF phasor

Fig. 2.2. Coil EMF phasor of 12/11 stator/rotor poles proposed HE machine.

2.2.3 Operation Principle

With the assistance of 2D finite element (FE) calculation, the PM excited open-circuit flux line distributions at four typical positions are illustrated in Fig. 2.3. The initial rotor position, viz. θ_e =0º, is aligned when phase A flux linkage is maximized.

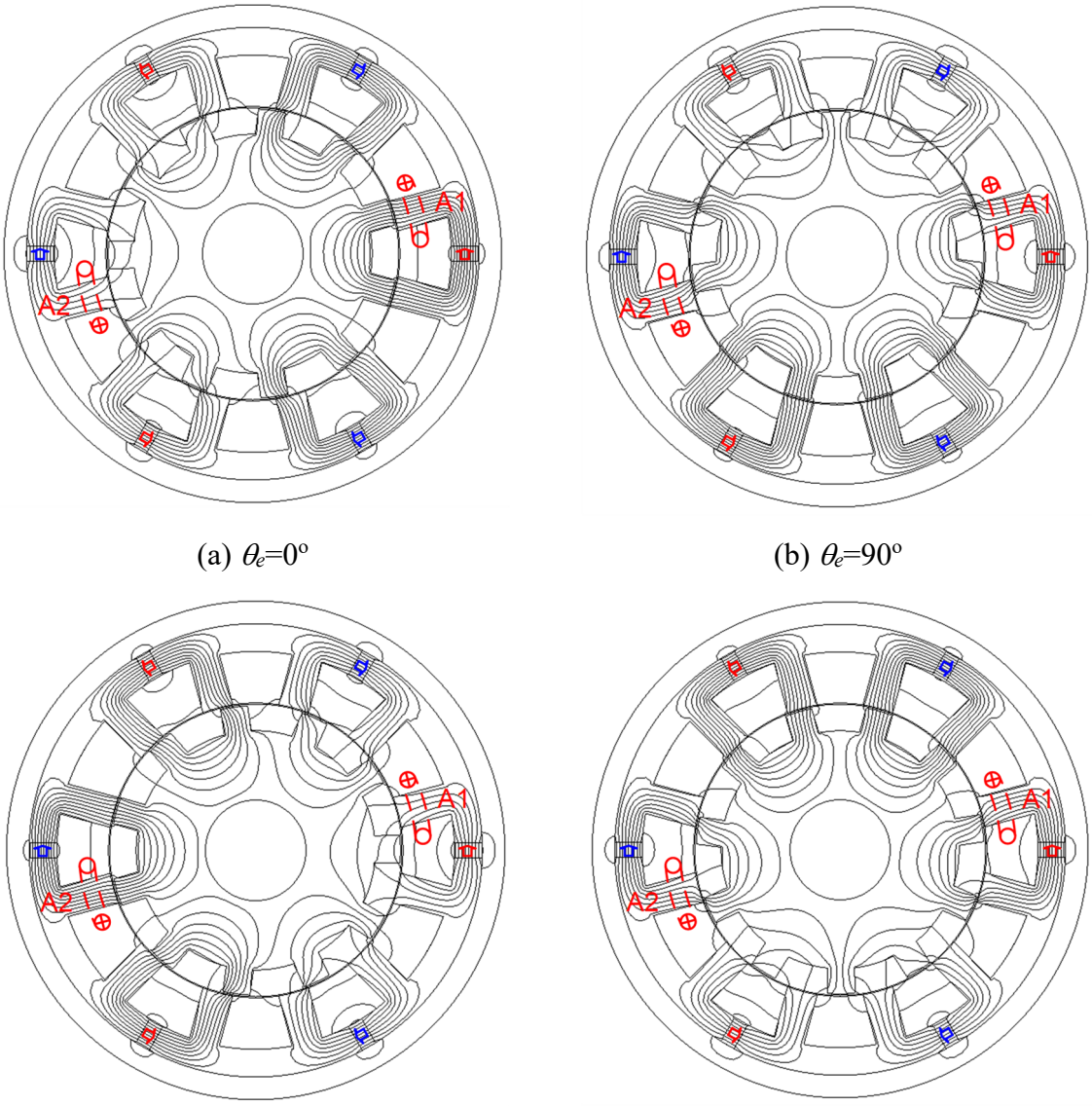

(a) θ_e=0º (b) θ_e=90º

(c) θ_e=180º (d) θ_e=270º

Fig. 2.3. Open-circuit (PM excited only) equipotential distribution at four typical rotor positions.

As can be observed, the flux linkages coupled with coil A1 and coil A2 vary with the movement of salient rotor. The open-circuit flux linkage waveforms over one electrical period are illustrated in Fig. 2.4. Although the flux linkage in single coil is unipolar, the phase flux linkage is bipolar with DC-biased value eliminated. The positive and negative maximum phase flux linkages are achieved at the rotor position of θ_e =0º and θ_e =180º, respectively. The synthesized zero phase flux linkage occurs when the rotor works at θ_e =90º and θ_e =270º.

The alternating phase flux linkage produces certain-frequency back-EMF in the winding. When identical frequency alternating current is injected, electromagnetic torque can be produced to transmit mechanical energy.

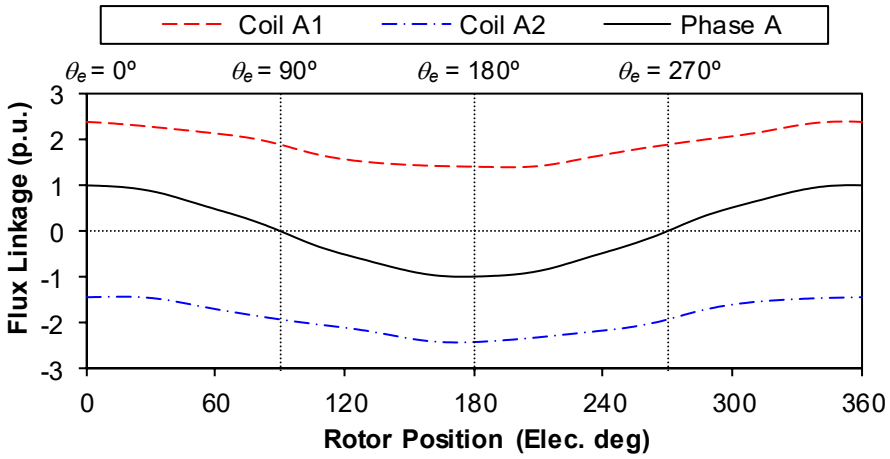

Fig. 2.4. Normalized PM excited open-circuit flux linkage waveforms over one electrical period.

2.3 Flux Regulation Mechanism

In this section, the flux regulation mechanisms of original T-segment HE machine and proposed Π-segment parallel HE machine will be discussed individually. To simply verify the theoretical analysis, FE calculation is conducted on the two HE machines with initial parameters, as shown in Table 2.1. The initial parameters of two HE machines are kept the same, except the thickness of iron bridge. The iron bridge is required in the original design for the consideration of flux regulation ratio [XU16] [OWE10], whereas it can be saved in the proposed structure to achieve modular assembling.

Table 2.1 Initial parameters of investigated machines before optimization

Parameter	Value	Parameter	Value
Stator teeth number	12	Rotor pole number	11
Stator outer diameter	90mm	Stack length	25mm
Air-gap length	0.5mm	Split ratio	0.6
Pm thickness	2mm	Stator yoke thickness	4mm
Stator tooth pitch	0.4	Rotor pole pitch	0.4
Iron bridge thickness	0.5mm/0		

2.3.1 Original HE Machine with Iron Bridge

To demonstrate the flux regulation mechanism of original T-segment machine, the flux paths with PM excitation, DC excitation, flux enhancing (PM and positive DC excitations), flux weakening (PM and negative DC excitations) are illustrated in Fig. 2.5. It should be noted only armature coil is drawn to show open-circuit coil linked flux. The solid lines with arrow indicate the flux path for each consequence. To illustrate the effect of DC excitation during flux enhancing and flux weakening, the DC contributed flux is marked with dashed green arrow lines in Figs. 2.5 (c) and (d).

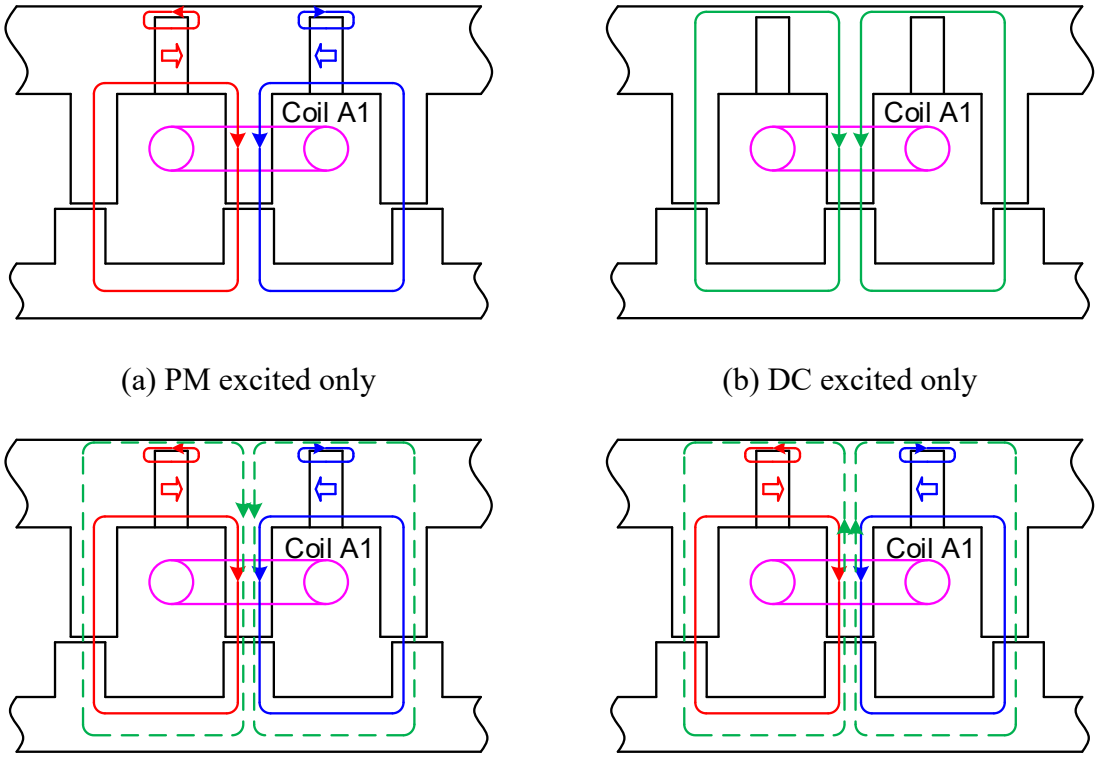

(a) PM excited only

(b) DC excited only

(c) Flux enhancing (PM and positive DC excited)

(d) Flux weakening (PM and negative DC excited)

Fig. 2.5. Flux path of original T-segment HE machine with different excitations.

When PM excitation is applied merely, part of the PM flux lines link with the coil whereas the others are short circuited by the magnetic bridge. When DC excitation is applied, the flux lines pass through the magnetic bridge. The existence of the ribs improves the demagnetization withstanding capability since the flux lines of DC excitation pass by the PMs. However, with PMs and field winding excited together, the reluctance of the ribs is still significant because the short-circuited PM flux saturates the ribs, as shown in Figs. 2.5(c) and (d). Therefore, the

flux regulation mechanism of the original T-segment machine is to regulate the tooth flux linkage through the saturated magnetic bridge.

The normalized phase flux linkages with different excitations are shown in Fig. 2.6. The DC excitation can regulate the magnetic field, and consequently, the coil-coupled flux linkage. Besides, the flux linkage with DC excitation only is significant, fundamental being more than 0.5 normalized value. However, when PMs and DC excitations are applied together, the flux linkage caused by DC is limited, fundamental being ~0.25 normalized value, owing to the saturation of magnetic bridge.

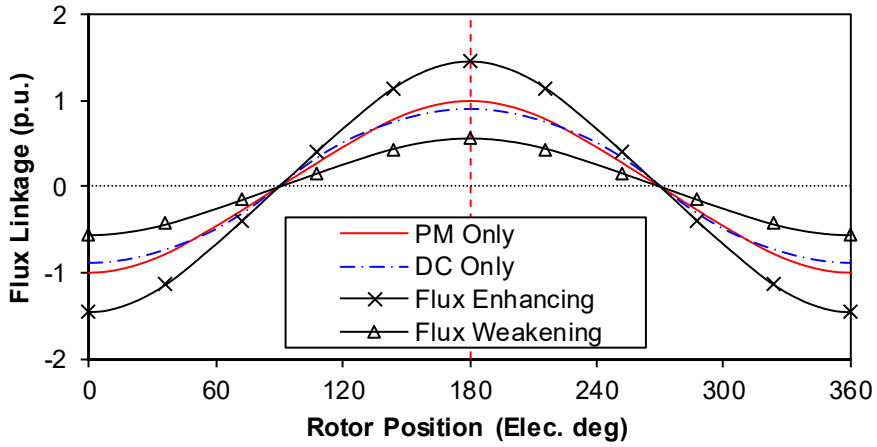

(a) Waveforms

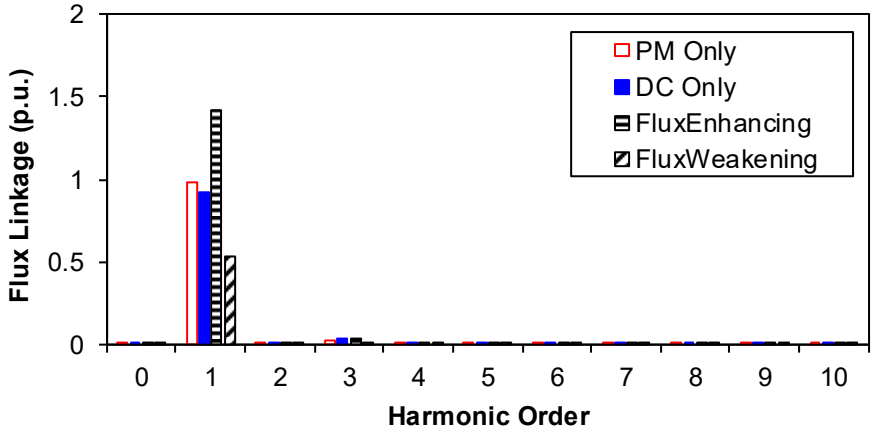

(b) Spectra

Fig. 2.6. Normalized phase flux linkage of original T-segment HE machine with different excitations.

2.3.2 Proposed HE Machine

Similarly, the flux paths of proposed Π-segment machine with different excitations are illustrated in Fig. 2.7. The red and blue arrow lines indicate the flux paths of two adjacent PMs with reverse polarity. The green arrow lines demonstrate the flux path of DC excitation. The synthesized flux lines of either flux-enhancing or flux-weakening are further shown in Figs. 2.7 (c) and (d).

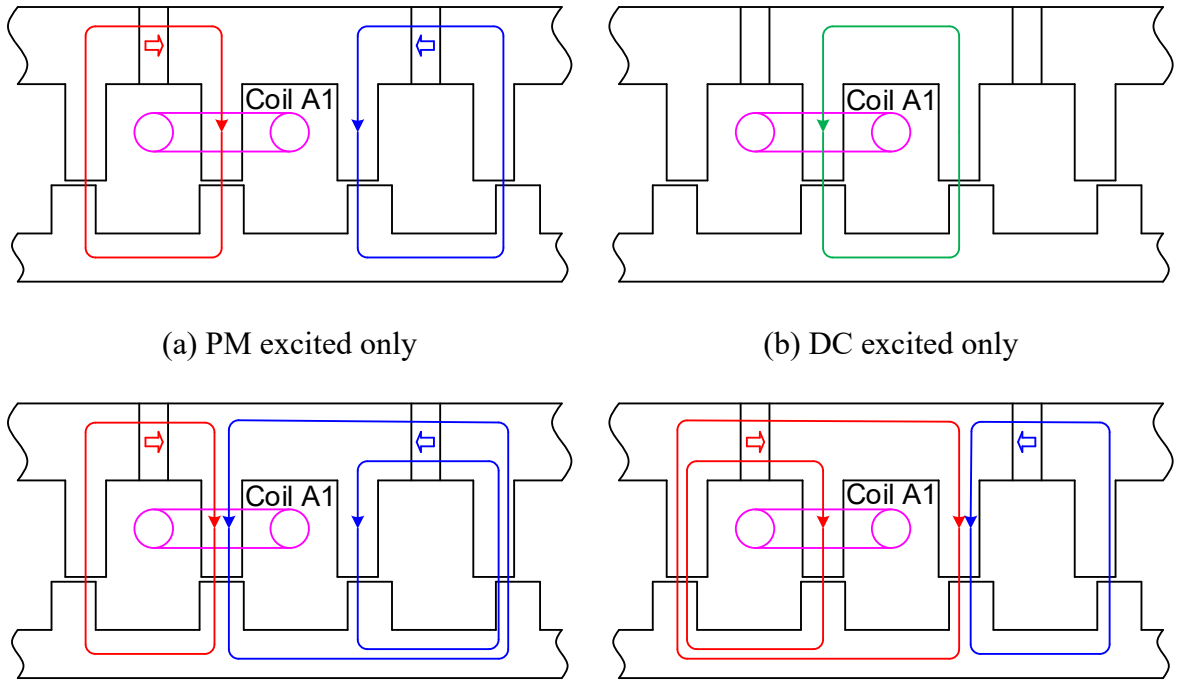

(a) PM excited only

(b) DC excited only

(c) Flux enhancing (PM and positive DC excited)

(d) Flux weakening (PM and negative DC excited)

Fig. 2.7. Flux path of proposed Π-segment HE machine with different excitations.

As can be observed, the flux paths of PMs and DC excitation are separate inherently. The flux lines of DC excitation pass through the two teeth in one segment, with reduced magnetic reluctance compared with the original T-segment HE machine. When operating with flux enhancing, the function of DC excitation can be perceived as pulling the PM fluxes from armature coil wound tooth to field coil wound tooth. When operating with flux weakening, the function of DC excitation can be perceived as pushing the PM fluxes from the armature coil wound tooth to the field coil wound tooth. Therefore, the flux regulation mechanism of the proposed Π-segment machine is to allocate the flux in the two teeth of one stator segment, of which are wound with field coil and armature coil, respectively.

The phase flux linkages with different excitations are shown in Fig. 2.8. The axis of PM induced flux linkage, which is marked with red dashed line, is unaligned with the axis of DC induced flux linkage, which is marked with blue dotted line. This can be explained from the separated flux paths of PM and DC excitations in Fig. 2.7. Although the phase of flux linkage is shifted with DC excitation, the amplitude can be regulated flexibly due to less reluctance. Since the axis of DC flux is close to PM flux with a similar number of stator and rotor poles, the flux-enhancing is more effective than flux-weakening, phase fundamental flux linkage being ~1.8 and ~0.5 normalized value, respectively. With half PM utilization, the PM flux linkage can be reduced to achieve parallel hybridization and better flux regulation capability. The benefit can be identified as the less PM consumption, enhanced flux regulation ratio and fault tolerance, whereas the limitations are sacrificed PM torque density and efficiency.

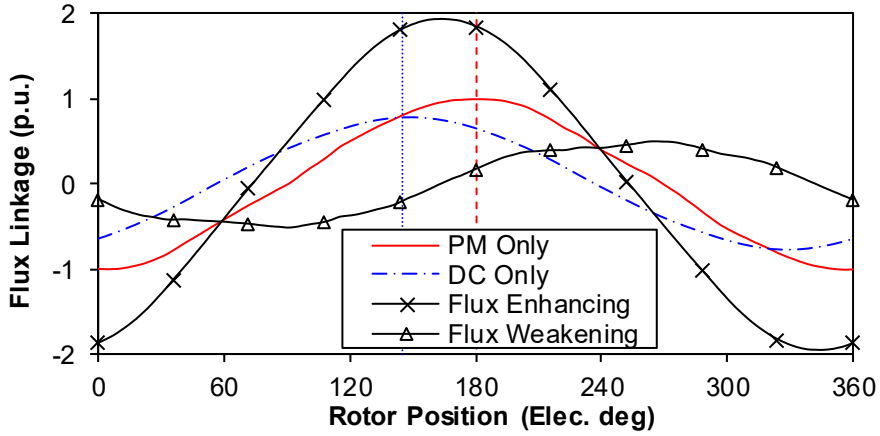

(a) Waveforms

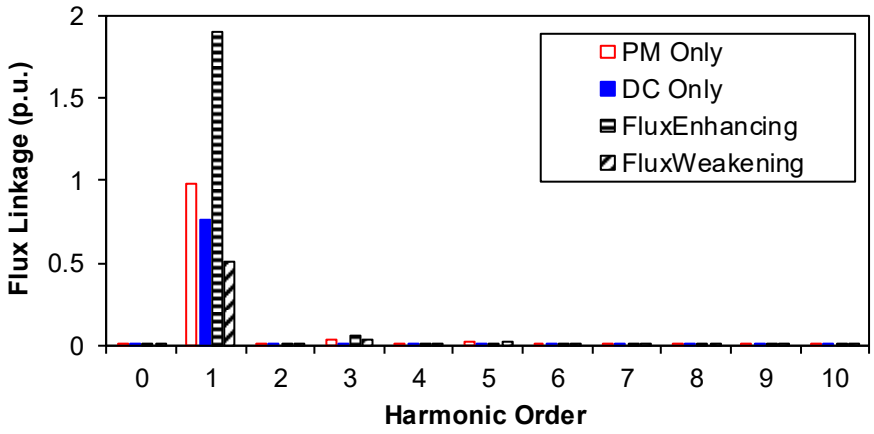

(b) Spectra

Fig. 2.8. Normalized phase flux linkage of proposed Π-segment HE machine with different excitations.

Since the flux regulation principle of proposed HE machine is to allocate the flux in the adjacent two teeth, the PM flux is not countered at flux-weakening operation. The flux linkage waveform under flux-weakening is more distorted, indicating the abundant field harmonics with negative field excitation. The air-gap flux density harmonics may have implications, e.g. iron loss and sacrificed efficiency particularly at high speed operation.

2.4 Slot and Pole Number Combination

For the stator PM machine with doubly salient structure, the air-gap flux density is of abundant harmonics with field modulation effect. Therefore, the back-EMF of single coil is asymmetric and potentially has even order harmonics [CHE10b]. The even order harmonics in the phase back-EMF are harmful to the voltage waveform and tend to produce low order pulsating torques. Therefore, it is of high significance to select appropriate stator and rotor pole combination to obtain the symmetrical phase back-EMF waveforms.

Firstly, the lowest stator slot number should be determined. In the proposed HE machine with Π-segment, one stator segment consists of two stator teeth and the unit machine should have two stator segments per phase. Therefore, the number of stator slots should be multiples of 4. For an m-phase machine, the stator slot number can be expressed in (2.3), where k_1 is an integer. Subsequently, the minimum stator slot number is N_s=12 for a 3-phase machine.

According to the flux path illustration in Fig. 2.7, the rotor pole number should be close to the stator slot number. Therefore, the rotor pole number is expressed in (2.4), where k_2 is an integer. For the proposed HE machine with 12-stator slot, the rotor pole number can be selected as N_r=10, 11, 13, 14…

$$N_s = 4mk_1 \tag{2.3}$$

$$N_r = N_s \pm k_2 \tag{2.4}$$

The coil mechanical angle and corresponding back-EMF phasor diagram of 12/11 stator/rotor poles have been illustrated in Fig. 2.2. Similarly, the coil back-EMF phasors for the HE machines with other rotor pole numbers can be extended as well, as shown in Fig. 2.9.

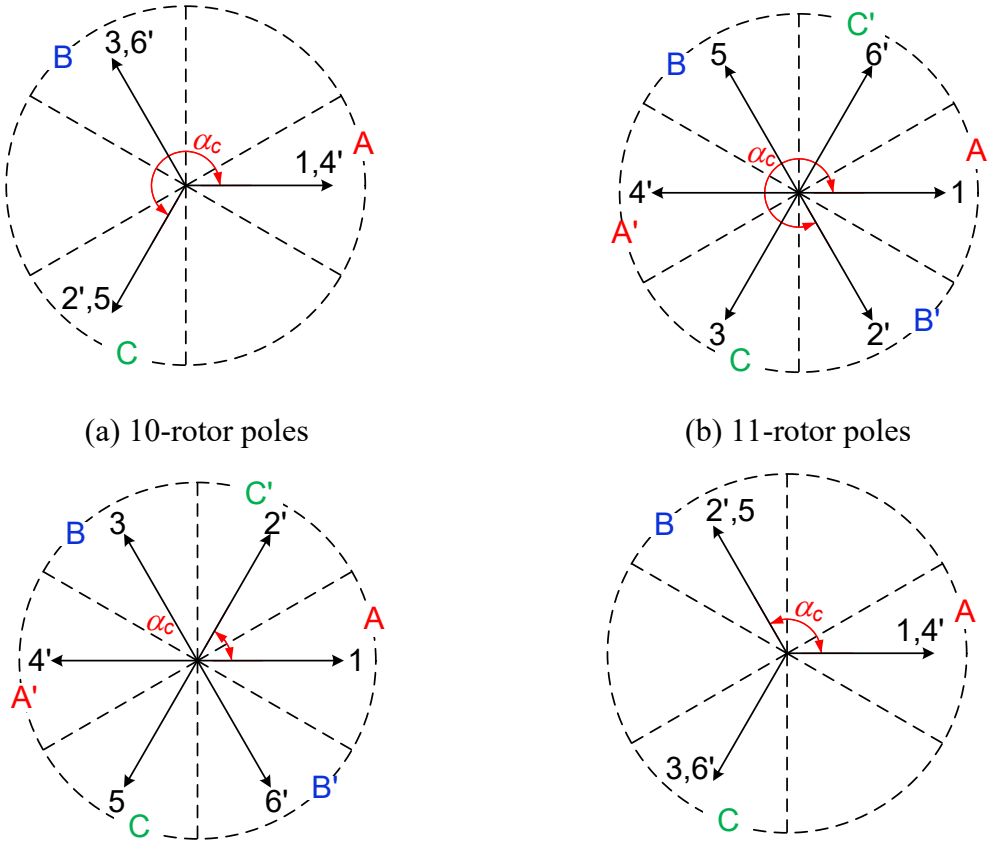

(a) 10-rotor poles (b) 11-rotor poles

(c) 13-rotor poles (d) 14-rotor poles

Fig. 2.9. Coil back-EMF phasors for the proposed HE machines with 12-stator slot.

The open-circuit armature coil flux linkage of 'coil 1' can be expressed in (2.5) in Fourier series, where ω_e represents the electrical rotating speed, ψ_ν is the amplitude of νth harmonic, φ_ν is the phase of νth harmonic. Subsequently, the flux linkage of 'coil i' can be expressed in (2.6), with the consideration of phase shift as reversed polarity in adjacent two segments as well as electrical angle shift. It can be observed that various harmonics exist in the coil flux linkage due to unipolar flux and abundant field harmonics.

According to the coil back-EMF phasors in Fig. 2.9, phase A is composed by coil 1 and coil 4 for the HE machines with rotor pole of N_r=10, 11, 13, 14. Meanwhile, coil 1 and coil 4 are connected in series for the HE machines with rotor pole of N_r=11, 13, whereas the two coils are reversely connected for N_r=10, 14. Therefore, the phase flux linkage can be expressed in (2.7).

$$\psi^1(t) = \sum_{\nu=0,1,2,3\cdots}^{+\infty} \psi_\nu \cos(\nu\omega_e t - \varphi_\nu) \tag{2.5}$$

$$\psi^i(t)=\sum_{\nu=0,1,2,3\cdots}^{+\infty}\psi_\nu\cos\left[\nu\omega_e t-\varphi_\nu-\pi(i-1)-\frac{2\nu\pi}{N_s/2}N_r(i-1)\right] \tag{2.6}$$

$$\psi_A(t)=\begin{cases}\psi^1(t)-\psi^4(t), N_r=10,14\\ \psi^1(t)+\psi^4(t), N_r=11,13\end{cases} \tag{2.7}$$

By combining (2.5) - (2.7), the phase flux linkages of the HE machines with different stator/rotor pole combinations can be expressed in (2.8). It can be identified that even order harmonics are cancelled in the phase flux linkages of 11- and 13-rotor pole HE machines, whereas the 10- and 14-rotor pole HE machines inherit the various harmonics of the coil flux linkages. Moreover, the phase flux linkages are unipolar in the rotor pole of N_r=10, 14, and bipolar in the rotor pole of N_r=11, 13.

$$\psi_A(t)=\begin{cases}2\psi_0+\sum_{\nu=1,2,3\cdots}^{+\infty}2\psi_\nu\cos(\nu\omega_e t-\varphi_\nu), N_r=10,14\\ \sum_{\nu=1,2,3\cdots}^{+\infty}\left[1+(-1)^{\nu+1}\right]\psi_\nu\cos(\nu\omega_e t-\varphi_\nu), N_r=11,13\end{cases} \tag{2.8}$$

To further illustrate this phenomena, 2D FE calculation is conducted on the proposed HE machines with initial parameters in Table 2.1. Different stator and rotor pole numbers are extended, and the armature winding connections are determined according to the back-EMF phasors in Fig. 2.9.

The 2D FE predicted open-circuit coil flux linkages for the HE machines with different stator/rotor pole number combinations are compared in Fig. 2.10. As illustrated in the operation principle section, the coil flux linkages are maximized at the aligned rotor position and minimized at the unaligned rotor position. Therefore, the coil flux linkage waveforms are unipolar with various harmonics regardless of stator/rotor pole number combinations.

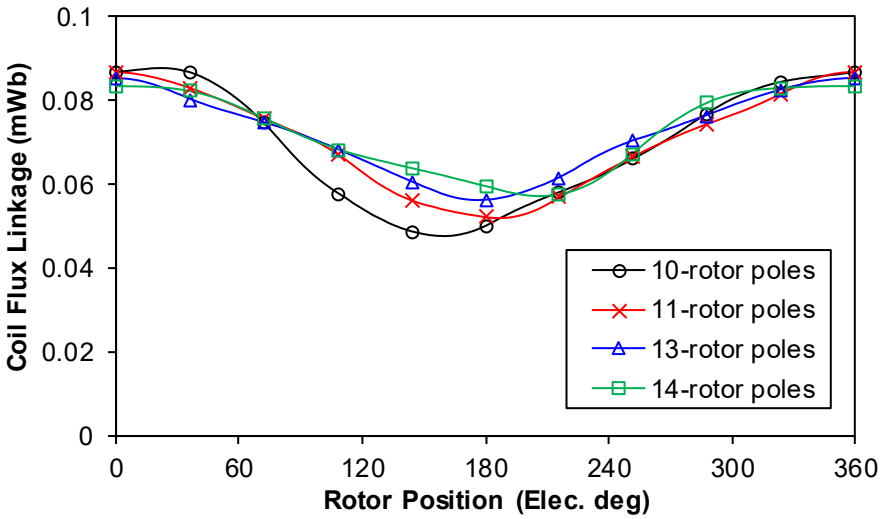

(a) Waveforms

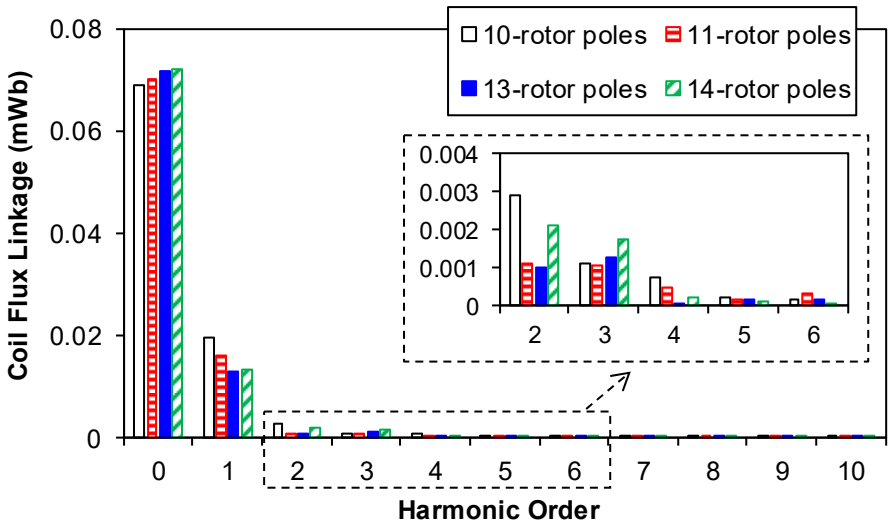

(b) Spectra

Fig. 2.10. Open-circuit coil flux linkages for the proposed HE machines with 12-stator slot without DC excitation (1 turn per coil).

Furthermore, the synthesized open-circuit phase flux linkages for the HE machines with different rotor poles are illustrated in Fig. 2. 11. As analyzed in (2.8), the phase flux linkages of rotor poles with N_r=11, 13 are bipolar with the elimination of even order harmonics. Meanwhile, the HE machines with 10- and 14-rotor poles exhibit unipolar phase flux linkage and the even order harmonics are inherited from the coil flux linkages. Since the even order harmonics in the phase flux linkage will potentially produce asymmetric back-EMF and additional pulsating torques, the HE machines with rotor poles of N_r=11, 13 are preferred although the potential unbalanced magnetic force (UMF) should be considered.

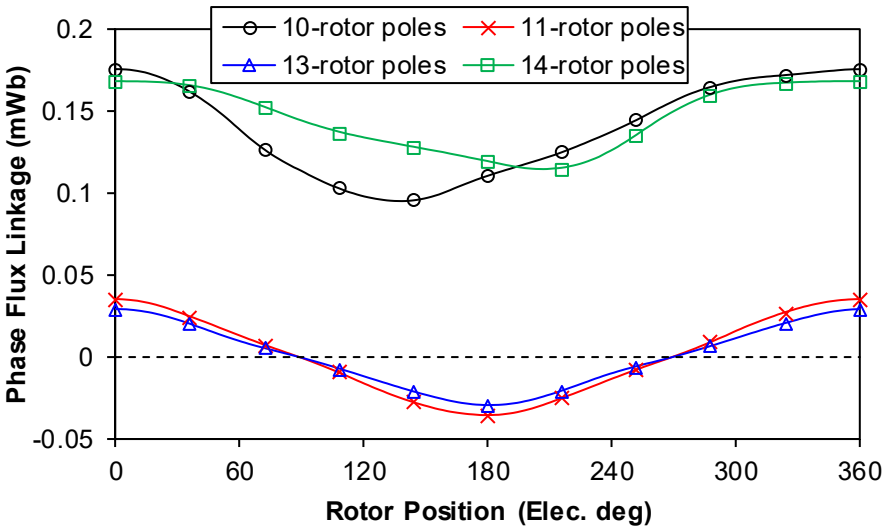

(a) Waveforms

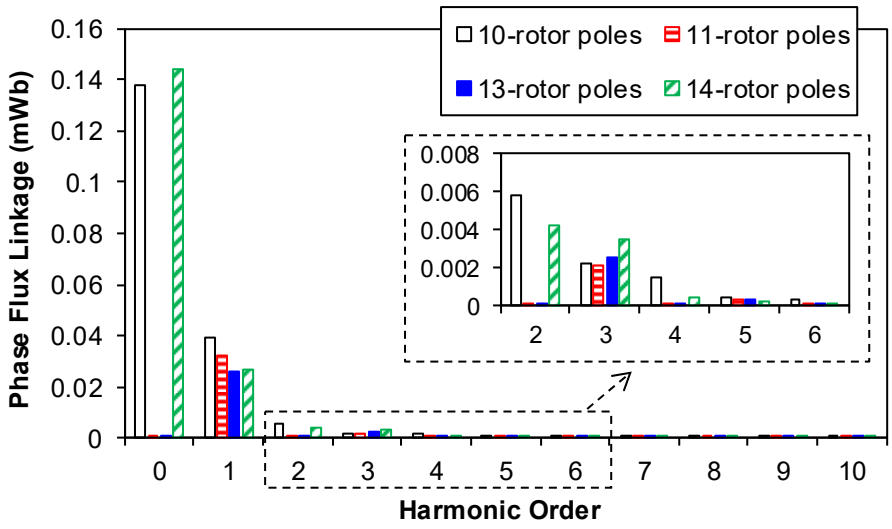

(b) Spectra

Fig. 2.11. Normalized open-circuit phase flux linkages for the proposed HE machines with 12-stator slot without DC excitation (1 turn per coil).

It is worth noting that the HE machines with odd-rotor pole number inevitably suffer from UMF which may cause noise and vibration. The UMFs of the 11- and 13-rotor pole HE machines are further illustrated in Fig. 2.12. At open-circuit, the 11-rotor pole HE machine exhibits higher UMF than the counterpart. However, the effect of armature reaction on the UMF of 13-rotor pole is more significant compared with 11-rotor pole HE machine. Moreover, it can be observed that the UMF is increased significantly with the DC excitation for both HE machines. Although the UMF of the HE machines with odd-rotor pole number can be eliminated by doubling the numbers of stator and rotor poles together, a high rotor pole number

would significantly increase the fundamental frequency and the machine would be unsuitable for high speed operation.

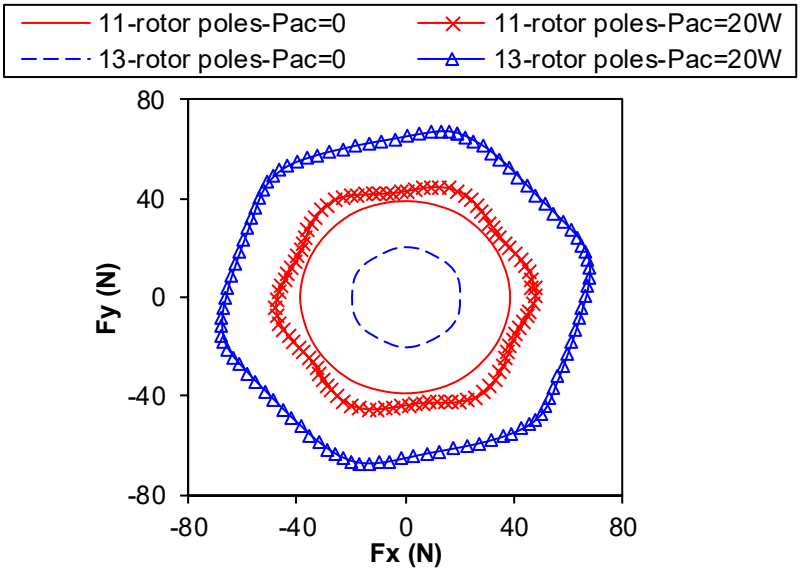

(a) Without DC excitation

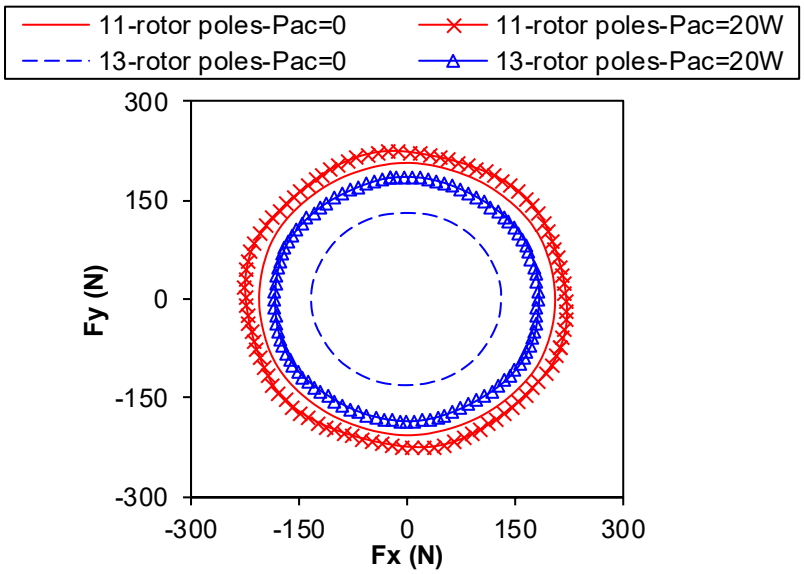

(b) With positive DC excitation of MMF=+1000Amp.Turns

Fig. 2.12. UMF in 11- and 13-rotor pole HE machines.

2.5 Design and Optimization

To evaluate the electromagnetic performances of the proposed Π-segment machine, 2D-FE calculations are conducted in this section. According to the above discussion, the 12/11 stator/rotor pole number combination is selected for further investigation. In order to gain high torque density as well as flexible flux regulation capability, the HE machines are optimized

with flux-enhancing for maximized average torque. Under the constraints of fixed stator outer diameter d_{so} = 90mm, air-gap length l_g = 0.5, axial stack length l_{st} = 25mm, armature copper loss p_{ac} = 20W, field current density J_{dc} = +10A/mm^2, NdFeB PM thickness of h_{PM} = 2mm, the machines are globally optimized with genetic algorithm embedded in FE commercial Maxwell software. To gain a fair comparison, the same optimization is conducted for the original 12/11 stator/rotor poles HE machine with T-segment stator as the benchmark. The relationship between armature copper loss and machine parameters is given by

$$p_{ac} = \frac{\rho_{Cu} \cdot N_s \cdot l_{st} \cdot N_{ac}^{\ 2} \cdot I_{ac}^{\ 2}}{S_c \cdot k_p} \tag{2.9}$$

where ρ_{Cu} is the copper electrical resistivity, N_{ac} is the number of turn per armature coil, I_{ac} is the RMS of armature current, S_c is the single slot area, and k_p is the packing factor.

It should be noted that the skin effect and proximity effect of the conductors on the copper loss are not taken into consideration in (2.9). This constraints on armature winding copper loss is more favourable in the design of machines for low speed applications since the iron loss together with the skin effect wound not contribute to the major loss component at rated speed of 400rpm. The armature winding copper loss and field winding current density are determined to allow for the experiments on the same thermal condition as in [HUA16b] [HUA16c] and [HUA16d].

To simplify the analyses, the number of turns of field coil is kept the same as that of armature coil whereas the current amplitudes can be different. The numbers of turns in two HE machines are determined proportional to the slot area. Therefore, the current density is kept identical with same current value, e.g. J_{dc} = 20A/mm2 with i_{dc} = 10A. The maximum field current density to evaluate the field regulation capability is 20A/mm^2, which is not the continuous operation mode. The maximum field current is utilized to calculate the flux regulation ratio and saturated field current.

After global optimization for maximum torque, the main design parameters are listed in Table 2.2. It should be noted PM volume and material cost are not taken into consideration during the optimization. Obviously, the proposed HE machine consumes less PMs since the number of PM pieces is reduced to half.

Table 2.2 Main design parameters of investigated machines after global optimization

Symbol	Parameters	Unit	Original	Proposed
-	Stator segment type	-	T-Shape	Π-Shape
N_s	Stator slot number	-	12	
N_r	Rotor pole number	-	11	
d_{so}	Stator outer diameter	mm	90	
l_{st}	Stack length	mm	25	
l_g	Air-gap length	mm	0.5	
k_p	Slot packing factor	-	0.6	
B_r	PM remanence	T	1.1	
H_c	PM coercivity	kA/m	824	
h_{PM}	PM height	mm	2	
h_{rib}	Stator rib thickness	mm	0.5	N/A
γ_{sp}	Split ratio	-	0.58	0.61
h_y	Stator yoke thickness	mm	6.0	4.3
θ_{sp}	Stator pole arc	º	10.8	11.1
θ_{rp}	Rotor pole arc	º	11.5	11.1
S_c	Slot area	mm^3	156	166
N_{dc}	Turns per field coil	-	93	99
N_{ac}	Turns per armature coil	-	93	99

The effect of iron bridge on the open-circuit back-EMF fundamentals for two optimized HE machines is evaluated in Fig. 2.13. The existence of iron bridge causes PM flux leakage and reduces the PM excited back-EMF for both two machines. Besides, the iron bridge provides additional flux path for DC excitation in original HE machine, and increases the DC flux regulation ratio. Meanwhile, the introduction of ribs has little influence on the DC flux path as well as flux regulation capability for the proposed structure.

Therefore, the thickness of iron bridge in the original structure should be determined as the trade-off between PM excited output capability and flux regulation capability. However, the iron bridge can be removed in the proposed machine and modular technique can be employed to further improve the winding packing factor [AKI03] [LIB06].

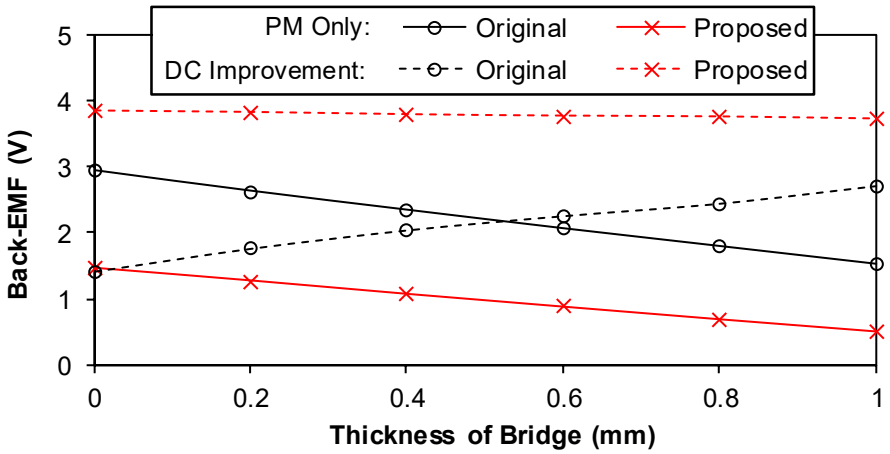

Fig. 2.13. Open-circuit back-EMF fundamentals versus thickness of bridge with PM excited only and DC excitation improvement (i_{dc} = 10A).

2.6 Performance Evaluation

2.6.1 Air-Gap Flux Density

The FE calculated air-gap flux densities for the 12/11 stator/rotor poles HE machines with different field excitations are shown in Fig. 2.14 and Fig. 2.15. The abundant harmonics are observed in the two HE machines due to doubly salient structure and flux modulation effect [WAN17b].

To illustrate the flux regulation mechanisms for two types of machines, the stator teeth are divided into two groups, one wound with armature coil marked with green arrow line, and the adjacent tooth wound with field coil. For the original T-segment HE machine, the DC excitation adjusts the flux density through the magnetic bridge. Therefore, the flux density within each tooth pitch is increased with flux-enhancing and reduced with flux-weakening. For the proposed HE machine, the DC excitation regulates the flux density by allocating the flux in the adjacent two teeth, as shown in section 2.3. Therefore, with positive DC excitation, the air-gap flux density under armature coil wound tooth is increased whereas that under field coil wound tooth is reduced. On the contrary, with negative DC excitation, the air-gap flux density under field coil wound tooth is increased whereas that under armature coil wound tooth is reduced.

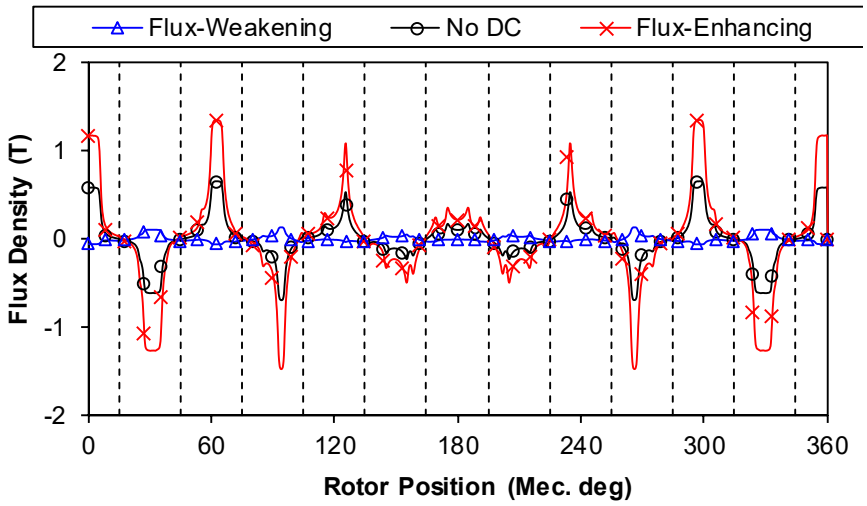

Fig. 2.14. Air-gap flux density waveforms with different field excitations for original 12/11 stator/rotor poles T-segment HE machine.

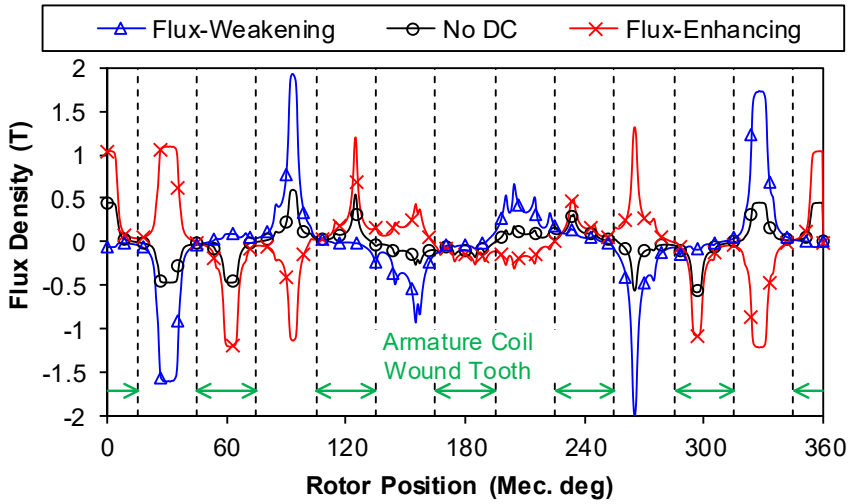

Fig. 2.15. Air-gap flux density waveforms with different field excitations for proposed 12/11 stator/rotor poles Π-segment HE machine.

2.6.2 Flux Linkage

The effect of DC excitation on the open-circuit phase flux linkage for two HE machines has been discussed in section 2.3. The *d*-*q* axis flux linkages variation with DC excitation for two types of machines are compared in Fig. 2.16. For the original HE machine, the DC excitation only regulates the *d*-axis flux linkage and has little influence on the *q*-axis flux linkage. However, for the proposed parallel HE machine, both the *d*-axis and *q*-axis flux linkage can be adjusted by the DC excitation. Although the inherent *d*-axis flux linkage of original T-segment machine is larger owing to more PM usage, the flux regulation capability of proposed parallel HE machine is improved significantly.

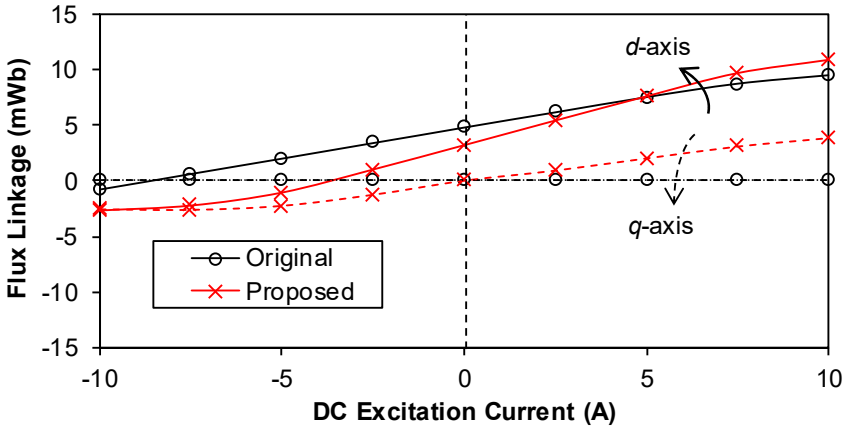

Fig. 2.16. Open-circuit *d*-*q* axis flux linkage variation with DC excitation current for the original and proposed HE machines.

2.6.3 Back-EMF

The open-circuit phase back-EMFs for the original and proposed parallel HE machines are compared in Fig. 2.17. Without field current excitation, the fundamental back-EMF of proposed Π-segment machine is smaller since only half volume of PM is employed. However, with positive field excitation of i_{dc} = +10A, the back-EMF of proposed HE machine is higher owing to the enhanced flux regulation capability, albeit with additional field winding copper loss. Due to the coil connection with the 12/11 stator/rotor poles HE machines, even order harmonics are cancelled and the waveform is symmetrical in the phase back-EMF [HUA18b].

To evaluate the effect of DC excitation on the fundamental back-EMF, the phase flux linkage and fundamental back-EMF versus PM and DC excitation are deduced in (2.10) and (2.11), respectively, where ψ_{PM} is the PM flux linkage, M_{df} and M_{qf} represent the mutual inductance between field winding with *d*-axis and *q*-axis armature winding, respectively. For the original T-segment HE machine, the mutual inductance between field winding and *q*-axis is negligible, i.e. M_{qf}= 0, as illustrated in Fig. 2.16. Therefore, as can be observed in (2.11), the amplitude of fundamental back-EMF versus DC excitation current is linear neglecting magnetic saturation. However, the coupling between field winding with both *d*-axis and *q*-axis exists for proposed HE machine, and consequently, the fundamental back-EMF amplitude varies non-linearly with DC excitation. Meanwhile, the effect of DC excitation on the *d*- and *q*-axis fluxes imposes controlling challenges. However, the cross-coupling effect between *d*-axis and *q*-axis exists even in conventional interior PM (IPM) machine [STU03]. Moreover, adaptive control of PM machine considering magnetic saturation and cross-coupling has been investigated in [UND10].

$$\psi_A = \left(\psi_{PM} + M_{df} i_{DC}\right)\cos\theta_e + M_{qf} i_{DC} \sin\theta_e \tag{2.10}$$

$$e_{A-1} = \omega_e \sqrt{\left(\psi_{PM} + M_{df} i_{DC}\right)^2 + \left(M_{qf} i_{DC}\right)^2} \tag{2.11}$$

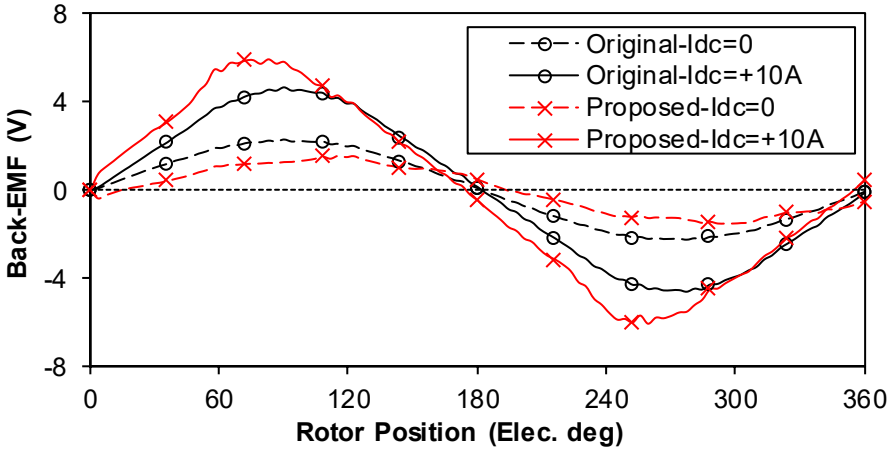

(a) Waveforms

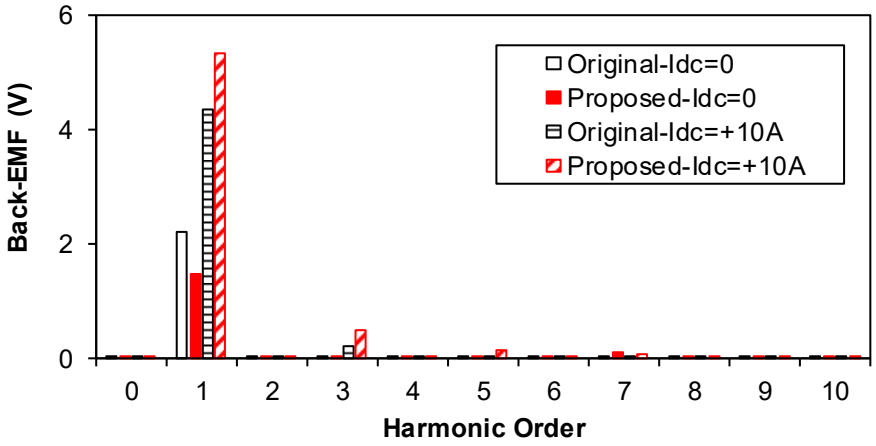

(b) Spectra

Fig. 2.17. Open-circuit phase back-EMF at the rotor speed of 400rpm with different DC excitations for two HE machines.

The open-circuit phase back-EMF fundamental against DC excitation current is illustrated in Fig. 2.18. The variation of fundamental phase back-EMF with DC excitation current agree well with above theoretical analyses. Within the original regulated EMF limits, the regulation of proposed machine is still linear, and the flux regulation ratio is enhanced significantly (i.e. much less DC excitation current is required to regulate the voltage). It should be noted the negative fundamental back-EMF is used to illustrate the flux regulation ratio and it denotes the back-EMF phase is shifted to more than 180º.

The fundamental back-EMF of the original HE machine is larger when the DC excitation is zero, being 2.2V for the original HE machine and 1.5V for the proposed HE machine. However, the fundamental back-EMF of proposed Π-segment HE machine can be more advantageous when the DC excitation current density is higher than 3A, which indicates the torque density can be higher for proposed HE machine even with reduced PM usage.

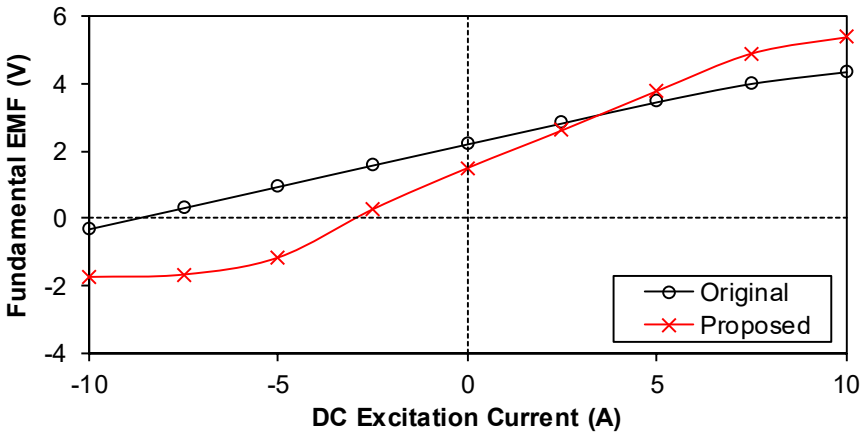

Fig. 2.18. Open-circuit phase back-EMF fundamental at the rotor speed of 400rpm against DC excitation current for the original T-segment and proposed Π-segment HE machines.

The fundamental back-EMF regulation ratio of DC excitation is defined as (2.12) to evaluate the flux regulation capability, and the variation with DC excitation current is shown in Fig. 2.19. The back-EMF regulation ratio for the proposed HE machine is non-linear whereas it is almost linear for the original HE machine as theoretical analyses. Moreover, it is apparent that the flux regulation capability has been intensified significantly.

$$\gamma_{DC} = \frac{e_{PM\pm DC} - e_{PM}}{e_{PM}} \tag{2.12}$$

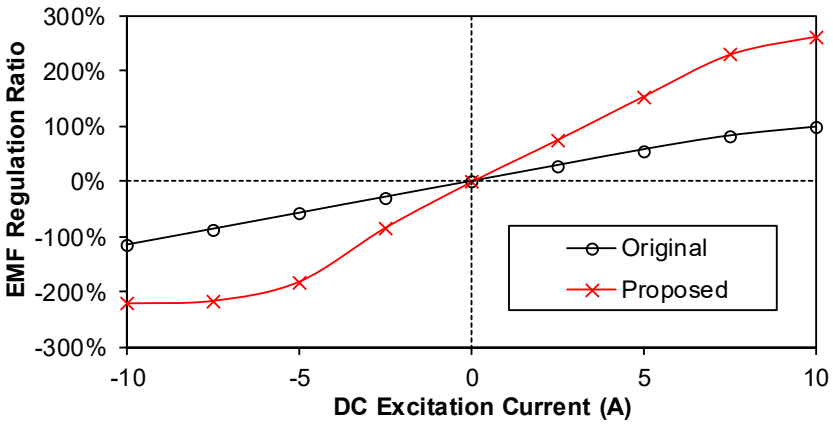

Fig. 2.19. Fundamental back-EMF regulation ratio against DC excitation current density for the T-segment machine and Π-segment machine.

2.6.4 Electromagnetic Torque

The electromagnetic torque performances of two HE machines with no DC excitation and positive DC excitation, viz. flux-enhancing, are presented in Fig. 2.20. The current angle is determined by maximum torque per current control (MTPA). Since the field excitation has effect on both *d*- and *q*-axis flux linkages, the MTPA current angle is dependent on the dc excitation. Furthermore, the torque performances of two HE machines with different field excitations are compared in Table 2.3.

The electromagnetic torques of both HE machines can be regulated by the field current. The average torque of proposed HE machine is smaller without field current excitation. However, with positive DC excitation of +10A, the average torque can be larger than the original HE machine thanks to the enhanced flux regulation capability. Moreover, the torque ripple of the proposed machine is slightly more serious than the original HE machine since the torque ripple is not considered during optimization. The techniques to suppress pulsating torque of doubly salient machine can be found in [JIN10] [ZHU17a].

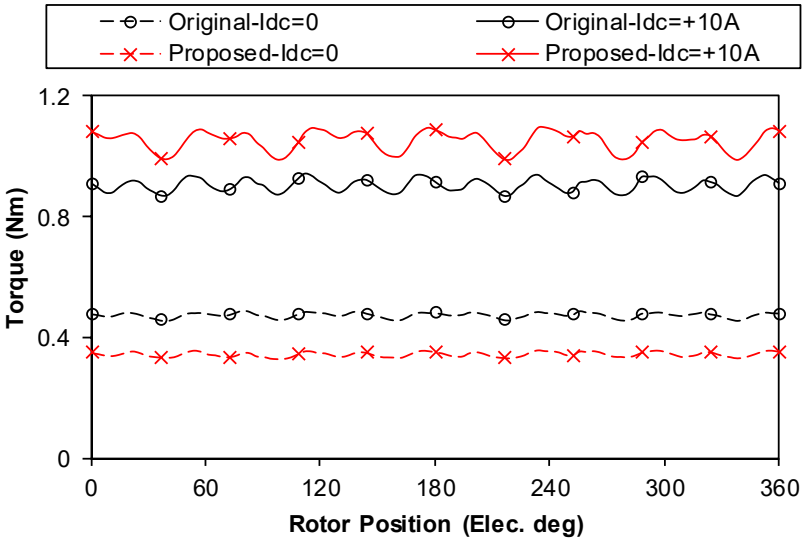

Fig. 2.20. Electromagnetic torque waveforms with armature copper loss of p_{ac}=20W at different field currents for two HE machines.

Table 2.3 Torque performance of original and proposed HE machines with 20W armature copper loss

	Original	Proposed	Original	Proposed
Field excitation	i_{dc} = 0		i_{dc} = 10A	
Average torque	0.48 Nm	0.35 Nm	0.90 Nm	1.05 Nm
Torque ripple	6.7%	9.3%	8.4%	9.9%

Moreover, the average torques versus armature copper loss for the HE machines under MTPA control are evaluated in Fig. 2.21. The field currents are kept the same for fair comparison and not included in the armature copper loss. Without field current excitation, the torque density of the proposed HE machine is weaker compared with the original HE machine. With positive DC excitation of +10A, the average torque of the proposed HE machine is larger at rated current. However, the proposed HE machine is easier to get magnetically saturated due to less reluctance on the stator yoke, and consequently, the average torque gets smaller when the armature copper loss is higher than 60W.

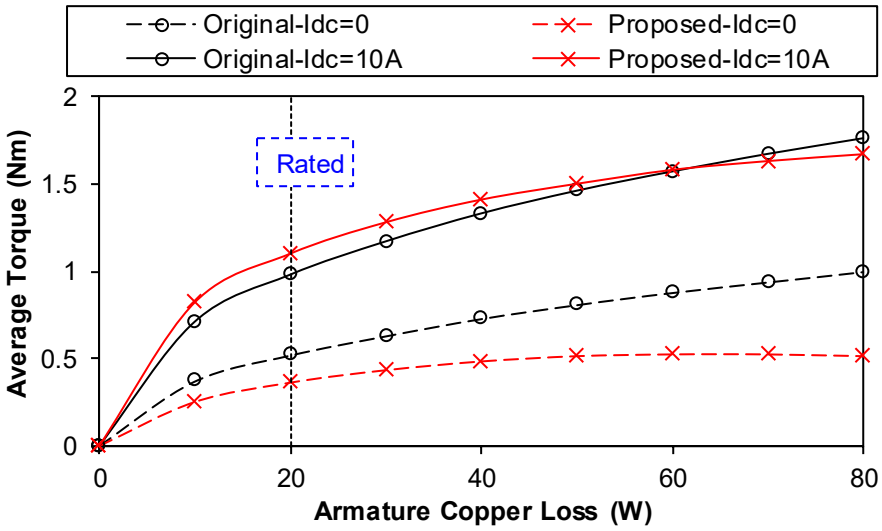

Fig. 2.21. Average torque versus armature copper loss for two HE machines with different field current excitations under MTPA control.

The average torques against field winding current for the two HE machines are predicted in Fig. 2.22. The current electrical angle is determined by MTPA control. The proposed HE machine exhibits lower torque without field excitation, whereas the average torque is higher when the DC excitation current is large than +3A. It is revealed that the torque density of the proposed HE machine is higher operating with flux-enhancing condition, albeit with reduced PM usage.

Moreover, the torque performances at negative DC excitation is different accounting for the flux regulation mechanism. The magnetic field of original HE machine is regulated by the field excitation through the magnetic bridge. Therefore, the magnetic field can be counteracted entirely by the field winding current, and the average torque is reduced to zero at the field excitation of -8A. For the proposed HE machine, as shown in Fig. 2.16, the field current has

the impact on both *d*-axis and *q*-axis flux linkages and the overall flux linkage cannot be zero. Subsequently, the average torque can be weakened but not reduced to zero.

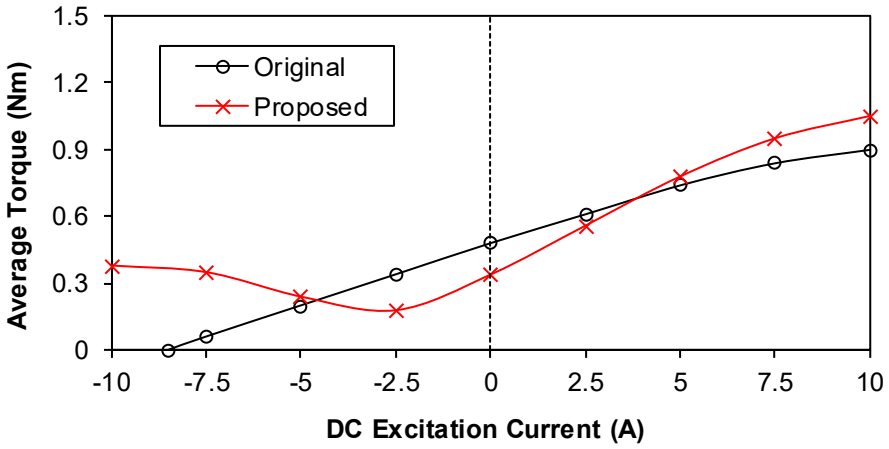

Fig. 2.22. Average torque versus field winding current with maximum torque per armature current control.

2.6.5 Torque-Speed Envelope

An essential benefit of HE machine is wide constant torque region with the regulation of field current. The inductance and flux-weakening characteristics of two HE machines with different DC excitations are compared in Table 2.4, in which the flux weakening factor is defined as (2.13). The HE machines have infinite flux weakening region when the flux weakening factor $k_{fw} > 1$ [SOO02]. The proposed HE machine exhibits infinite flux weakening region regardless of DC excitations, due to larger inductance.

$$k_{fw} = \frac{L_d i_d}{\psi_{PM \pm DC}} \tag{2.13}$$

Table 2.4 Inductance and flux-weakening characteristics

	Original Machine		Proposed Machine	
	$i_{dc} = 0$	$i_{dc} = 10$A	$i_{dc} = 0$	$i_{dc} = 10$A
ψ_{PM} or ψ_{PM+DC}	4.8mWb	9.5mWb	3.1mWb	11.5mWb
L_d	1.8Mh	1.6Mh	3.5Mh	2.7Mh
k_{fw}	1.88	0.84	5.65	1.17

The torque-speed curves under voltage and current limits of inverter with the consideration of magnetic saturation and cross-coupling effect are predicted by the flux linkage method proposed in [QI19]. The average torque is calculated within the *d*- and *q*-axis flux linkages in

(2.14), where the *d*- and *q*-axis flux linkages ψ_d and ψ_q are predicted by the 2D FE simulation and dependent on the field excitation i_{dc}, *d*-axis current i_d, and *q*-axis current i_q. Furthermore, the phase current and voltage are under the limits of inverter and expressed in (2.15). By scanning different *d*- and *q*-axis currents at various operation speed, the maximum torque at corresponding speed can be obtained.

$$T = \frac{3}{2} p\left[\psi_d\left(i_{dc}, i_d, i_q\right) i_q - \psi_q\left(i_{dc}, i_d, i_q\right) i_d\right] \tag{2.14}$$

$$\begin{cases} \sqrt{i_d^{\,2} + i_q^{\,2}} \le I_m \\ \sqrt{\left[R_p i_d - \omega_e \psi_q\left(i_{dc}, i_d, i_q\right)\right]^2 + \left[R_p i_q + \omega_e \psi_d\left(i_{dc}, i_d, i_q\right)\right]^2} \le U_m \end{cases} \tag{2.15}$$

Within the same DC bus voltage and phase current limits of U_m=12V and I_m=5A, the torque-speed curves of two HE machines are evaluated in Fig. 2.23. With positive DC excitation, the torque density is enhanced during the operation region and torque-speed envelopes are broadened. Moreover, the proposed HE machine exhibits highest torque and power with flux enhancing, thanks to the extended flux regulation capability.

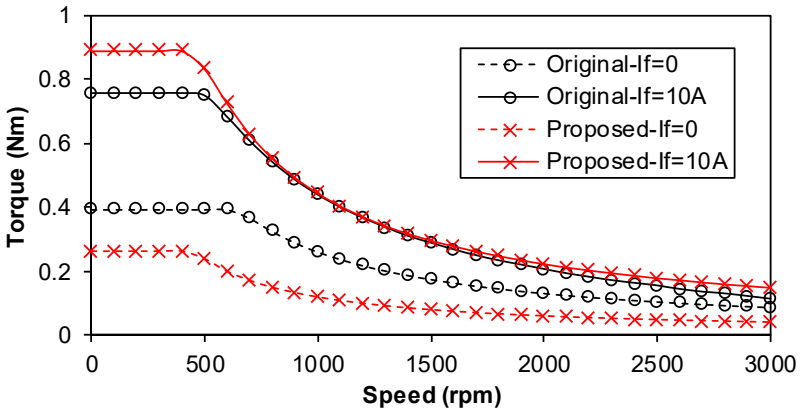

(a) Torque-speed curve

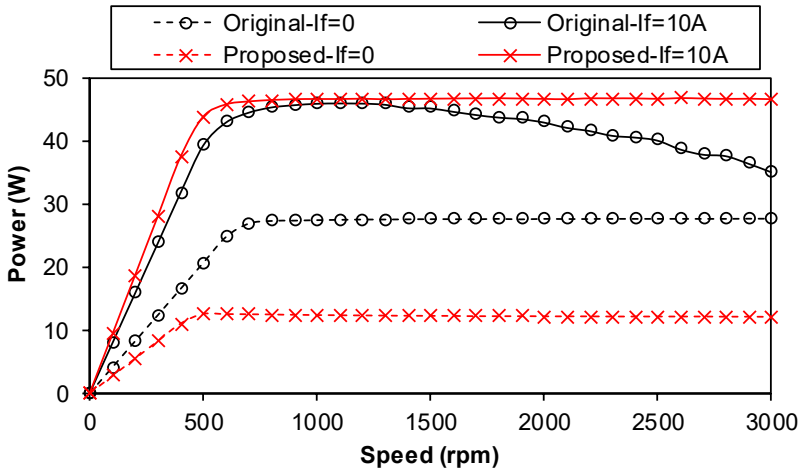

(b) Power-speed curve

Fig. 2.23. Torque and power-speed envelopes with different DC excitations.

Furthermore, the efficiency maps of two HE machines considering field and armature winding copper losses and iron losses are compared in Fig. 2.24. Although the proposed HE machine exhibits higher torque density with flux-enhancing due to wider field regulation capability, the maximum efficiency is sacrificed due to additional field winding copper losses. Therefore, the optimization of the HE machine in the future work will be focused on the optimization considering the additional field winding copper loss and corresponding efficiency reduction.

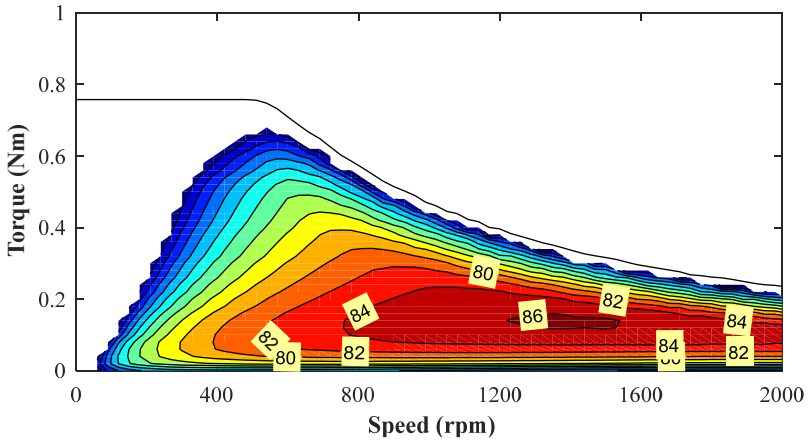

(a) Original HE machine

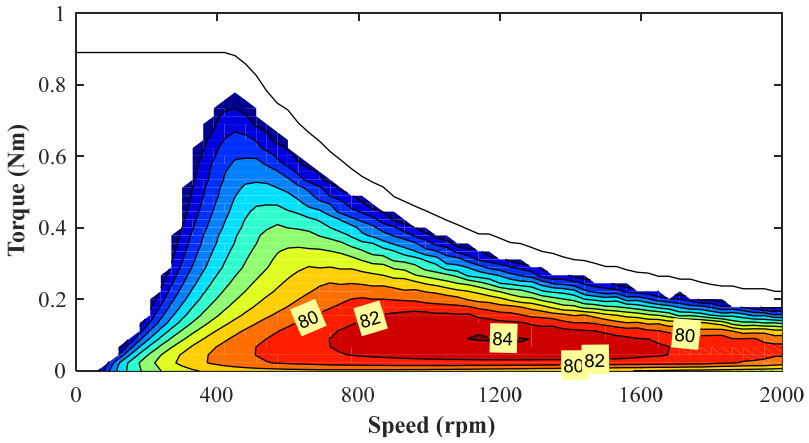

(b) Proposed HE machine

Fig. 2.24. Operation efficiency considering field, armature winding copper losses and iron losses. (colored contour indicating efficiency higher than 60%)

2.6.6 Fault Tolerant Capability

For the proposed HE machine, each armature coil belongs to one stator segment, and consequently, is isolated from each other both mechanically and electrically. When single coil is under unhealthy operation, other coils will not be influenced, which is critical for high fault tolerant application [CAO12b].

Furthermore, the line back-EMF fundamental versus operating speed under different DC excitations is illustrated in Fig. 2.25 for the two HE machines. To improve the output capability, a positive DC excitation can be employed and the back-EMF can be increased. When operating at high speed, the back-EMF with positive DC excitation is higher than the DC bus voltage, and flux weakening current is demanded. However, the high voltage can be potentially dangerous if the flux weakening signal suddenly disappears, which is recognized as uncontrolled generator fault [JAH99]. The winding with high back-EMF becomes a large voltage source and delivers regenerative current to the DC-link. If the DC-link capacitor cannot absorb abruptly regenerative energy, both the capacitor and the inverter may be damaged as the result of overvoltage.

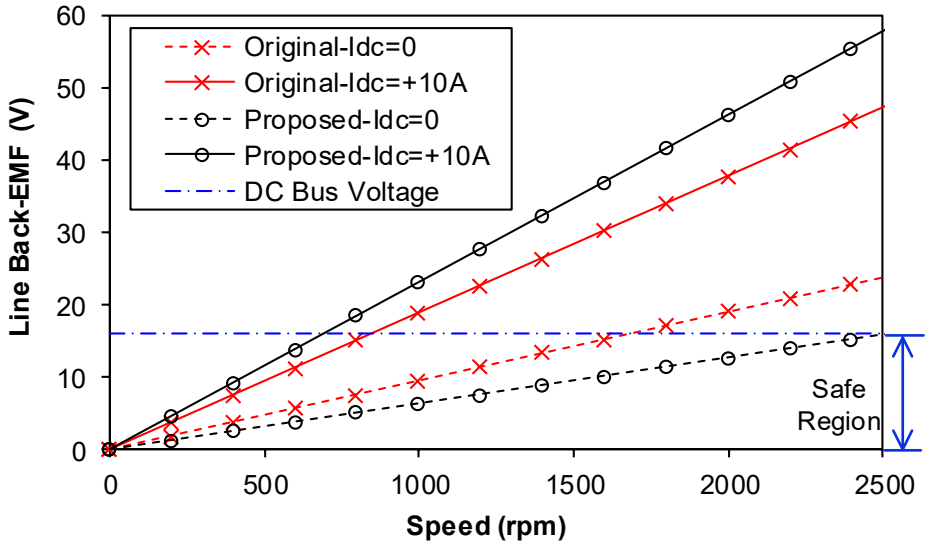

Fig. 2.25. Open-circuit line back-EMF fundamental versus operating speed for two HE machines.

The uncontrolled generator fault for the proposed HE machine can be overcome by removing DC excitation directly [ZHU19a], since the line back-EMF produced by the PMs only is always less than DC bus voltage. Consequently, the high DC regulated back-EMF is advantageous to the output capability, and the low PM excited back-EMF is beneficial to the fault tolerant capability.

2.7 Improved DC Coil Free HE Machine

The electromagnetic performances of the proposed HE machine with DC and AC excitations supplied separately have been discussed above. Furthermore, the field winding can be integrated with armature winding with the utilization of dual electric port inverter in Fig. 2.26 [ZHU17b]. In the separated field and armature winding HE machine, the armature current is controlled by three-phase inverter with neutral point star-connection and the field excitation is controlled by additional H-bridge inverter. Therefore, the field and armature excitations can be expressed in (2.16). By utilizing the dual electric port inverter in Fig. 2.26, the neutral point is released in the three-phase armature winding and biased AC excitation can be suppled. Subsequently, the field winding can be eliminated and the integrated winding excitation can be expressed in (2.17).

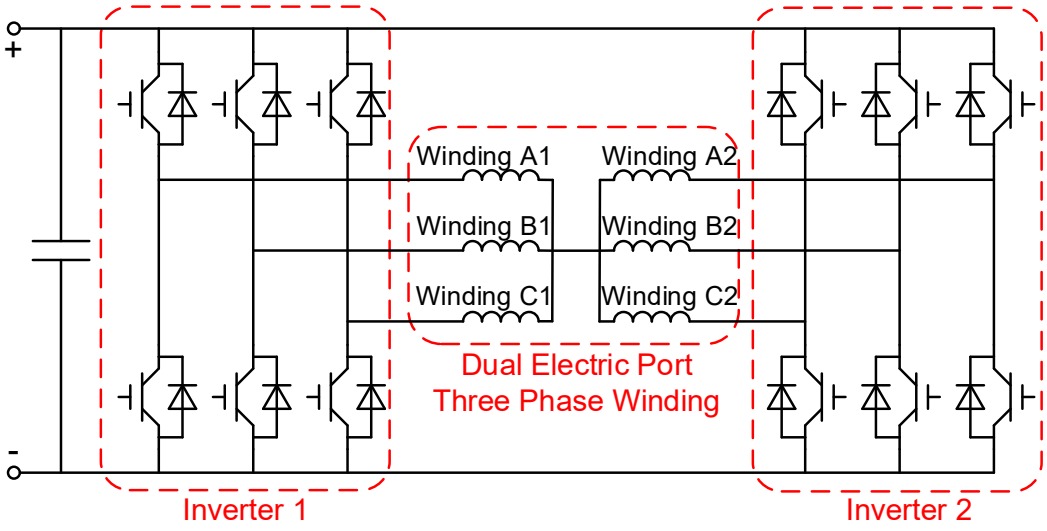

Fig. 2.26. Dual electric port inverter with a single voltage source.

$$\begin{cases} i_f = I_{dc} \\ i_{A1} = i_{A2} = I_m \cos\left(\omega_e t + \alpha_e\right) \\ i_{B1} = i_{B2} = I_m \cos\left(\omega_e t + \alpha_e - \dfrac{2}{3}\pi\right) \\ i_{C1} = i_{C2} = I_m \cos\left(\omega_e t + \alpha_e + \dfrac{2}{3}\pi\right) \end{cases} \tag{2.16}$$

$$\begin{cases} i_{A1} = I_m \cos\left(\omega_e t + \alpha_e\right) + I_{dc} \\ i_{A2} = I_m \cos\left(\omega_e t + \alpha_e\right) - I_{dc} \\ i_{B1} = I_m \cos\left(\omega_e t + \alpha_e - \dfrac{2}{3}\pi\right) + I_{dc} \\ i_{B2} = I_m \cos\left(\omega_e t + \alpha_e - \dfrac{2}{3}\pi\right) - I_{dc} \\ i_{C1} = I_m \cos\left(\omega_e t + \alpha_e + \dfrac{2}{3}\pi\right) + I_{dc} \\ i_{C1} = I_m \cos\left(\omega_e t + \alpha_e + \dfrac{2}{3}\pi\right) - I_{dc} \end{cases} \tag{2.17}$$

In the integrated winding HE machine, the additional field winding is eliminated and the spatial conflicts in the improved DC coil free HE machine is solved. Since the conducting area for either DC or AC excitation is enlarged, the resistance as well as copper loss can be reduced.

In order to evaluate the benefit of integrated winding, the electromagnetic performances of the proposed HE machine with separated and integrated windings are compared with 2D FE calculation. To simplify the analysis, the machine parameters are kept constant as section 2.4,

whereas the original field coils are removed with doubly number of turns for armature coils and biased AC excitation is injected for the integrated winding.

The phase back-EMF fundamental versus DC excitation current for separated and integrated windings are shown in Fig. 2.27. Without DC excitation, the back-EMF fundamental is doubled since the slot area for field coils are spared out. Besides, the EMF regulation ratio is increased since the turns of DC excitation is doubled with integrated winding. It should be noted over-saturation is easier to occur for the integrated winding, in which back-EMF fundamental even reduces with DC excitation [FOD07].

To gain the same ampere-turns of excitation, the current of integrated winding is reduced to half since half of the original field winding slot area is spared for the armature excitation. Therefore, the copper loss can be reduced neglecting the slightly enlarged axial length in the integrated winding. The overall assessment of thermal model will be established in the future work accounting for the increased end-winding length. The electromagnetic torque waveforms at different DC excitations for the proposed HE machine with separated and integrated windings are compared in Fig. 2.28. The average torque of integrated winding is enhanced since the slot area of field winding is saved. Besides, the torque density at flux enhancing condition is further improved since the slot area for DC excitation is expanded. The torque ripple of integrated winding is slightly increased due to magnetic saturation caused by higher ampere-turns within same copper loss.

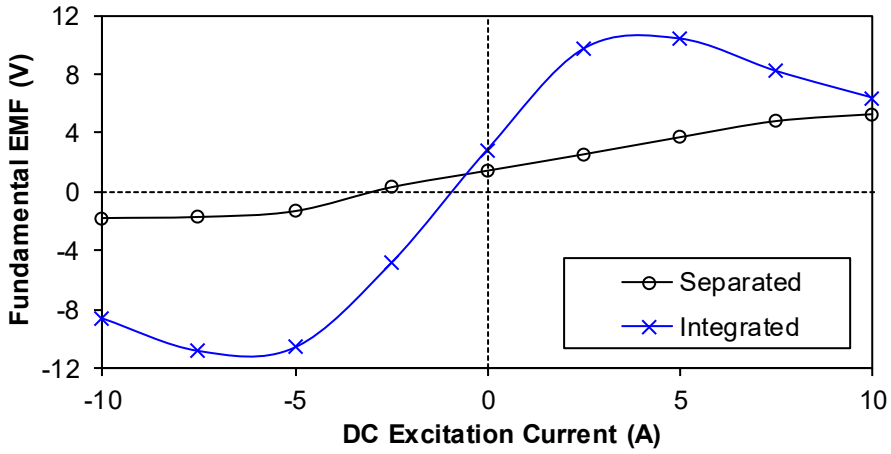

Fig. 2.27. Open-circuit phase back-EMF fundamental at the rotor speed of 400rpm against DC excitation current for the proposed HE machine with separated and integrated windings.

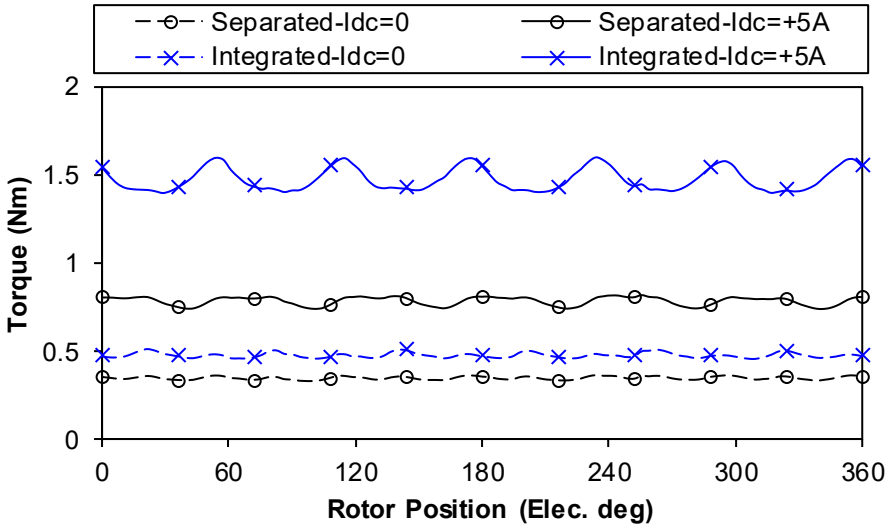

Fig. 2.28. Electromagnetic torque waveforms with armature copper loss of p_{ac}=20W MTPA control at different field currents for proposed HE machine with separated and integrated winding.

2.8 Experimental Validation

In order to validate the forgoing analyses and FE predictions, a prototype of the proposed HE machine is manufactured. To ease the assembling and winding process, the stator laminations are linked with iron bridge whose thickness is 0.5mm, and the slot packing factor is reduced to 0.25. The HE machine is re-optimized and the main parameters of the prototype are listed in Table 2.5. The photos of the assembled stator and salient rotor are shown in Figs. 2.29 (a) and (b), respectively.

Table 2.5 Main parameters of prototype

Parameter	Value	Parameter	Value
Stator outer diameter	45mm	Stack length	25mm
Air-gap Length	0.5mm	PM height	3mm
PM remanence	1.1T	PM coercivity	824Ka/m
Stator yoke thickness	5.5mm	Stator tooth width	6.1mm
Split ratio	0.65	Rib thickness	0.5mm
Rotor pole width	5.4mm	Rotor pole height	5mm
Turns per armature coil	30	Turns per field coil	30

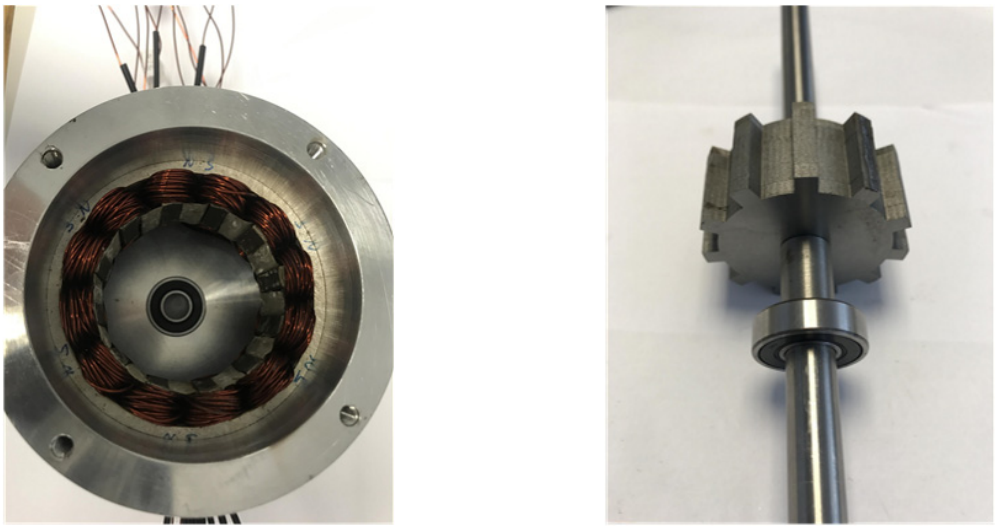

(a) Assembled stator (b) Rotor

Fig. 2.29. Photos of proposed HE prototype.

The open-circuit phase back-EMF waveforms with different DC excitations are measured, in comparison with FE predictions in Fig. 2.30. Good agreement is achieved although FE predicted back-EMFs are slightly higher due to 3D end-effect. Besides, the fundamental back-EMF versus DC excitation current is illustrated in Fig. 2.31. The measured and FE predicted fundamental back-EMFs vary with DC excitations, indicating the flux regulation effect of field winding. Overall, the measured back-EMFs agree well with the 2D-FE predictions.

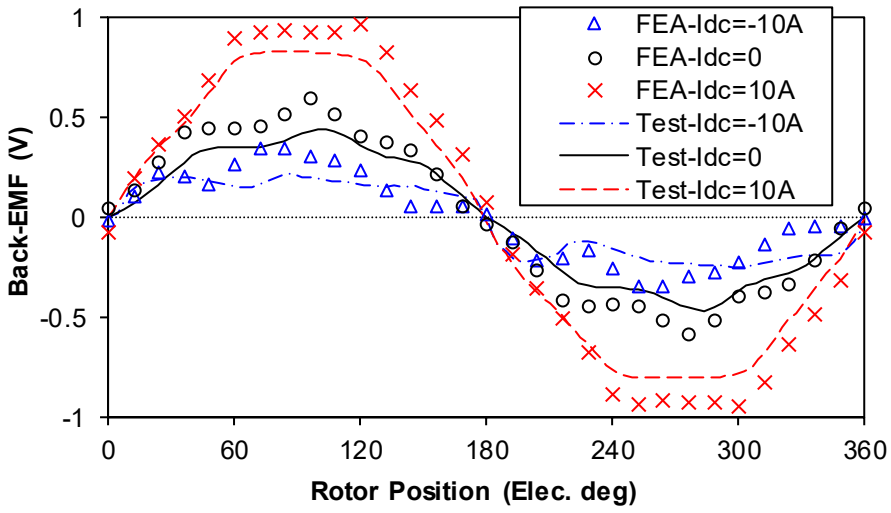

Fig. 2.30. Measured and FE predicted open-circuit phase back-EMF waveforms at the rotor speed of 400rpm with different DC excitations.

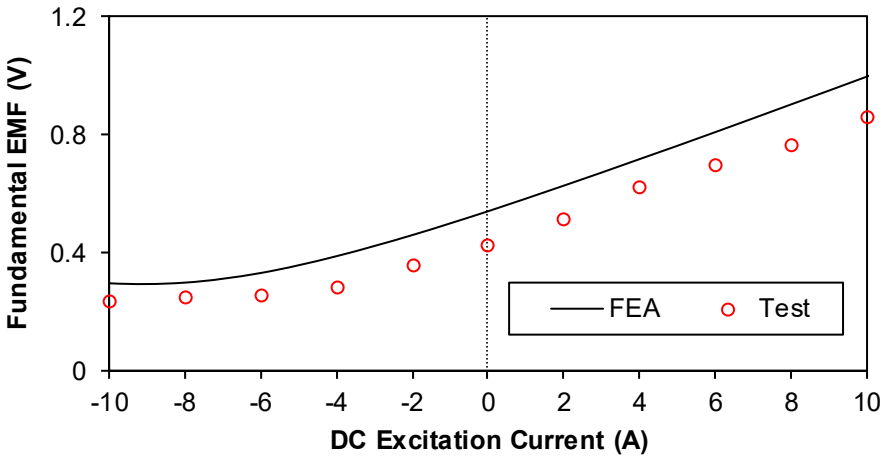

Fig. 2.31. Measured and FE predicted open-circuit phase back-EMF fundamentals versus DC excitation currents at the rotor speed of 400rpm.

The on-load static torque is measured within the method developed in [ZHU09] and the test rig is shown in Fig. 2.32. The prototype is clamped by the jaws of lathe, with the rotor shaft connecting to the balance beam. The weight is added on the balance beam to ensure the beam bar always contact the digital scale. Two DC supplies are employed to feed to field winding and armature winding, respectively. By measuring the force via the digital gauge, the static torque transmitted through the rotor shaft can be calculated.

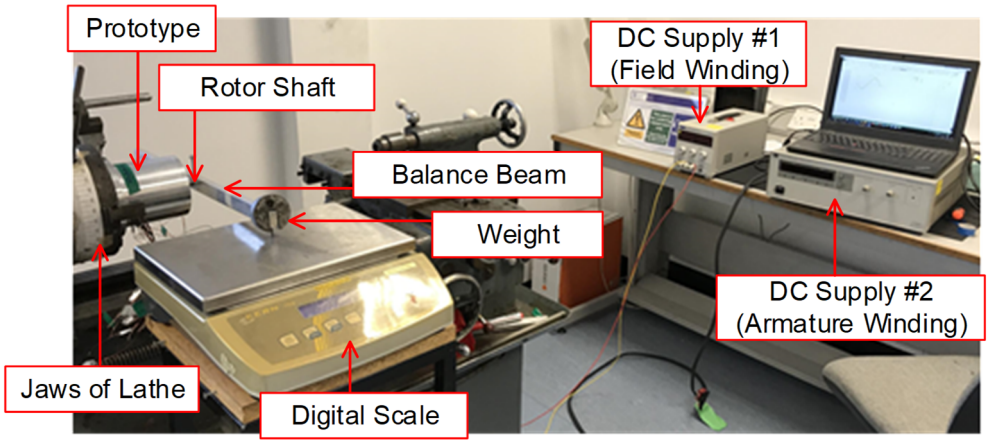

Fig. 2.32. Test rig for static torque measurement.

Therefore, the static torque with the armature current of i_a = -2i_b =-2i_c = 8A and various field currents at different rotor positions can be measured, in comparison with FE predictions in Fig. 2.33. The measured static torques are smaller than the FE calculations due to end effect and friction. Overall, the measured static torques agree well with FE predictions, proving the accuracy of FE torque calculations.

According to the measurement in Fig. 2. 33, the rotor positions of *d*-axis and *q*-axis can be identified. By fixing the rotor position with the alignment of stator phase A-axis and rotor *q*-axis, the measured and FE predicted torques variation with i_a and i_{dc} are shown in Fig. 2.34. Again, the test results are in good agreement with FE predictions and it is verified that the DC excitations can regulate the output torque effectively.

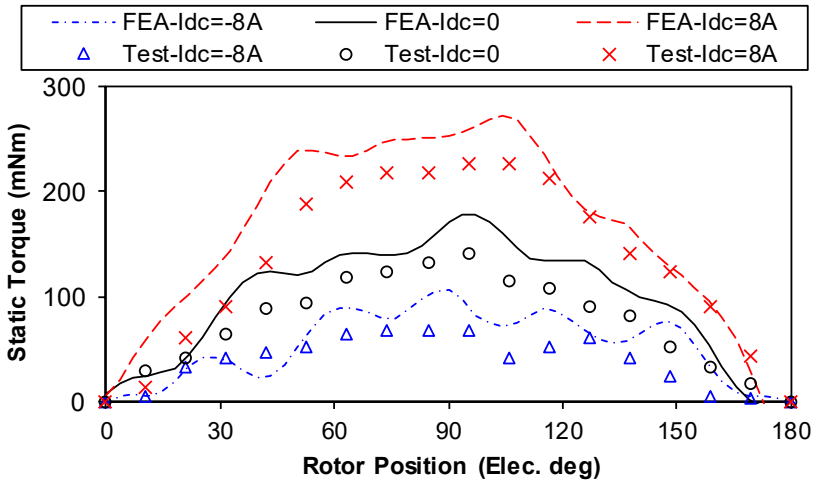

Fig. 2.33. Measured and FE predicted static torques under the armature current of $i_a = -2i_b = -2i_c = 8$A and different field currents.

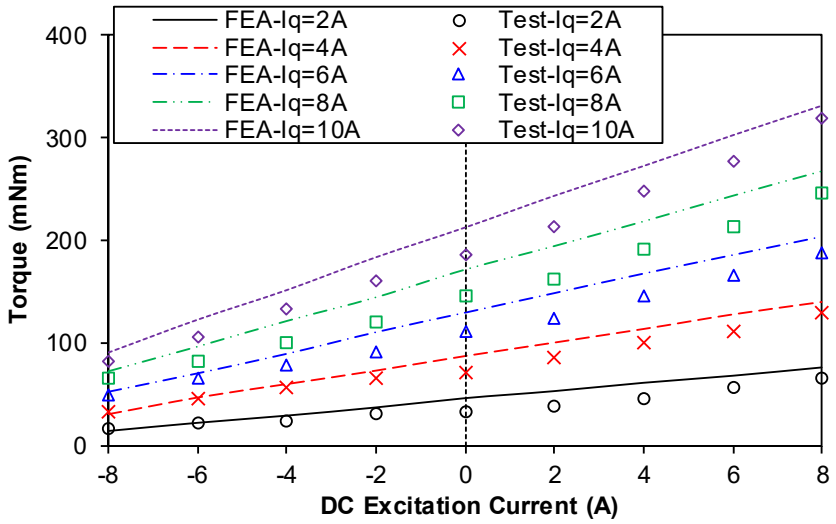

Fig. 2.34. Measured and FE predicted torques variation with DC excitation current at different *q*-axis currents.

To fully illustrate the benefit of hybrid excitation during the whole operation region, the torque-speed envelopes of the prototype with different DC excitations are measured. The flux-weakening experiment is conducted within the limit of 8A phase current and 3V DC bus voltage. The measured torque-speed curves with both zero DC and positive DC excitations are

shown in Fig. 2.35, in comparison with FE simulations. Although the measured torques are always smaller than the simulated results due to friction of the load machine (particularly for the small prototype machine), the flux-weakening trends agree well. Moreover, the torque-speed envelops can be broadened with positive DC excitation, verifying the benefits of hybrid excitation.

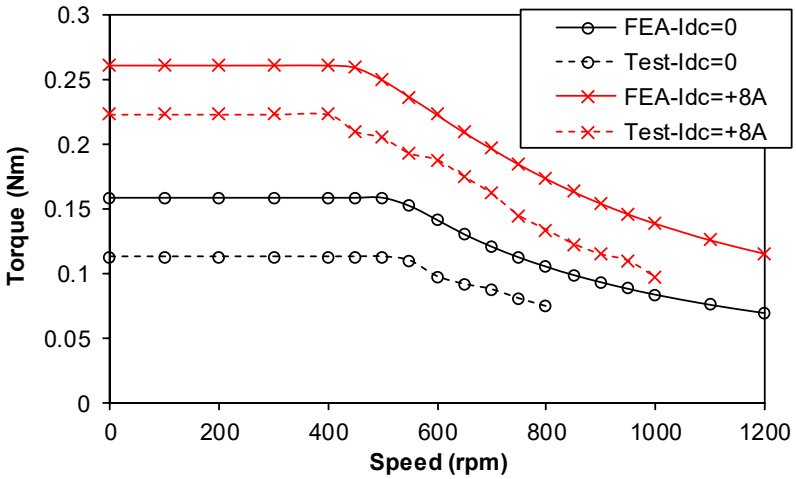

Fig. 2.35. Measured and FE predicted torque-speed envelopes with different DC excitations.

2.9 Summary

In this chapter, a novel parallel hybrid excited machine with wide flux regulation range is introduced. All the excitations, including PMs, field and armature windings are located in the stationary part, which is beneficial of heat management. The flux paths of PMs and field excitations are separate and in parallel, which extends the flux regulation capability. The electromagnetic performances of the proposed HE machines are evaluated in comparison with the original counterpart. It is revealed that the proposed HE machine exhibits lower PM excited back-EMF, and consequently, good fault tolerant capability at high speed flux weakening region. Meanwhile, the torque density can be higher with positive DC excitation, albeit with less PM usage. Moreover, dual-electric port inverter can be employed to integrate the field winding with armature winding and a DC-coil free HE machine is obtained. Since the slot area for field winding is saved, both the flux regulation ratio and torque density can be further improved. Finally, a prototype is manufactured to validate the analyses and FE predictions, and the measured back-EMF and static torque agree well with the FE predictions.

Chapter 3

Investigation of Novel Doubly Salient Hybrid Excited Machine with Non-Overlapped Field Winding

Hybrid excited machines, which synthesize the high torque density of permanent magnet (PM) machine and controllable flux of wound field (WF) machine, are perceived as promising candidate for variable speed application. A novel doubly salient hybrid excited (DSHE) machine with non-overlapped field winding is presented in this chapter. It inherits simple structure of conventional doubly salient PM (DSPM) machine and facilitates the regulation of magnetic field by field winding. The electromagnetic performances of the proposed machine with different stator and rotor pole number combinations are investigated by finite element method (FEM), confirming these advantages. Furthermore, the effect of the iron bridge on the hybridization between PM and WF excitations is analyzed to obtain a trade-off between high torque density and wide flux regulation range with the frozen permeability method (FPM). Finally, a prototype is fabricated and tested to validate the theoretical analysis.

3.1 Introduction

Permanent magnet (PM) synchronous machines have been widely investigated for decades, due to the rapid development of magnetic materials, power electronics, and advanced control techniques [BIA06a]. The stator PM machines with doubly salient structure are popular and the flexible location of PM results in diverse machine topologies [WAN01] [HUA08] [CHE20]. The concept of stationary PM with rotary salient pole to alter flux linkage is firstly introduced in [RAU55] for single phase alternator, and then extended to the three phase doubly salient PM (DSPM) machine in [LIA95], as shown in Fig. 3.1 (a). The armature coils are non-overlapped wound around the stator teeth, with potential high winding packing factor and compact volume [RED12]. Since all the excitations are placed in the stationary component, there is no need of brushes/slip rings for field winding excitation, while the heat management is more effective. Moreover, the rotor is the same as that in switched reluctance machine, which is robust with less concern about centrifugal force [CHI15].

Although the employment of high-energy-product PM is beneficial for high torque density and compact structure, the magnetic field is fixed and the high reluctance of PM results in difficulty to regulate the flux by *d*-axis current [SOO02]. Therefore, the efficiency and power

factor are inevitably degraded at high speed operation, which has restricted the utilization in the variable speed application.

To achieve flexible regulation of magnetic field, hybrid excitation is proposed to combine the PM machine with wound field (WF) machine [FOD07]. Since an additional control degree, i.e. DC excitation, is introduced for field regulation, the flux weakening performance can be further improved compared with pure PM excitation [GIU15]. To achieve hybrid excitation for the DSPM machine, various doubly salient hybrid excited (DSHE) machine topologies have been investigated in [LI95] [CHE01] [CHA03] [ZHU05] [YU11] [CHE08] [ZHA12] [CHE14] [GEN15] [WU18], as shown in Fig. 1.14 of chapter 1. In [LI95] and [CHE01], the field winding is wound around the PM poles to regulate the magnetic field. However, the flux lines of DC excitation pass through the PMs, which restricts the flux regulation capability and potentially causes irreversible demagnetization. To avoid the flux path of field winding passing through the PM, additional air-gap and iron bridge are introduced for WF flux path in [CHA03] and [ZHU05], respectively. As the reluctance of the additional air-gap and iron bridge is reduced compared with PMs, the flux regulation capability can be enhanced. Furthermore, a DSHE machine with outer rotor configuration is put forward in [YU11] for better spatial utilization. To further improve the flux regulation ratio, the DSHE machine with parallel PM and DC flux paths is proposed by allocating a pole-pair of PMs and a pole-pair of DC excitation coils alternatively in [CHE08] and [ZHA12]. Although the series DSHE machines generally possess simpler topology, the parallel counterparts obviously exhibit better flux regulation capability [CHE14]. Moreover, the stator incorporating PMs, field winding, and armature winding is complicated, resulting in difficulty for manufacturing as well as assembling in mass production. To separate the PM and WF flux paths, another parallel hybridization technique is presented in [GEN15] and [WU18] by combining the doubly salient wound field machine and the rotor PM machine axially.

The introduction of field winding facilitates magnetic field regulation for the DSHE machine compared with pure PM excitation, which is more promising for the variable speed applications [DRU17]. Nevertheless, the field winding as well as armature winding are overlapped for the DSHE machines presented in [LI95] [CHE01] [CHA03] [ZHU05] [YU11] [CHE08] [ZHA12] [CHE14] [GEN15] [WU18] with the field winding coil pitch of 3 slot pitches, as illustrated in Fig. 1.14 of chapter 1. Therefore, the hybridization is obtained as the sacrifice of less compact volume and reduced slot filling factor for the overlapped field winding. The purpose of this chapter is to present a novel DSHE machine with non-overlapped field

winding, which inherits the compact structure of conventional DSPM machine. To achieve hybrid excitation in the DSPM machine of Fig. 3.1 (a), field winding is introduced to replace part of armature winding in Fig. 3.1 (b). It is worth emphasizing that iron bridge is attached beside the PM to provide additional flux path for DC excitation, which will be investigated subsequently. By allocating the stator teeth evenly, a novel DSHE machine with non-overlapped field winding is presented.

In this chapter, the proposed DSHE machine topology as well as the operation principle will be firstly illustrated from the perspective of PM and WF flux paths. Then, the possible stator and rotor pole number combinations are presented and compared under the genetic algorithm embedded global optimization. Furthermore, the effect of iron bridge on the hybridization is investigated with frozen permeability method. Finally, the electromagnetic performance of the proposed DSHE machine is evaluated with finite element (FE) analysis and validated with experiments.

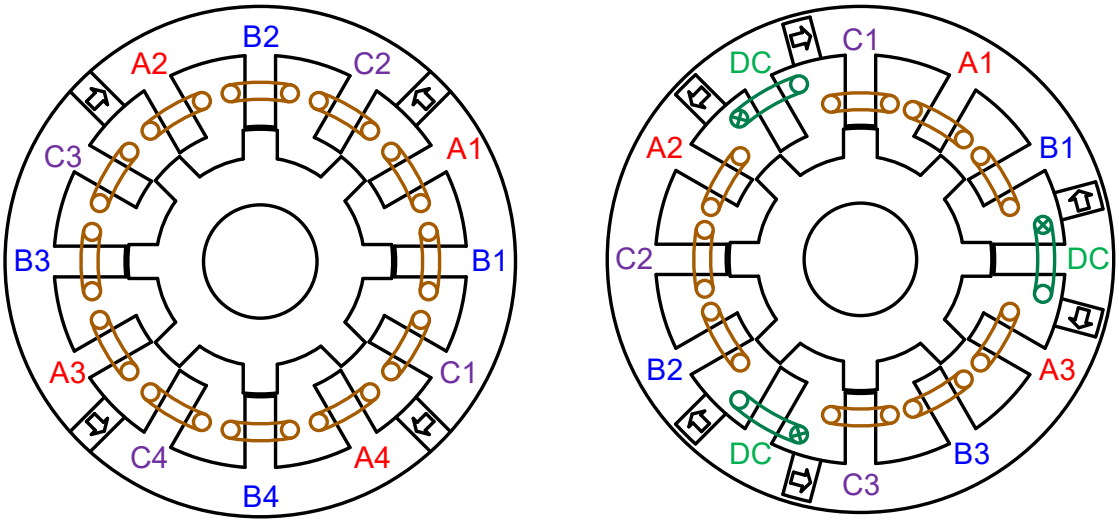

(a) Conventional DSPM machine with stator yoke PM [LIA95]

(b) Proposed DSHE machine

Fig. 3.1. Cross-sections of doubly salient machines (brown line coil indicates AC armature coil, and green line coil indicates DC field coil).

3.2 Machine Topology and Operation Principle

3.2.1 Machine Topology

The proposed DSHE machine with both non-overlapped armature and field windings is shown in Fig. 3.1 (b), with 12/8 stator-slots/rotor-poles (N_s/N_r) as an example. The circumferentially magnetized PMs are placed at the stator yoke, with adjacent pieces of

opposite directions. Therefore, the flux concentrating effect of the doubly salient PM machine is inherited. The field coils are wound around the PMs sandwiched 'one-tooth', whereas the armature coils are wound around the PMs sandwiched 'three-teeth'. The polarity of all the DC coils is identical, and the arrangement of armature coils will be discussed in section 3.3. The iron bridge is designed besides the PMs to provide additional flux path for DC excitation.

3.2.2 Operation Principle

The open-circuit flux paths of the proposed DSHE machine with PM excited only are illustrated in Fig. 3.2. At the rotor position of Fig. 3.2 (a), the coils A1, A2, and A3 wound stator teeth are aligned with the rotor teeth, and the coil flux linkages are maximized. As the rotor moves to the position of Fig. 3.2 (b), the coils B1, B2, and B3 wound stator teeth are aligned with the rotor teeth, and the coil flux linkages are maximized. Similarly, the flux linkages of coils C1, C2, and C3 are maximized in Fig. 3.2 (c). As the salient rotor moves, the coil flux linkage alternates in turns. When the rotor moves one rotor pole pitch, the single coil flux linkage changes one period. Therefore, the relationship between the electrical angle θ_e and mechanical angle θ_m can be defined in (3.1).

$$\theta_e = N_r \theta_m \tag{3.1}$$

To validate the theoretical analysis, finite element (FE) simulation is conducted on the proposed DSHE machine with initial parameters listed in Table 3.1. The normalized PM excited flux linkage waveforms with 2D FE calculation are shown in Fig. 3.3. The flux linkage waveforms of coils A1 and A3 are symmetrical, whereas the maximum flux linkage of coil A2 is smaller. This can be explained by the different flux path of coil A2 with coil A1/A3 in Fig. 3.2. The flux path of coil A2, which is wound around the middle tooth of 'three-armature-teeth', circulates from the iron bridge besides the PMs, which is of higher reluctance. Therefore, the maximum flux linkage of coils A2, B2, and C2 is smaller than the other counterparts. However, the flux linkage waveforms of different phases are identical, with 120º phase shift.

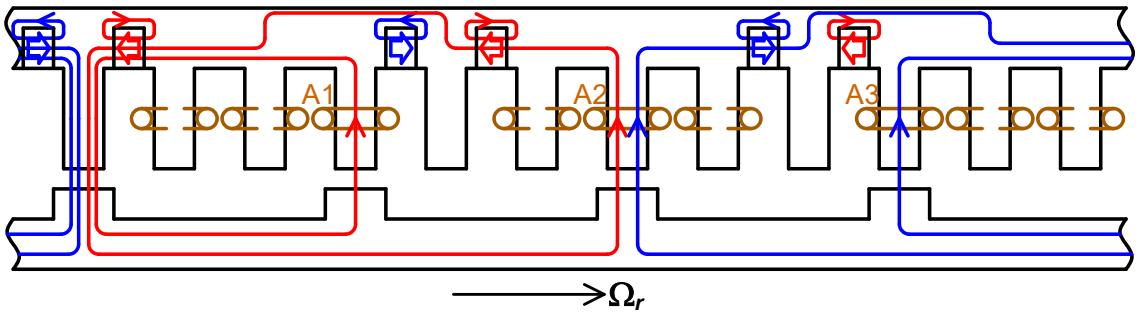

(a) Phase A flux linkage maximized rotor position

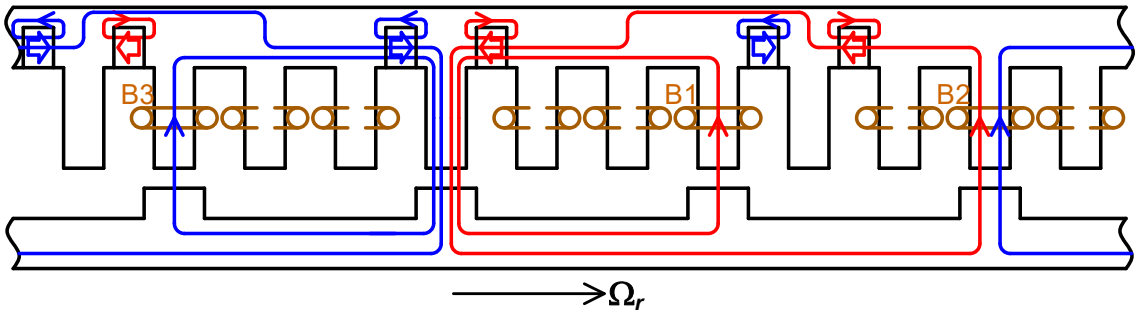

(b) Phase B flux linkage maximized rotor position

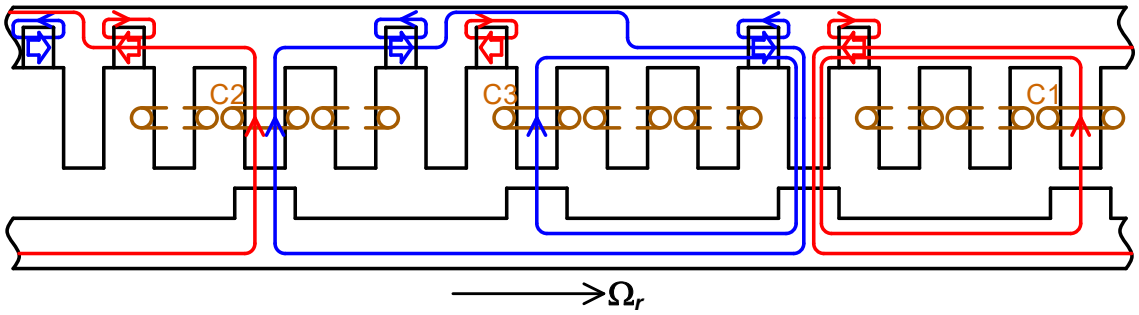

(c) Phase C flux linkage maximized rotor position

Fig. 3.2. Open-circuit flux path illustration of the proposed DSHE machine with PM excited only at typical rotor positions (N_s/N_r=12/4 as an example).

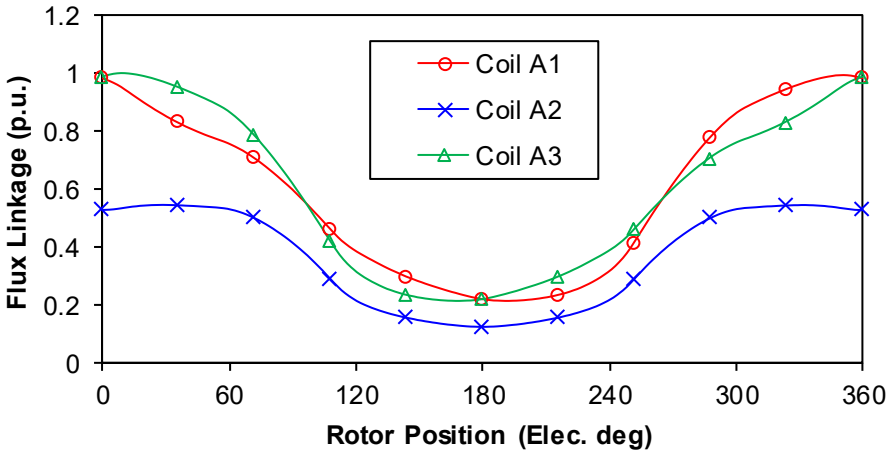

(a) Phase A single coil flux linkage waveforms

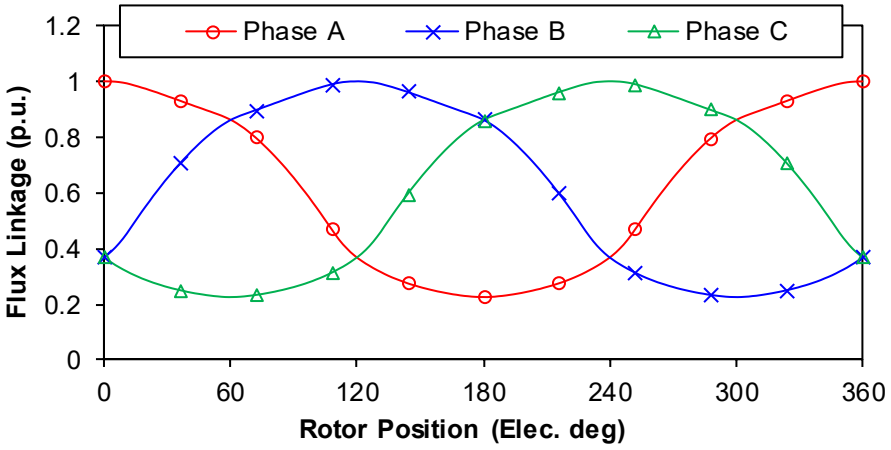

(b) Three-phase flux linkage waveforms

Fig. 3.3. Normalized PM excited flux linkage waveforms for proposed doubly salient HE machine with initial parameters.

Table 3.1 Initial parameters of proposed DSHE machine

Parameter	Value	Parameter	Value
Stator outer diameter	90mm	Stack length	25mm
Air-gap length	0.5mm	Split ratio	0.5
Stator yoke thickness	8mm	Iron bridge thickness	1mm
Stator tooth width	5mm	Rotor tooth pole arc	0.45
PM remanence	1.1T	PM coercivity	824Ka/m
PM thickness	5mm		

3.2.3 Flux Regulation Mechanism

To further illustrate the flux regulation mechanism of DC excitation, the DC excited open-circuit flux path is shown in Fig. 3.4. Compared with the PM excitation at the same rotor position of Fig. 3.2 (a), the flux path of WF is similar. The flux lines of DC excitation pass through the iron bridge besides the PMs, and the demagnetization withstanding capability is enhanced. Meanwhile, the flux path of PM excitation short-circuits through the iron bridge, and the existence of iron bridge causes PM leakage flux. The introduction of iron bridge ensures the two excitation flux paths in parallel and improves the flux regulation capability. Therefore, the thickness of iron bridge should be designed as the trade-off between PM excited output capability and DC excited flux regulation capability.

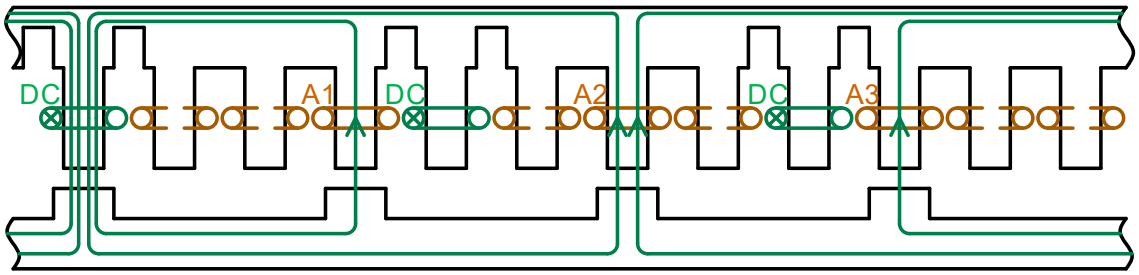

Fig. 3.4. Open-circuit flux path illustration of proposed doubly salient HE machine with DC excited only at the rotor position of maximum phase A flux linkage.

The effect of DC excitation on the phase flux linkages with the assistance of 2D FE is illustrated in Fig. 3.5. It can be observed that the DC excitation can regulate the phase flux linkages effectively. The fundamental flux linkage can be increased to several times of PM excitation with positive DC excitation, and the PM flux can be totally countered by negative DC excitation. Moreover, the flux weakening capability is better than the flux enhancing due to magnetic saturation with positive DC excitation.

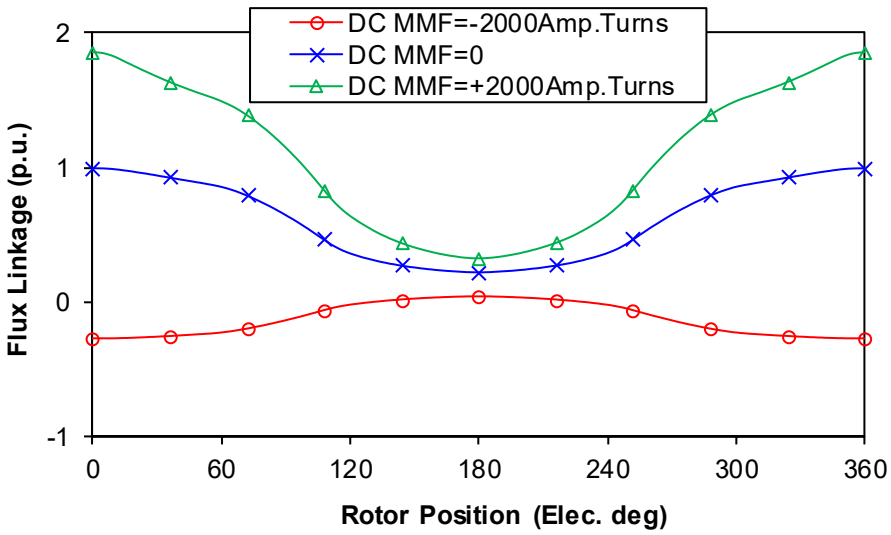

(a) Phase flux linkage waveforms with different DC excitations

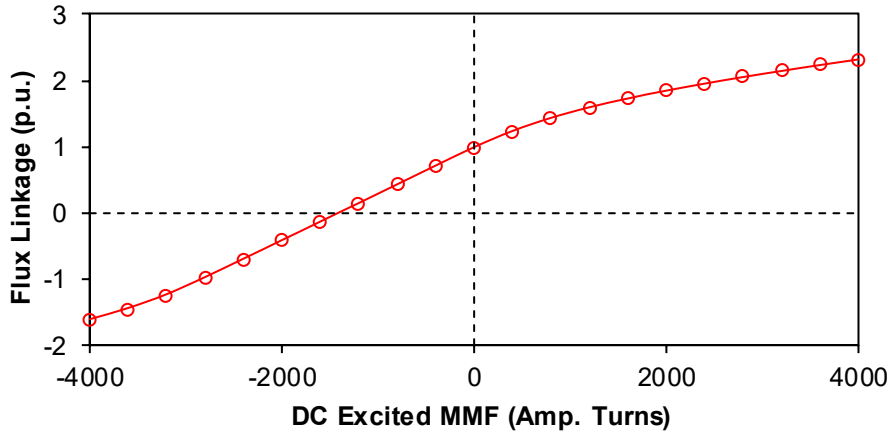

(b) Fundamental phase flux linkage versus DC excited magnetomotive force (MMF)

Fig. 3.5. Normalized phase flux linkage regulation of DC excitation for proposed doubly salient HE machine with initial parameters.

3.3 Stator and Rotor Pole Number Combination

3.3.1 Possible Stator and Rotor Pole Number Combination

As illustrated in Fig. 3.1 (b), the stator tooth of the proposed DSHE machine is composed by field coil wound tooth and armature coil wound tooth separately. The minimum stator element contains 1-field coil wound tooth and *m*-armature coil wound teeth for an *m*-phase machine. To achieve symmetrical phase flux linkage, the stator core should include at least *m*-unit machine. Therefore, the stator tooth and rotor pole number for an *m*-phase machine can be defined in (3.2) to obtain the starting torque for the multiphase machine.

$$\begin{cases} N_s = m(m+1)k_1 \\ N_r \neq k_2 m \end{cases} \tag{3.2}$$

where k_1 and k_2 are any integers.

The unit stator tooth number for the proposed 3-phase DSHE machine is N_s=12, and the rotor pole number can be N_r=4,5,7,8,10,11…. The following investigation will be focused on the three-phase machine with unit stator tooth number of N_s=12, and other stator tooth number can be extended as well. It should be noted that the unit machine with N_s=12 has three PM poles in Fig. 3.1 (d), which potentially results in unbalanced magnetic force (UMF). The asymmetric structure and UMF can be eliminated by doubling the stator and rotor poles.

3.3.2 Armature Winding Connection

The mechanical and electrical angles between two armature coils can be defined in (3.3) according to the previous analysis, in which the stator tooth number of n=4k (k=1, 2, 3) is wound with field coil. To illustrate the armature winding configuration, the coil EMF phasors and winding connections of 12/7 and 12/8-stator slots/rotor poles HE machines are shown in Fig. 3.6. Similarly, the armature winding connections of other rotor pole number with N_r=4,5,7,8,10,11… can be obtained. It is worth emphasizing that the EMF phasors in Fig. 3.6 indicate the phasor angle of corresponding tooth wound armature coil, whereas the amplitudes of different coils can be different as discussed in Fig. 3.3. Obviously, the armature winding distribution factor is 1 when the rotor pole number N_r=4k, which can result in higher phase flux linkage as well as back-EMF.

$$\begin{cases} \alpha_m^{n-1} = \dfrac{360}{N_s}(n-1), n \neq 4k \\ \alpha_e^{n-1} = \dfrac{360}{N_s} N_r (n-1), n \neq 4k \end{cases} \tag{3.3}$$

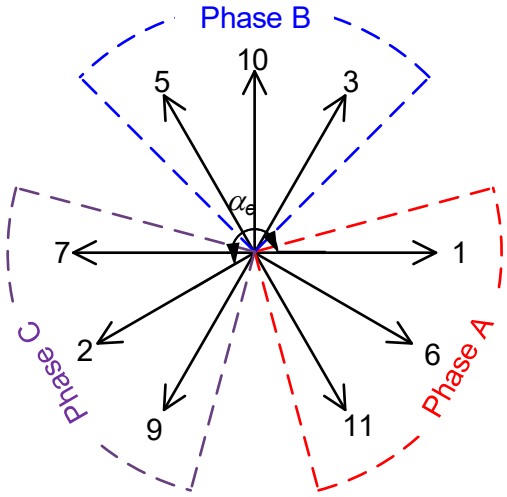

(a) Coil EMF phasor of N_r=7

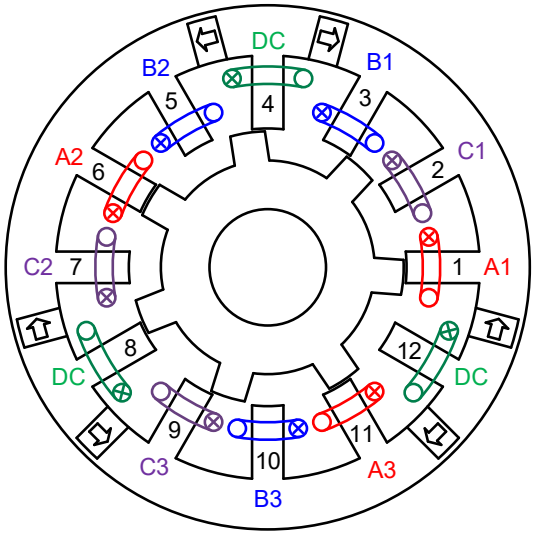

(b) Armature winding connection of N_r=7

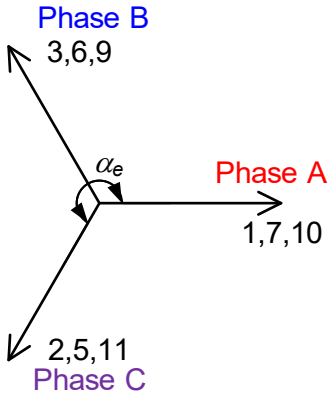

(c) Coil EMF phasor of N_r=8

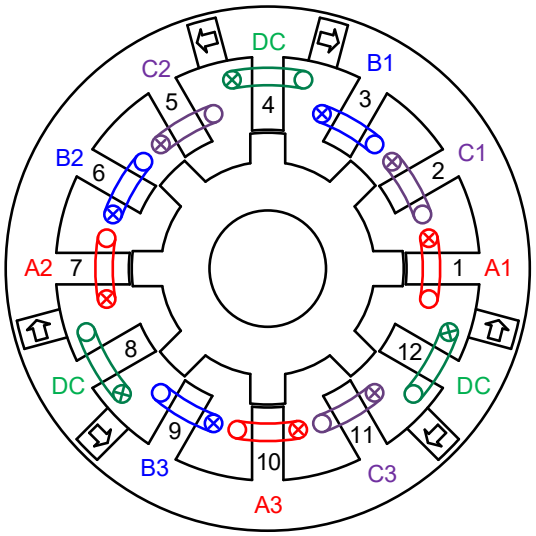

(d) Armature winding connection of N_r=8

Fig. 3.6. Coil EMF phasor and winding connection illustration with N_r=7 and N_r=8 as examples (at the rotor position of maximum phase A flux linkage).

3.4 Design Optimization

In order to evaluate the torque density of the proposed DSHE machine, global optimization is conducted in this section. The design parameters for the proposed DSHE machine are shown in Fig. 3.7. The split ratio is defined as the ratio of stator inner radius to outer radius, as shown in (3.4). It should be noted that the field and armature winding wound tooth widths can be different, and the ratio of field and armature coil wound teeth is defined as (3.5). The design constraints are set as stator outer radius as r_{so}=45mm, stack length l_{st}=25mm, air-gap length l_g=0.5mm, slot packing factor k_p=0.6. To simplify the analysis, the PM thickness and iron

bridge thickness are fixed as h_{PM}=6mm, and h_{rib}=0.5mm. The influence of iron bridge will be investigated in detail in next section.

$$\gamma_{sp} = \frac{r_{si}}{r_{so}} \tag{3.4}$$

$$\gamma_{t} = \frac{w_{t1}}{w_{t2}} \tag{3.5}$$

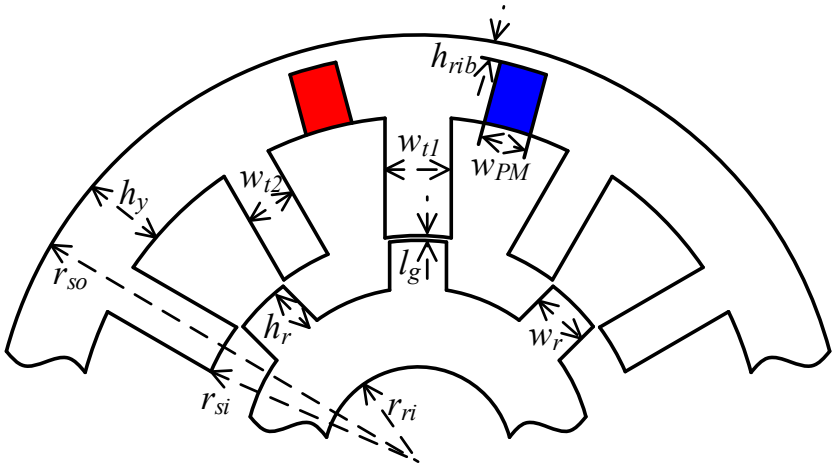

Fig. 3.7. Illustration of design parameters for the proposed DSHE machine.

Global optimization is conducted by utilizing genetic algorithm (GA) coupled FE embedded in the commercial software Ansys Maxwell. The design objective is set as maximum average torque under the field excitation of J_{dc}=+10A/mm^2 and armature winding copper losses of p_{ac}=20W for high torque density as well as flexible field regulation capability. This constraint on armature winding copper loss is more favorable in the design of machines for low speed applications since the iron loss together with the skin effect wound not contribute to the major loss component at rated speed of 400rpm. The armature winding copper loss and field winding current density are determined to allow for the experiments on the same thermal condition as in [HUA16b] [HUA16c] and [HUA16d]. The numbers of turns of field and armature windings are determined under the same copper loss and rated current. Take the 12/8 and 12/16-stator slot/rotor pole DSHE machines as example, the main parameters after global optimization are listed in Table 3.2, whereas the initial parameters are shown in Table 3.1. The electromagnetic torque waveforms before and after global optimization are compared in Fig. 3.8. It can be observed that the torque density can be improved significantly after global optimization. It is worth emphasizing that the torque ripple is not concerned during the optimization, since the objective of this chapter is to evaluate the torque density as well as flux regulation capability.

Table 3.2 Design parameters of DSHE machine after optimization

Parameter	Symbol	Unit	8-rotor pole	16-rotor pole
Stator outer radius	r_{so}	mm	45	
Stack length	l_{st}	mm	25	
Air-gap length	l_g	mm	0.5	
PM thickness	w_{PM}	mm	6	
Iron bridge thickness	h_{rib}	mm	0.5	
Split ratio	γ_{sp}	N/A	0.55	0.62
Stator yoke thickness	h_y	mm	8.6	9.0
Armature coil wound stator tooth width	w_{t1}	mm	6.4	4.3
Field to armature coil wound tooth ratio	γ_t	N/A	1.6	1.6
Rotor tooth width	w_r	mm	6.0	3.9
Rated field current	i_{dc}	A	8	
Rated armature current	i_{ac}	A	8	

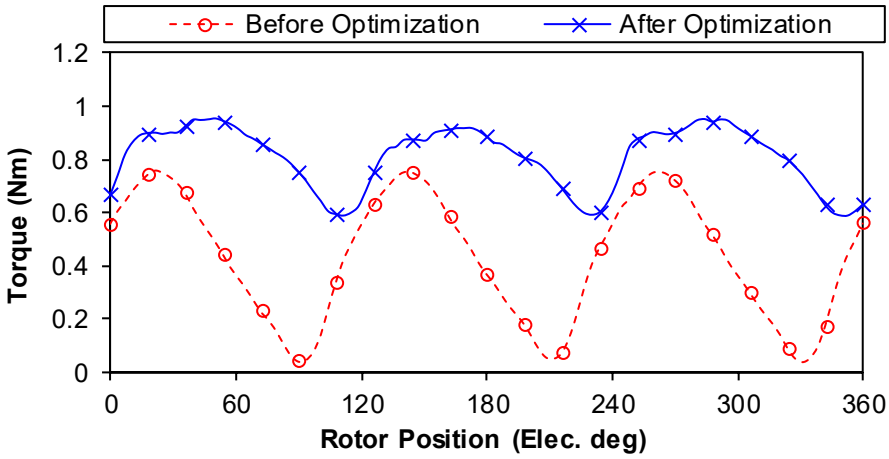

(a) 8-rotor pole number

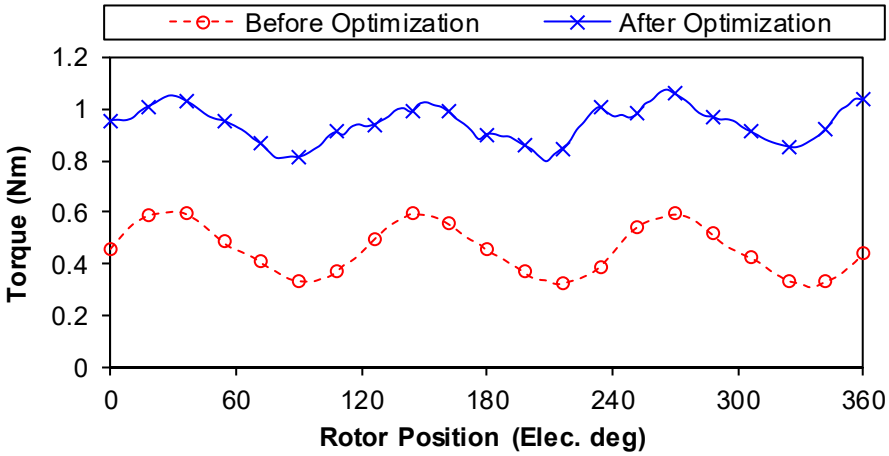

(b) 16-rotor pole number

Fig. 3.8. Electromagnetic torque waveforms of proposed DSHE machines with field excitation of J_{dc}=+10A/mm^2 and armature excitation of p_{ac}=20W, i_d=0 control before and after global optimization.

Furthermore, global optimization is conducted on the proposed DSHE machine with different stator/rotor pole number combinations for maximum average torque under flux enhancing. After global optimization, the torque densities of the proposed DSHE machines are compared in Fig. 3.9, in which the field winding regulation ratio is defined as (3.6). The proposed DSHE machines with 8- and 16-rotor poles exhibit higher torque density. This can be explained by the EMF phasor in Fig. 3.6, and the winding distribution factor is 1 when the rotor pole number satisfies N_r=4k. Therefore, the 12/8 and 12/16-stator slots/rotor poles DSHE machines are chosen for further investigation.

$$\delta_{DC} = \frac{T_{fe} - T_{fw}}{T_{PM}} \tag{3.6}$$

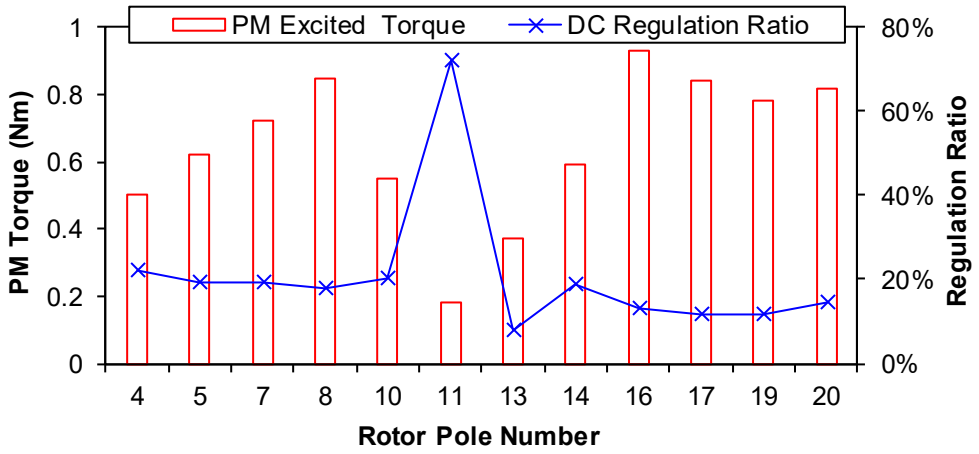

Fig. 3.9. Electromagnetic torque comparison of different rotor poles under the rated current of 8A with i_d=0 control.

3.5 Influence of Iron Bridge on Hybridization

Since the magnetic field of HE machine is excited by both PM and field winding, it is worth investigating the hybridization of two magnetic sources. The intense PM magnetic field is beneficial for high torque density and compact structure, whereas the flexible DC excited field contributes to wide operation for variable speed application. Therefore, a trade-off between the PM and field winding hybridization should be determined according to the application requirement.

It has been revealed that the iron bridge has a significant influence on the HE machines in [WAN17d] and [OWE10]. To investigate the effect of iron bridge on the proposed HE machine, frozen permeability method (FPM) is employed to segregate the PM and DC excited magnetic fields in the following steps [WAL05]

- Step 1: Non-linear FE calculation is employed with PM and DC excitations together.
- Step 2: The permeability of each component is calculated and fixed with non-linear FE simulation.
- Step 3: Linear FE calculation is applied with PM or DC excited individually under fixed permeability.

The open-circuit field distributions of proposed HE machine without iron bridge under PM and DC excitations are compared in Figs. 3.10 (a) and (b). It can be observed that the flux lines

of DC excitation pass through PM, and the flux paths of PM and DC excitations are in series [WAN17d]. Since the PMs are of large reluctance, the flux regulation capability of field winding is limited. Moreover, the negative WF flux passing through PMs may potentially cause irreversible demagnetization. For comparison, the PM and WF fluxes for the HE machine with iron bridge are shown in Figs. 3.10 (c) and (d), respectively. It can be observed that the majority of WF flux passes through the iron bridge, and the flux paths of PM and DC excitations are in parallel [WAN17d]. Therefore, the demagnetization withstanding capability can be enhanced with the utilization of iron bridge.

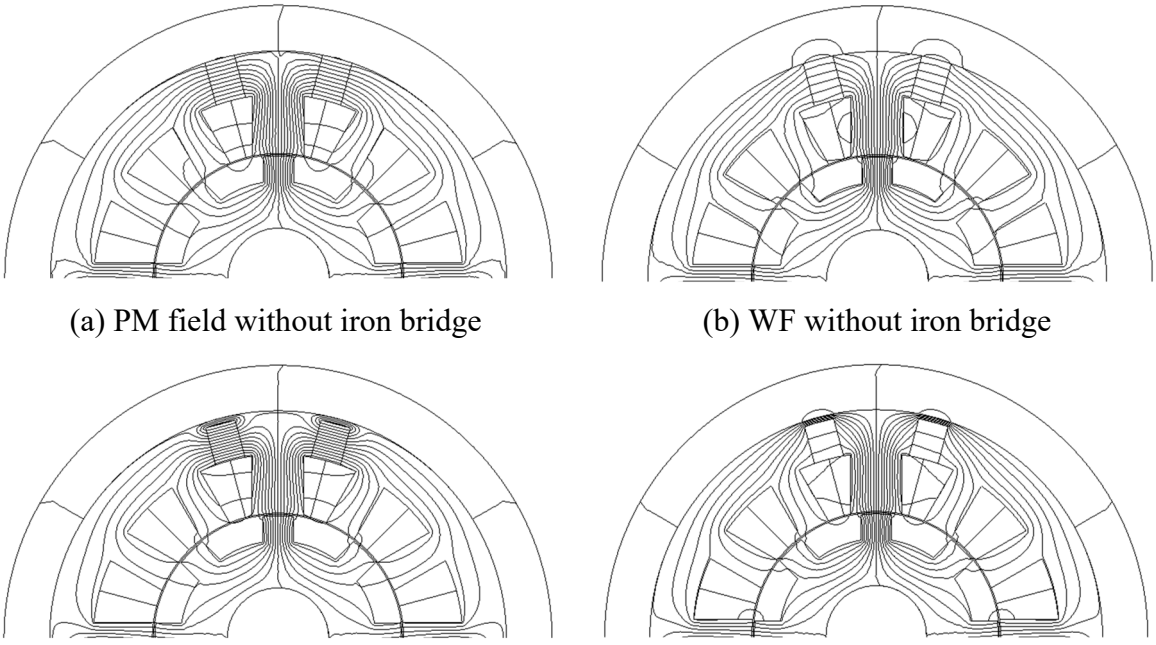

(a) PM field without iron bridge (b) WF without iron bridge

(c) PM field with iron bridge (d) WF with iron bridge

Fig. 3.10. Open-circuit field distribution segregation of proposed DSHE machine with FPM.

According to the flux paths of PM and DC excitations, a simplified open-circuit magnetic circuit model of proposed DSHE machine with iron bridge is illustrated in Fig. 3.11, where F_{PM} and F_{DC} represent the magnetomotive forces (MMFs) of PM and DC excitations, respectively, R_{PM} is the PM reluctance, R_{rib} is the iron bridge reluctance, R_{tf} and R_{ta} are the reluctances of field and armature coils wound tooth, respectively, R_{gf} and R_{ga} are the reluctances of air-gap at field and armature coils wound tooth, respectively, R_{tf} is the rotor tooth reluctance, and ϕ_g is the air-gap flux.

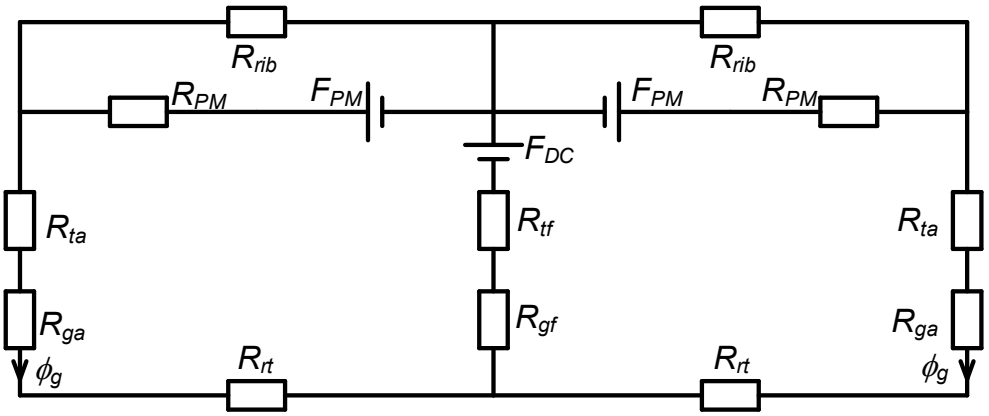

Fig. 3.11. Simplified open-circuit magnetic circuit model of the proposed DSHE machine with iron bridge.

With the utilization of Kirchhoff's Law, the air-gap flux ϕ_g can be deduced in (3.7), in which the iron bridge reluctance R_{rib} is shown in (3.8). It can be concluded from (3.7) and (3.8) that the PM excited air-gap flux reduces with the thickness of iron bridge h_{rib}, whereas a large iron bridge thickness h_{rib} is beneficial to the DC excited air-gap flux. Subsequently, the optimization of iron bridge should be considered as a trade-off between PM and DC excitations.

$$\phi_g = \frac{1}{R_{rt}+R_{ga}+R_{ta}+2\left(R_{tf}+R_{gf}\right)+R_{PM}+\dfrac{R_{PM}R_g}{R_{rib}}}F_{PM} + \frac{1}{R_{rt}+R_{ga}+R_{ta}+2\left(R_{tf}+R_{gf}\right)+\dfrac{1}{\dfrac{1}{R_{PM}}+\dfrac{1}{R_{rib}}}}F_{DC} \tag{3.7}$$

$$R_{rib} = \frac{w_{PM}}{\mu l_{st} h_{rib}} \tag{3.8}$$

To further illustrate the effect of iron bridge thickness on the electromagnetic performance, the PM excited average torque as well as DC regulation ratio versus iron bridge thickness are compared in Fig. 3.12. In consistent with the above theoretical analysis, the PM excited torque reduces with the iron bridge thickness, whereas the DC regulation ratio increases with the iron bridge thickness. To achieve high PM excited torque density as well as wide flux regulation range, the iron bridge thickness is selected as 0.5mm in this chapter.

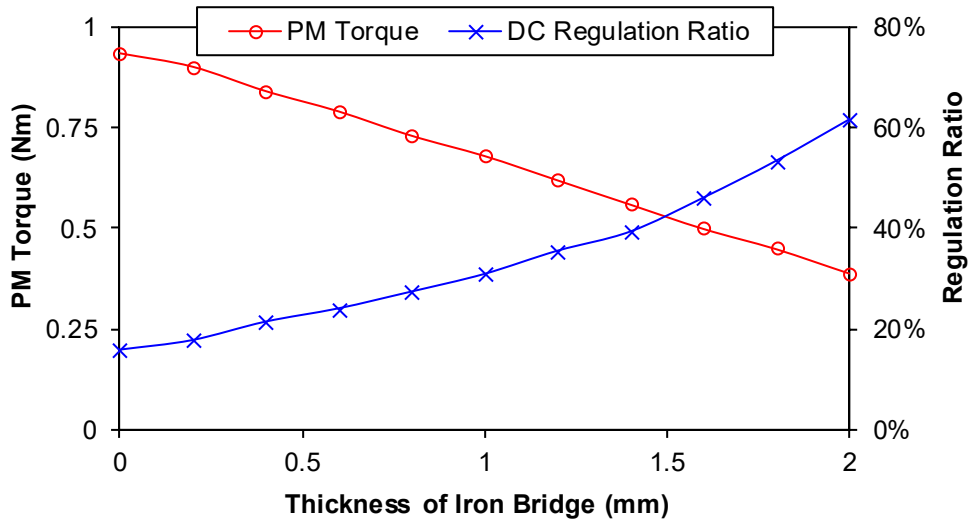

Fig. 3.12. PM excited average torque and torque regulation ratio versus iron bridge thickness under the copper loss of 20W with i_d=0 control.

3.6 Electromagnetic Performance Evaluation

3.6.1 Field Distribution

The open-circuit field distributions of the 12/8 and 12/16-stator slot/rotor pole DSHE machines with different field excitations are shown in Figs. 3.13 and 3.14, respectively. It can be observed that the DC excitation can regulate the magnetic field flexibly. With negative DC excitation, the magnetic field is weakened which is beneficial for high speed operation. With positive DC excitation, the magnetic field is enhanced to improve the output capability. Nevertheless, the stator and rotor cores are saturated with the positive DC excitation in Figs. 3.13 I and 3.14 I, which restricted the flux-enhancing capability. Therefore, the HE machine should be designed with consideration of operation requirement.

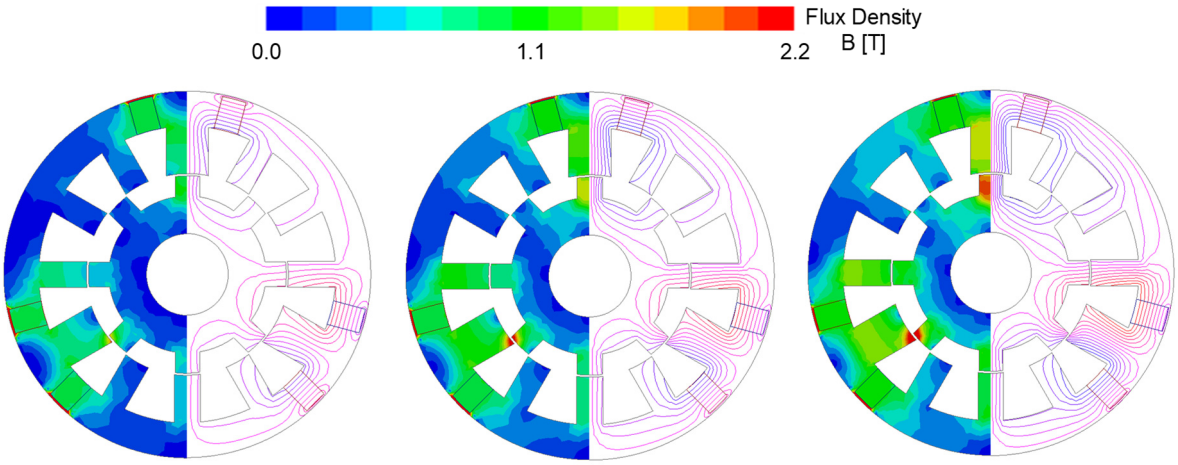

(a) Negative DC excitation (b) No DC excitation (c) Positive DC excitation

Fig. 3.13. Open-circuit field distribution for the 12/8-stator slots/rotor poles HE machine with different DC excitations.

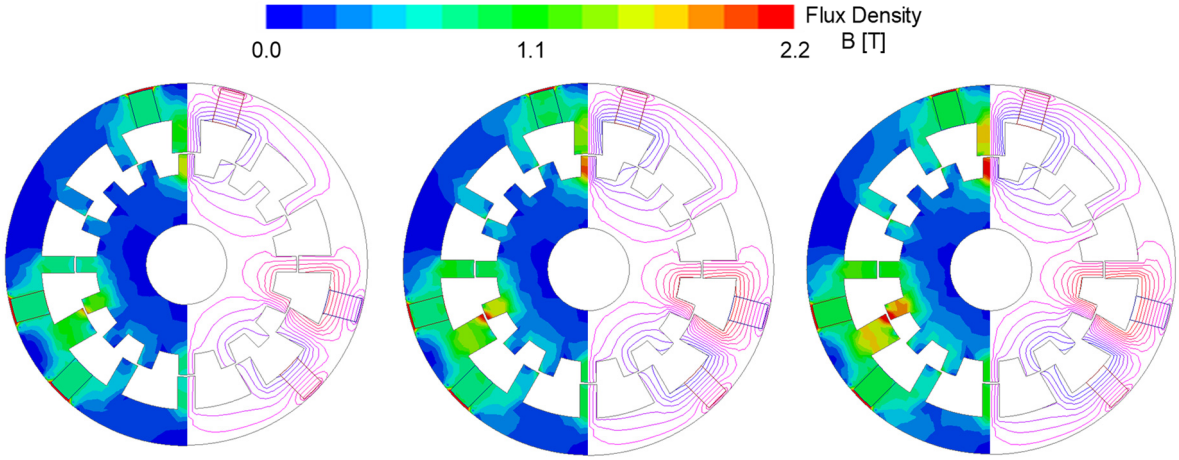

(a) Negative DC excitation (b) No DC excitation (c) Positive DC excitation

Fig. 3.14. Open-circuit field distribution for the 12/16-stator slots/rotor poles HE machine with different DC excitations.

3.6.2 Back-EMF

Furthermore, three-phase back-EMF waveforms at the rated speed are compared in Fig. 3.15. Unlike the conventional DSPM machine with asymmetric back-EMF waveforms [ZE18], the three phase back-EMF waveforms are identical in the proposed DSHE machine. Moreover, the phase back-EMFs of the DSHE machines with 8- and 16-rotor poles at the rated speed of 400rpm are compared in Fig. 3.16. Even order harmonics are presented in the back-EMF, which may potentially produce 3rd order pulsating torque. Overall, it can be identified that the DSHE machine with 16-rotor poles exhibits higher back-EMF and less harmonics.

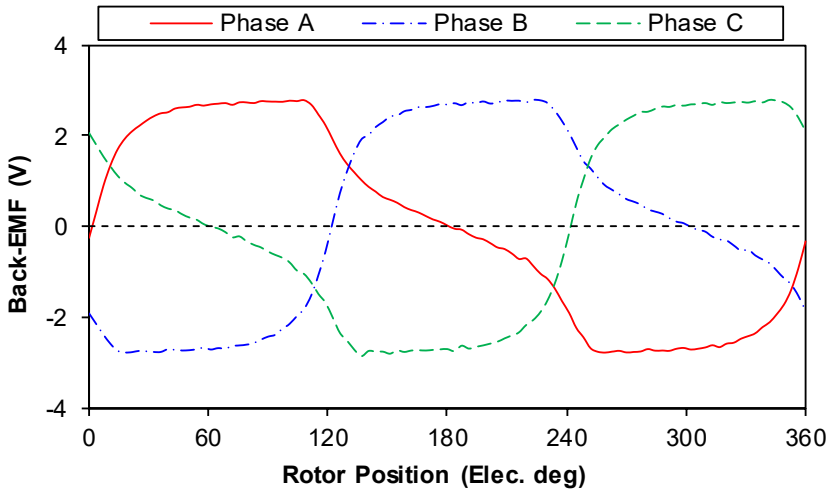

Fig. 3.15. Open-circuit three-phase back-EMF waveforms without DC excitation for the 12/8 stator-slot/rotor-pole DSHE machine.

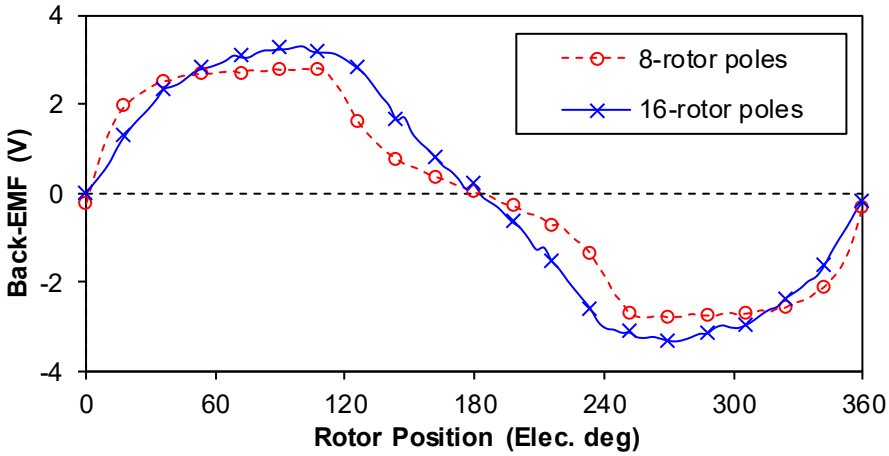

(a) Waveforms

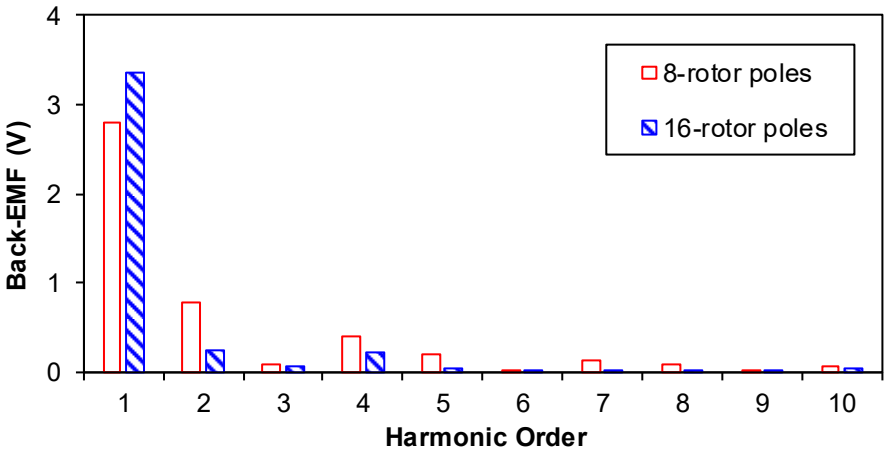

(b) Spectra

Fig. 3.16. Open-circuit phase back-EMFs without DC excitation at the rotor speed of 400rpm.

For the HE machine with field excitation, the flux regulation ratio is an essential characteristic to evaluate the capability of field winding to regulate the magnetic field. The variation of phase back-EMF fundamental as well as back-EMF regulation ratio with DC excitation current, which is defined in (3.9), are compared in Figs. 3.17 (a) and (b), respectively. It can be found that the field excitation can regulate the back-EMF effectively for both HE machines. Although the DSHE machine with 16-rotor poles possesses higher PM excited back-EMF, the field regulation ratio is lower than the 8-rotor poles DSHE machine. Moreover, the flux regulation ratio at flux-enhancing is limited compared with flux-weakening due to magnetic saturation with positive DC excitation, as verified in Figs. 3.13 and 3.14.

$$\gamma_{DC} = \frac{e_{PM\pm DC} - e_{PM}}{e_{PM}} \tag{3.9}$$

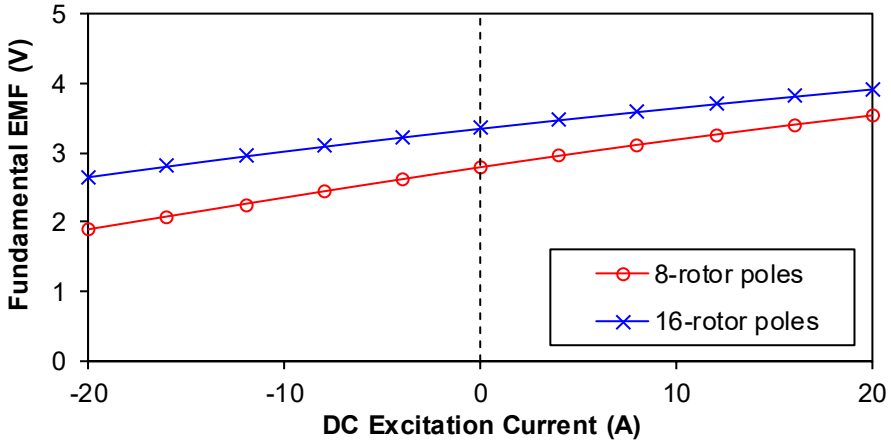

(a) Fundamental back-EMF

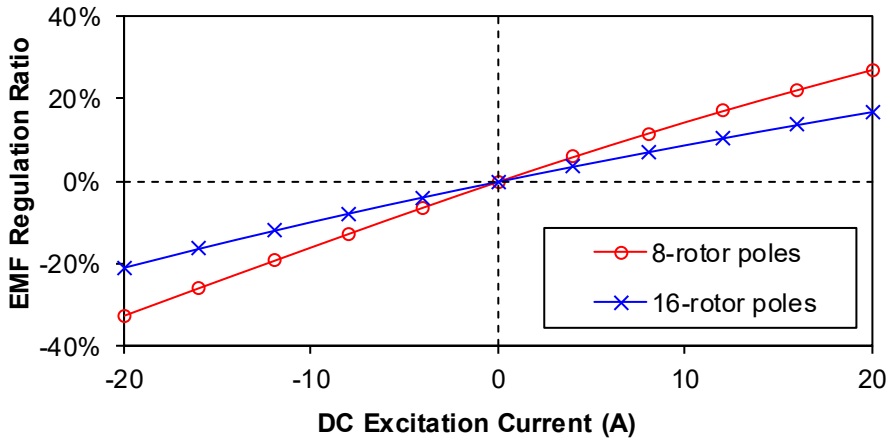

(b) Back-EMF regulation ratio

Fig. 3.17. Phase back-EMF fundamental and regulation ratio versus DC excitation current @400rpm.

3.6.3 Cogging Torque

Figs. 3.18 (a) and (b) show the cogging torque of the DSHE machines without field excitation, and the cogging torque peak value variation with DC excitation current is illustrated in Fig. 3. 18 (c). The harmonic orders of cogging torque in two DSHE machines are identical, whereas the 8-rotor pole DSHE machine exhibits higher cogging torque without field excitation. Meanwhile, the cogging torque amplitude varies with the DC excitation. The variation of cogging torque with DC excitation in the 8-rotor pole DSHE machine is larger, consistent with the magnetic field regulation ratio in Fig. 3.17. The cogging torque reduction of the DS machine has been investigated in [ZHU19d], which is not the focus of this chapter.

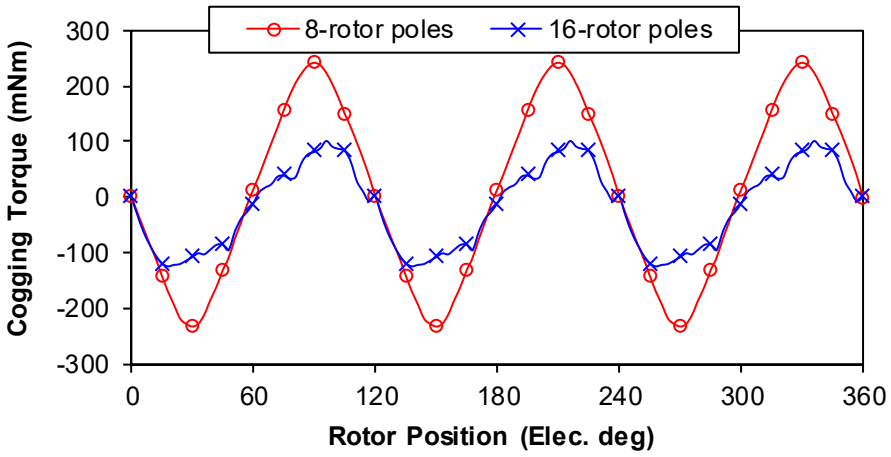

(a) Cogging torque waveforms without DC excitation

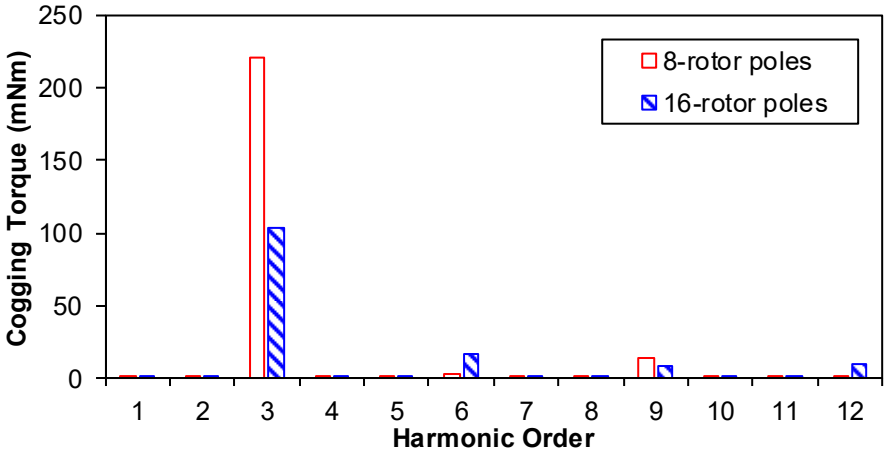

(b) Cogging torque spectra without DC excitation

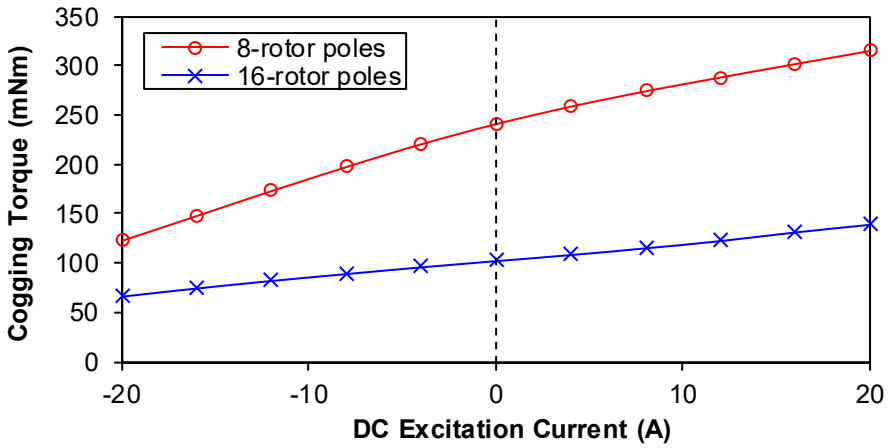

(c) Cogging torque peak value versus DC excitation current.

Fig. 3.18. Cogging torque comparison of the DSHE machines with 8- and 16-rotor poles.

3.6.4 Inductance

Furthermore, the *d*- and *q*-axis inductances versus corresponding currents are illustrated in Fig. 3. 19. The 8-rotor pole DSHE machine exhibits higher inductances than the counterpart. Moreover, the negative *d*-axis current alleviates the PM excited magnetic saturation, and the *d*-axis inductance hardly varies with the *d*-axis current. Nevertheless, the *q*-axis current tends to increase the magnetic saturation, and the *q*-axis decreases with the current. Overall, the *d*- and *q*-axis inductances of both DSHE machines are similar, indicating the machine saliency is negligible.

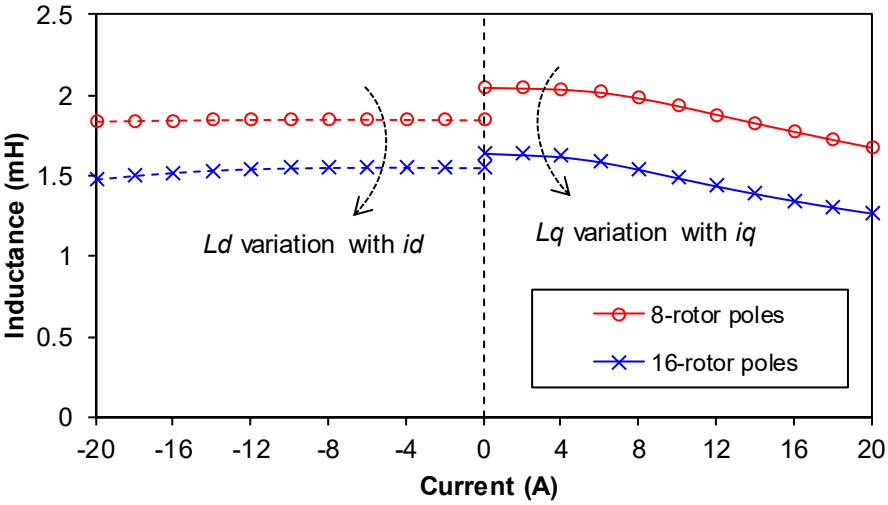

Fig. 3.19. *D*- and *q*-axis inductances versus corresponding currents.

3.6.5 Electromagnetic Torque

The electromagnetic torque waveforms and spectra of two DSHE machines at the rated armature current of i_q=8A, i_d=0 and no field excitation are shown in Figs. 3.20 (a) and (b), respectively. It can be observed that the 16-rotor poles DSHE machine exhibits higher torque density as well as lower torque ripple. To further illustrate the torque pulsating components, the instantaneous electromagnetic torque with ideal sine-wave current drive is derived in (3.10) when i_d=0 control is utilized, where Ω_r and ω_e are the mechanical and electrical rotating speeds, T_c represents the cogging torque. It can be observed that both the cogging torque and the even order harmonics in the phase back-EMF contribute to the 3rd pulsating torque. The torque ripple of the PM machine can be suppressed with both design and control techniques [JUN18] [COL99].

$$T_e = \frac{e_a i_a + e_b i_b + e_c i_c}{\Omega_r} + T_c = \frac{3 I_m E_1}{2\Omega_r} + \frac{3 I_m E_{3k-1} \cos 3k\omega_e t}{2\Omega_r} + \frac{3 I_m E_{3k+1} \cos 3k\omega_e t}{2\Omega_r} + T_c \qquad (3.10)$$

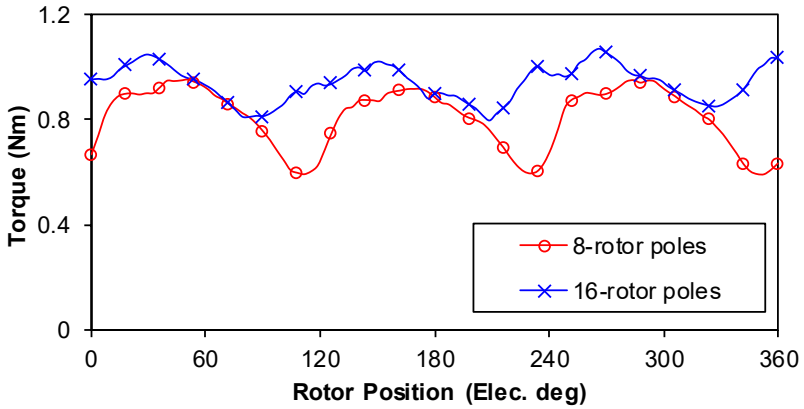

(a) Waveforms

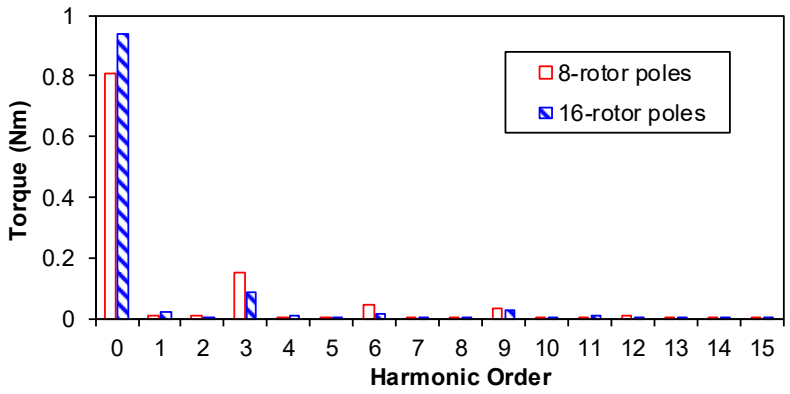

(b) Spectra

Fig. 3.20. Electromagnetic torque waveforms with rated current of i_q=8A, i_d=0 and no DC excitation.

Moreover, the electromagnetic torque is segregated with PM aligned torque and reluctance torque in Fig. 3.21. Due to the similar *d*- and *q*-axis inductances in Fig. 3.19, the reluctance torque is negligible, and the optimal current angle is ~0 for both DSHE machines.

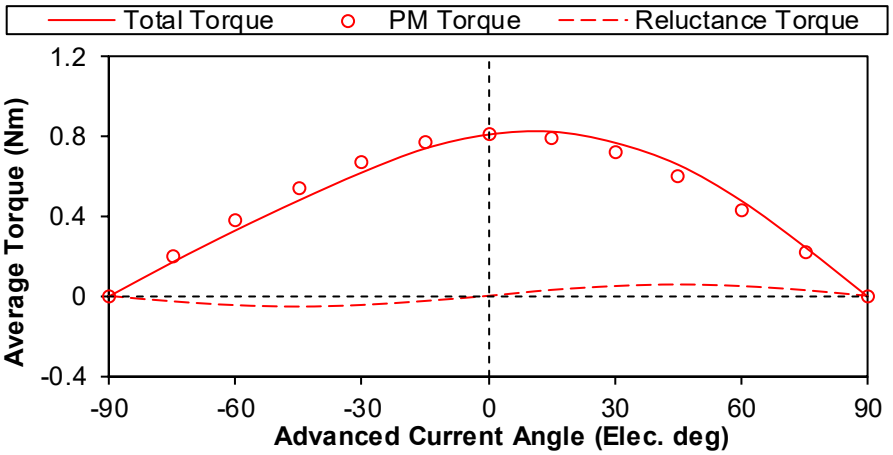

(a) 8-rotor-pole DSHE machine

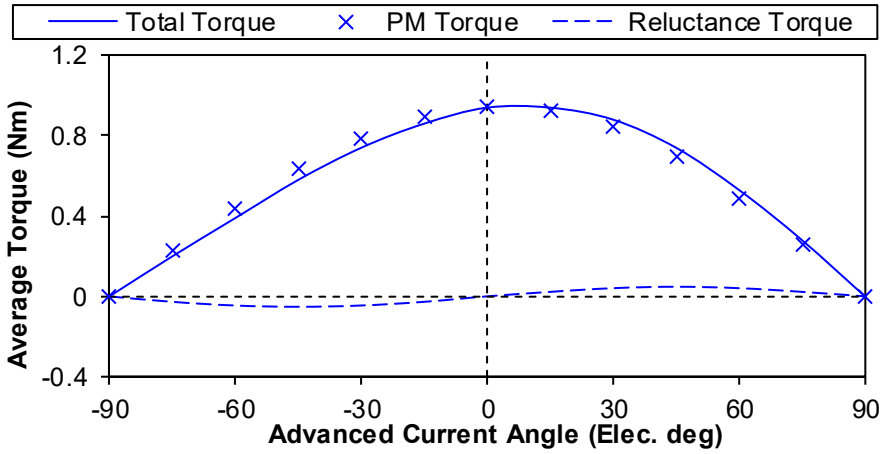

(b) 16-rotor-pole DSHE machine

Fig. 3.21. Average torque against advanced current angle with armature current of I_m=8*A* and no DC excitation.

Fig. 3.22 shows the average torques of two DSHE machines against DC excitation and *q*-axis current with i_d=0 control. It can be observed that the average torque can be regulated by both field and *q*-axis currents. Similar with the back-EMF variation, the 16-rotor pole DSHE machine exhibits superior torque density, albeit with sacrificed field regulation capability. Moreover, the overload capability of 16-rotor pole DSHE machine is limited. At rated current, the 16-rotor pole DSHE machine exhibits higher torque whereas the torque density is similar with that of 8-rotor pole DSHE machine under heavy load.

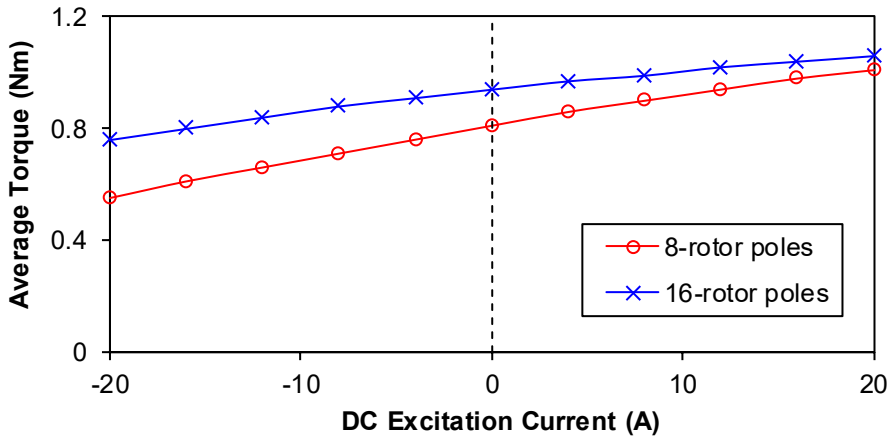

(a) Average torque versus DC excitation current with i_q=8A

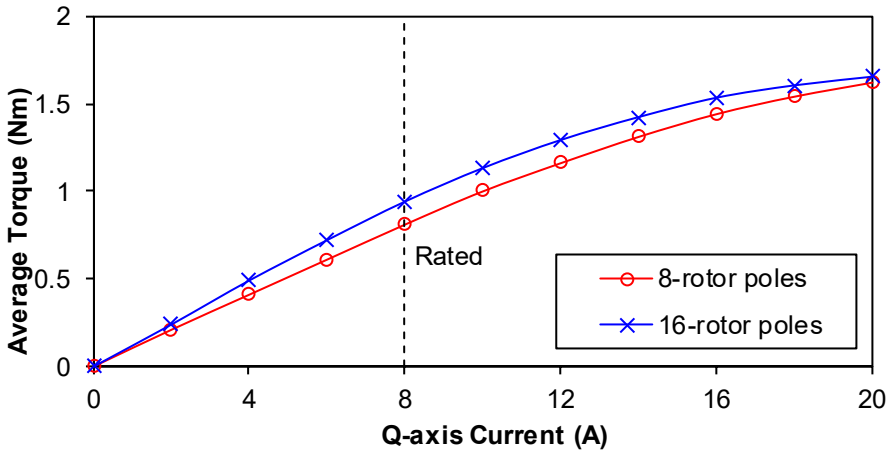

(b) Average torque against q-axis current without DC excitation

Fig. 3.22. Average torque against DC and q-axis current with i_d=0 control.

3.7 Experimental Validation

As foregoing stated, the 12/16-stator slots/rotor poles DSHE machine exhibits higher torque density and satisfied field regulation capability compared with the other counterparts. In this section, the DSHE machine with 12-stator slots and 16-rotor poles is fabricated and tested to validate the theoretical analyses and FE simulations. Fig. 3.23 shows the photo of the DSHE prototype stator and rotor, which are of the same parameters in Table 3.2. Both the field and armature coils are non-overlapped wound around the stator teeth, and the field winding is wound around wider stator tooth to allow for WF flux path.

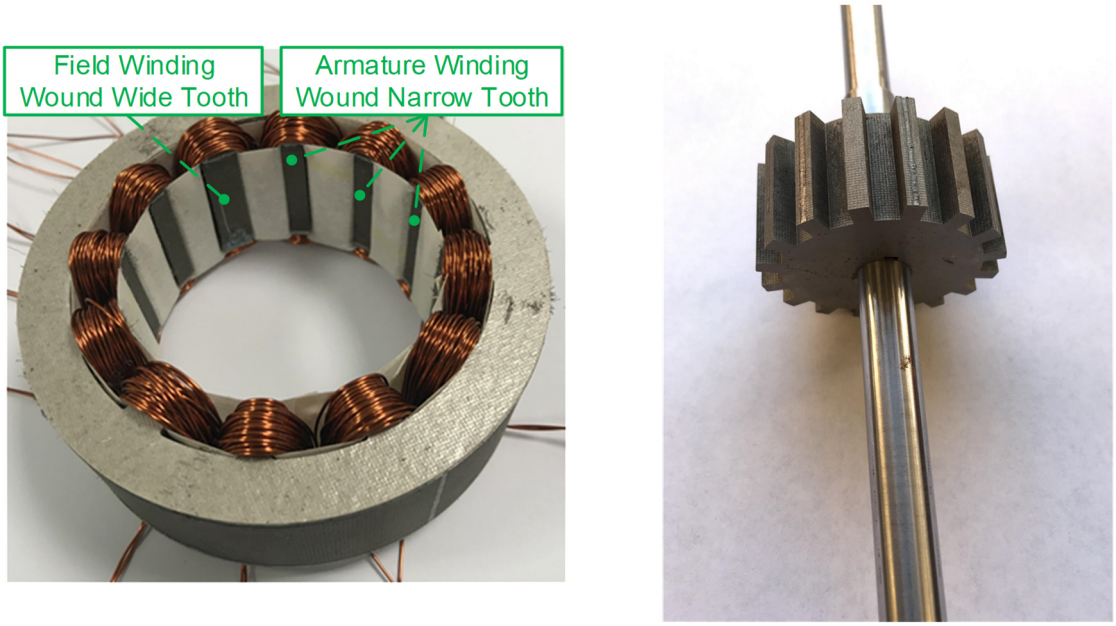

(a) Stator (b) Rotor

Fig. 3.23. Photo of DSHE prototype with 12/16-stator slots/rotor poles.

A notable benefit of HE machine is the back-EMF regulation with field excitation, which can potentially eliminate the uncontrolled generator fault at high speed operation [LIA05]. The measured phase back-EMFs with various field excitations @400rpm are shown in Fig. 3.24, in comparison with the FE predictions. The measured and predicted back-EMF waveforms agree well, although the amplitudes of test results are slightly lower due to 3D end effect. As analysed above, even order harmonics are presented in both the simulated and measured phase back-EMFs regardless of DC excitations. Moreover, the field excitation can regulate the back-EMF effectively, as can be seen in both predicted and tested results. Positive DC excitation can be employed at low speed operation to enhance output capability, whereas negative field excitation can be injected to reduce the back-EMF for higher speed operation.

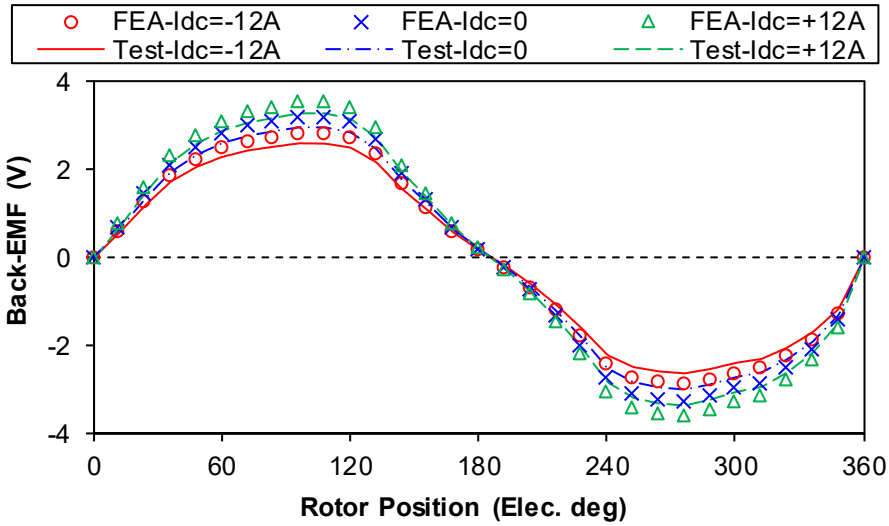

(a) Back-EMF waveforms with different DC excitations

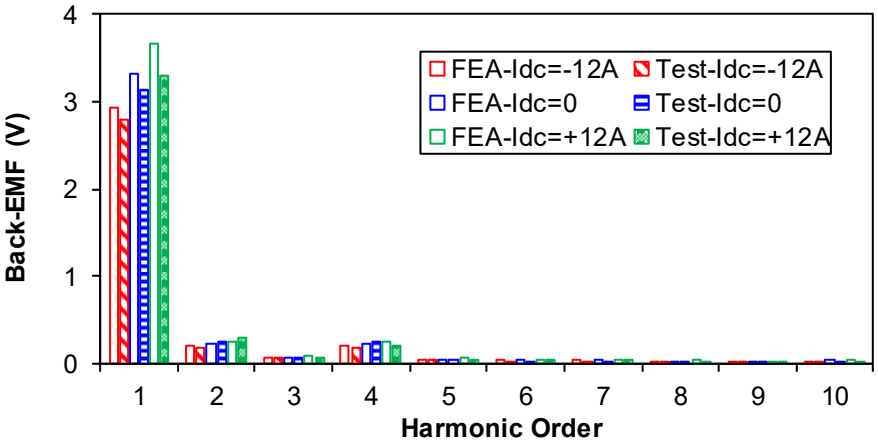

(b) Back-EMF spectra with different DC excitations

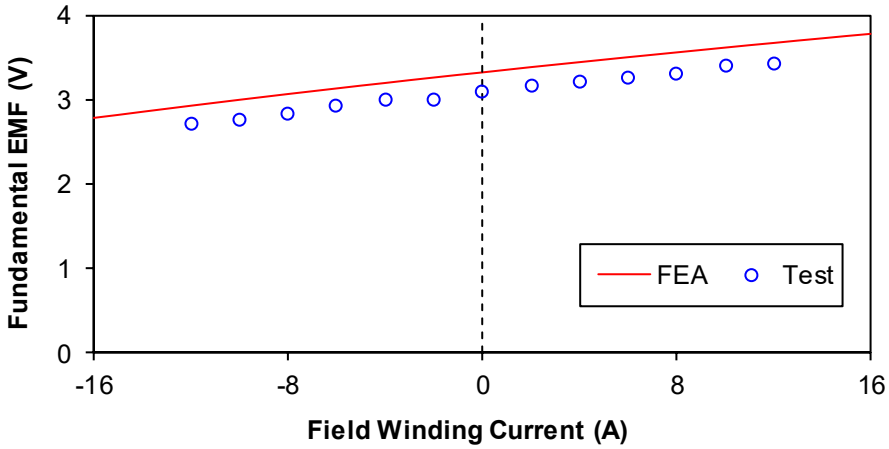

(c) Fundamental phase back-EMF versus field winding current

Fig. 3.24. Measured and FE predicted open-circuit phase back-EMF at the rotor speed of 400rpm.

The cogging torque originates from the PM excited magnetic field with the salient rotor teeth, and consequently, the mechanical period angle of cogging torque in the proposed DSHE machine can be expressed in (3.11). Under open circuit, the cogging torque waveform is measured in Fig. 3.25 (a) and the spectrum is further illustrated in Fig. 3. 25 (b) in comparison with the FE simulation. As can be observed, the waveform of the measured cogging torque is slightly distorted due to manufacturing tolerance and test error. Besides, the measured cogging torque amplitude is lower than the FE prediction due to the 3D-end effect. Moreover, the cogging torque amplitude varies with the DC excitation, as shown in Fig. 3.25 (c). Overall good agreement is achieved between the simulated and measured cogging torques.

$$\theta_{cogging} = \frac{360°}{LCM\left(N_s/4, N_r\right)} \tag{3.11}$$

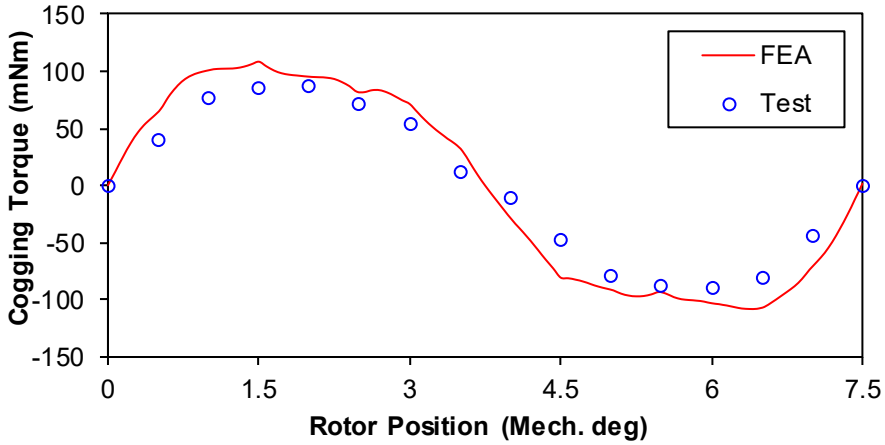

(a) Cogging torque waveforms without DC excitation

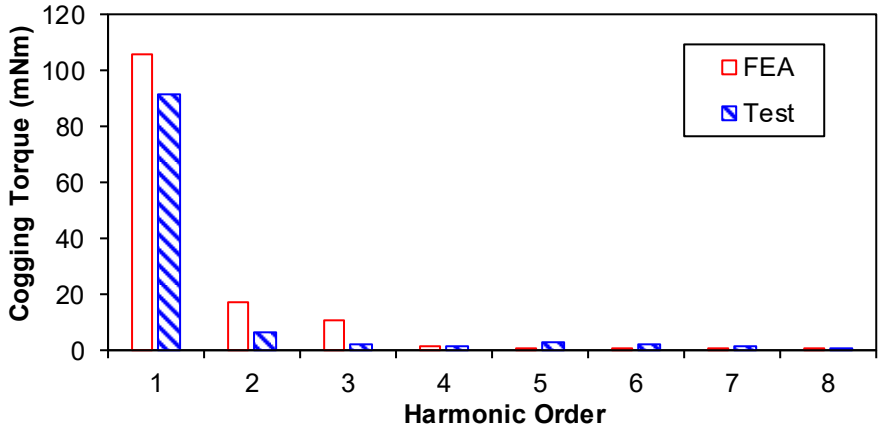

(b) Cogging torque spectra without DC excitation

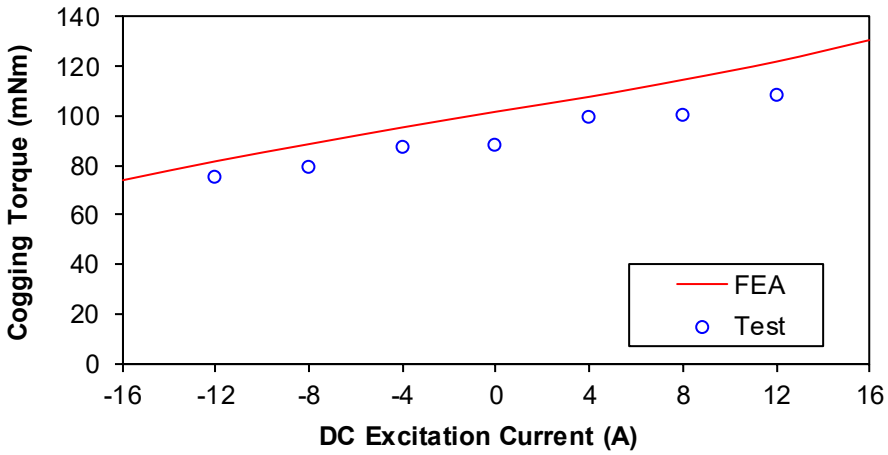

(c) Cogging torque amplitude versus field winding current

Fig. 3.25. Measured and FE predicted cogging torque.

Furthermore, the static torques of the prototype are measured with the three phase armature excitations of i_a=-2i_b=-2i_c. As the salient rotor moves at different positions, the static torque waveforms can be obtained. Fig. 3.26 shows the measured and FE predicted static torques with different excitations. Overall, there is a good agreement between the measured and FE predicted torques, although the measured results are slightly lower due to 3D flux leakage. Meanwhile, the static torque can be controlled by field excitation effectively, verifying the flexible flux regulation capability.

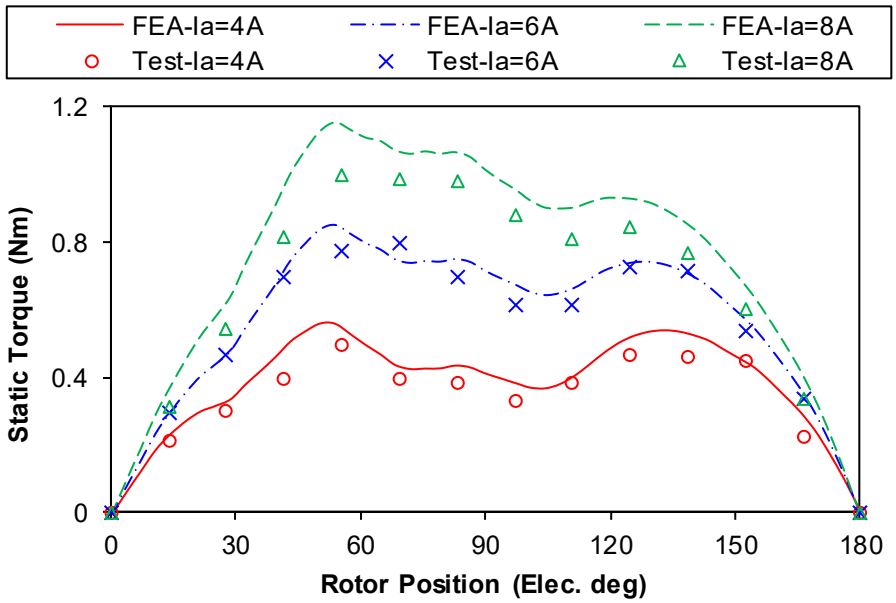

(a) Static torque waveforms without field excitation

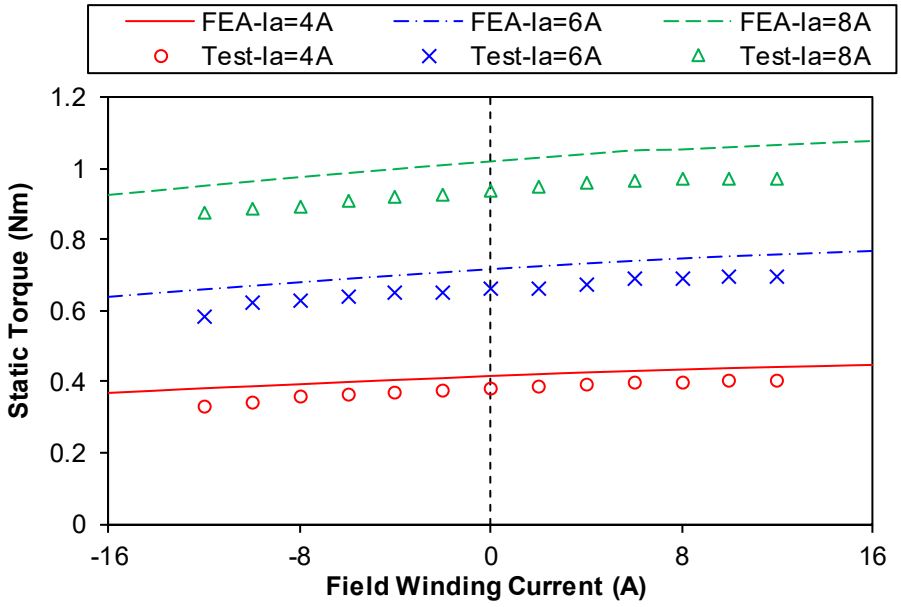

(b) Static torque versus field winding current at the rotor position of *q*-axis aligned with phase A axis

Fig. 3.26. Measured and FE predicted static torque.

In order to fully demonstrate the benefit of field regulation, the torque-speed envelopes with different field excitations are measured with the platform of Fig. 3.27. The prototype is connected to a brushed DC generator as load. The operation point of the prototype can be regulated by controlling the resistance linked to the armature winding of DC generator. Moreover, the encoder and torque transducer are employed to detect the rotor position as well as output torque of the prototype.

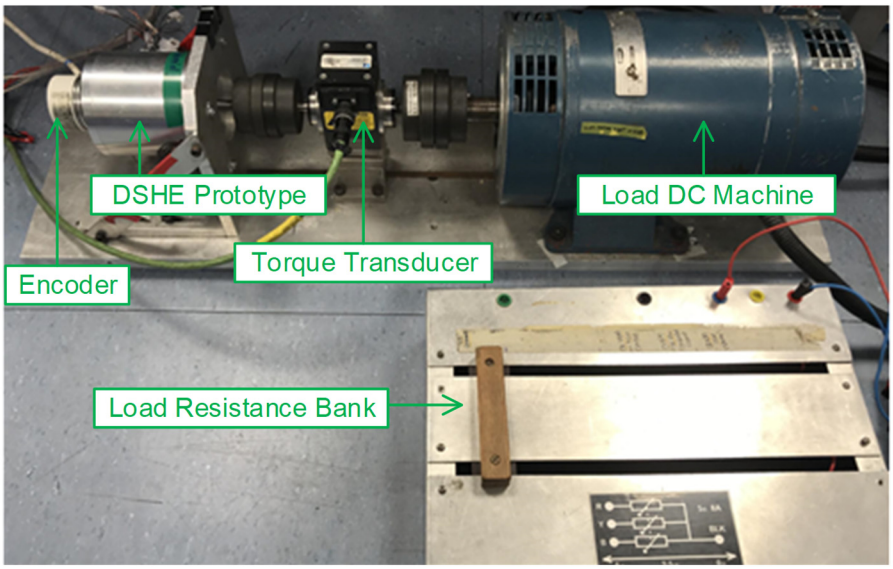

Fig. 3.27. Test platform of dynamic experiment.

The flux-weakening experiment is conducted within the limit of 8A phase current, and 15V DC bus voltage. The *d*- and *q*-axis currents within the operation limit are firstly predicted by the flux linkage method in [QI09], as shown in Fig. 3.28. Obviously, the armature current can totally contour the PM flux and the phase current is not maximized even at the maximum speed of 1000rpm. Subsequently, positive DC excitation is beneficial to enhance the magnetic field and torque density over the whole operation region.

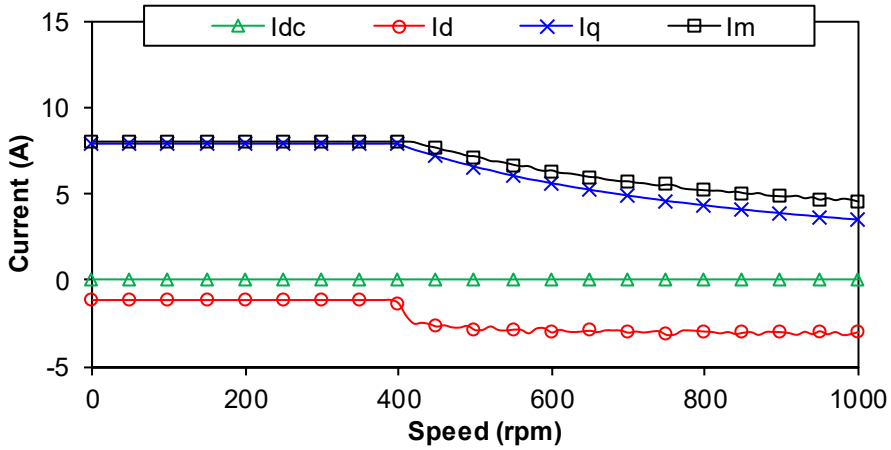

(a) i_{dc}=0

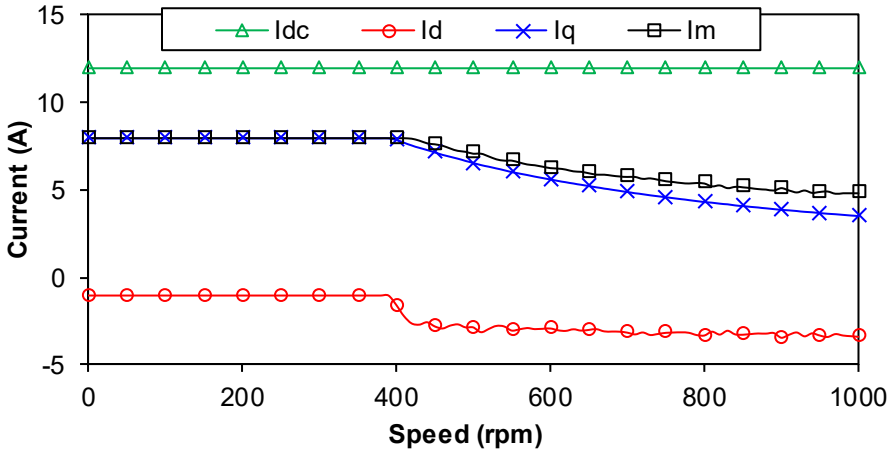

(b) i_{dc}=+12A

Fig. 3.28. 2D-FE predicted field, *d*- and *q*-axis currents with different DC excitations under the voltage and current limits.

Based on the predicted *d*- and *q*-axis currents, the torque-speed envelopes with different DC excitations are measured and compared with FE prediction in Fig. 3.29. It can be identified that the positive field excitation is beneficial to higher torque density at low speed operation. The difference between measurement and simulation can be summarized as follows. Firstly,

the test accounts for 3D end-effect and flux leakage. Secondly, the friction torque is significant especially for low-torque measurement. Thirdly, the manufacturing and assembling tolerances influence on the output capability, which will be assessed for future work.

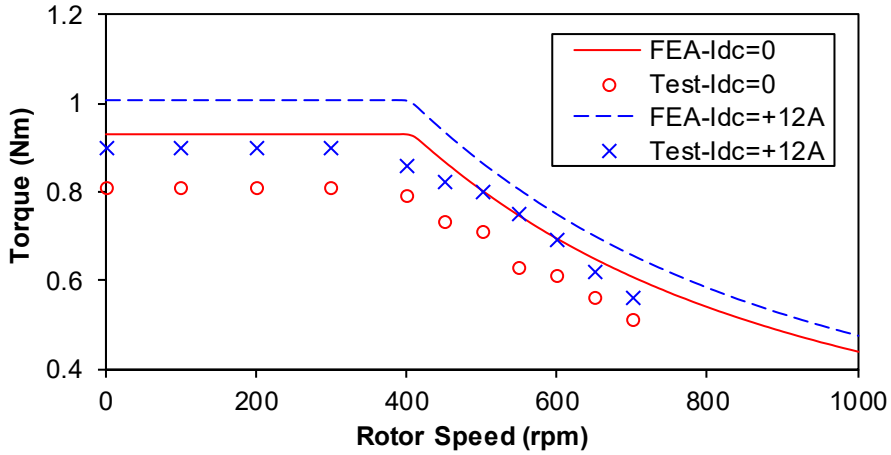

Fig. 3.29. Measured and 2D FE predicted torque-speed curves with different DC excitations.

3.8 Summary

In this chapter, a novel DSHE machine with non-overlapped field winding is proposed, which inherits the benefit of simple structure of conventional DSPM machine and facilitates the magnetic field regulation by field winding, which is beneficial to the variable speed application. Different stator and rotor pole number combinations are investigated. It has been revealed that the machines with rotor pole with N_r=4k exhibit higher torque density and satisfied field regulation ratio. Moreover, the effect of the iron bridge on the hybridization is investigated and the thickness of iron bridge should be designed carefully as the trade-off between PM excited torque density and field regulation capability. Finally, the electromagnetic performances of the proposed DSHE machine are evaluated with FE simulation and verified with experiments.

Chapter 4

A Novel Fractional Slot Non-Overlapping Winding Hybrid Excited Machine with Consequent-Pole PM Rotor

This chapter presents a novel fractional slot non-overlapping winding (FSNW) hybrid excited (HE) machine with consequent-pole permanent magnet (PM) rotor. The abundant harmonics in the stator magnetomotive force (MMF) of FSNW, which are harmful and tend to cause parasitic effects in conventional PM machines, are utilized to regulate the magnetic field and produce torque through field modulation. The DC excitation current can be injected by dual-electric-port drive circuit and a biased current excited HE machine without field winding can be achieved, which solves the spatial confliction of field and armature windings. The electromagnetic performances of the proposed HE machine are evaluated with finite element method (FEM). It is revealed that the DC excitation can effectively regulate the magnetic field, and consequently, the back-EMF as well as electromagnetic torque. Finally, a prototype is fabricated and tested to validate the theoretical analyses and FE calculations. This chapter is based on an accepted paper in [CAI20a] and extends the analyses.

4.1 Introduction

Permanent magnet (PM) machines have attracted extensive attention due to the distinct merits of high torque density and high efficiency [ZHU09]. The applications of PM machines can be found from more electric aircraft (MEA), wind power generation, electric vehicle/ hybrid electric vehicle (EV/HEV), automation, to domestic appliance [CAO12b] [FAN06b] [RED12] [RAM11]. More specifically, the PM machines equipped with fractional slot non-overlapping winding (FSNW) possess the benefits of compact structure, short end-winding length, high fault tolerant capability, low cogging torque, and good flux-weakening capability [ZHU11b] [CRO02]. Based on the FSNW PM machines, some modular-stator structures can be developed to facilitate the manufacturing and transportation, and further improve the slot filling factor [LI14].

However, some parasitic effects, such as iron loss, demagnetization, unbalanced magnetic forces, and acoustic noise are significant in the FSNW PM machines due to the abundant spatial harmonics in the non-overlapped armature winding magnetomotive force (MMF) [RAF10]. To reduce the low-order spatial harmonics, various techniques have been proposed, such as multi-

layer tooth concentrated winding [CIS10], winding coils with unequal turns per coil side [DAJ11], coil pitch of two slot-pitches [WAN14], and novel stator design with yoke flux barrier [DAJ14]. Nevertheless, these techniques inevitably result in complex manufacturing and assembling, and even sacrificed output capability.

Moreover, PM machines have inherent drawback of fixed magnetic field, which restricted the spread in the variable speed application. Although negative *d*-axis current can be utilized to weaken the magnetic field, the *d*-axis current excited flux passes through the PM and may potentially cause irreversible demagnetization [SOO02]. Meanwhile, the negative *d*-axis current reduces the efficiency and power factor, and consequently, a higher power rating inverter is demanded for the drive system. An alternative solution is to develop hybrid excited (HE) machines, which combine the high-energy PM excitation and controllable DC excitation together. At low speed operation, positive DC excitation is employed to enhance the peak torque for starting region. At high speed operation, negative DC excitation can be utilized to weaken the magnetic field for wider operation region. In [AMA09] [ZHU09] and [WAN12b], numerous HE machines have been investigated as the alternatives for variable speed application.

In this chapter, a novel FSNW HE synchronous machine with consequent-pole PM rotor is proposed, as shown in Fig. 4.1 (a). The abundant harmonics in the FSNW MMF, which originally causes parasitic effect, are utilized to regulate the magnetic field and produce torque through field modulation. Since the proposed HE machine accommodates the PMs in the rotor and field winding in the stator, the mechanical slides, i.e. brushes and slip rings are removed, and the systematic reliability is enhanced. Moreover, the field current can be injected through the dual-electric-port drive circuit [ZHU16] [JIA17a] [WAN19], and a biased current excited HE machine without field winding can be further achieved in Fig. 1 (b) to solve the spatial confliction of field and armature windings.

This chapter is organized as follows. In section 4.2, the novel HE machine topology is presented, together with the biased current excited DC coil free topology. Then in section 4.3, the operating principle is analyzed from the perspective back-EMF and electromagnetic torque production. In section 4.4, the HE machine is optimized and the electromagnetic torque is evaluated with finite element (FE) method. Furthermore, the proposed HE machine is compared with the conventional SPM machine in section 4.5. Finally, in section 4.6, a prototype is fabricated and tested to validate the theoretical analysis and FE calculation.

4.2 Machine Topology

The proposed HE machine with FSNW and consequent-pole rotor PM is shown in Fig. 4.1, with 12/14 stator-slots/rotor-poles single-layer winding as an example. The stator accommodates field winding and armature winding alternatively, and the rotor is allocated with PMs. The PMs are inset into the rotor surface with the same magnetization direction, and therefore, the rotor pole-pairs are equal to the PM pieces. The DC conductors are identically located in each stator slot, and all the DC coils are of the same polarity as shown in Fig. 4.1. The armature winding connection diagram of FSNW rotor PM machine can be found in [BIA06b]. Furthermore, the field winding can be integrated with armature winding through dual-electric-port driving circuit [ZHU16], as shown in Fig. 4.1(b). It can be identified that the proposed HE machine possesses similar topology with the FSNW PM machine with consequent pole rotor [CHU16] [LI18], except with the introduction of field winding. The utilization of field winding in the proposed HE machine facilitates the regulation of magnetic field, and is more beneficial for variable speed applications.

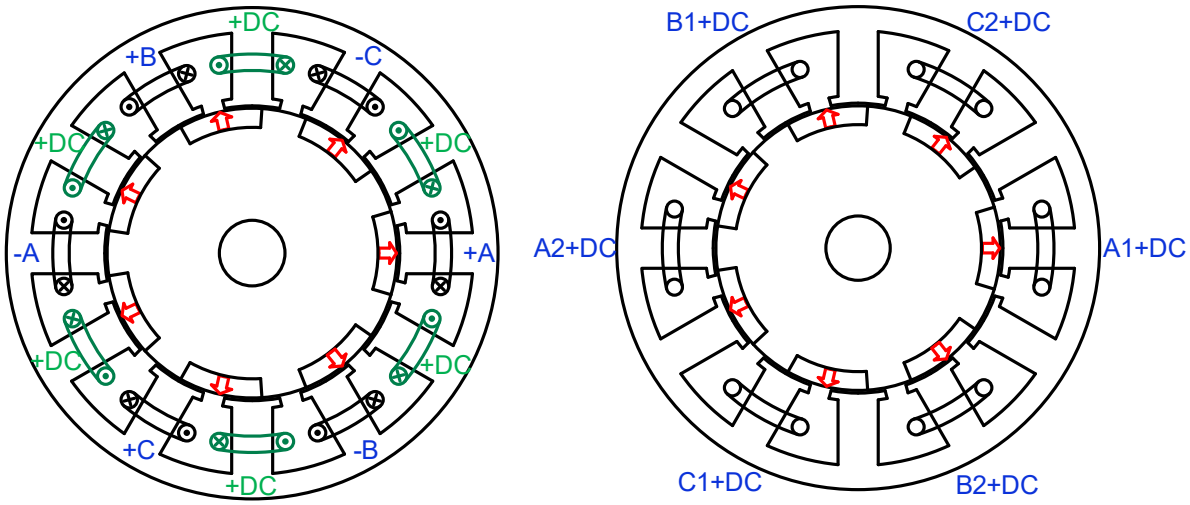

(a) Separated AC and DC windings (b) Integrated AC and DC windings

Fig. 4.1. The proposed FSNW consequent pole rotor PM HE machine topology (12/14 stator slots/rotor poles single-layer armature winding as an example).

It is worth emphasizing that the proposed HE machines in Figs. 4.1 (a) and (b) share the same operating principle, albeit with different winding configurations. In Fig. 4.1 (a), the armature winding is excited by a single inverter and the field winding is fed through an H-bridge. Meanwhile, the field and armature windings are synthesized in Fig. 4.1 (b), and dual-electric-port drive circuit can be employed to feed biased AC excitation directly [ZHU16]. Since the conducting area for both DC and AC excitations is enlarged with integrated winding

in Fig. 4.1 (b), the winding resistance as well as copper loss can be reduced. To simplify the analysis, only the principle of the HE machine with field winding (i.e. Fig. 4.1 (a)) is investigated in this chapter. The DC coil free HE machine with biased current (i.e. Fig. 4.1 (b)) can be obtained correspondingly and the electromagnetic performance will be investigated in next chapter.

4.3 Operation Principle

The PM excited MMF generated by rotor consequent-pole PM considering rotor saliency, i.e. alternate location of PM and iron on the rotor surface, can be expressed by (4.1) [LI19].

$$f_{PM}(\theta,t)=\sum_{i=1,2,3\cdots}^{\infty}F_{PM_i}\cos\left[ip_r(\theta-\Omega_r t)\right] \tag{4.1}$$

where p_r is the number of rotor pole-pairs, e.g. p_r=7 for the investigated 14-rotor pole machine in Fig. 1, θ is the mechanical position in stationary coordinate, and Ω_r is the rotor rotating speed.

Similarly, the stator field winding excited MMF can be expressed in (4.2), since the DC excitations in adjacent slots are in opposite polarities.

$$f_{DC}(\theta)=\sum_{k=1,3,5\cdots}^{\infty}F_{DC_k}\cos\left(\frac{kN_s\theta}{2}\right) \tag{4.2}$$

where N_s is the number of stator slots, e.g. N_s=12 for the investigated machine in Fig. 4.1.

Meanwhile, the air-gap permeance model accounting for stator slots and rotor slots, respectively, can be expressed in Fourier series, as shown in (4.3) and (4.4).

$$\Lambda_s(\theta)=\sum_{j=0,1,2,}^{\infty}\Lambda_{sj}\cos\left(jN_s\theta\right) \tag{4.3}$$

$$\Lambda_r(\theta,t)=\sum_{l=0,1,2\cdots}^{\infty}\Lambda_{rl}\cos\left[lp_r(\theta-\Omega_r t)\right] \tag{4.4}$$

Therefore, the air-gap flux density excited by PM and DC only can be deduced as (4.5) and (4.6), respectively. The PM and DC excited air-gap field harmonics are further summarized in Table 4.1.

$$B_{g\_PM}(\theta,t)=f_{PM}(\theta,t)\Lambda_s(\theta)=\sum_{i=1,2,3\cdots}^{\infty}\sum_{j=0,1,2\cdots}^{\infty}B_{PM_{(i,j)}}\cos\left[\left(ip_r\pm jN_s\right)\theta-ip_r\Omega_r t\right] \tag{4.5}$$

$$B_{g\_DC}(\theta,t)=f_{DC}(\theta)\Lambda_r(\theta,t)=\sum_{k=1,3,5\cdots}^{\infty}\sum_{l=0,1,2\cdots}^{\infty}B_{DC_{(k,l)}}\cos\left[\left(lp_r\pm\frac{kN_s}{2}\right)\theta-lp_r\Omega_r t\right] \tag{4.6}$$

Table 4.1 Characteristics of PM and DC excited air-gap field harmonics

	Harmonic Order	Rotating Speed
PM Excited	$\left\|ip_r \pm jN_s\right\|$	$\frac{ip_r\Omega_r}{\left\|ip_r \pm jN_s\right\|}$
DC Excited	$\left\|lp_r \pm \frac{kN_s}{2}\right\|$	$\frac{lp_r\Omega_r}{\left\|lp_r \pm \frac{kN_s}{2}\right\|}$

With the assistance of finite element (FE) calculation, the open-circuit air-gap flux density of proposed HE machine is shown in Fig. 4.2. The corresponding harmonics in related to the *I*, *j*, *k*, *l* in Table 4.1 are further marked in the spectra. It should be noted that the same number of *i*, *j* can produce diverse harmonics according to the modulation in Table 4.1. Therefore, abundant harmonics are observed in the air-gap flux density due to field modulation effect. Moreover, the magnetic fields excited by PM and DC are of different harmonic orders, as illustrated in Table 4.1.

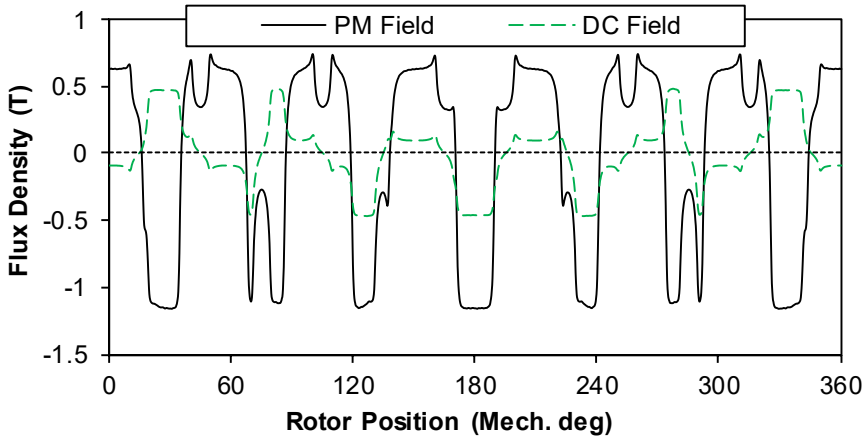

(a) Waveforms

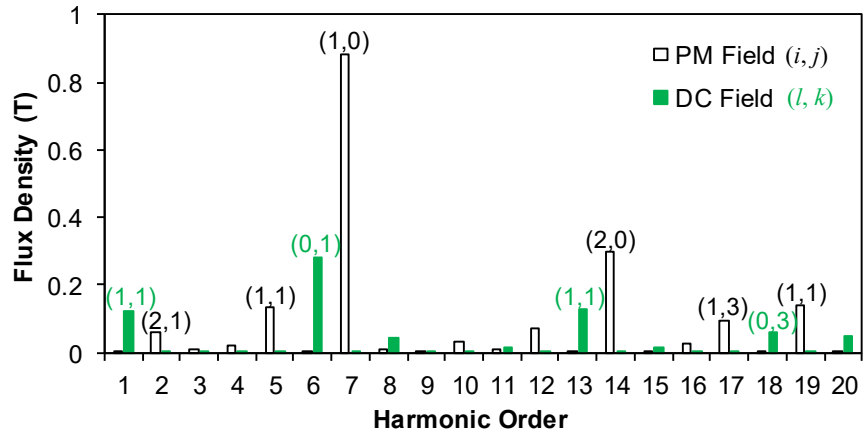

(b) Spectra

Fig. 4.2. Open-circuit air-gap flux density produced by PM and DC excitations.

Subsequently, the phase back electromotive force (EMF) can be obtained in (4.7).

$$E_{ph}(t) = -\frac{d}{dt}\left[r_g l_{st} \int_0^{2\pi} B_g(\theta, t) N_{ph}(\theta) d\theta \right] \tag{4.7}$$

where r_g is the air-gap radius and l_{st} is the stack length. N_{ph} is the phase winding function, which is expressed in (4.8) and shown in Fig. 4.3 for the 12/14 stator-slot/rotor pole single layer non-overlapping winding.

$$N_{ph}(\theta) = \sum_{m=1,3,5\cdots}^{\infty} N_{ph_m} \cos(m\theta) \tag{4.8}$$

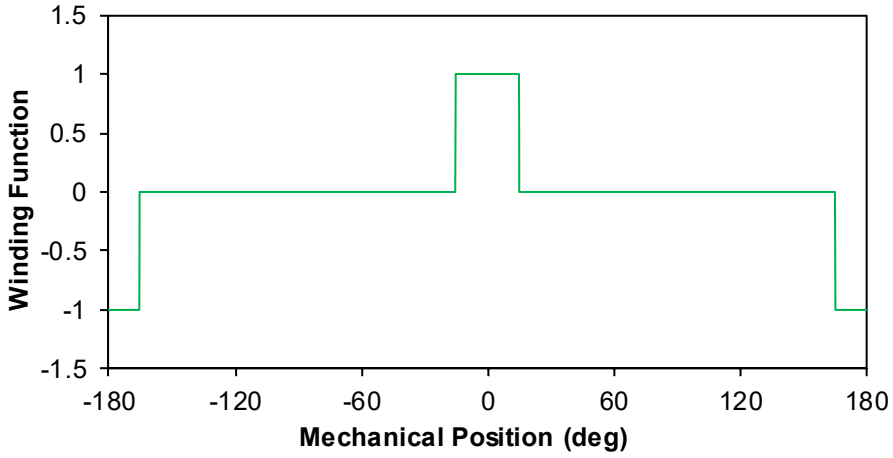

(a) Waveform

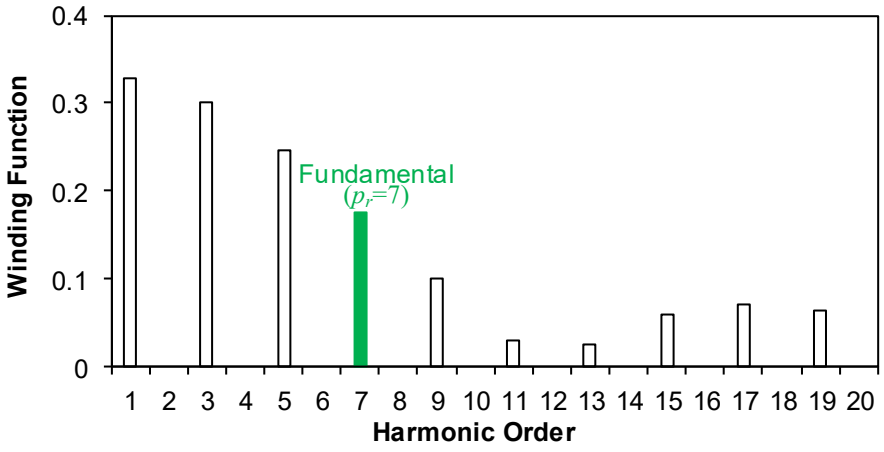

(b) Spectrum

Fig. 4.3. Single phase winding function of 12/14 stator-slot/rotor-pole single layer non-overlapping winding (Normalized value).

It can be observed that abundant harmonics exist in the winding function N_{ph} of fractional slot non-overlapping winding machine. The harmonics are of low order and high amplitude, especially the sub-harmonics. Although the 3rd harmonics are cancelled in the three-phase

synthesized armature winding MMF, other harmonics, e.g. 1st, 5th, 11th…, are remained and cause parasitic effects [RAF10].

Combining (4.5) – (4.8), the PM and DC excited phase back-EMFs can be expressed in (4.9) and (4.10), respectively. Therefore, the PM and DC excited phase back-EMF fundamentals are not zero in the condition that the harmonic orders of (4.11) and (4.12) are satisfied.

$$E_{ph\_PM}(t) = r_g l_{st} \sum_{i=1,2,3\cdots}^{\infty} \sum_{j=0,1,2\cdots}^{\infty} \sum_{m=1,3,5\cdots}^{m=\left|ip_r \pm jN_s\right|} E_{PM_{(i,j)}} \sin\left(ip_r \Omega_r t\right) \tag{4.9}$$

$$E_{ph\_DC}(t) = r_g l_{st} \sum_{k=1,3,5\cdots}^{\infty} \sum_{l=0,1,2\cdots}^{\infty} \sum_{m=1,3,5\cdots}^{m=\left|lp_r \pm \frac{k}{2}N_s\right|} E_{PM_{(i,j)}} \sin\left(lp_r \Omega_r t\right) \tag{4.10}$$

It can be observed from (4.11) that not only the winding function fundamental (p_r) but also the slot harmonics ($p_r \pm jn_s$) contribute to the PM excited back-EMF fundamental, which is denoted as magnetic gearing effect in fractional slot non-overlapping winding machine [LIU17b]. Overall, the winding function fundamental, i.e. p_r=7th, and the corresponding slot harmonics, e.g. 5th,17th,19th...are utilized to interact with the PM excited magnetic field and produce fundamental back-EMF as illustrated in (4.9) (4.11) and agree well with the conclusion in [LIU17b]. Similarly, it can be concluded from (4.10) and (4.12) that the other harmonics in the winding function satisfying $|p_r \pm k/2N_s|$, e.g. 1st,11th,13th…, interact with the DC excited magnetic field and produce the fundamental back-EMF. It should be noted that the 6th order field harmonic excited by DC winding will not contribute to the phase back-EMF, albeit with significant amplitude in Fig. 4.2 (b), since the same order is not present in the winding function of Fig. 4.3 (b). The abundant harmonics in the winding function of fractional slot non-overlapping winding, especially the 1st sub-harmonic which is acknowledged as the main harmful source of parasitic effects, are utilized to produce back-EMF through field modulation.

$$m_{PM} = \left|p_r \pm jN_s\right|, j = 0,1,2... \tag{4.11}$$

$$m_{DC} = \left|p_r \pm \frac{k}{2}N_s\right|, k = 1,3,5... \tag{4.12}$$

The open-circuit phase back-EMFs of the proposed HE machine with PM and DC excitations @400rpm in one mechanical period are illustrated in Fig. 4 with FE simulation. The fractional slot non-overlapping winding interacts with the PM and DC excited magnetic fields and periodic back-EMFs can be produced. As illustrated in (4.9) and (4.10), the least order of back-EMFs produced by PM and DC are identical and the order is p_r=7 in one

mechanical period. Therefore, the relationship between electrical and mechanical speeds can be defined as (4.13). When the corresponding three phase currents with identical frequency are applied, electromagnetic torque can be produced.

$$\omega_e = p_r \Omega_r \tag{4.13}$$

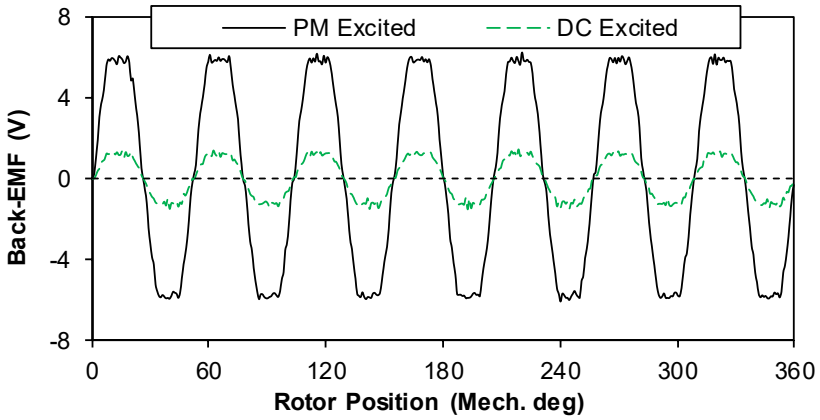

(a) Waveforms

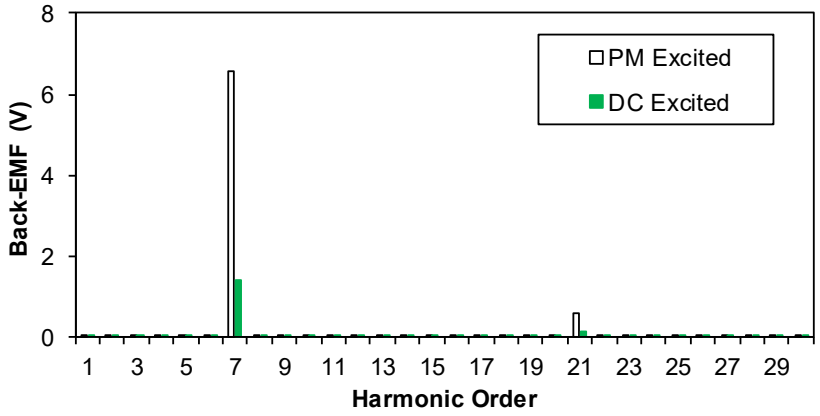

(b) Spectra

Fig. 4.4. Open-circuit phase back-EMF with PM and DC excitations at 400rpm.

4.4 Performance Evaluation

In this section, the performance of the proposed HE machine is analyzed with FE calculation in detail. To gain high torque density as well as flexible flux regulation capability, the HE machine is optimized with flux-enhancing for maximized average torque. Under the constraints of fixed stator outer diameter d_{so} = 90mm, air-gap length l_g = 0.5, axial stack length l_{st} = 25mm, armature copper loss p_{ac} = 20W, field current density J_{dc} = +10A/mm^2, the machines are globally optimized with genetic algorithm embedded in FE commercial Maxwell

software. The relationship between the armature copper loss and the machine parameters is given by (4.14) supposing the slot areas for field and armature windings are identical.

$$p_{ac} = \frac{\rho_{Cu} \cdot N_s \cdot l_{st} \cdot N_{ac}^{\ 2} \cdot I_{ac}^{\ 2}}{S_c \cdot k_p} \tag{4.14}$$

where ρ_{Cu} is the copper electrical resistivity, N_{ac} is the number of turns per armature coil, I_{ac} is the amplitude of armature current, S_c is the complete single slot area including both field and armature windings, and k_p is the packing factor. For the concentrated winding, the typical packing factor (slot filling factor) is chosen as 0.6 [JAC00]. After global optimization, the main parameters are listed in Table 4.2, in which the split ratio is defined as the ratio of rotor outer diameter to stator outer diameter.

Table 4.2 Main design parameters of the HE machines after global optimization

Parameter	Value	Parameter	Value
Stator slot number, N_s	12	Rotor pole number, $2p_r$	14
Stator outer diameter, d_{so}	90mm	Stack length, l_{st}	25mm
Air-gap length, l_g	0.5mm	PM height, h_{PM}	2mm
PM remanence, B_r	1.1T	PM coercivity, H_c	830Ka/m
PM pole arc ratio, α_{PM}	0.65	Split ratio, γ_{sp}	0.6
Stator yoke thickness, h_y	4.5mm	Stator tooth width, w_t	7.5mm
Tooth tip thickness, h_t	1.5mm	Slot opening, w_s	4mm
Slot packing factor, k_p	0.6	Stator slot per area, S_c	127 mm^2
Turns per phase, N_p	120	Turns of field winding, N_{dc}	360
Rated Current, I_r	8A	DC bus voltage, U_{dc}	24V
Rated Speed. Ω_r	400rpm	Phase resistance, R_p	0.16

4.4.1 Open-Circuit Field Distribution

The open-circuit field distributions with different DC excitations are compared in Fig. 4.5. The corresponding air-gap radial flux densities are shown in Fig. 4.6. With PM excited only, the flux path is short in Fig. 4.5 (b), and consequently, the stator yoke is generally designed to be thin for FSNW PM machines. With PM and DC excitations together, either flux-enhancing or flux-weakening, the flux path is lengthened as the result of rotor modulation effect with DC established magnetic field. Therefore, the FSNW HE machine should be re-designed considering hybridization and the thickness of stator yoke should be increased.

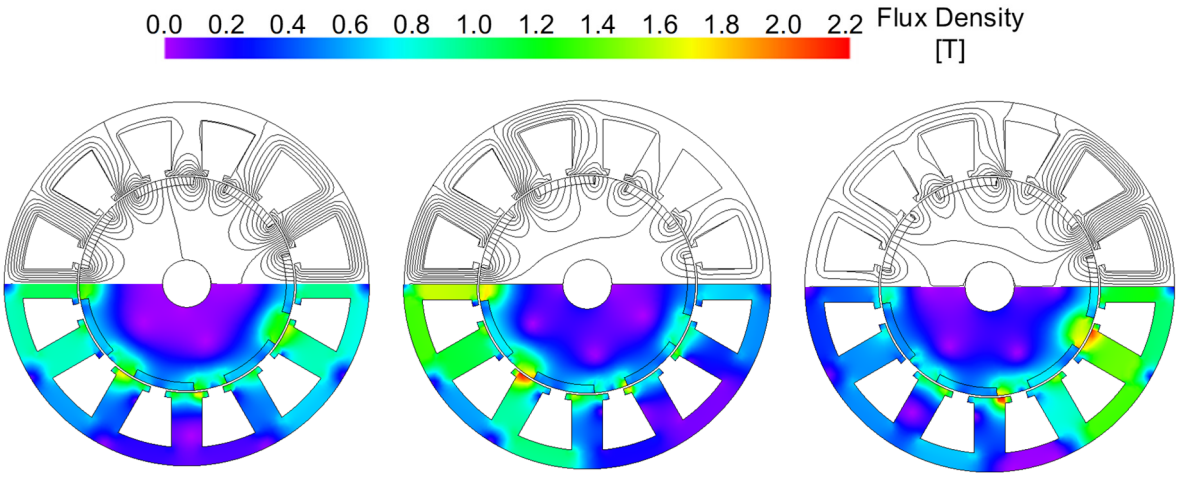

(a) Negative DC of i_{dc}=-6A (b) PM excited only (c) Positive DC of i_{dc}=+6A

Fig. 4.5. Field distributions at open-circuit with different DC excitations.

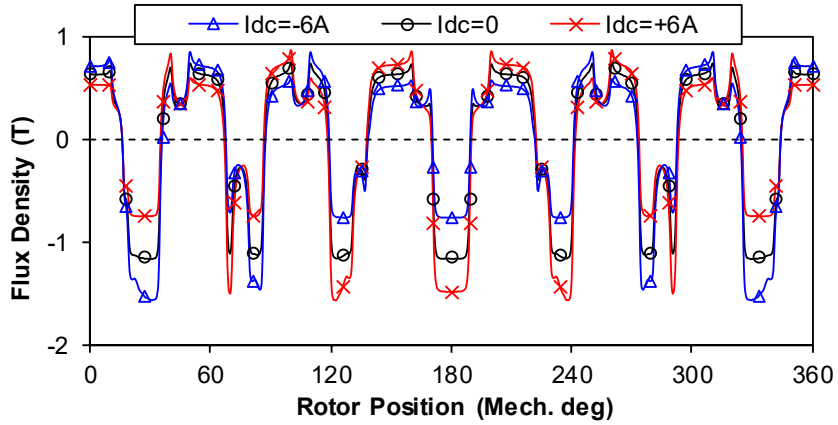

(a) Waveforms

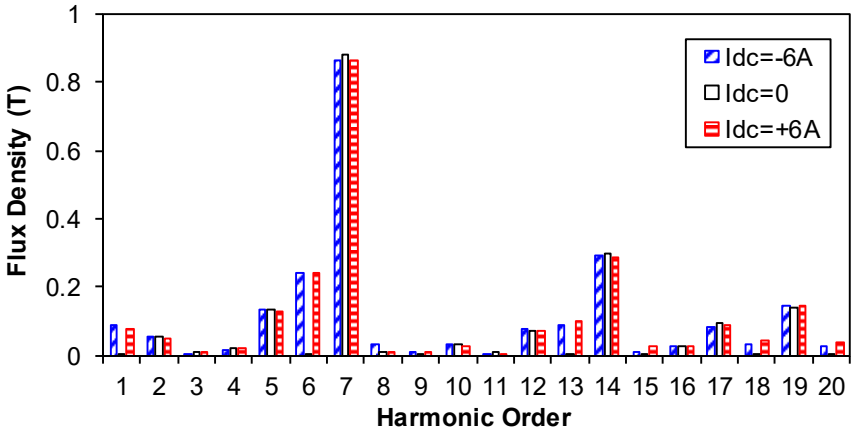

(b) Spectra

Fig. 4.6. Air-gap radial flux density at open-circuit with different DC excitations.

Corresponding phenomena can be explained from the air-gap flux density. The fundamental air-gap flux density, i.e. rotor pole-pair number p_r=7, is reduced for either flux-

enhancing or flux-weakening. Since the magnetic fields of PM and DC excitations are of different harmonic orders, both positive and negative DC excitations intensify the magnetic saturation. Besides, additional harmonics are introduced for the DC excitation and salient rotor modulation, e.g. 1st, 6th, 13th. The low order harmonic in the DC excited magnetic field accounts for the long flux path in Fig. 4.5.

4.4.2 Back-EMF

The open-circuit back-EMFs with different DC excitations are compared in Fig. 4.7. The back-EMF waveforms are trapezoidal with a 3rd order harmonic regardless of DC excitation. However, the 3rd order harmonic can be cancelled in the line-line back-EMF with star-connection. It is obvious that the DC excitations can regulate the amplitude of back-EMF effectively. Besides, the regulated EMF of flux enhancing is less significant compared with flux-weakening as the result of magnetic saturation.

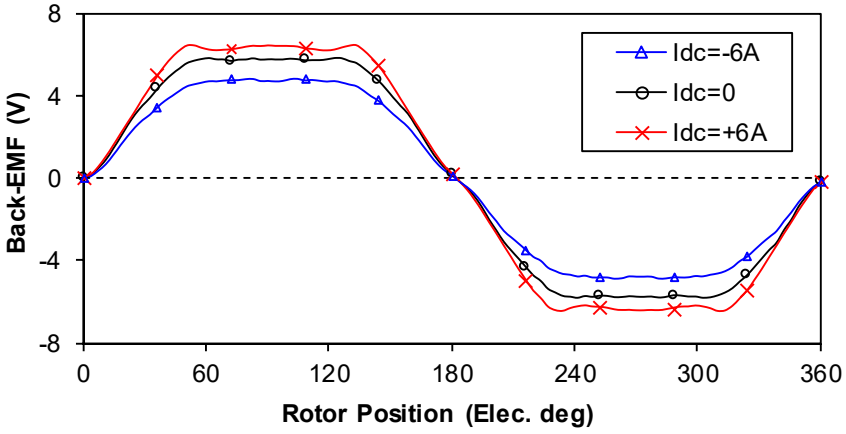

(a) Waveforms

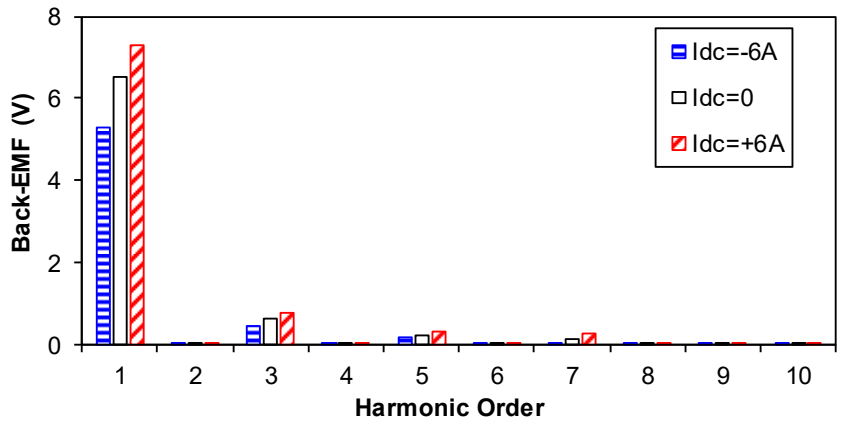

(b) Spectra

Fig. 4.7. Open-circuit phase back-EMF @400rpm with different DC excitations.

The fundamental back-EMF versus DC excitation current is shown in Fig. 4.8. With the increase of DC excitations, the increase of fundamental EMF regulation ratio slows down and even reduces. The magnetic saturation is severe with heavy DC excitation, and the phase flux linkage even tend to reduce with the field current. Therefore, the HE machine should be optimized with the consideration of DC regulation range to avoid over-saturation.

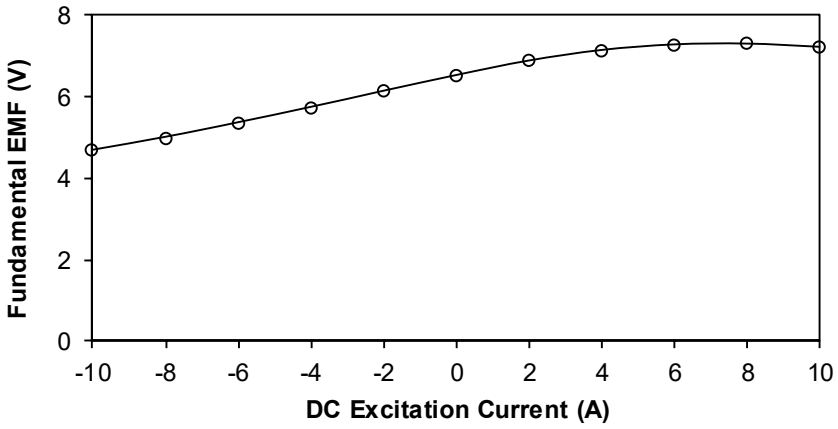

Fig. 4.8. Open-circuit phase fundamental back-EMF @400rpm versus DC excitation current.

4.4.3 Cogging Torque

Since the PM and DC excited magnetic fields co-exist in the HE machine, the cogging torque components are more complex. The periodicity of PM caused cogging torque in one electrical cycle can be expressed by (4.15), as the result of PM excited magnetic field ($2p_r$-poles) with the stator slots (N_s-teeth). Similarly, the periodicity of DC caused cogging torque in one electrical cycle can be expressed by (4.16), as the result of DC excited magnetic field (N_s-poles) with salient rotor iron poles (p_r-teeth). When the rotor PM and stator DC excitations are applied together, the synthesized cogging torque originates from the interaction between PM field (p_r-pole pairs) and WF (N_s/2-pole pairs). Therefore, the synthesized cogging torque periodicity is expressed in (4.17), which differs from that with PM and DC excitations separately.

$$N_{c_{PM}} = \frac{LCM\left(2p_r, N_s\right)}{p_r} \tag{4.15}$$

$$N_{c_{DC}} = \frac{LCM\left(N_s, p_r\right)}{p_r} \tag{4.16}$$

$$N_{c_{HE}} = \frac{LCM\left(p_r, N_s/2\right)}{p_r} \tag{4.17}$$

For the investigated HE machine with 12-stator slots and 7-rotor poles, the PM and DC excited individual cogging torque periodicities are N_{c_PM}= N_{c_DC}=12 whereas the synthesized value is N_{c_HE}=6. Therefore, the utilization of hybridization is disadvantageous to the cogging torque regardless of flux-enhancing or flux-weakening.

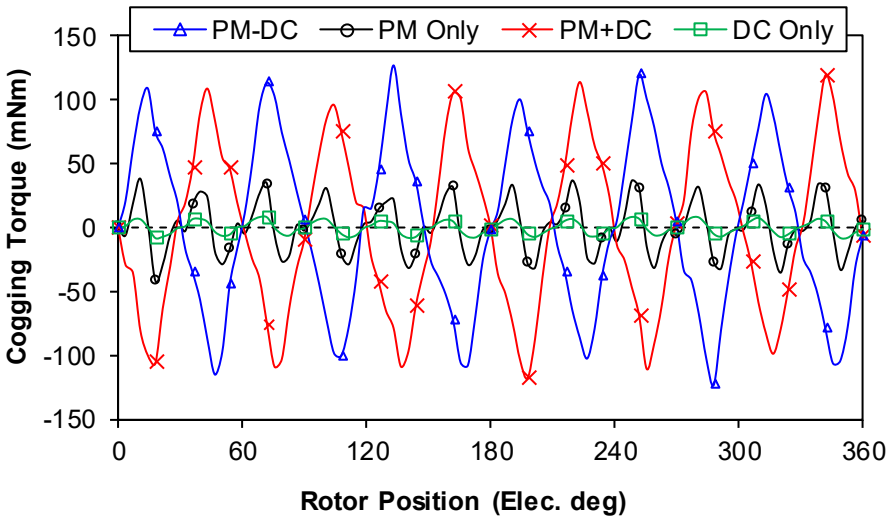

(a) Waveforms

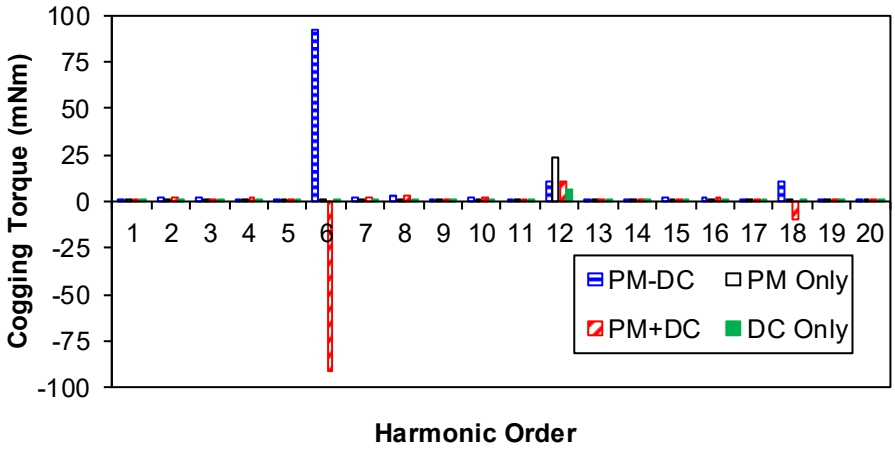

(b) Spectra

Fig. 4.9. Cogging torque with different DC excitations (the DC excitation amplitude is i_{dc}=6A).

To further illustrate this phenomenon, the cogging torques of the HE machine with different DC excitations are shown in Fig. 4.9. It can be identified that the amplitude of cogging torque is small either with PM or DC excitation. However, the synthesized cogging torque with PM and DC excitations together is significantly increased. With both positive and negative DC excitations, the 6th order harmonic is introduced in the cogging torque with reversed phases. Since the 6th order harmonic in the cogging torque is caused by the interaction between rotor

consequent-pole PM and stator DC excitations, positive and negative DC excitations result in opposite torque from aligned rotor position. It should be noted that some low order harmonics are present in the cogging torque, which is mainly caused by the FE mesh symmetry and calculation accuracy.

4.4.4 Inductance

The variation of *d*- and *q*-axis inductances with corresponding currents with different DC excitations is illustrated in Fig. 4.10. It can be identified that the *d*-axis and *q*-axis inductances are similar regardless of DC excitations, indicating the reluctance torque of the proposed HE machine is negligible. The negligible saliency can be explained by the non-overlapped armature winding and significant harmonic leakage inductance caused by the abundant harmonics in armature winding function. Moreover, the *q*-axis inductance reduces with the *q*-axis current due to the magnetic saturation caused by armature current. Meanwhile, the *d*-axis inductance increases with the negative *d*-axis current at the DC excitation of i_{dc}=0 and +6A, since the negative *d*-axis current tends to alleviate the PM excited magnetic field. Nevertheless, the phenomenon is reversed with the DC excitation of i_{dc}=-6A since the PM excited magnetic field has been countered by the field excitation and the negative *d*-axis current intensifies magnetic saturation.

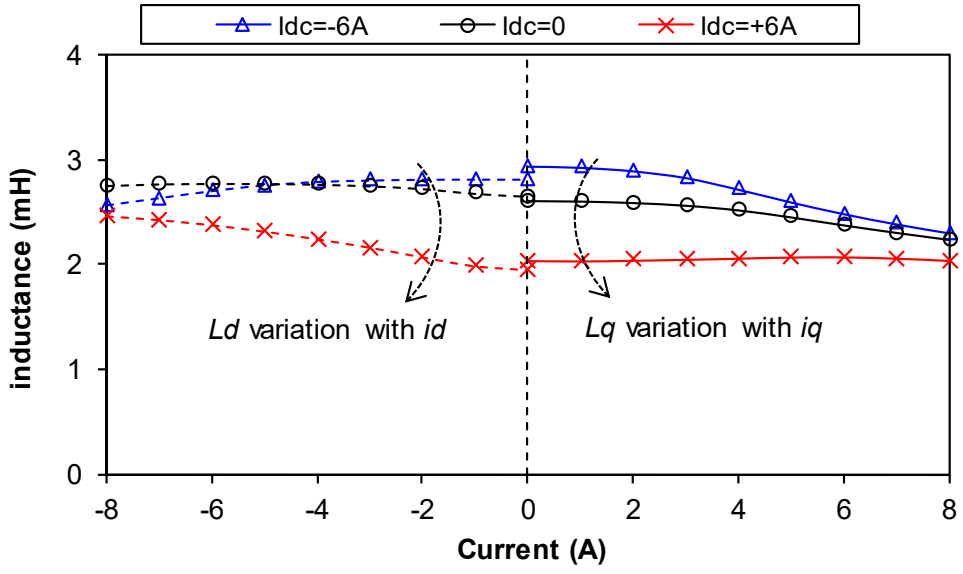

Fig. 4.10. *D*- and *q*-axis inductances variation with corresponding currents.

4.4.5 Electromagnetic Torque

The electromagnetic torques at the rated armature current of 8A and zero *d*-axis current i_d=0 control with different DC excitations are compared in Fig. 4.11. Obviously, the average

torque can be controlled with different DC excitations. Besides, the torque regulation with flux-weakening is more obvious than flux-enhancing, in accordance with back-EMF variation in Fig. 4.8. The main pulsating torque component is the 6th in the torque spectra. The DC excitation amplifies the 6th fluctuating torque, especially with flux-enhancing.

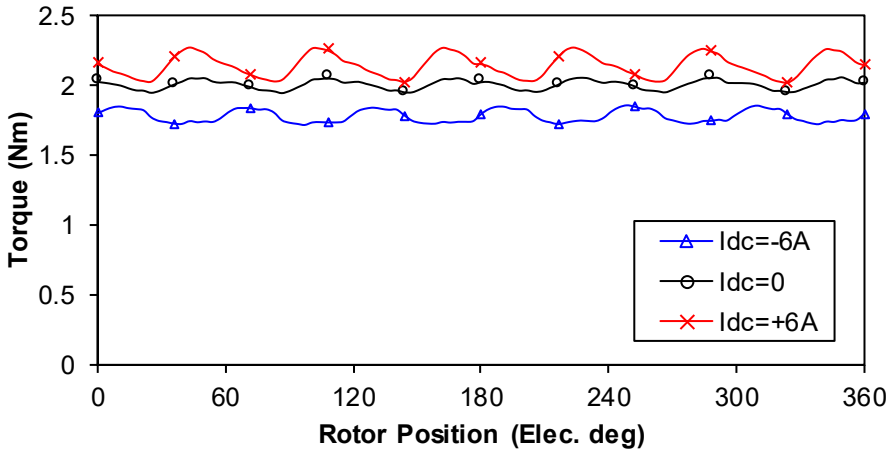

(a) Waveforms

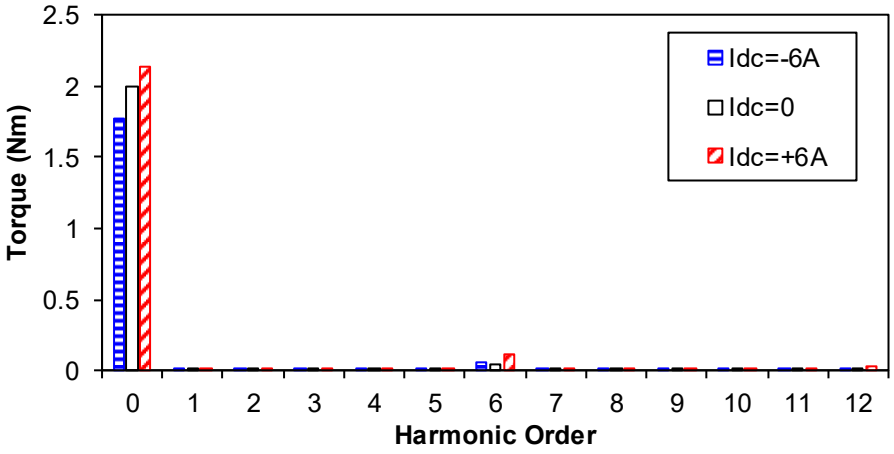

(b) Spectra

Fig. 4.11. Electromagnetic torque at the armature excitation of i_d=0, i_q=8A with different DC excitations.

Moreover, the average torque against current angle at the rated armature current is illustrated in Fig. 4.12. Since the *d*- and *q*-axis inductances for the FSNW consequent-pole rotor PM machine are similar as illustrated in Fig. 4. 10, the reluctance torque is negligible and the optimal current angle is ~ 0. Subsequently, i_d=0 control is preferred at constant torque region regardless of DC excitation. Moreover, the flux-enhancing phenomena (positive DC excitation) is more effective with i_d<0, since the negative *d*-axis current tends to alleviate the magnetic saturation.

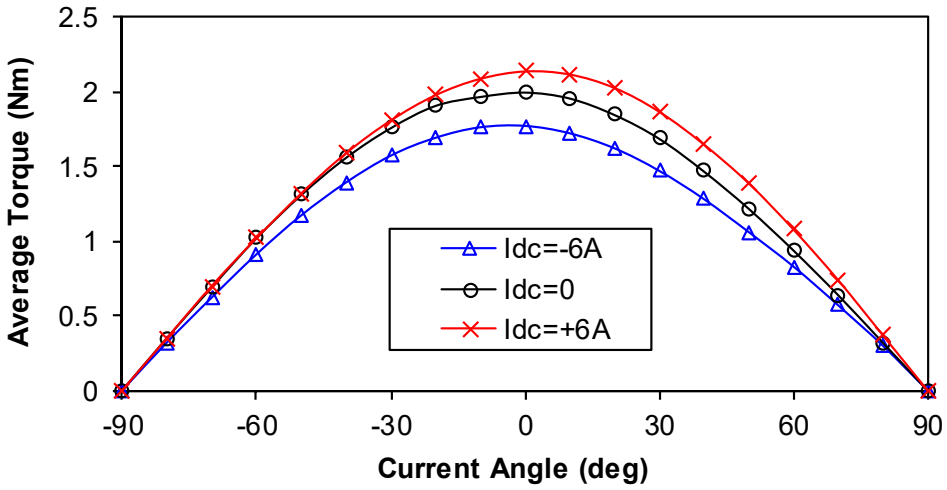

Fig. 4.12. Average torque against current angle at the armature current of 8A with different DC excitations.

The average torque versus DC and AC excitation currents is illustrated in Fig. 4.13. With the increase of *q*-axis current, the magnetic saturation becomes severe and the torque improvement ratio slows down. Moreover, the DC excitation current can regulate the air-gap flux density, back-EMF, and consequently the electromagnetic torque effectively. In accordance with the back-EMF regulation, the flux-enhancing effect is less obvious compared with flux-weakening due to magnetic saturation. Therefore, the output capability can be regulated by both the field and *q*-axis currents according to the requirements.

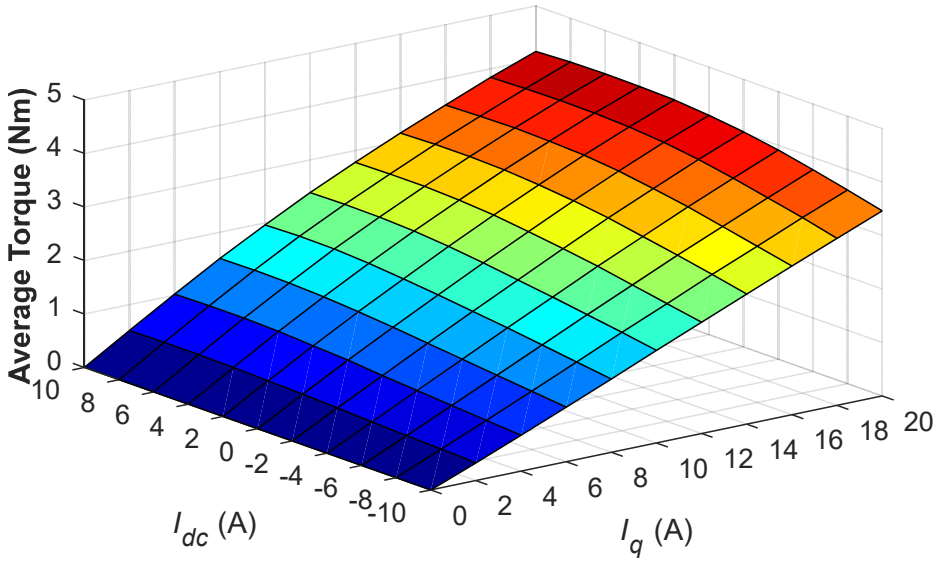

Fig. 4.13. Variation of average torque against DC and AC excitation currents with i_d=0 control.

4.4.6 Torque/Power-Speed Envelope

One of the distinct advantages to adopt HE machine is the wide constant power speed range. Therefore, it is essential to evaluate the flux-weakening capability and operating range. The flux-weakening factor k_{fw} has been introduced in (2.7) to evaluate the flux weakening capability. If the flux weakening factor k_{fw}>1, the PM and DC flux linkage can be countered and ideally infinite flux weakening operation can be achieved.

Within the rated current and maximum bus voltage in Table 4.2, the flux linkage, inductance and flux weakening factor are shown in Table 4.3. The flux weakening factor can be regulated by DC excitation effectively, and k_{fw}>1 can be achieved with negative DC excitation. Based on the FE predicted flux linkage method in [QI09], the torque- and power-speed curves within the voltage and current limits can be obtained. The torque and power-speed envelopes with/without DC regulations are compared in Fig. 4.14. The corresponding field, *d*-axis and *q*-axis currents with/without DC regulation are compared in Fig. 4.15. At low speed operation, positive DC excitation is employed to enhance the torque of constant torque region. At high speed operation, negative DC excitation is injected to weaken the magnetic field and achieve wider flux-weakening region. Subsequently, the torque-speed envelopes and flux weakening capability are improved with the regulation of DC excitation, verifying the benefit of hybrid excitation.

Table 4.3 PM flux linkage, *d*-axis inductance and flux weakening factor with different DC excitations

	$\psi_{PM} \pm \psi_{DC}$	L_d	k_{fw}
Positive DC i_{dc}=+6A	27.2mWb	2.45Mh	0.72
No DC	25.0mWb	2.75Mh	0.88
Negative DC i_{dc}=-6A	21.2mWb	2.72Mh	1.03

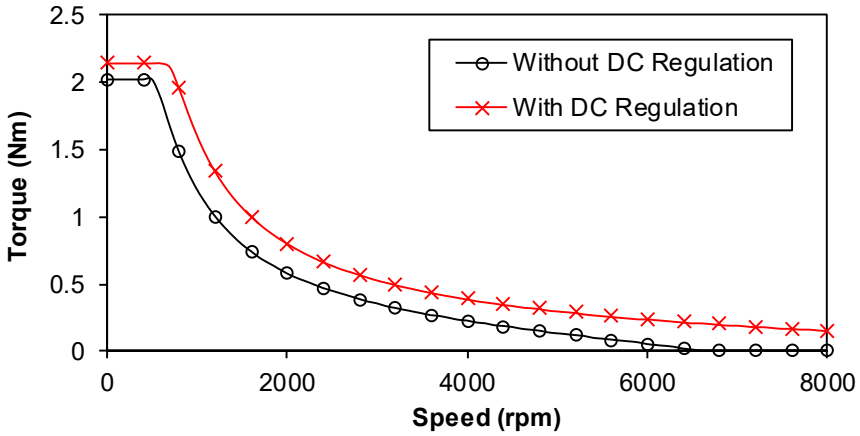

(a) Torque-speed curve

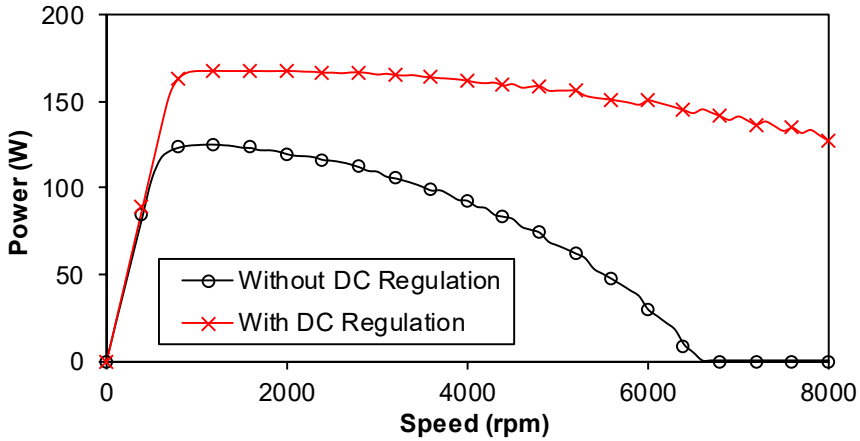

(b) Power-speed curve

Fig. 4.14. Torque and power-speed envelopes with different DC excitations.

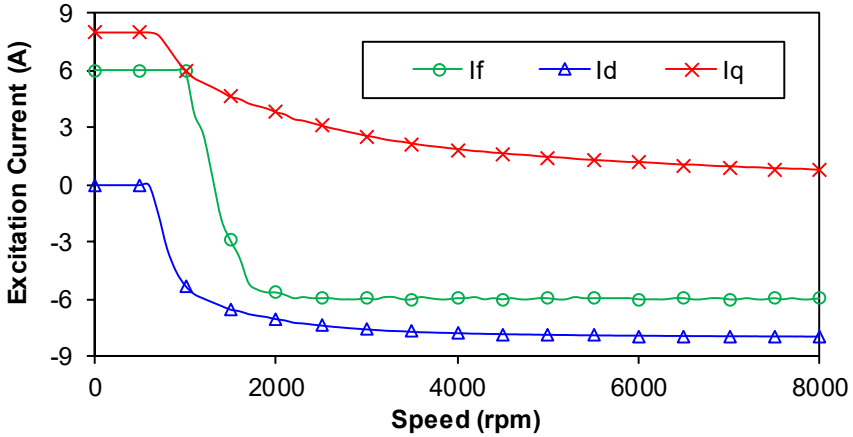

Fig. 4.15. Excitation currents along torque-speed envelope with the regulation of both field and armature currents.

Furthermore, the efficiency maps with/without field excitations are compared in Fig. 4.16. The torque-speed envelope is extended and high efficiency region can be enlarged with the control of DC excitation. It is worth emphasizing that although the operation range is broadened with the regulation of field excitation, the efficiency at extended range is limited due to the field excitation copper loss.

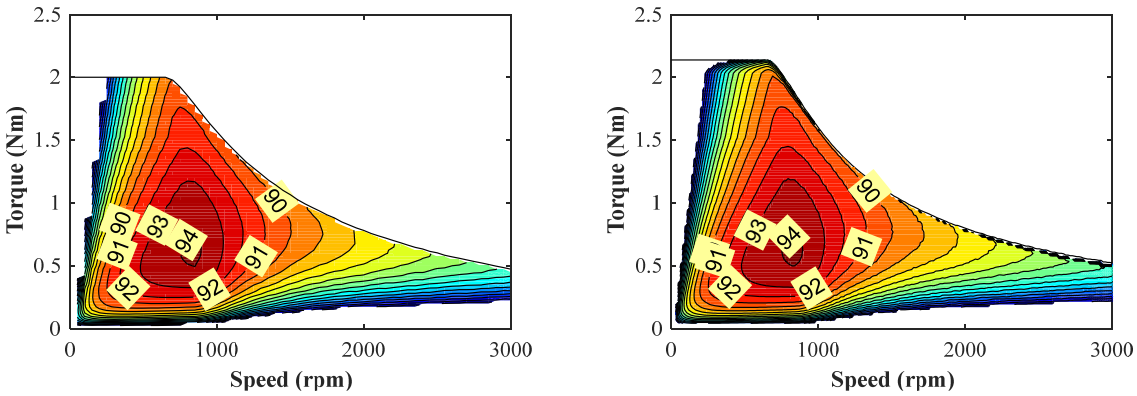

(a) Without field excitation (b) With field excitation

Fig. 4.16. Efficiency maps with/without field excitations.

4.5 Comparison with Conventional SPM Machine

To further illustrate the characteristics of the proposed HE machine, a comparison with the conventional surface mounted PM (SPM) machine is conducted in this section.

The stator/rotor pole combination, armature winding configuration, as well as stator geometry of the SPM machine are kept the same as the HE machine in Table 4.2, except that the field winding is removed. The thickness of PMs is maintained the same as the proposed HE machine for simplification, and the PM pole arc ratio of α_{PM}=1 (shown in Fig. 4.17 (a)) and 0.65 (i.e. the same as the HE machine, shown in Fig. 4.17 (b)) are chosen for comparison, respectively.

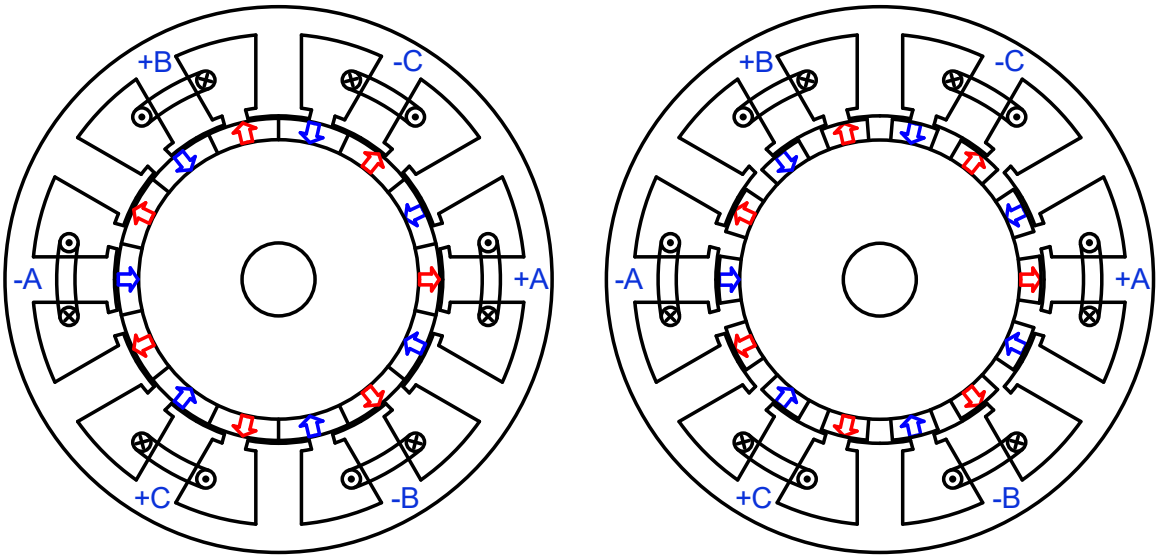

(a) PM pole arc ratio of 1 (b) PM pole arc ratio of 0.65

Fig. 4.17. Machine topology of conventional SPM machine.

The average torques of the HE and SPM machines at the same rated armature current of i_q=8A, i_d=0 are compared in Fig. 4.18. The average torque of SPM machine is constant, while the torque of HE machine can be regulated by DC excitation. Without DC excitation, the average torque of proposed HE machine is higher than the SPM machine with the same PM consumption. With positive DC excitation of i_{dc}=+6~8A, the average torque of the HE machine can be comparable with conventional SPM machine of PM pole arc ratio α_{PM}=1, whereas the PM usage is reduced significantly.

Furthermore, at the DC excitation of i_{dc}=+6A (to gain maximum average torque for HE machine from Fig. 4.18), the average torques versus q-axis current of the HE machines are compared with the SPM machines in Fig. 4.19. Within the same PM usage, the torque density of proposed HE machine at flux-enhancing is higher than the SPM machine. Moreover, the torque density of the HE machine is comparable with the SPM machine of PM pole arc ratio α_{PM}=1 at rated armature current. However, the magnetic saturation of the HE machine is more severe, and the torque density becomes lower than the SPM machine of α_{PM}=1 at heavy load. It should be noted that the introduction of DC excitation produces additional field winding copper loss compared with the conventional SPM machine, and the operation efficiency should be evaluated.

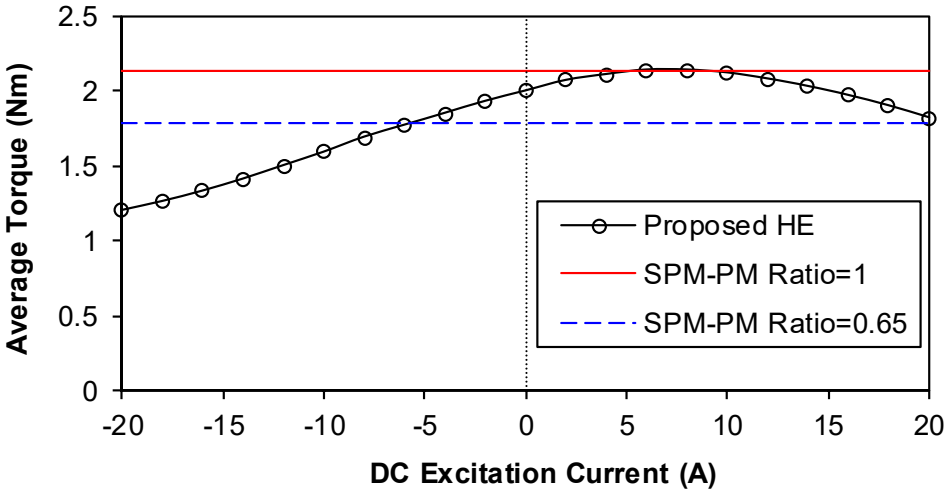

Fig. 4.18. Average torque against DC excitation current with the armature current of i_d=0, i_q=8A.

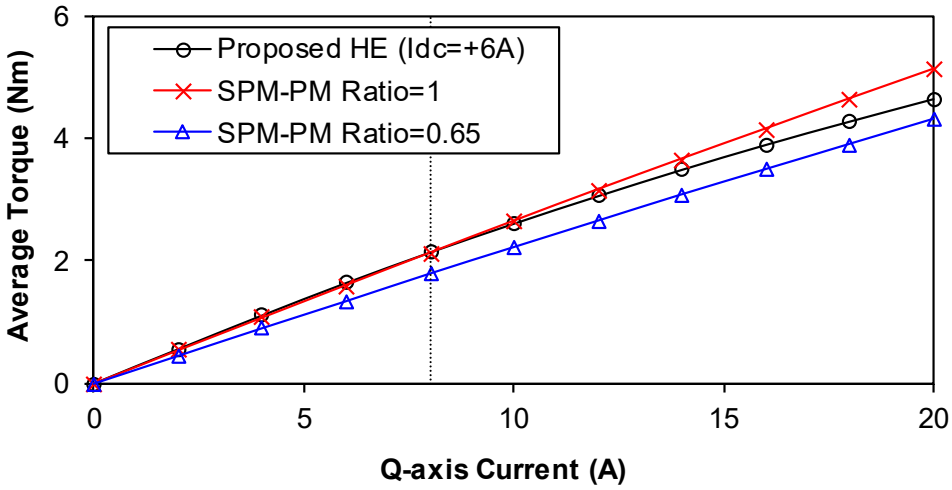

Fig. 4.19. Average torque against q-axis current (i_{dc}=+6A for the HE machine).

To further illustrate the flux weakening performance and operating efficiency, the efficiency maps of three machines are compared in Fig. 4.20 under the same operation limit of Table 4.2. In constant torque region, the output capability of the proposed HE machine is comparable with the SPM machine of PM pole arc ratio α_{PM}=1, albeit with reduced PM usage. Nevertheless, the efficiency at high torque operation is slightly lower due to additional field winding copper loss. For the HE machine, an extra degree, i.e. DC excitation, is introduced to regulate the magnetic field, and the flux weakening control strategies are more flexible. The flux-weakening regions for the two SPM machines are limited whereas the HE machine has a wider operating range, as illustrated in section 4.4.6. Moreover, the colored contour in the efficiency map indicates the operating region with efficiency higher than 75%. Although the

highest efficiency region (=94%) is shrunk in the HE machine due to the introduction of additional field winding copper loss, the potential operating region efficiency is enhanced, which is beneficial for the frequently variable speed application, e.g. EV/HEV and domestic appliances.

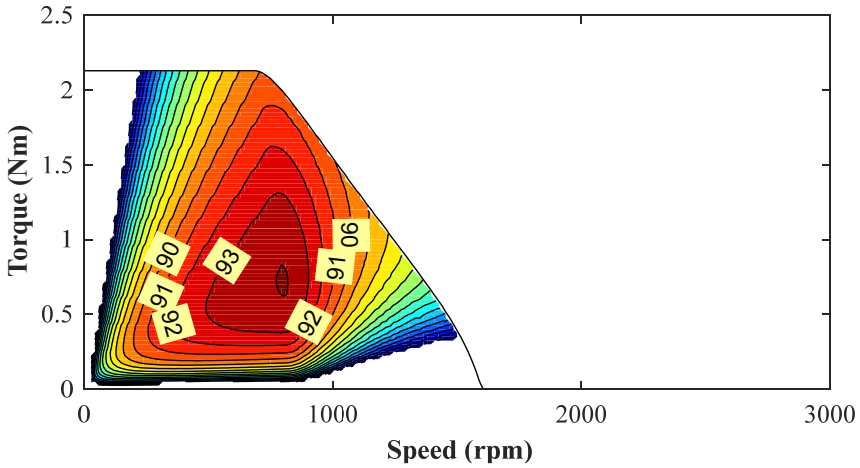

(a) SPM machine with PM pole arc ratio of 1

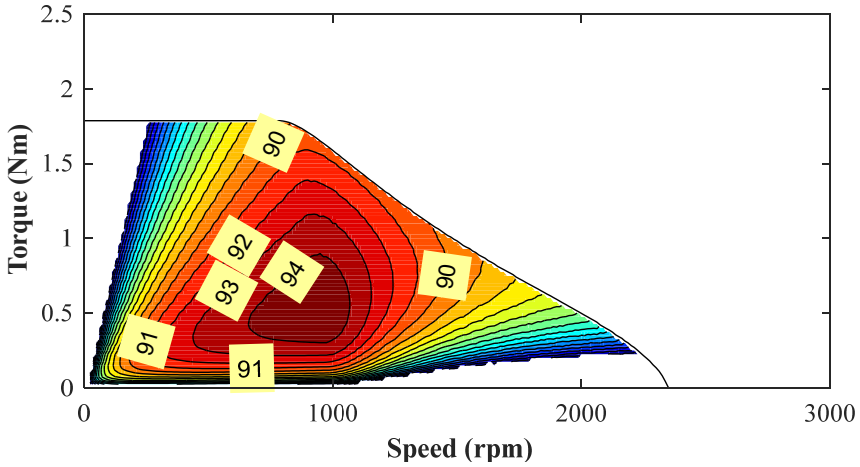

(b) SPM machine with PM pole arc ratio of 0.65

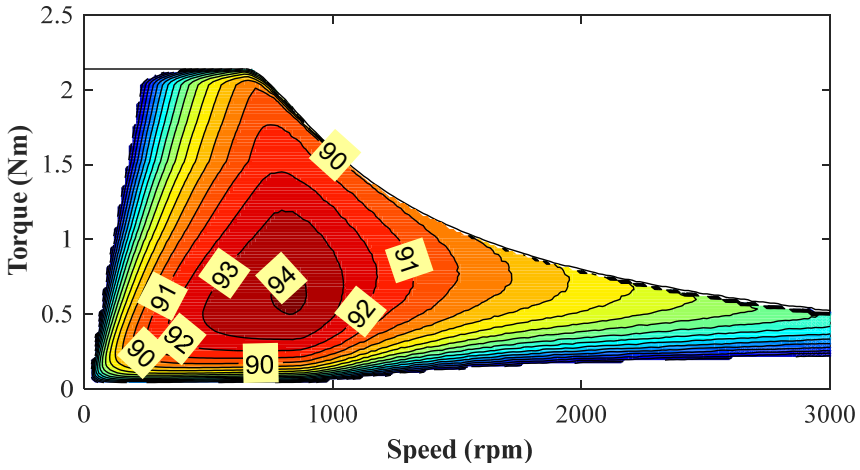

(c) Proposed HE machine

Fig. 4.20. Efficiency map comparison (colored contour indicating efficiency higher than 75%).

Since DC coils and correspondingly additional field winding copper loss are introduced in the HE machine, it is important to evaluate the copper losses compared with pure PM machine. The copper losses of three machines in the operation region are compared in Fig. 4.21. Since additional field copper loss is introduced in the HE machine, the copper loss is higher compared with SPM machines, albeit with wider operation range. The copper loss is significant for the HE machine at the low-speed high-torque region and high-speed region, since the field excitations are employed to either enhance or weaken the magnetic field. Therefore, the HE machine exhibits wider operation region with the sacrifice of additional field winding copper loss, and the heat management should be considered.

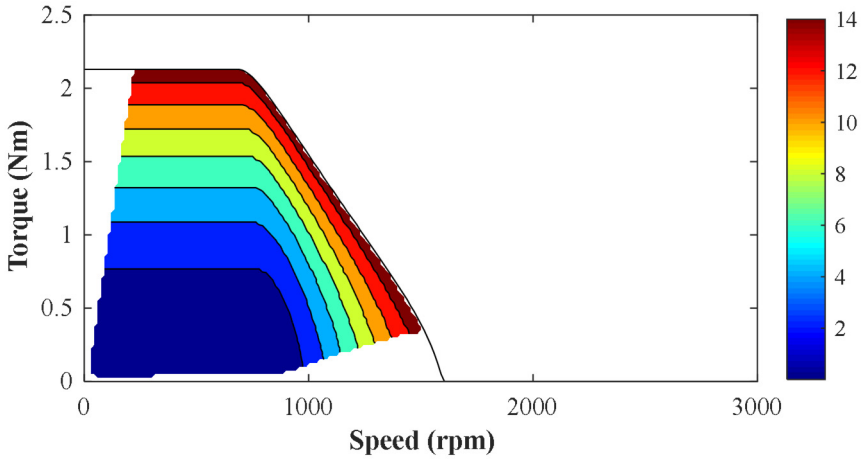

(a) SPM machine with PM pole arc ratio of 1

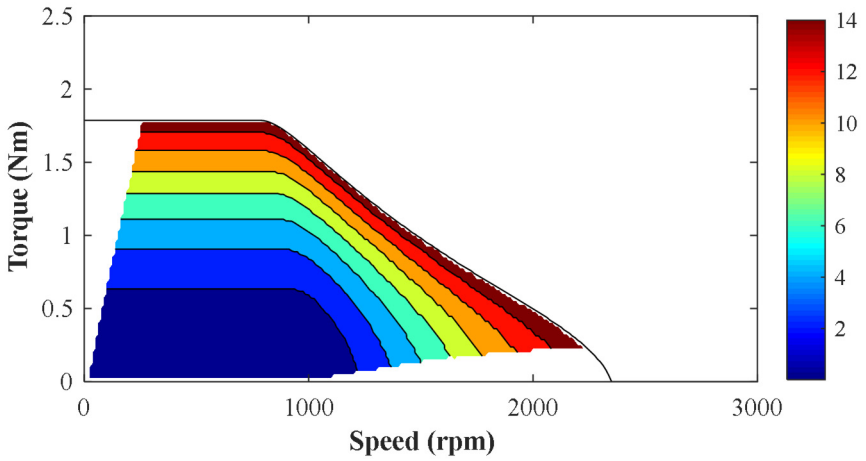

(b) SPM machine with PM pole arc ratio of 0.65

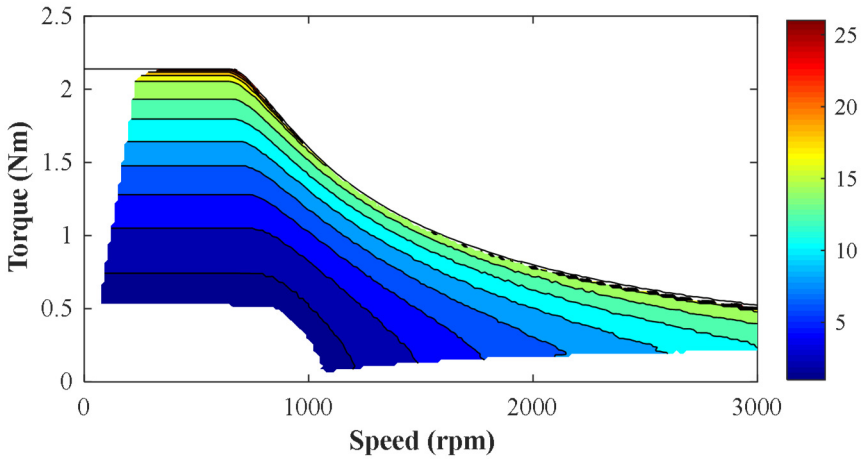

(c) Proposed HE machine

Fig. 4.21. Copper loss comparisons (colored contour indicating efficiency higher than 75%).

4.6 Experimental Validation

In order to validate the theoretical analysis and FE calculation, a prototype of the proposed HE machine is manufactured, as shown in Fig. 4.22. The main design parameters are kept the same as Table 4.2. The field winding and armature winding are wound separately and alternatively around the stator teeth, as shown in Fig. 4.22 (a). The PMs are inset in the slot of salient rotor with glue, as shown in Fig. 4.22 (b). It is worth mentioning that the purpose of this section is to verify the theoretical flux regulation capability, and the accuracy of FE calculations. Therefore, the winding turns are not the same as in the previous analyses, and the armature winding is reduced to 80 turns per phase, and the field winding is reduced to 240 turns to ease the hand winding process in academic laboratory.

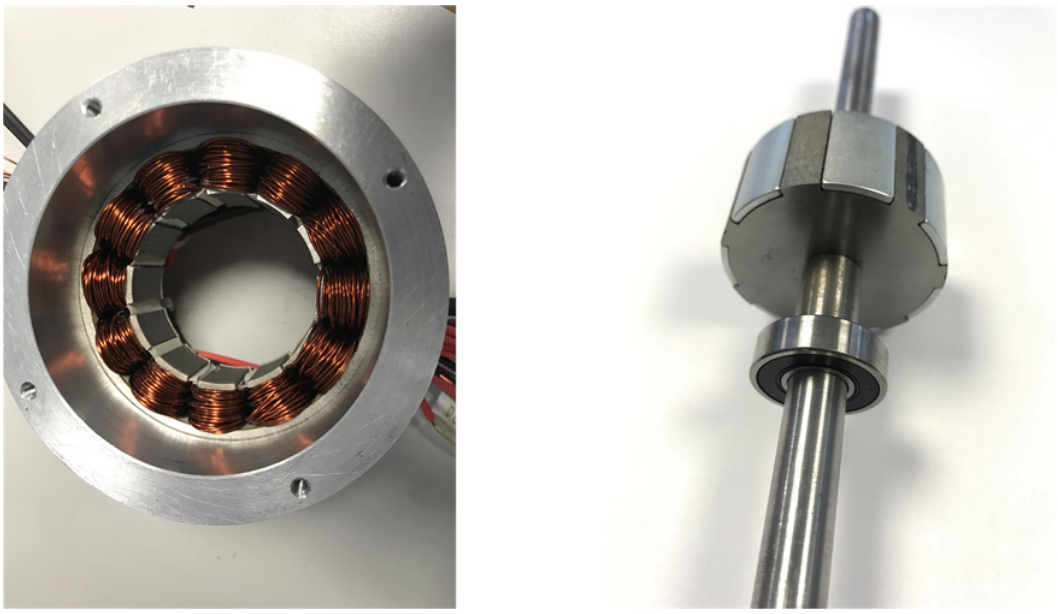

(a) Stator (b) Rotor

Fig. 4.22. Prototype of proposed HE machine.

The measured open-circuit three phase back-EMFs with different DC excitations @400rpm are compared in Fig. 4.23. The three phase back-EMF waveforms are symmetrical regardless of DC excitation and the DC excitation can regulate the back-EMF effectively. In Fig. 4.24, the phase back-EMF with different DC excitations are compared with FE calculation, in which good agreement is observed. To validate the flux regulation effect of field winding, the fundamental back-EMF against DC excitations is shown in Fig. 4.25. Although the measured back-EMF fundamental is slightly smaller than the FE prediction due to the end effect, satisfied agreement is achieved, indicating the field regulation effect of DC excitation.

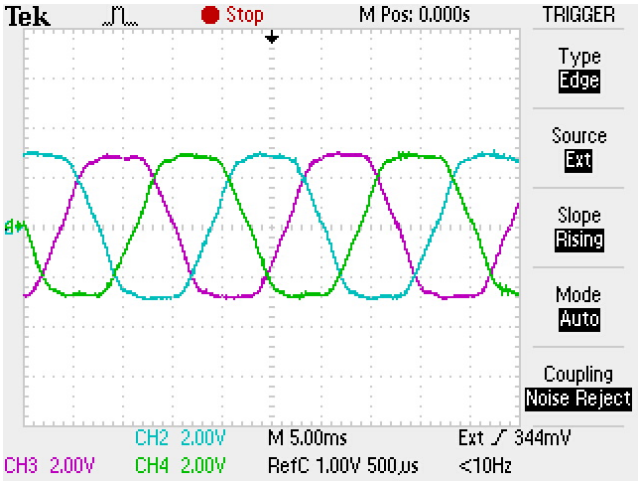

(a) i_{dc}=-8A

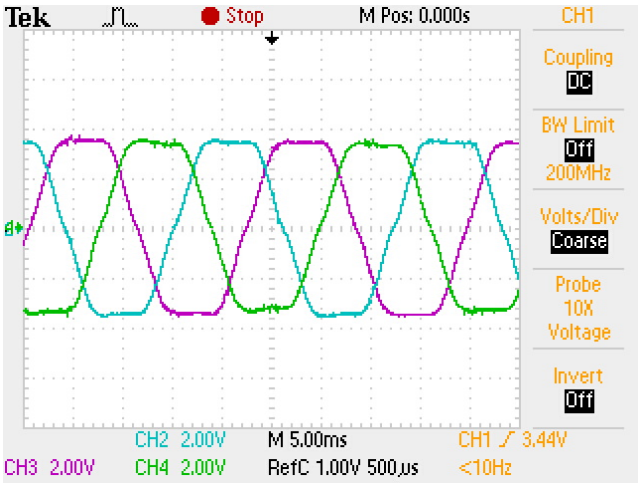

(b) i_{dc}=0

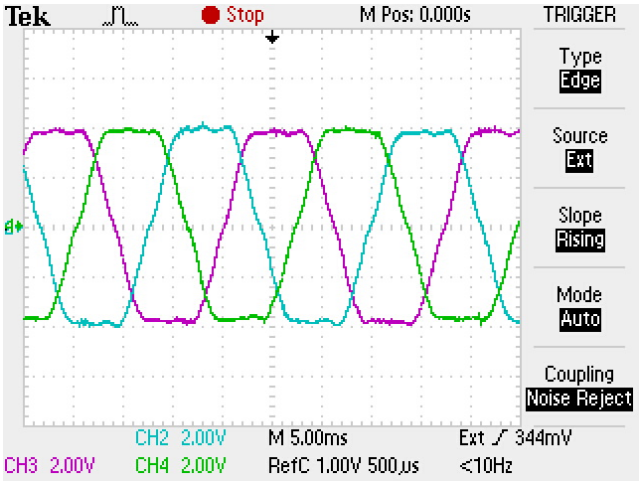

(c) i_{dc}=+8A

Fig. 4.23. Measured open-circuit three phase back-EMF waveforms at the rotor speed of 400rpm with different DC excitation currents.

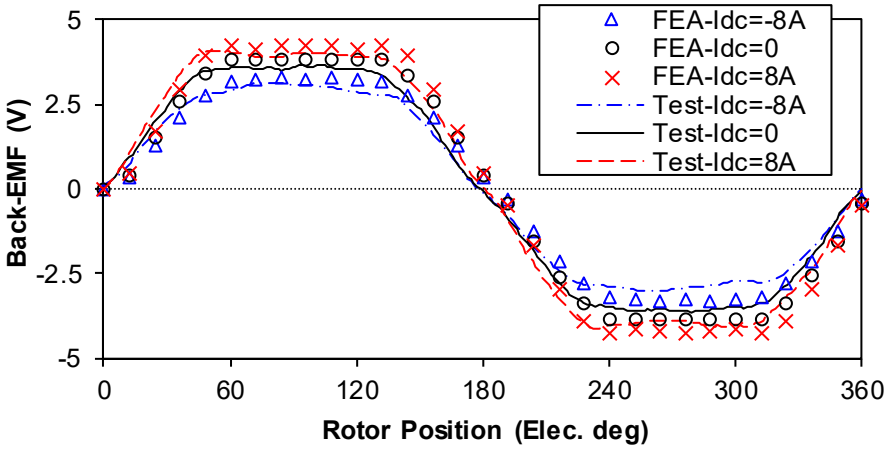

Fig. 4.24. Measured and FE predicted open-circuit phase back-EMF waveforms at the rotor speed of 400rpm with different DC excitation currents.

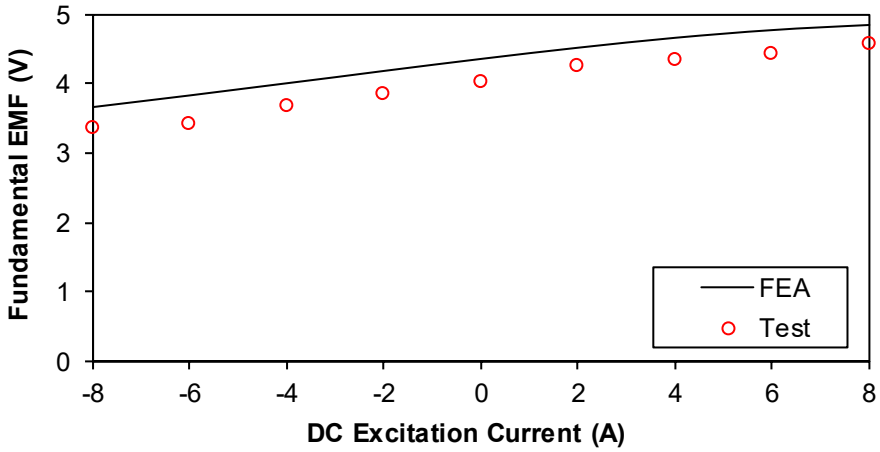

Fig. 4.25. Measured and FE predicted open-circuit phase back-EMF fundamental versus DC excitation currents at the rotor speed of 400rpm.

The phase self- and mutual-inductances are calculated with (4.18) in FE simulation and measured with LCR meter for validation. The mutual-inductance is indirectly measured from the self-inductance of phase A, phase B, and the series connection of phase A and B according to (4.20).

$$L_{aa(FE)} = \frac{\psi_a(i_a = I_a) - \psi_a(i_a = 0)}{I_a} \tag{4.18}$$

$$M_{ba(FE)} = \frac{\psi_b(i_a = I_a) - \psi_b(i_a = 0)}{I_a} \tag{4.19}$$

$$M_{ba(TEST)} = \frac{L_{a+b} - L_{aa} - L_{bb}}{2} \tag{4.20}$$

The measured and FE predicted phase self- and mutual-inductances are compared in Fig. 4.26. The mutual inductance is negligible as the result of non-overlapped single layer armature winding, and the proposed HE machine exhibits highly fault tolerant capability. Besides, the self-inductance reduces with the DC excitation since the field excitation aggravate the magnetic saturation and the reluctance is reduced correspondingly. The measured inductances are always slightly larger than the FE prediction due to the 3D end effect. Overall, the measured inductances agree well with the simulations, verifying the validity of FE calculations.

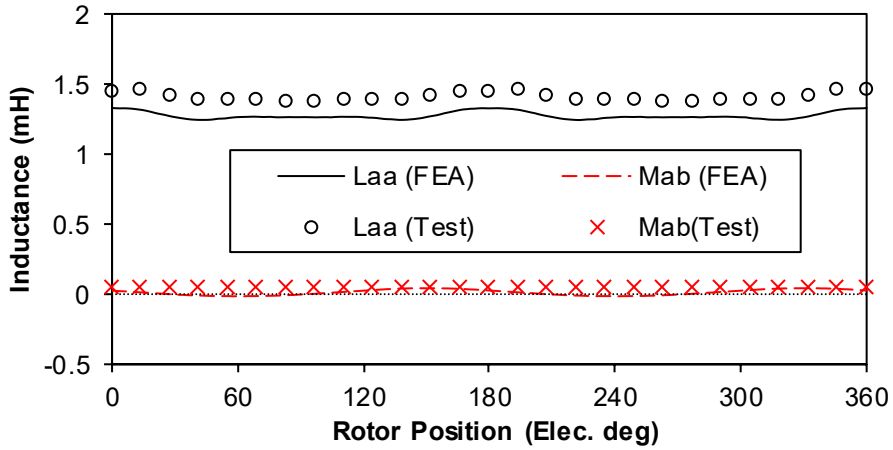

(a) Inductance waveforms

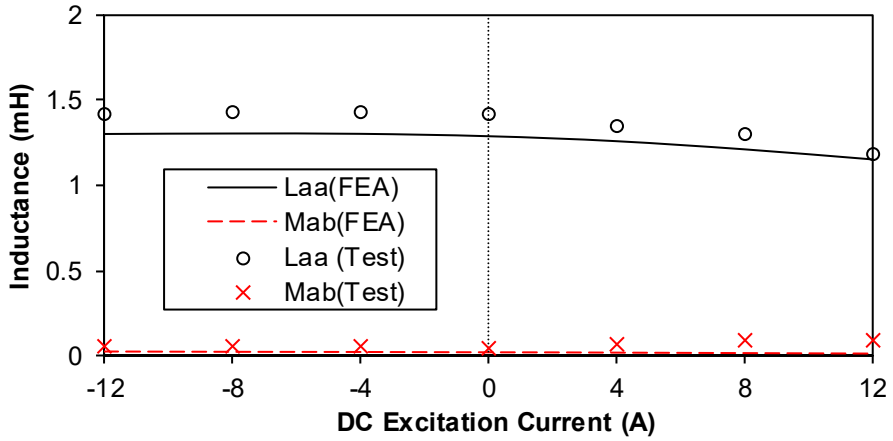

(b) Average inductance variation with DC excitation current

Fig. 4.26. Measured and FE predicted phase self- and mutual-inductances.

To validate the effect of DC excitation on cogging torque, the cogging torques with different DC excitations are measured. Without DC excitation, the cogging torque is negligible due to the fractional pole-slot combination with the amplitude of ~40mNm, as illustrated in Fig. 4.9. When the DC excitation is employed, the cogging torque is increased significantly,

and measured in comparison with FE prediction in Fig. 4.27. It can be observed that the cogging torque amplitudes are similar with positive and negative DC excitations, whereas the phases are reversed as analyzed above. Although a significant difference between the simulated and measured amplitudes is observed due to test error for the relatively small amplitude of cogging torque, the periodicity of cogging torque agrees well, verifying the theoretical analyses.

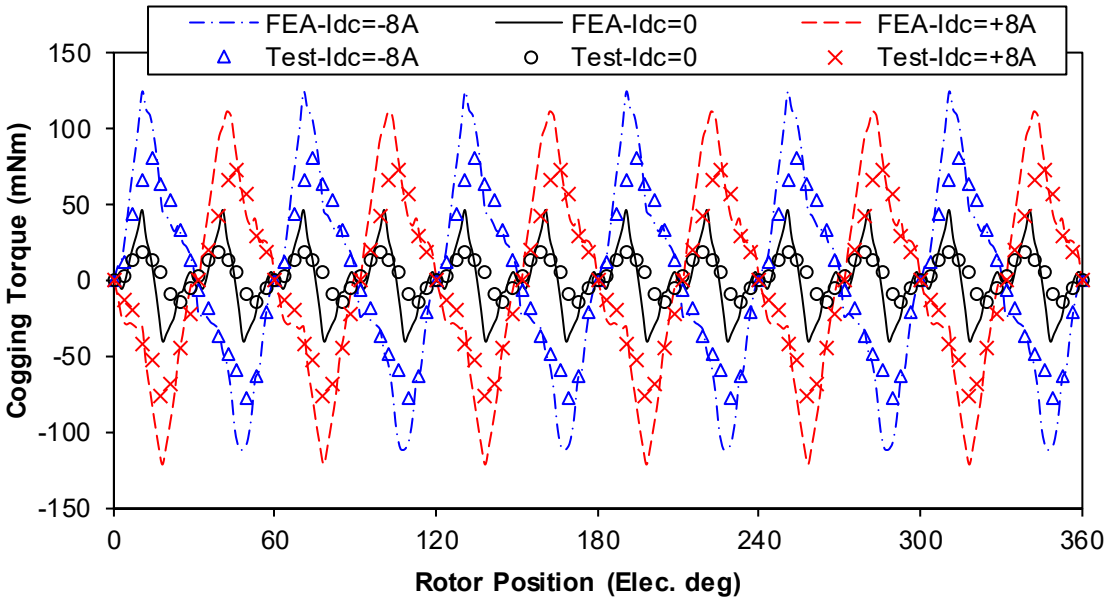

(a) Waveforms

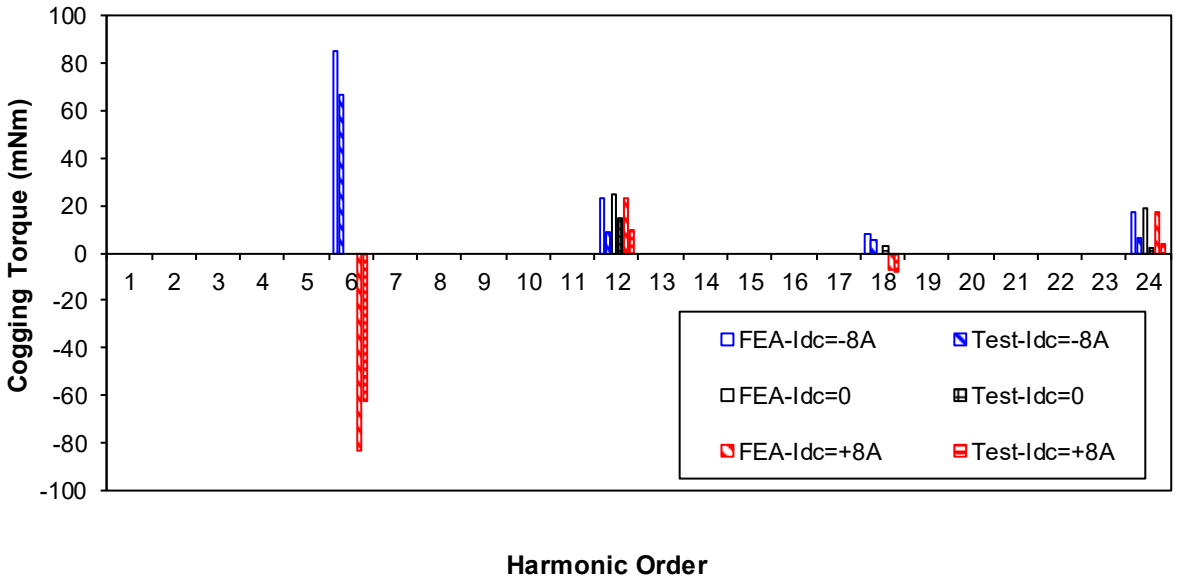

(b) Spectra

Fig. 4.27. Measured and FE predicted cogging torques with different DC excitations.

Furthermore, the static torques are measured with the three-phase armature excitations of i_a=-2i_b=-2i_c. As the rotor moves at different positions, the static torque waveforms can be obtained with the method present in [ZHU09]. The measured static torques are compared with FE calculations in Fig. 4.28. By fixing the rotor position to align q-axis with phase A axis, the variation of measured and FE-predicted torque with i_{dc} and i_a is shown in Fig. 4.29. Again, the test results are in good agreement with FE prediction and it is verified that the DC excitation can regulate the output torque according to the output requirement.

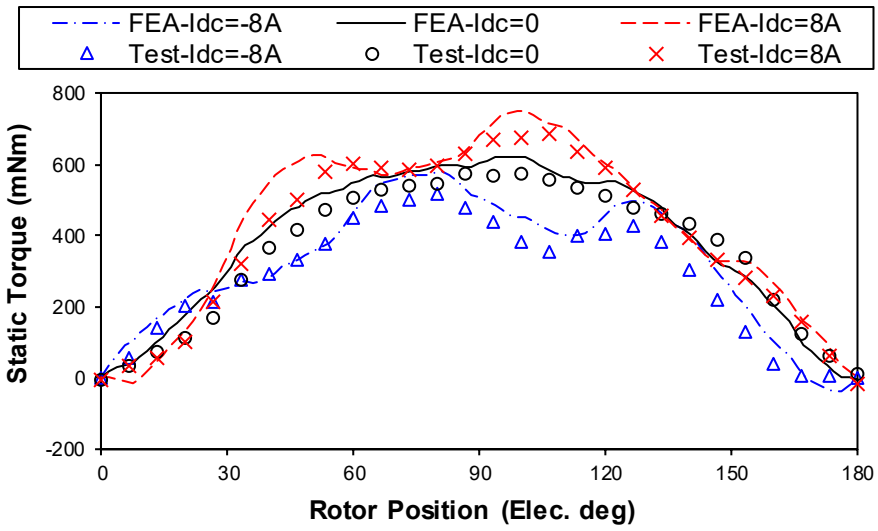

Fig. 4.28. Measured and FE predicted static torque with I_a=4A and different DC excitation currents.

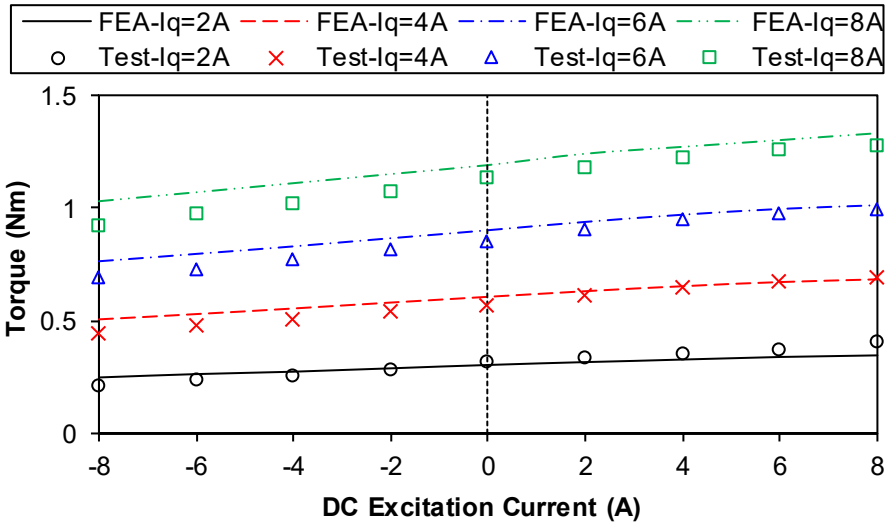

Fig. 4.29. Variation of measured and FE-predicted torque with DC excitation at different q-axis current.

To further illustrate the benefit of hybrid excitation, the torque-speed curves of the prototype with different DC excitations are measured with the test platform in Fig. 4.30. The prototype is connected with a brushed DC generator as load. The output requirement of the prototype can be adjusted flexibly by regulating the field current of DC generator through the DC Supply #1 as well as the resistance bank. Besides, an individual DC Supply #2 is connected with the field winding of prototype to adjust the field current continuously. The DC Supply #3 is utilized to feed the armature winding through the inverter, which is based on the Dspace controller.

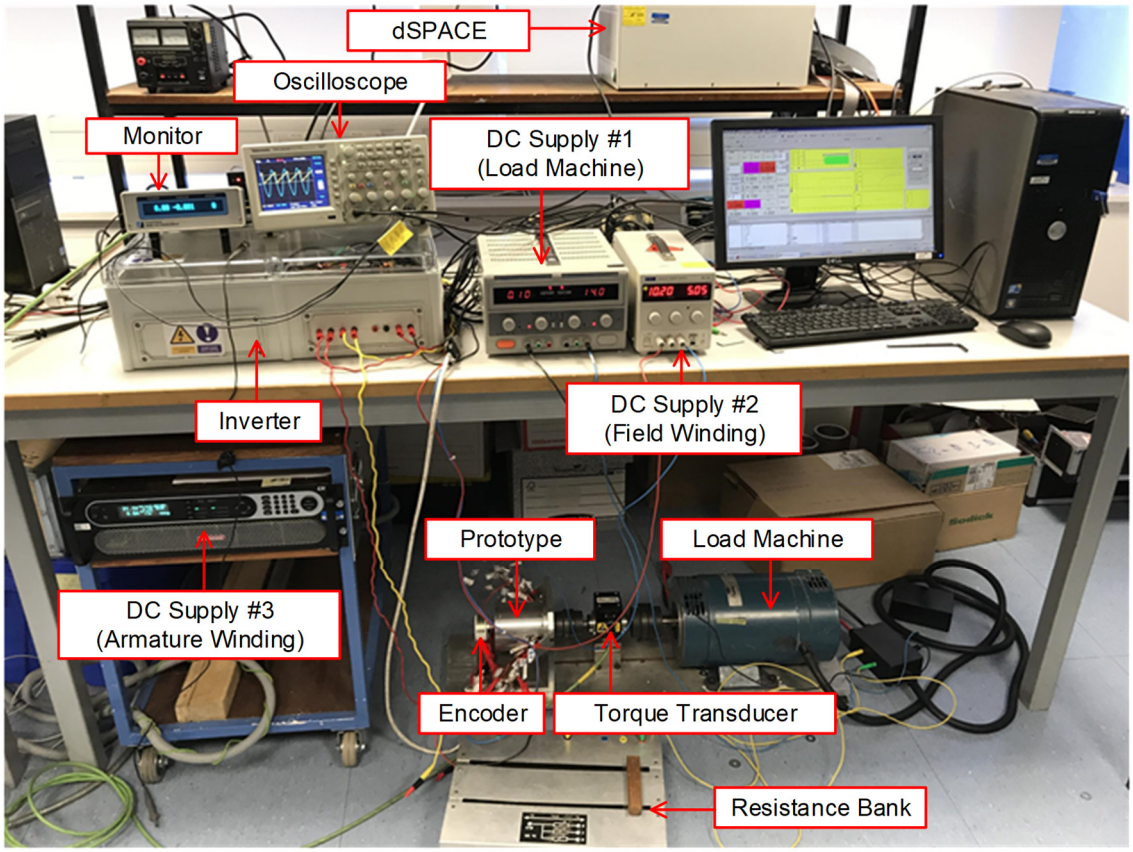

Fig. 4.30. Test platform for dynamic experiments.

The flux-weakening experiment is conducted within the limit of 5A phase current, and 15V DC bus voltage. With the utilization of flux-linkage method in [QI09], the field winding, *d*- and *q*-axis currents under the voltage and current limits are predicted in Fig. 4.31. In constant torque region, the *d*-axis current is almost 0 regardless of DC excitation as the result of negligible reluctance torque. As the rotor speed increases, the line-line voltage approaches the DC bus voltage and flux-weakening control is required to reduce the back-EMF. When the machine operates at the flux-weakening region, negative *d*-axis current is applied to contour the PM flux and reduce the back-EMF to satisfy the limit of DC bus voltage. Under the limit

of phase current, the *q*-axis current is inevitably decreased and the output torque reduces in the flux weakening region.

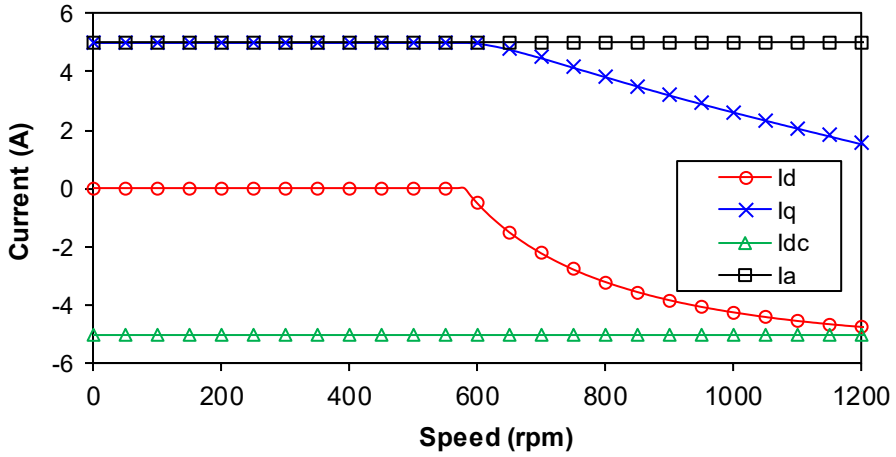

(a) i_{dc}=-5A

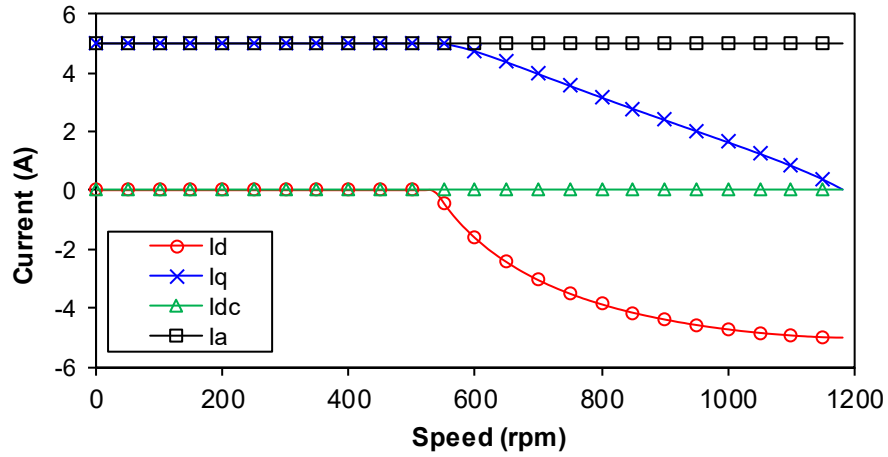

(b) i_{dc}=0

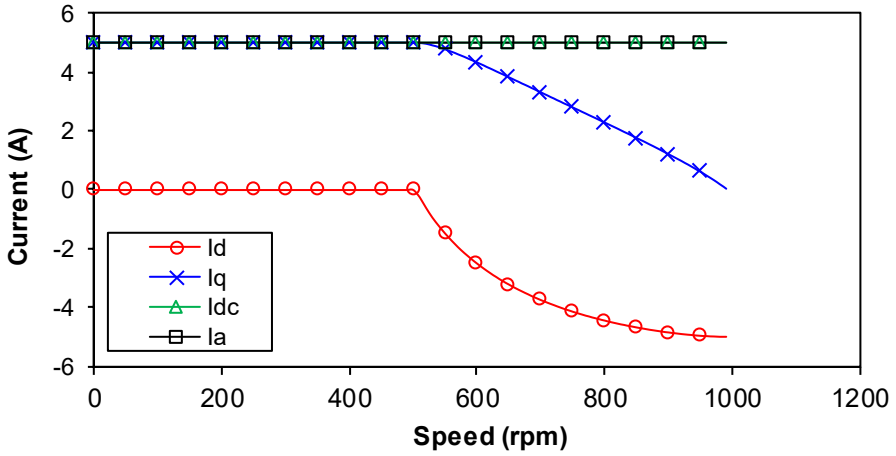

(c) i_{dc}=+5A

Fig. 4.31. FE predicted field winding, *d*- and *q*-axis currents with different DC excitations under the voltage and current limits.

With zero and positive DC excitations in Figs. 4.31 (b) and (c), the PM flux cannot be cancelled with the limit of armature current, and the machine exhibits limited operating range. However, with the utilization of negative DC excitation, the PM flux can be totally contoured by the field and *d*-axis currents together. The *d*-axis current is not negative maximized even at the rotor speed of 1200rpm, indicating the machine operation region is broadened with the assistance of flux-weakening field current.

With the employment of field and armature currents in Fig. 4.31, the torque-speed envelopes with different DC excitations are measured in comparison with FE prediction in Fig. 4.32. Overall, the measured torques are smaller than FE calculation regardless of DC excitation currents, due to 3D flux leakage and friction at low speed operation. However, the benefit of hybrid excitation can still be observed from the test results. At constant torque region, the output torque is higher with positive DC excitation. Nevertheless, the output capability is superior with negative DC excitation at high speed region. Subsequently, the torque-speed envelopes can be broadened with the regulation of field excitations among the operation region.

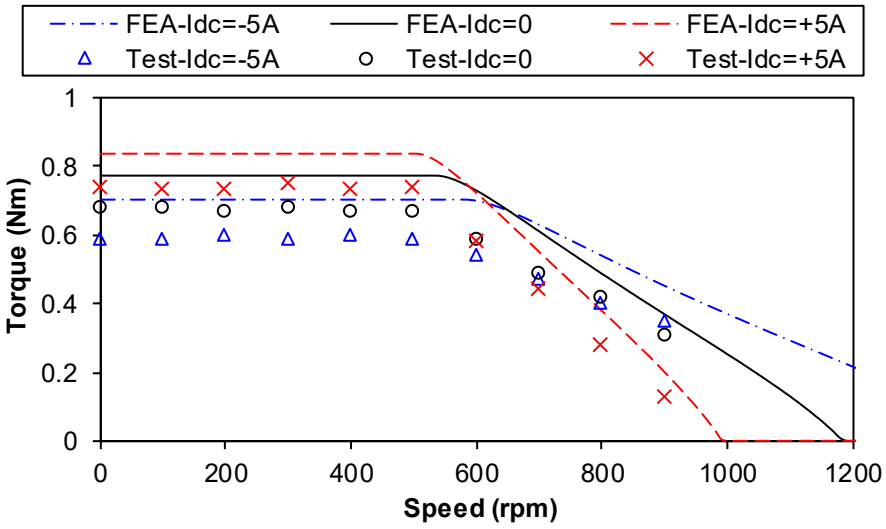

Fig. 4.32. Measured and FE predicted torque-speed curves with different DC excitation currents.

Moreover, the efficiency map with/without DC regulations are predicted in Fig. 4.33 firstly. The predicted efficiency map has taken the copper loss and iron loss into consideration. To simplify the measurement, the field, *d*- and *q*-axis currents to achieve the maximum efficiency at specific torque and speed point are calculated based on the FE simulation. By employing the field, *d*- and *q*-axis currents, the output and input powers at each point are measured. Furthermore, the efficiency map with/without DC regulations are gained and shown in Fig.

4.34. With the utilization of field excitation, the low-speed high-torque region as well as high-speed operation region are broadened. Nevertheless, the efficiency of broadened region is limited due to additional field winding copper loss. As stated above, the measured torques as well as efficiency are always lower than the FE simulations due to 3D end effect as well as friction loss at low speed operation. The maximum operation efficiency in simulation is 90%, whereas that for the test result is only 88%. The difference between measurement and simulation can be summarized as follows. Firstly, the test accounts for 3D end-effect and flux leakage. Secondly, the friction torque is significant especially for low-torque measurement. Thirdly, the manufacturing and assembling tolerances influence on the output capability, which will be assessed for future work. Although there exists difference between the simulation and test results, the benefit of hybrid excitation can be identified. As expected, the overall efficiency is improved with the regulation of DC excitation especially at low speed high torque region, which is beneficial for starting operation.

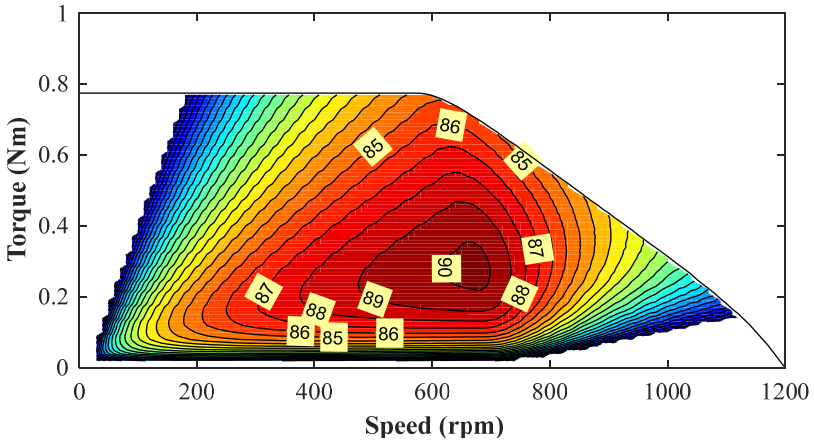

(a) Without DC excitation

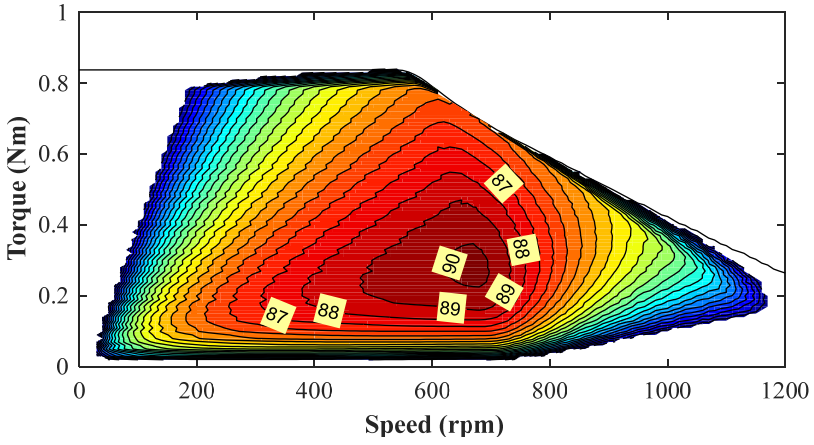

(b) Utilizing optimal DC excitation for maximum efficiency

Fig. 4.33. FE Predicted efficiency map against torque-speed (colored contour indicating efficiency higher than 65%).

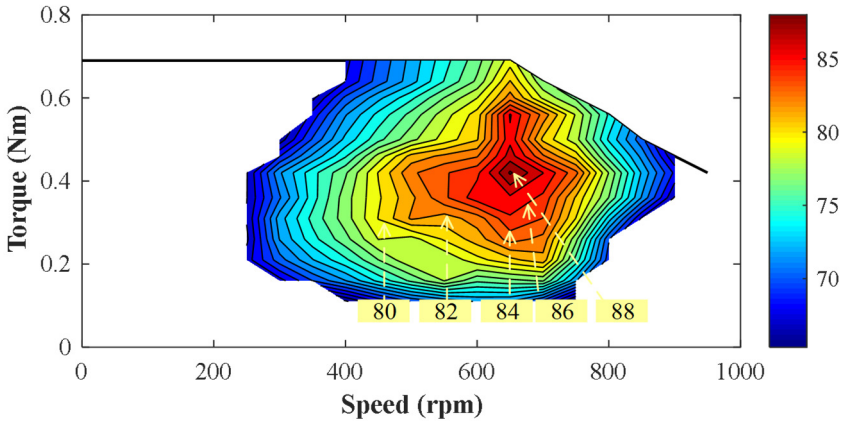

(a) Without DC excitation

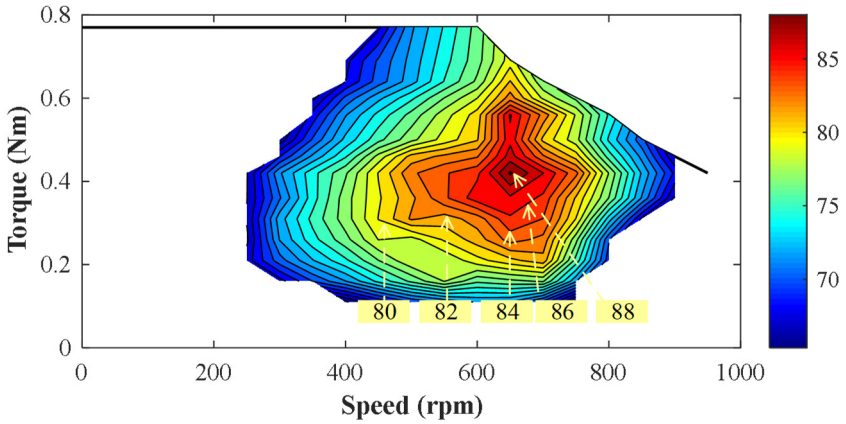

(b) Utilizing optimal DC excitation for maximum efficiency

Fig. 4.34. Measured efficiency map against torque-speed (colored contour indicating efficiency higher than 65%).

4.7 Summary

In this chapter, a novel FSNW HE machine with consequent-pole PM rotor is proposed. The abundant field harmonics in the FSNW, which tend to cause parasitic effects, are utilized to regulate the magnetic field and produce electromagnetic torque through field modulation. The electromagnetic performances are evaluated with FE simulation, and it is revealed that the DC excitation can effectively regulate the air-gap flux density, phase back-EMF, and consequently, electromagnetic torque flexibly. Moreover, the torque density of the proposed

HE machine can be comparable with the SPM machine under positive DC excited flux enhancing, and meanwhile, the PM usage can be saved significantly. Finally, a prototype is fabricated to validate the theoretical analyses and FE simulation. Overall, the test results, including back-EMF, static torque and torque-speed envelope, agree well with the FE analyses.

Chapter 5

Comparative Analysis of Novel Fractional Slot Non-Overlapping Winding Hybrid Excited Machines Having Different Consequent Pole Rotor Topologies

This chapter further investigates novel fractional slot non-overlapping winding hybrid excited (HE) machines with consequent pole permanent magnet (PM) rotors presented in chapter 4. Different consequent pole interior PM rotor configurations are employed to retain the PMs and utilize the flux concentrating effect. The optimal current ratio between the field and armature windings is identified theoretically and the torque improvement ratio by hybrid excitation is demonstrated to show the benefits of hybrid excitation. It is revealed that the machine topologies utilizing flux concentrating effect exhibit higher PM torque but sacrificed flux regulation capability due to magnetic saturation. Moreover, the DC coil free HE machine can be obtained with dual electric port inverter to supply biased AC excitation and solve the spatial confliction of field and armature windings. Finally, the prototypes with different rotor configurations are fabricated and tested to validate the analyses. This chapter is based on a paper presented at ECCE 2019 [CAI19b] and extends the analysis.

5.1 Introduction

Due to rapid development of magnetic materials, power electronics, and micro-processors, permanent magnet (PM) brushless machines have attracted much attention in decades [ZHU07]. The PM synchronous machines are generally classified into stator PM and rotor PM types [ZHU07] [CHE11a]. Various stator PM machine topologies have been investigated in [LIA95] [DEO97] [HOA97] for different location of stator PMs, e.g. doubly salient PM machines, flux reversal PM machines, and switched flux PM machines. However, the stator PM machines mainly suffer from two distinct disadvantages, which have restricted the wide spread for industrial applications. Firstly, the stator is crowded with PMs and armature windings, and the magnetic saturation is severe which limits the overload capability [CAO12a]. Besides, iron loss as well as PM eddy current loss are significant as a result of doubly salient structure and abundant field harmonics, which sacrifices the operation efficiency [ZHU08b]. Therefore, the rotor PM machines are more popular and have been commercialized in electric and hybrid

electric vehicles (EV/HEV), power generation, domestic appliance, marine propulsion, and aerospace [SAT11] [LI08] [REF10] [CAO12b].

Although the utilization of high-energy-product PM is beneficial for high torque density and compact structure, the shortcoming is also obvious due to the fixed PM excitation and difficulty in flux weakening due to high reluctance of PMs [REF05]. Therefore, the hybrid excited (HE) machines are developed to combine the synergies of high torque density of PM machines and flexible flux regulation of wound field (WF) machines [AMA09] [WAN12a].

To achieve hybrid excitation and better flux regulation in the rotor PM machines, numerous rotor PM HE machine topologies have been investigated in decades [ZHU19c]. The HE machines with rotor PMs can be developed by attaching DC coils around PM poles [HEN94a], replacing some PM pole-pairs with DC pole-pairs [LUO00], or combining PM rotor and WF rotor axially [SYV95]. However, brushes and slip rings are required to feed the DC excitation to the rotary part, which degrades the system reliability and increases the maintenance cost. To eliminate the brushes and slip rings, HE machines based on brushless wound rotor synchronous machine are proposed in [ALI16] and [HUS18]. Nevertheless, additional harmonic winding is required to feed the excitation to the field winding, and therefore, the rotor is crowded with PM, harmonic and field windings. Besides, extra techniques are required to produce the current in the harmonic winding, e.g. third harmonic current injection [YAO15], unequal turns of armature coil [HUS17], etc., making the system complicated. Another hybridization method is to introduce a toroidal field winding and produce an axial flux for DC excitation. In [FRE87] and [VID05a] [ZHA08], HE machines with a toroidal field winding are proposed for consequent pole PM machine and spoke-type IPM machine, respectively. Nevertheless, 3D magnetic fields make manufacturing and assembling complex, and soft magnetic composites (SMC) material is usually required to allow for axial DC flux.

In this chapter, novel HE machines with fractional slot non-overlapping winding and different consequent pole PM rotors are investigated, as shown in Fig. 5.1. The stator accommodates field and armature coils, and consequently, brushes and slip rings can be eliminated. The consequent pole PM rotor topology can be extended to various interior PM (IPM) configurations to retain the magnets, and even achieve flux concentrating, like the conventional IPM machines [LEE13], as shown in Figs. 5.1 (a)-(f). Different from the HE machines presented in [WAN18] [QU19] with salient and unequal length stator teeth, the proposed HE machines possess evenly distributed stator teeth and less field harmonics. It can

be observed that the proposed HE machines have a similar topology with the conventional consequent-pole PM machine [CHU16] [LI18], but the introduction of field winding facilitates flexible magnetic field regulation, making it more promising for variable speed applications.

This chapter is organized as follows. In section 5.2, the machine topologies and flux regulation mechanism are presented. Then in section 5.3, the optimal current ratio between the DC and AC excitations and the torque improvement with optimal current ratio are derived theoretically. Moreover, the electromagnetic performances of the HE machines are comparatively analyzed with finite element (FE) simulations in section 5.4. Furthermore, the DC coil free HE machines with dual electric port inverter are further developed to eliminate the field winding in section 5.5. Finally, in section 5.6, prototypes with various rotors are fabricated and experiments are carried out to verify the above analyses.

5.2 Machine Topology and Operation Principle

5.2.1 Machine Topology

The investigated fractional slot non-overlapping winding HE machine configurations are shown in Fig. 5.1. The stator accommodates the field winding and the armature winding alternatively, and the rotor is equipped with PMs. The field winding is in stator slots, with adjacent conductors of opposite polarities. The armature winding connection diagram of fractional slot non-overlapping winding can be found in [BIA06b]. All the PMs are magnetized with the same direction and the consequent-pole PM rotor is employed. Correspondingly, the proposed HE machines with inset-PM, interior PM (IPM), double layer IPM (2IPM), V-shaped IPM (VIPM), U-shaped IPM (UIPM), and spoke-type IPM rotors are illustrated in Figs. 5.1 (a)-(f), respectively.

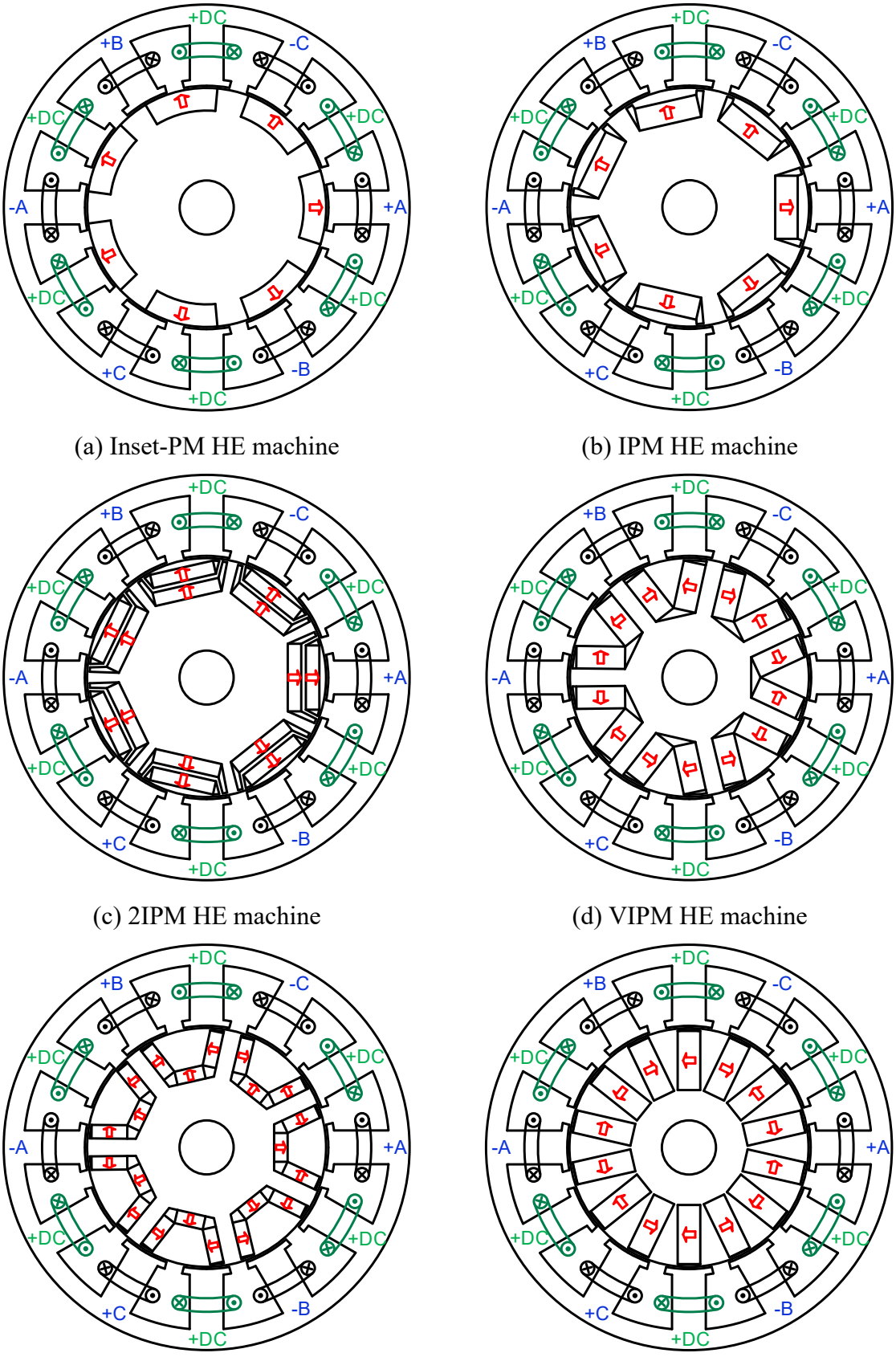

(a) Inset-PM HE machine

(b) IPM HE machine

(c) 2IPM HE machine

(d) VIPM HE machine

(e) UIPM HE machine

(f) Spoke-IPM HE machine

Fig. 5.1. Novel fractional slot non-overlapping winding HE machines with consequent pole rotor.

5.2.2 Operation Principle

The operation principle of the HE machine has been investigated in chapter 4 from the perspective of interaction between PM and DC excited magnetic fields with the armature winding function. To demonstrate the flux regulation mechanism of DC excitation and to further illustrate the difference between different rotor configurations in Fig. 5.1, the flux paths of the proposed Inset-PM HE machine with PM and WF excitations are illustrated in Figs. 5.2 (a) and (b), respectively. To simplify the analysis, only single armature coil is drawn to show open-circuit linked flux and the rotor is aligned at the position of maximum coil flux linkage. The PM flux path circulates from the PM pole to the rotor iron pole for the consequent-pole machine. Meanwhile, the flux lines of DC excitation pass from the one rotor iron pole to adjacent iron pole, since the reluctance of iron is smaller than the PM. Subsequently, the DC excitation can regulate the flux linkage, with both flux-enhancing and flux-weakening capability.

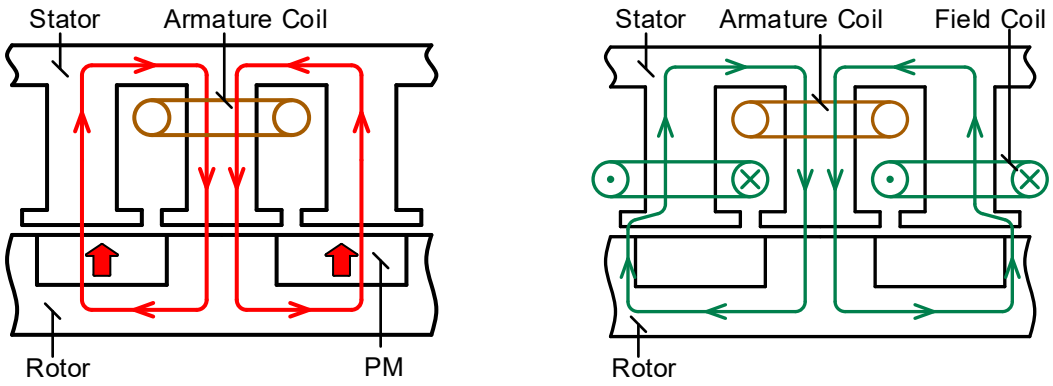

(a) PM flux (b) WF flux

Fig. 5.2. Linear illustration of open-circuit flux paths at the rotor position of maximum coil flux linkage (Inset-PM HE machine as an example).

As the rotor moves by one rotor pole pitch, the PM flux alternates by one period. Meanwhile, the reluctance of rotor changes once and the DC linked flux varies by one period as the same. To achieve PM flux as well as WF flux varying one period when the rotor moves from one iron pole to the adjacent one, consequent pole PM rotor is required. The relationship between the mechanical position and the electrical position can be defined by

$$\theta_e = p_r \theta_m \tag{5.1}$$

where p_r is the number of rotor pole pairs.

The normalized open-circuit phase flux linkages with different excitations are illustrated in Fig. 5.3. Both the PM and DC flux linkages alter by one period as the rotor moves by one rotor pole pitch, verifying the theoretical analysis. The phase flux linkage can be enlarged with positive DC excitation and weakened by negative DC excitation, without even order harmonics. Nevertheless, the DC flux linkage at flux-enhancing is limited due to magnetic saturation. With the increase of DC excitation, the armature coil flux linkage even tends to reduce, as shown in Fig. 5.4. Under heavy magnetic saturation, the field winding excited flux hardly increases with the current, whereas the PM excited flux reduces due to increased reluctance, which is denoted as 'over-saturated effect' in the HE machine [ZHA11].

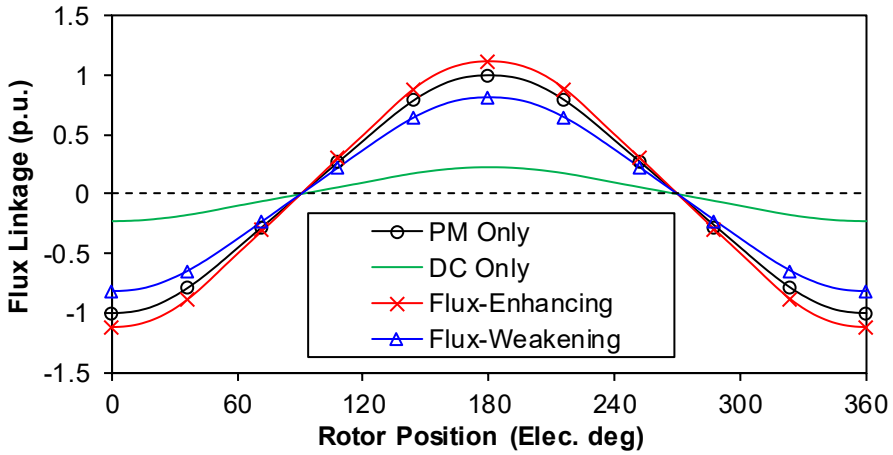

(a) Waveforms

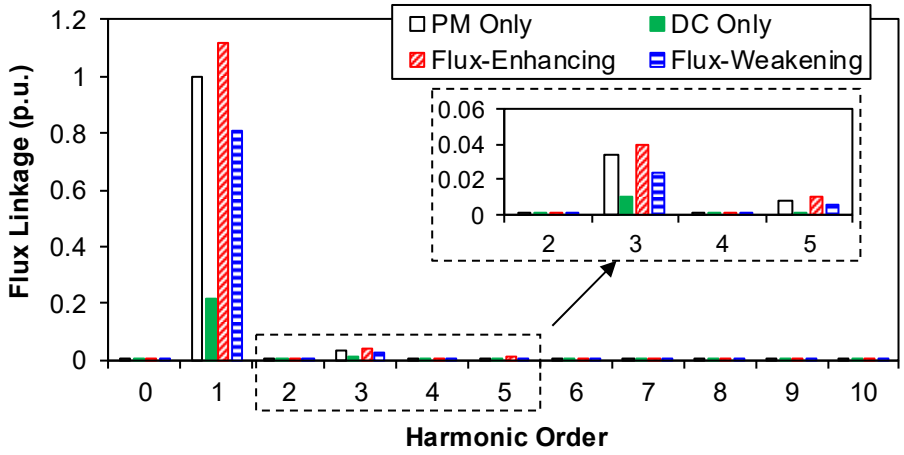

(b) Spectra

Fig. 5.3. Normalized open-circuit phase flux linkages for the HE machine with different excitations (Inset-PM rotor as an example).

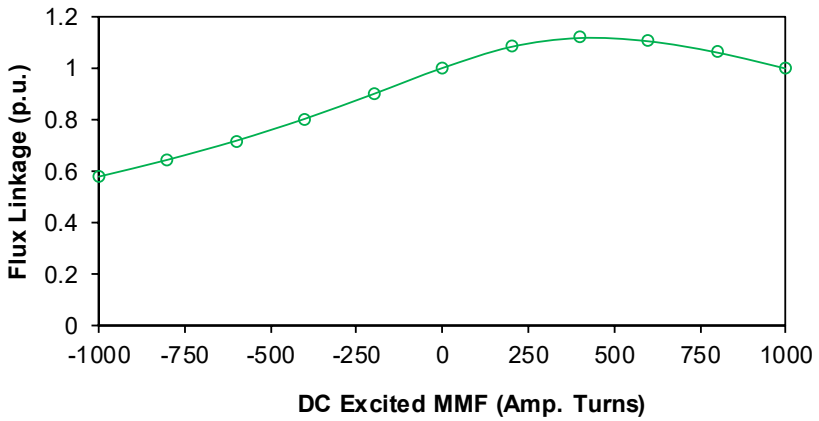

Fig. 5.4. Normalized open-circuit fundamental phase flux linkage versus DC excited MMF for the HE machine with different excitations (Inset-PM rotor as an example).

The flux paths of HE machines with IPM, 2IPM, VIPM, and UIPM rotors in Fig. 5.1 are similar, and the IPM-HE machine is taken as an example in Fig. 5.5 (a). Therefore, the flux regulation mechanism and operating principle discussed above are still valid for these HE machines. However, the flux paths of spoke-IPM HE machine is different, as illustrated in Fig. 5.5 (b). The flux lines of DC excitation are blocked by the spoke-type PMs. Since the permeance of PM is similar with air, the reluctance of DC excitation flux path hardly changes as the rotor moves. Therefore, the flux regulation capability of DC excitation is limited compared with the other counterparts, and the spoke-IPM HE machine will not be discussed.

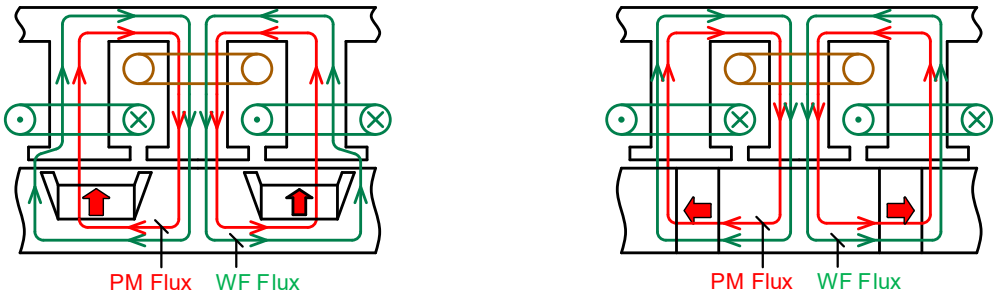

(a) IPM HE machine (b) Spoke-PM HE machine

Fig. 5.5. Open-circuit flux paths of PM and DC excitations at the rotor position of maximum coil flux linkage under positive DC flux-enhancing.

5.3 Torque Improvement with Hybrid Excitation

For the rotor consequent-pole PM machine with fractional slot non-overlapping winding, the reluctance torque is negligible and i_d=0 control is preferred according to the discussion in chapter 4. Therefore, the average torque with i_d=0 control can be expressed in (5.2), where ψ_{PM} is the PM flux linkage, M_{df} is the mutual inductance between the field winding and the d-axis,

i_{dc} and i_q are the field current and the q-axis current, respectively. To simplify the analysis, the number of turns and dimensions for the armature coil as well as the field coil are kept the same. Subsequently, the resistances of field coil and armature coil are identical, and the copper loss can be expressed in (5.3), where R_p is the phase resistance of armature winding and the ratio between the armature current RMS and the field current is defined as (5.4).

$$T_{ave} = \frac{3}{2} p_r \left(\psi_d i_q - \psi_q i_d \right) = \frac{3}{2} p_r \left(\psi_{PM} + M_{df} i_f \right) i_q \tag{5.2}$$

$$p_{Cu} = 3 i_{dc}{}^2 R_p + \frac{3}{2} i_q{}^2 R_p \tag{5.3}$$

$$k_f = \frac{\sqrt{2} i_{dc}}{i_q} \tag{5.4}$$

With fixed copper loss in (5.3), the optimal current ratio to achieve the maximum average torque can be solved by (5.5). The optimal current ratio is shown in (5.6), where k_h is defined as the hybridization factor and I_m is the maximum phase current as shown in (5.7). Correspondingly, the torque improvement ratio γ_T, with optimal current ratio compared with AC excitation only under the same copper loss and thermal condition can be expressed in (5.8). It can be concluded from (5.5) – (5.8) that the optimal current ratio and torque improvement ratio are only determined by the hybridization factor k_h if the PM flux linkage and inductances are constant.

$$\left. \frac{\partial T_{ave}}{\partial k_f} \right|_{p_{Cu}=Const} = 0 \tag{5.5}$$

$$k_{f(opt)} = \begin{cases} \sqrt{\dfrac{k_h{}^2 + 1 - \sqrt{4k_h{}^2 + 1}}{k_h{}^2 - 2}}, k_h \neq \sqrt{2} \\ \dfrac{1}{\sqrt{3}}, k_h = \sqrt{2} \end{cases} \tag{5.6}$$

$$k_h = \frac{M_{df} I_m}{\psi_{PM}}, I_m = \sqrt{\frac{2 p_{Cu}}{3 R_s}} \tag{5.7}$$

$$\gamma_T = \frac{T_{ave}(k_f = k_{f(opt)}) - T_{ave}(k_f = 0)}{T_{ave}(k_f = 0)} \tag{5.8}$$

According to (5.6) and (5.8), the variations of optimal current ratio and torque improvement ratio with hybridization factor k_h are shown in Fig. 5.6. For the PM synchronous machine, the hybridization factor k_h=0, and consequently, both the optimal current ratio and torque improvement ratio are 0. For the WF synchronous machine, the hybridization factor is infinite,

and the optimal current ratio is 1 according to (5.6), in consistent with [CHE10]. Theoretically, the optimal current ratio and the torque improvement ratio increase with the hybridization factor. Consequently, it is beneficial to employ hybrid excitation with a relatively large hybridization factor, e.g. low PM flux linkage or high current. Moreover, the PM torque is dominant when the hybridization factor $k_h<\sqrt{6}$, and the DC component can be regarded as assisted field regulation. Otherwise the DC torque outweighs the PM torque and the machine can be perceived as PM assisted WF machine.

It should be noted that the PM flux linkage and inductances are perceived as constant during the above derivation. In fact, the machine parameters vary when considering magnetic saturation and cross-coupling effect [STU03]. However, the hybridization factor can still be utilized to calculate the initial current ratio between the AC and DC excitations and identify the benefit of hybrid excitation considering torque improvement.

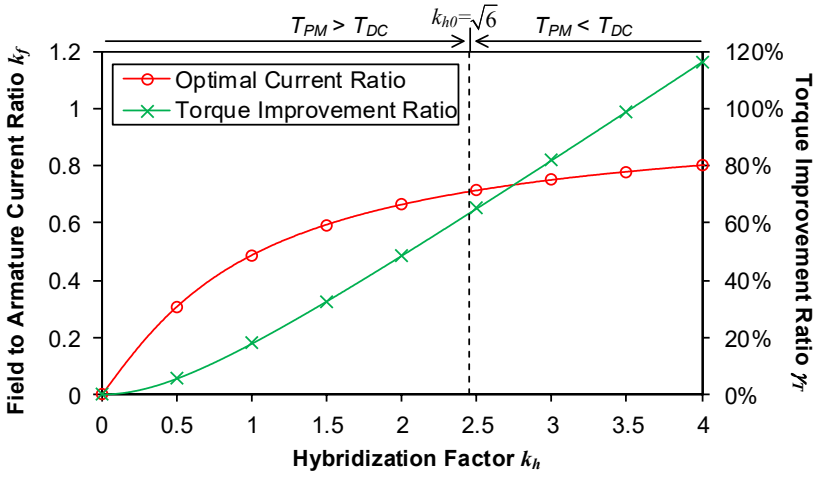

Fig. 5.6. Variation of optimal current ratio between DC and AC excitations and torque improvement ratio with hybridization factor (under fixed copper loss of field and armature winding).

5.4 Comparison of Electromagnetic Performance

5.4.1 Design and Optimization

In this section, the above HE machines with different rotor configurations are compared comprehensively. Firstly, the parametric model is established in a commercialized FE software, in which the machine geometric parameters can be adjusted flexibly. Afterwards, the parametric sensitivity analysis about the key design parameter is carried out individually to obtain the maximum output capability. Then the genetic algorithm base global optimization is

utilized for maximizing the average torque output with the fixed copper losses in armature windings under flux-enhancing operation, with which both the torque output and the flux regulation range (the contribution of field current on back-EMF) can be considered.

The machine dimension is constrained as 45mm outer radius and 25mm active axial length. Moreover, the fixed 20W copper loss in armature windings is applied, in which the applied phase current will change with the variation of the slot area. If the slot area is increased, the available area for winding is boosted and hence the phase current could be higher for the fixed copper loss. The *d*-axis current is kept at zero. In addition, the fixed 5A/mm^2 current density is injected to field coil slots to realize flux-enhancing operation

Global optimization is conducted with the flowchart shown in Fig. 5.7, with genetic algorithm (GA) coupled FE embedded in the commercial software Ansys Maxwell. After global optimization, the main parameters of the HE machines are listed in Table 5.1. Obviously, the 2IPM, VIPM, and UIPM-HE machines consume higher PM usage owing to more pieces of magnets. The winding turns are chosen for a fixed slot filling factor for the four HE machines.

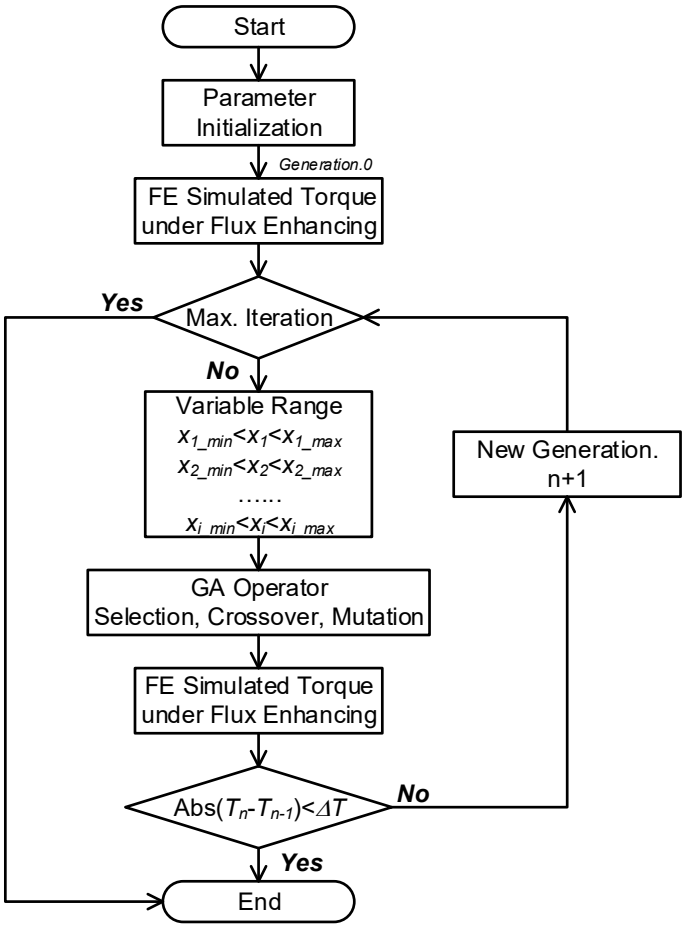

Fig. 5.7. Flowchart of GA coupled FE multi-parameter global optimization.

Table 5.1 Main parameters of HE machines with different rotors after optimization

Parameter	Inset-PM	IPM	2IPM	VIPM	UIPM
Stator slot number	12				
Rotor pole-pairs	7				
Stator outer diameter (mm)	90				
Stack length (mm)	25				
Air-gap length (mm)	0.5				
PM remanence (T)	1.1				
PM coercivity (Ka/m)	830				
PM thickness (mm)	2				
Split ratio	0.6	0.64	0.64	0.63	0.63
Stator yoke thickness (mm)	4.5	4.1	3.9	4.2	4.3
Stator tooth width (mm)	7.5	7	6.8	7.5	7.6
PM length (mm)	N/A	15.3	13.5 13.1	11.4	8.9 5.4 8.9
PM buried depth (mm)	N/A	1.6	1.6 4.6	N/A	
Angle between PMs (º)	N/A			70	40
Iron bridge thickness (mm)	N/A	0.5			
Area per slot (mm^2)	127	123	128	120	118
Turns per phase	120	116	120	114	112
Turns of field winding	360	348	360	342	336
PM volume (mm^3)	5513	5355	9310	7980	8120

5.4.2 Back-EMF

The open-circuit back-EMFs of the five HE machines without DC excitation are compared in Fig. 5.8. The UIPM- and VIPM-HE machines exhibit higher back-EMF fundamental due to the flux concentrating effect, although the PM usage is more than that of Inset-PM and IPM HE machines. Meanwhile, the IPM-HE machine possesses the lowest fundamental EMF due to flux leakage in the iron bridge. The main phase back-EMF harmonic in Inset-PM, VIPM, and UIPM-HE machines is the 3rd order, and it can be eliminated in the line back-EMF with star connection.

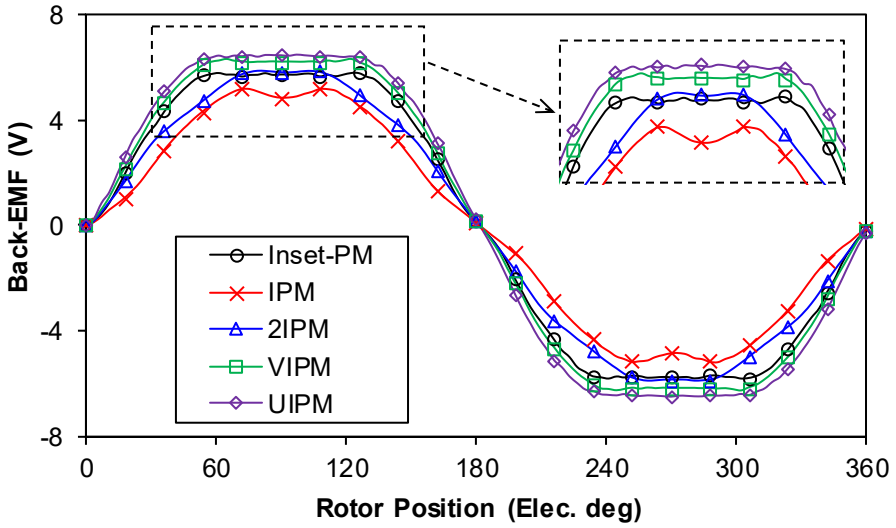

(a) Waveforms

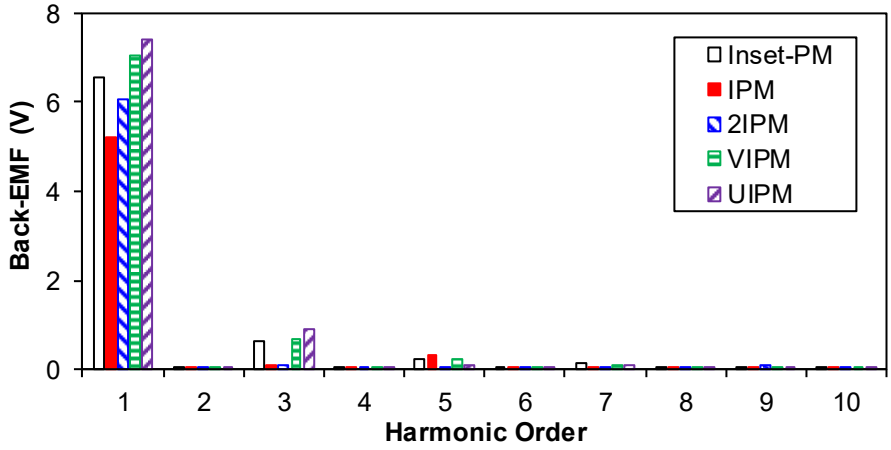

(b) Spectra

Fig. 5.8. Open-circuit phase back-EMFs at the rotor speed of 400rpm without DC excitation.

Flux regulation capability is an essential characteristic of HE machine, which reflects the effect of field excitation on the magnetic field. Fig. 5.9 shows the open-circuit phase back-EMF fundamental against DC excitation current density. Without DC excitation, the back-EMF fundamental of UIPM-HE machine is the highest due to the flux concentrating effect. However, the back-EMF tends to reduce with DC excitation after the knee point. The knee point DC excitation current of VIPM and UIPM-HE machines are relatively low, indicating the magnetic saturation is severe.

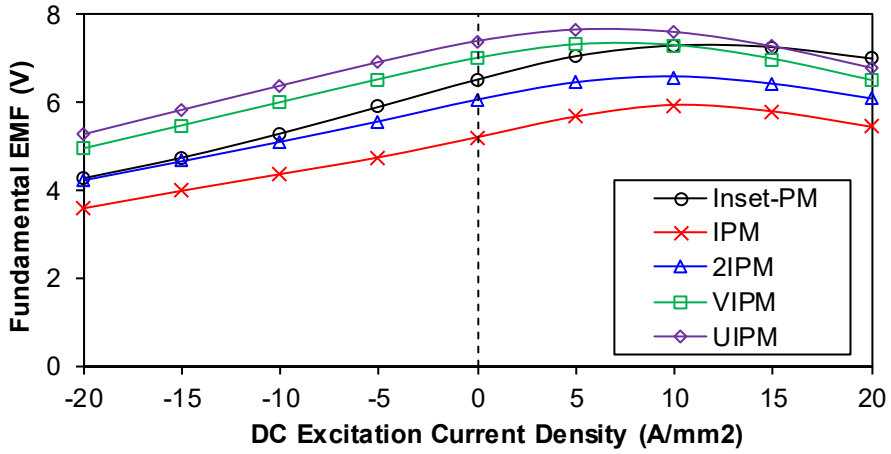

Fig. 5.9. Open-circuit phase back-EMF fundamental versus DC excitation current at the rotor speed of 400rpm.

To evaluate the flux regulation potential, the back-EMF regulation ratio is defined as (5.9), and the regulation ratio against DC excitation current is shown in Fig. 5.10. Obviously, the flux enhancing capability is limited due to magnetic saturation, regardless of rotor configurations. With negative DC excitation, the flux regulation of Inset-PM HE machine is the best, and the others are similar. With positive DC excitation, the flux regulation ratio tends to reduce after the knee point due to magnetic saturation, in accordance with the flux linkage variation in Fig. 5.4.

$$\gamma_{DC} = \frac{e_{PM\pm DC} - e_{PM}}{e_{PM}} \tag{5.9}$$

When the stator and rotor cores of HE machine are designed to operate around the knee point of B-H curve with PM excitation only, magnetic saturation becomes severe with DC excited flux enhancing. However, when the stator and rotor cores are designed to operate far below the knee point of B-H curve with PM excitation only, the materials are not fully utilized, although flux regulation of DC excitation can be increased. Therefore, the optimization of HE

machine should be conducted with the consideration of DC excitation range, as the trade-off between PM excited output capability and DC excited flux regulation capability.

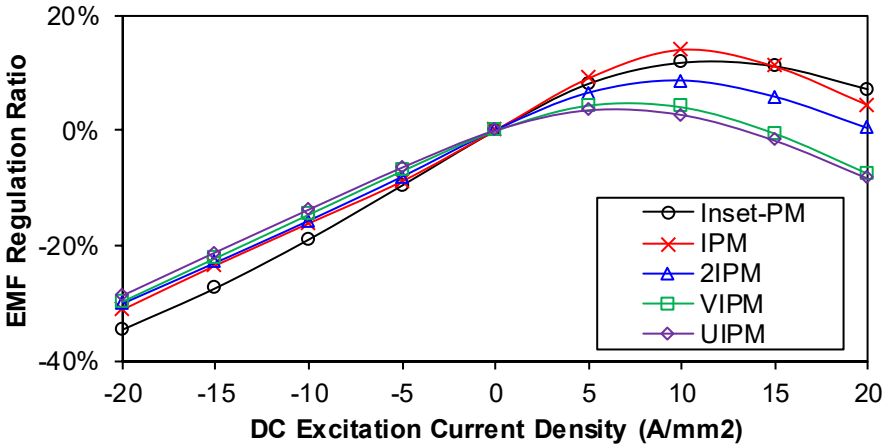

Fig. 5.10. Open-circuit phase back-EMF regulation ratio versus DC excitation current at the rotor speed of 400rpm.

5.4.3 Cogging Torque

It has been illustrated in chapter 4 that the periodicity and amplitude of cogging torque in the proposed HE machine is influenced by the field excitation. The cogging torques of the five HE machines with/without DC excitation are compared in Figs. 5. 11 and 5.12, respectively. The Inset-PM HE machine exhibits the highest cogging torque amplitude regardless of DC excitation. In consistent with the analyses in chapter 4, the least cogging torque periodicity without DC excitation is $N_{cogging}$=12 in Fig. 5.11 (b), whereas the least periodicity is 6 with DC excitation in Fig. 5.12 (b). Without DC excitation, the cogging torque of the HE machine originates from the interaction between the rotor PM excitation and the stator slots. When stator field winding is excited, the stator DC excited magnetic field interacts with the rotor PM excited magnetic field, and additional cogging torque component is produced. Subsequently, the cogging torque amplitudes are increased with DC excitation for the five HE machines.

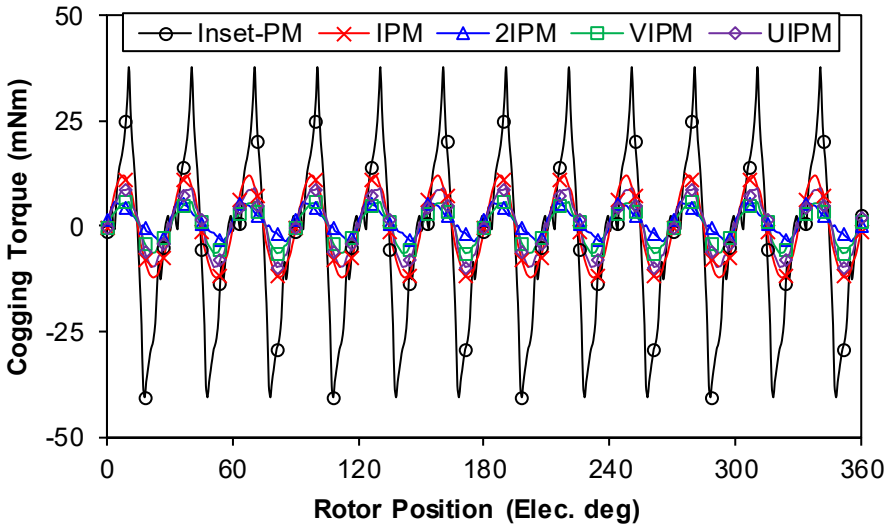

(a) Waveforms

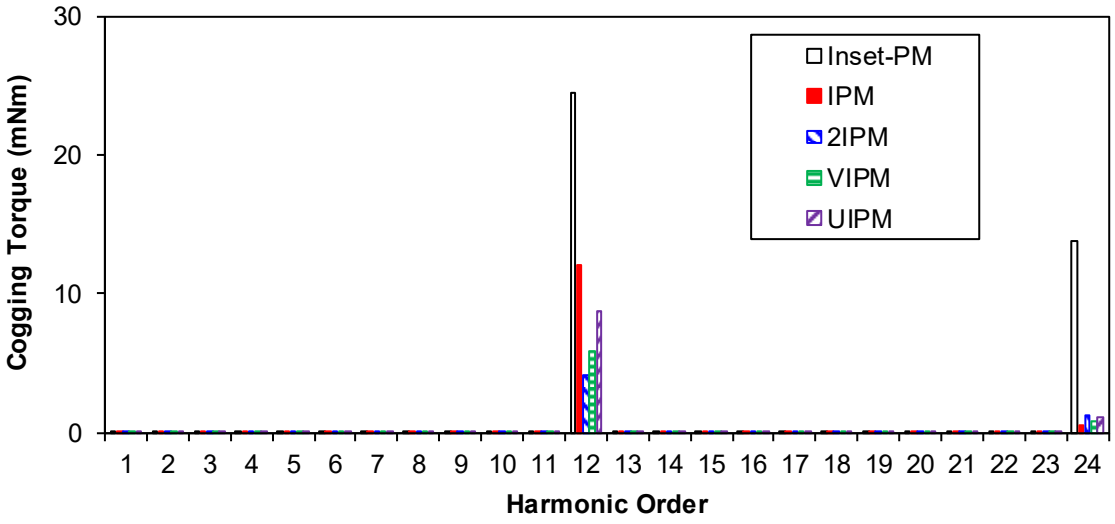

(b) Spectra

Fig. 5.11 Cogging torques without DC excitation.

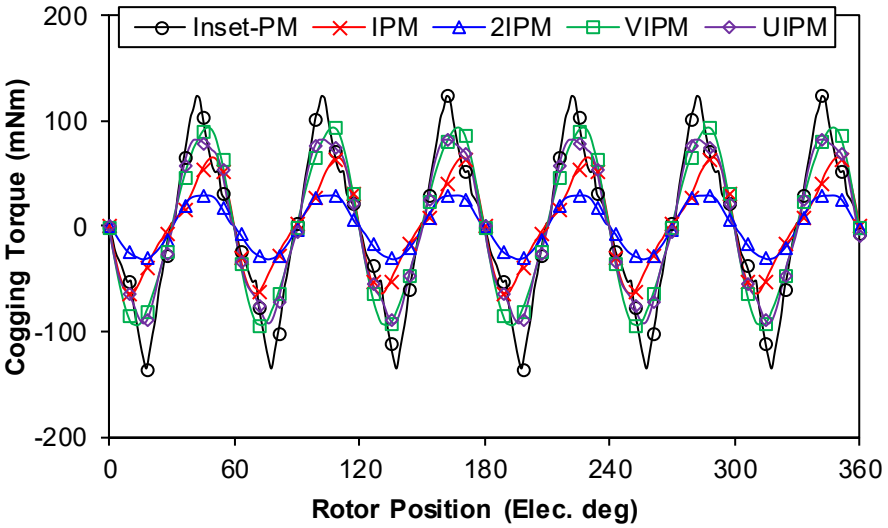

(a) Waveforms

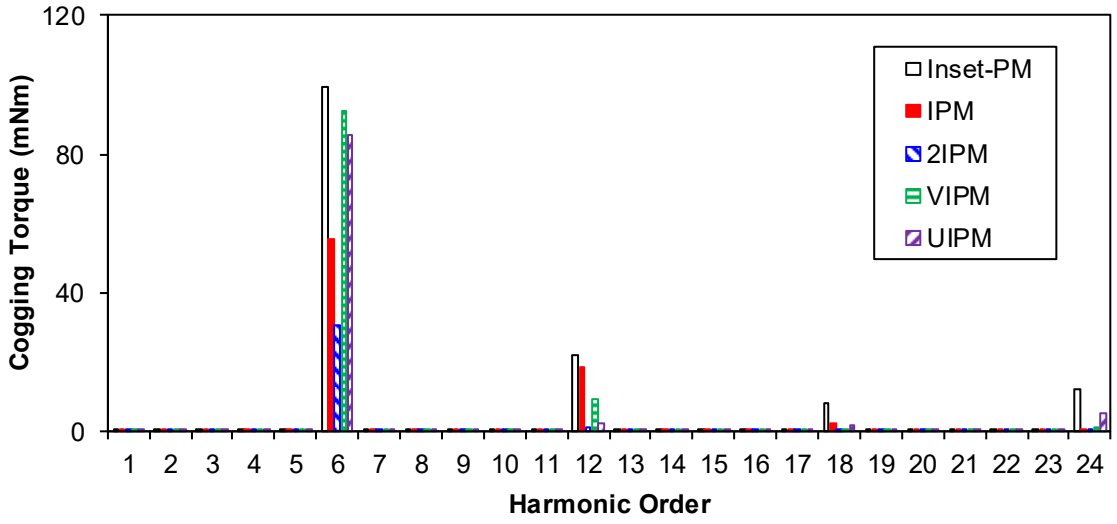

(b) Spectra

Fig. 5.12. Cogging torques with DC excitation of J_{dc}=+10A/mm^2.

5.4.4 Inductance

The variations of *d*- and *q*-axis inductances with corresponding currents of the five HE machines are compared in Fig. 5. 13. With the increase of negative *d*-axis current, the *d*-axis inductance increases slightly and then reduces. This can be explained by the magnetic saturation alleviation of negative *d*-axis current, whereas a large amplitude of flux weakening current causes reversed magnetic saturation. Meanwhile, the *q*-axis current intensifies the magnetic saturation and the inductance reduces with the current. Overall, the *d*- and *q*-axis inductances are similar for all the HE machines, indicating the reluctance torque is negligible.

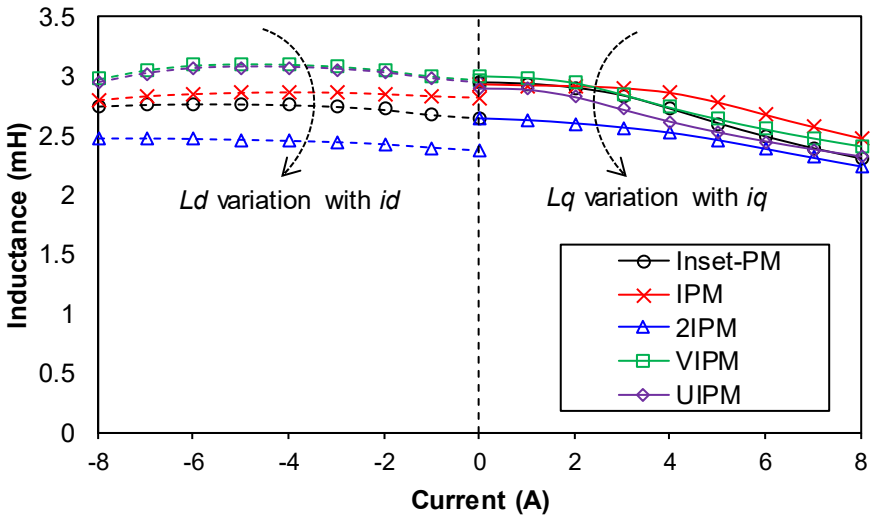

Fig. 5.13. Variation of *d*- and *q*-axis inductances with corresponding currents (without field excitation).

5.4.5 Electromagnetic Torque

The electromagnetic torque waveforms of five HE machines without DC excitation (under i_d=0 control) are compared in Fig. 5.14. The UIPM-HE machine possesses the highest torque, whereas the IPM HE machine has the lowest average torque, in accordance with back-EMF fundamentals in Fig. 5.9. To further illustrate the optimal current angle, the average torque against current angle is shown in Fig. 5.15. The optimal current angle is ~0 for the five HE machines, indicating that the reluctance torque is negligible due to fractional slot concentrated winding and the difference between *d*- and *q*-axis inductances is less obvious.

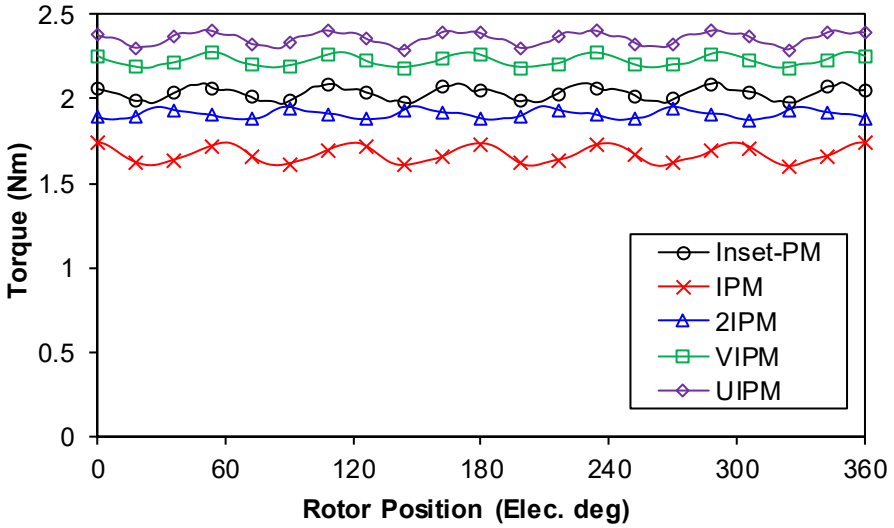

Fig. 5.14. Electromagnetic torque waveforms under armature winding copper loss of 20W (I_d=0) without DC excitation.

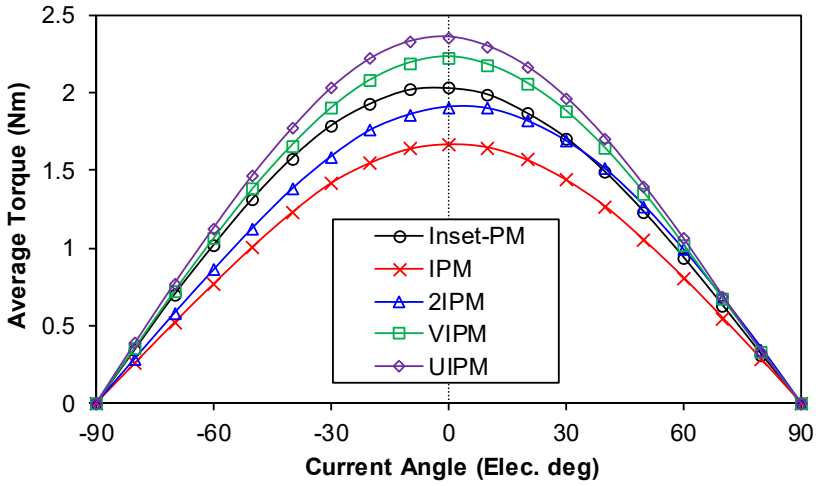

Fig. 5.15. Average torque against current angle under armature winding copper loss of 20W without DC excitation.

Furthermore, the average torques against AC and DC excitations are compared in Fig. 5.16 and Fig. 5.17, respectively. Without DC excitation, the average torque of UIPM-HE machine is the highest whereas the IPM HE machine exhibits the lowest torque. The overload capability of four HE machines and the variation of average torque with armature winding copper loss are similar. Moreover, the DC excitation can regulate the average torque effectively, as shown in Fig. 5.17. In accordance with back-EMF regulation, the flux weakening capability is better than the flux enhancing effect due to magnetic saturation alleviation. The UIPM-HE machine is the easiest to become saturated, and the average torque even reduces with increasing DC excitation current. The maximum current density to evaluate the flux regulation ratio is 20A/mm^2 in Fig. 5.17. This is not the continuous mode, but to evaluate the maximum regulation ratio and saturated field current.

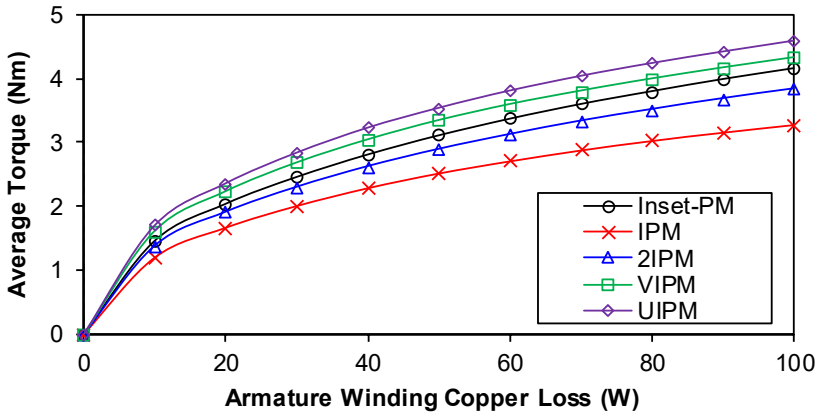

Fig. 5.16. Average torque against armature winding copper loss for the HE machines without DC excitation (i_d=0 control).

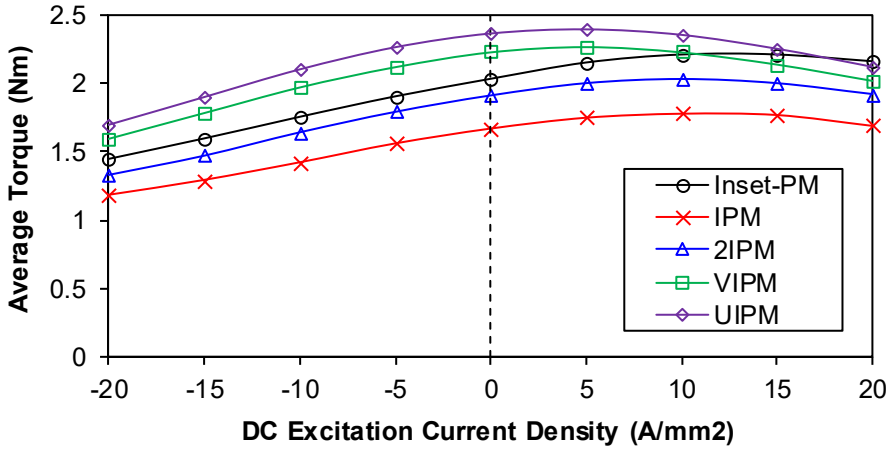

Fig. 5.17. Average torque against DC excitation current density under the armature winding copper loss of 20W (i_d=0 control).

5.4.6 Flux Weakening Capability

A distinct merit of HE machine is the flexible field regulation and wide operation range compared with pure PM machine. The characteristic current is defined in (5.10), which describes the required current to counter the PM and DC excited magnetic field. The maximum phase current should be higher than the characteristic current to achieve infinite flux weakening operation.

$$I_c = \frac{\psi_{PM} \pm \psi_{DC}}{L_d} \tag{5.10}$$

The characteristic currents of the HE machines with different DC excitations are compared in Table 5.2. The IPM-HE machine requires lowest characteristic current due to lowest PM flux linkage, in accordance with Fig. 5.8. Moreover, the characteristic current can be reduced significantly with negative DC excitation, which decreases the power rating of inverter. Therefore, the benefit with the introduction of field winding and hybrid excitation can be observed as better flux weakening capability as well as wider operation range.

Table 5.2 Characteristic currents of five HE machines

	Inset-PM	IPM	2IPM	VIPM	UIPM
Flux-enhancing J_{dc}=+10A/mm^2	9.3A	7.4A	9.9A	8.8A	9.3A
No DC J_{dc}=0	8.3A	6.4A	9.1A	8.4A	9.0A
Flux-weakening J_{dc}=-10A/mm^2	6.7A	5.4A	7.7A	7.2A	7.8A

5.5 Improved DC Coil Free HE Machine

Although the introduction of field winding facilitates the regulation of magnetic field in the HE machine, the stator is crowded with field as well as armature windings in Fig. 5.1. The spatial confliction of DC and AC coils inevitably results in sacrificed torque density compared with pure PM excitation. To improve the space utilization, a dual electric port drive circuit is employed in [ZHU17b] to supply biased AC excitation and integrate the field and armature windings for the variable flux reluctance machine. The biased AC excitation is further extended to the HE machines to eliminate the field windings in [JIA17b] and [WAN19].

The investigated HE machines in Fig. 5.1 can be developed into DC coil free HE machines to further enhance the performances. Figs. 5.18 (a) and (b) show the improved DC coil free HE machines with Inset-PM and IPM rotors as example, and the other HE machines in Fig. 5.1 can be extended as well. The windings are excited by a dual electric port inverter with a single voltage source as shown in Fig. 5.19. Since the neutral point of two sets of windings are connected, DC excitation can flow in the armature winding, and the excitation currents are expressed in (5.11). Compared with the separate field/armature windings in Fig. 5.1, the conducting areas for DC and AC excitations are enlarged with integrated technique. Therefore, the winding resistance is reduced and operating efficiency can be further enhanced.

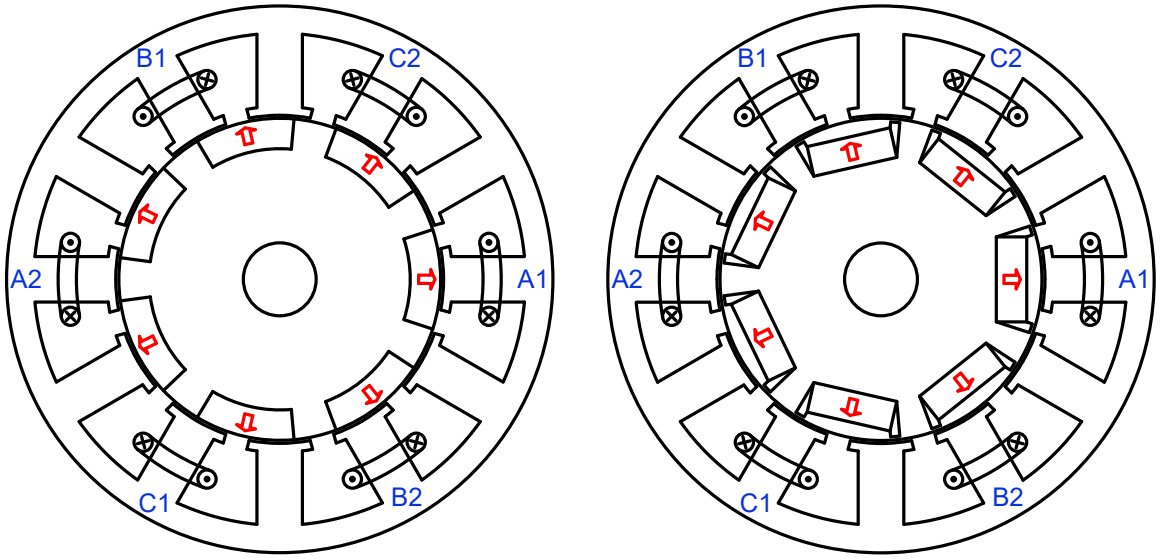

(a) Inset-PM HE machine (b) IPM HE machine

Fig. 5.18. Improved DC coil free HE machine topologies.

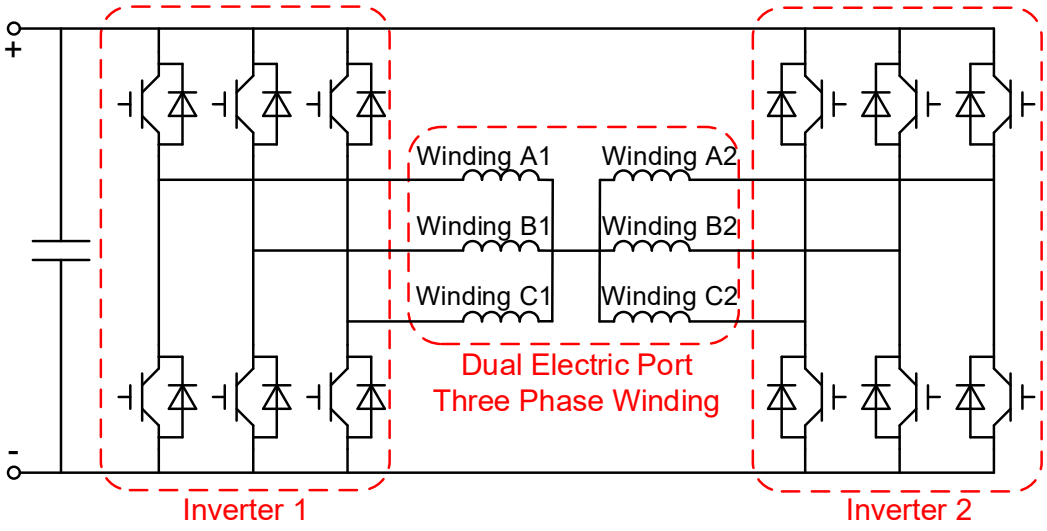

Fig. 5.19. Dual electric port inverter with a single voltage source.

$$\begin{cases} i_{A1} = I_m \cos(\omega t) + I_{DC} \\ i_{A2} = I_m \cos(\omega t) - I_{DC} \\ i_{B1} = I_m \cos\left(\omega t - \frac{2}{3}\pi\right) + I_{DC} \\ i_{B2} = I_m \cos\left(\omega t - \frac{2}{3}\pi\right) - I_{DC} \\ i_{C1} = I_m \cos\left(\omega t + \frac{2}{3}\pi\right) + I_{DC} \\ i_{C2} = I_m \cos\left(\omega t + \frac{2}{3}\pi\right) - I_{DC} \end{cases} \tag{5.11}$$

The variation of average torques with AC and DC excitations for the DC coil free HE machines are illustrated in Fig. 5.20 and Fig. 5.21, respectively. Compared with the average torques of separate winding HE machines in Fig. 5.16 and Fig. 5.17, the torque density as well as torque regulation capability are enhanced in the integrated winding counterparts. This can be accounted for the enlarged conducting areas for the DC and AC excitations. Moreover, the average torque variations with different rotors are similar with the separate winding HE machines. The HE machines utilizing flux concentrating effect, i.e. VIPM- and UIPM-HE machines, exhibits higher torque density, in accordance with the above analysis.

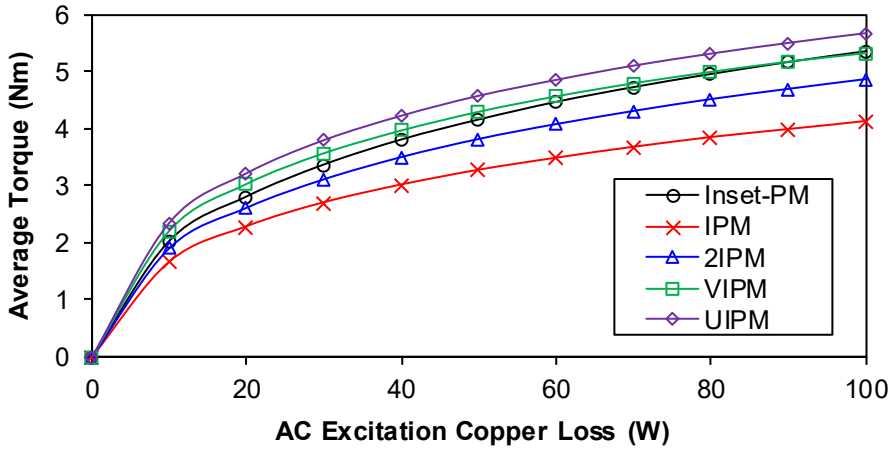

Fig. 5.20. Average torque against AC excitation copper loss for the HE machines without DC excitation (i_d=0 control).

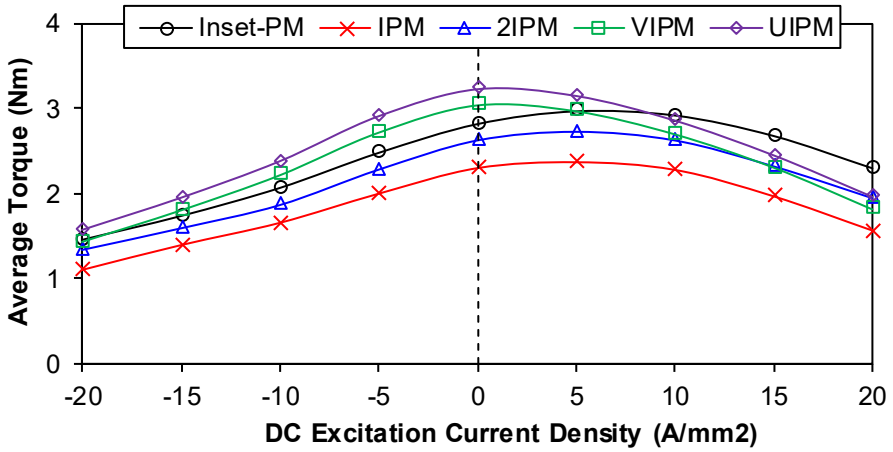

Fig. 5.21. Average torque against DC excitation current density with AC excitation copper loss of 20W (i_d=0 control).

Furthermore, the efficiency maps of the HE machines having different rotor configurations with separate and integrated field/armature windings are compared in Fig. 5.22. Since the winding resistance is reduced in the HE machines with integrated field/armature windings, the copper losses of both DC and AC excitations are reduced and the overall efficiency is enhanced. The maximum efficiency for the separate winding HE machine is ~93%, whereas the maximum efficiency can be increased to 95% with integrated winding technique. Besides, the potentially high efficiency operation region is broadened, which is more beneficial for variable speed applications.

Separate Field/Armatrue Windings

Integrated Field/Armatrue Windings

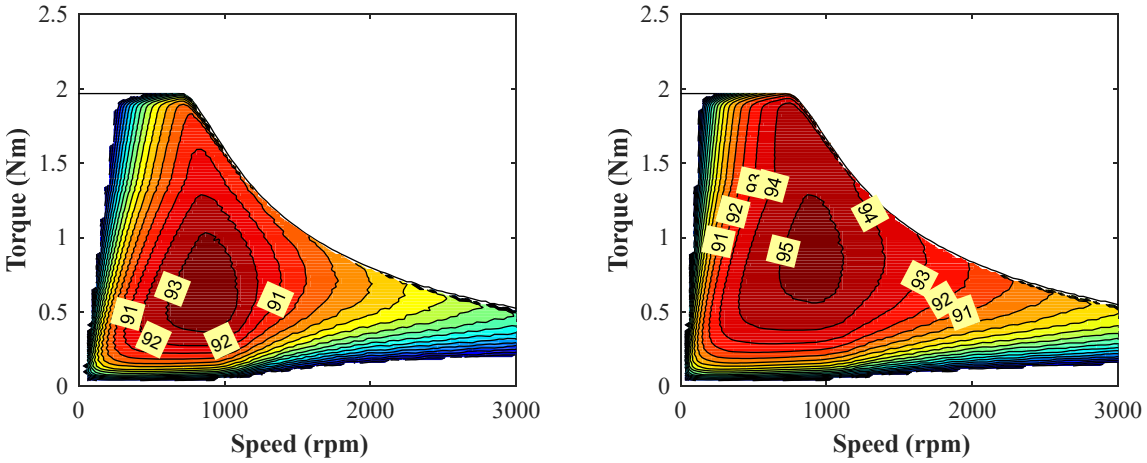

(a) Inset-PM HE machine

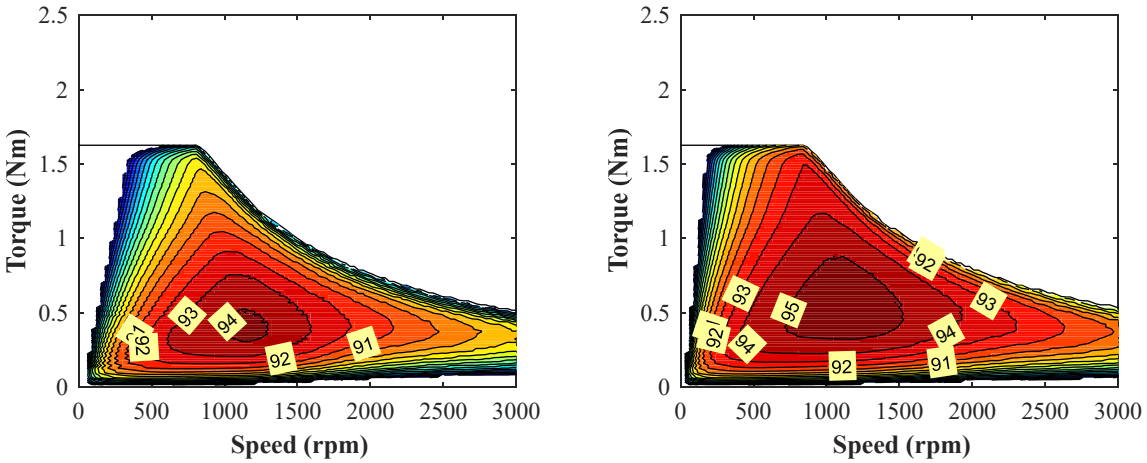

(b) IPM HE machine

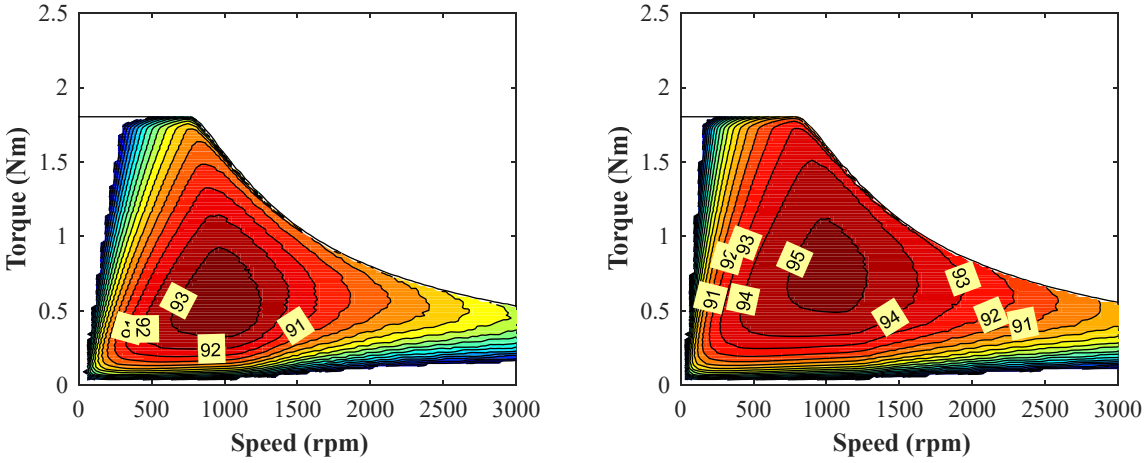

(c) 2IPM HE machine

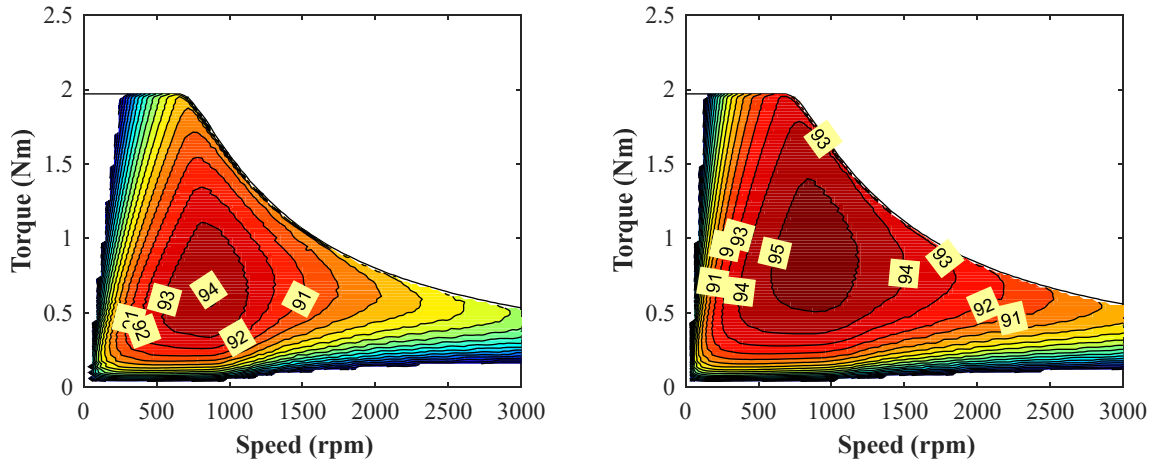

(d) VIPM HE machine

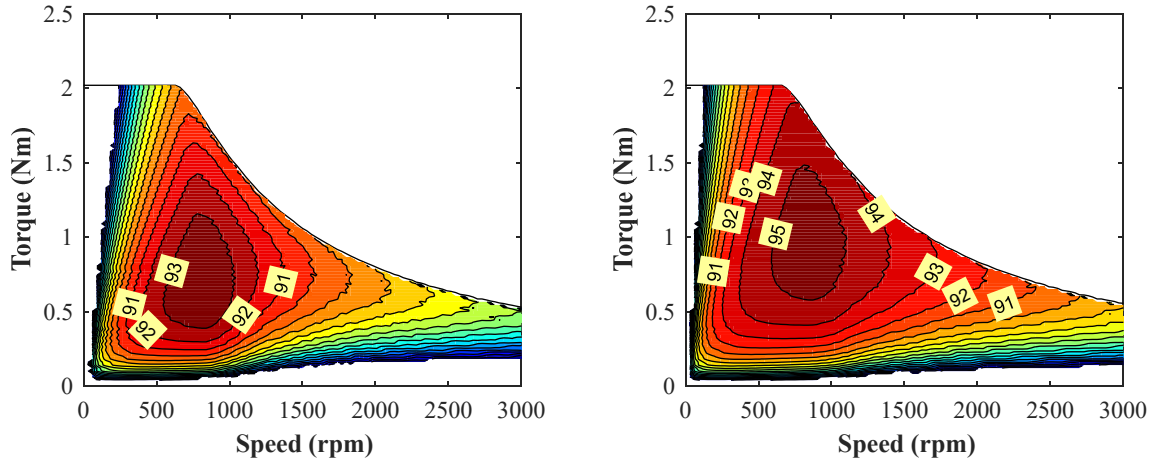

(e) UIPM HE machine

Fig. 5.22. Efficiency map comparison of the HE machines with separate and integrated field/armature windings within the limit of DC bus voltage U_{dc}=24V, maximum AC excitation current amplitude of I_m=8A, maximum DC excitation current of I_{fm}=6A.

5.6 Experimental Validation

To validate the above analyses, the NdFeB HE prototypes with Inset-PM, IPM, 2IPM, and VIPM rotors have been fabricated, as shown in Fig. 5.23. To simplify the manufacturing, all the HE machines share the same stator, and the rotors have been re-optimized. The main parameters of the re-optimized prototypes are listed in Table 5.3. The field winding and armature winding are wound alternately around the stator teeth, as shown in Fig. 5.23 (a). The slot packing factor is reduced to 0.35 in order to ease the winding process. The PM thickness is kept as 2mm, and obviously, the 2IPM- and VIPM-HE machines consume more magnets.

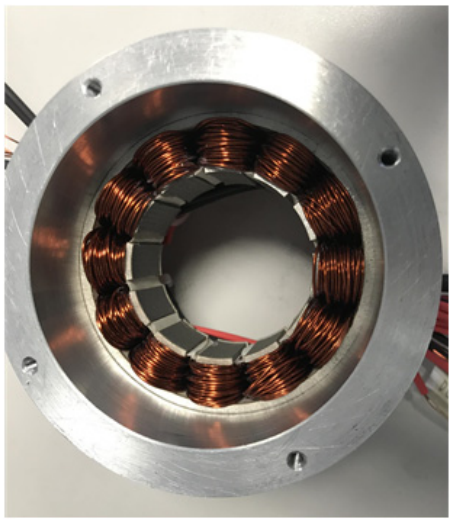

(a) Stator and winding

(b) Inset-PM rotor

(c) IPM rotor

(d) 2IPM rotor

(e) VIPM rotor

(f) UIPM rotor

Fig. 5.23. Photos of prototypes.

Table 5.3 Main parameters of HE prototypes

Parameter	Inset-PM	IPM	2IPM	VIPM	UIPM
Stator slot number	12				
Rotor pole-pairs	7				
Stator outer diameter (mm)	90				
Stack length (mm)	25				
Air-gap length (mm)	0.5				
PM remanence (T)	1.1				
PM coercivity (Ka/m)	830				
PM thickness (mm)	2				
Split ratio	0.6				
Stator yoke thickness (mm)	4.5				
Stator tooth width (mm)	7.5				
Turns per phase	80				
Turns of field winding	240				
PM pole arc ratio	0.65	0.7	0.65 0.8	0.6	0.55
PM length (mm)	N/A	15	14 15	10.4	9.0 4.7 9.0
PM buried depth (mm)	N/A	1.6	1.5 4.5	N/A	9.5
Angle between PMs (º)	N/A			70	40
Iron bridge thickness (mm)	N/A	0.5			
PM volume (mm^3)	5513	5250	10150	7280	7945

The prototypes are driven by a DC machine at constant speed, and the corresponding back-EMF can be measured. The measured and FE predicted open-circuit three phase back-EMF waveforms of the Inset-PM HE machine without DC excitation are compared in Fig. 5.24. Overall, the three phase back-EMF waveforms, both the FE simulated and measured results, are symmetrical. Fig. 5.25 shows the measured and FE predicted open-circuit back-EMF waveforms of different prototypes without DC excitation, in which good agreement can be observed. The back-EMF fundamental against DC excitation current for different HE machines

are compared in Fig. 5.26. The VIPM- and UIPM-HE machines exhibit higher PM excited back-EMFs due to flux concentrating effect, in accordance with the above analysis. However, it becomes magnetic saturated under positive DC excitation, and the back-EMF versus DC current curves becomes non-linear. Overall, the DC excitation can regulate the back-EMF effectively for the four HE prototypes.

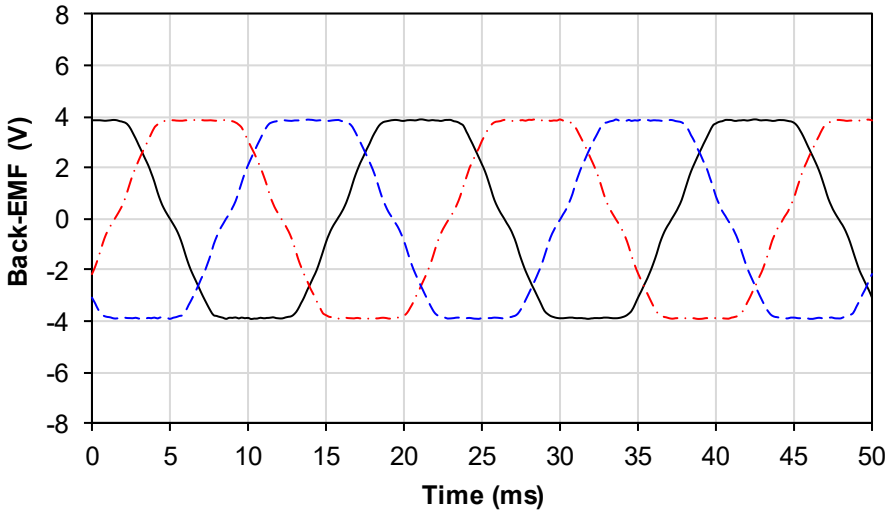

(a) FE simulation

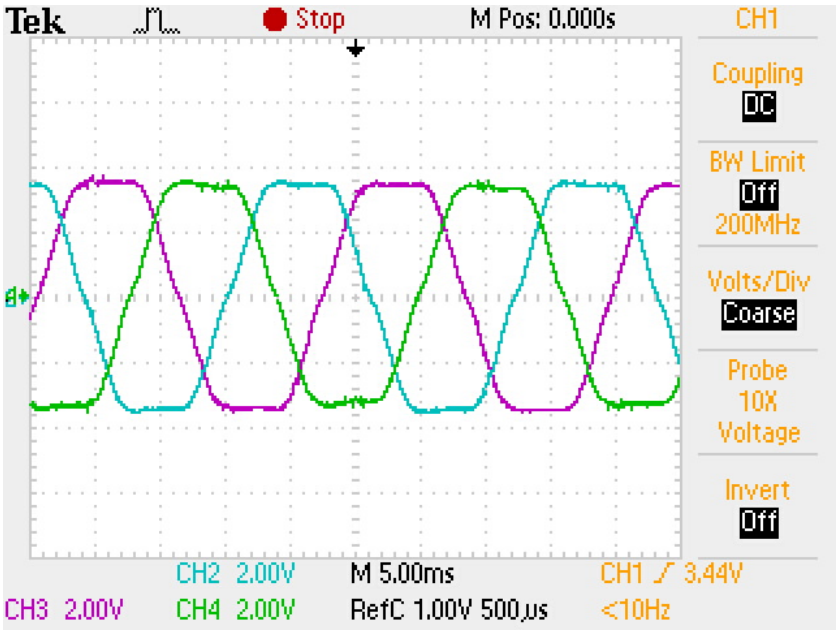

(b) Measured results

Fig. 5.24. Measured and FE predicted open-circuit three phase back-EMF waveforms of Inset-PM HE machine @400rpm without DC excitation.

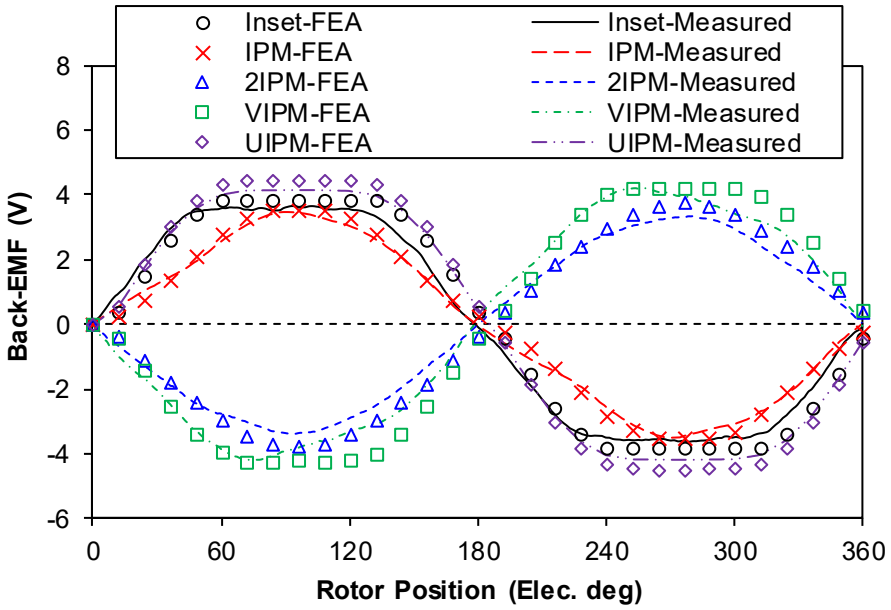

Fig. 5.25. Measured and FE predicted open-circuit phase back-EMF waveforms at the rotor speed of 400rpm without DC excitation.

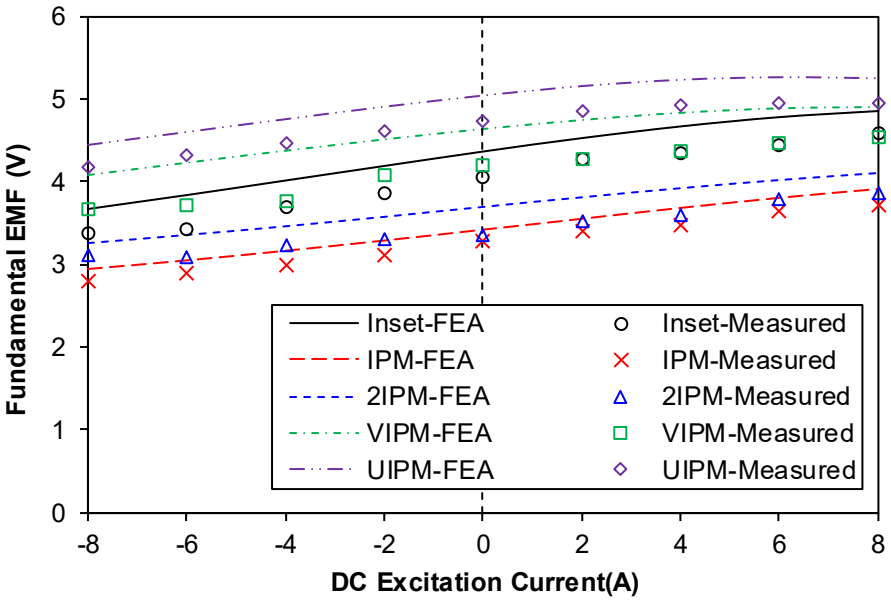

Fig. 5.26. Measured and FE predicted open-circuit phase back-EMF fundamental versus DC excitation current at the rotor speed of 400rpm.

Furthermore, the static torque is measured by supplying three phase currents of i_a=-2i_b=-2i_c. The rotor shaft is connected to an arm and cannot be rotated, which allows for measuring magnetic force. The stator is rotating step by step and enables varying advanced current angle with fixed current excitation. Correspondingly, the static torque can be obtained from the magnetic force on the shaft connected arm.

The measured and FE predicted static torque waveforms without DC excitation are shown in Fig. 5.27, and the torque against DC excitations are compared in Fig. 5.28. Similar with the back-EMF variation, the DC excitation can regulate the output torque with both flux-enhancing and flux-weakening. Besides, the VIPM- and UIPM-HE machines possess higher PM excited torques due to flux focusing, whereas IPM- and 2IPM-HE machines exhibit lower PM torque as the result of flux leakage in the rib. Overall, good agreements between the measured and FE predicted torques are achieved again.

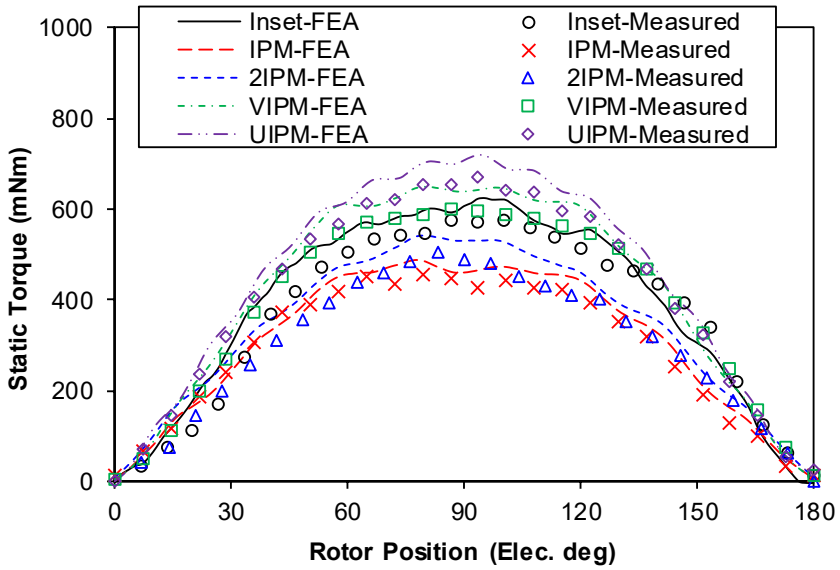

Fig. 5.27. Measured and FE predicted static torque waveforms at the armature current of i_q=4A, i_d=0 without DC excitation.

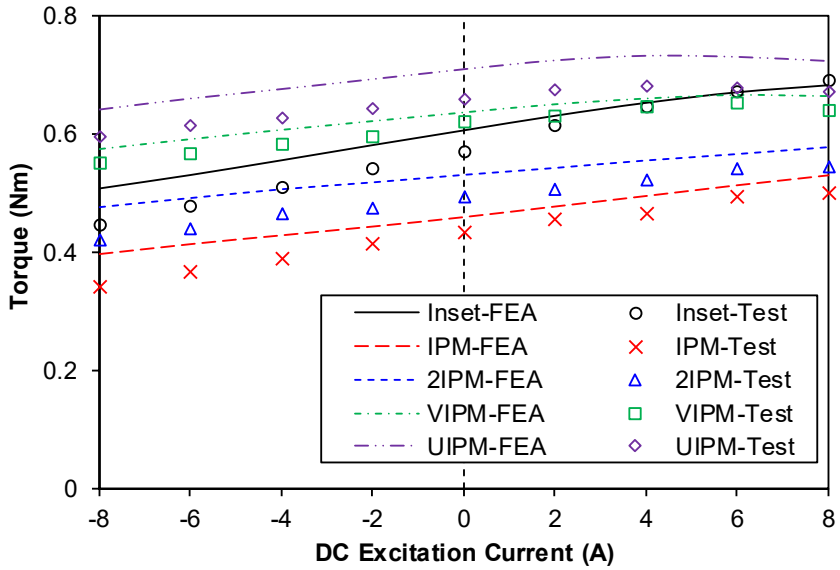

Fig. 5.28. Measured and FE predicted torque versus DC excitation current at the armature current of i_q=4A, i_d=0.

5.7 Summary

In this chapter, novel fractional slot non-overlapping winding HE machines with various consequent pole rotor configurations have been investigated. The proposed HE machines have similar rotor topology with conventional consequent-pole PM machine, which facilitates the manufacturing and assembling. Besides, the introduction of field excitation can help to regulate the magnetic field and is beneficial for variable speed application. Various rotor configurations, e.g. Inset-PM, IPM, 2IPM, VIPM, and UIPM, have been extended to retain the rotor PM and achieve flux concentrating effect.

It is revealed that the VIPM- and UIPM-HE machines utilize flux-concentrating effect and exhibit higher PM torque, albeit with sacrificed flux regulation capability. Since the reluctance torque is negligible in the proposed HE machine, the electromagnetic performance with multi-layer flux barrier IPM design is limited. Moreover, the field winding in the HE machine can be eliminated, and biased AC excited HE machines are further investigated. The torque density, regulation capability as well as operation efficiency can be enhanced as a result of enlarged conducting area and reduced winding resistance. Finally, the prototypes with various rotor configurations are manufactured and tested to verify the FE calculations.

Chapter 6

Comparison of Hybrid Excited Machines with Rotor Interior Permanent Magnet Machine for EV/HEV Application

In chapters 2-5, several novel HE machines are presented in detail, including the operation principle and electromagnetic characteristics. This chapter compares the electromagnetic performances of these proposed HE machines under the same optimization constraint. To demonstrate the feasibility for electric and hybrid electric vehicle (EV/HEV) application, a commercial interior PM (IPM) rotor machine for Toyota Prius 2010 has been selected as the benchmark. The electromagnetic performances, including back-EMF, average torque, torque-speed envelope, efficiency, and fault tolerant capability have been compared comprehensively. This chapter is based on a paper to be presented in PEMD 2020 and extends the analyses.

6.1 Introduction

Due to the increasing transportation demand and fuel energy supply shortage, electric vehicles (Evs) and hybrid electric vehicles (HEVs) have attracted more and more attentions in decades [CHA07] [REF13]. To satisfy the frequently variable speed requirement, numerous researches have been conducted to explore the onboard machine topologies [ZHU07].

Permanent magnet (PM) machines, especially equipped with high energy rare-earth material, possess high torque density, high efficiency, and compact volume. The interior PM machine (IPMM) can utilize reluctance torque and is eminently suitable for flux-weakening operation. To date, commercial products of IPMM have been widely employed in the EV/HEV, i.e. Nissan Leaf, Toyota Prius, and BMW i3 [SAT11] [KAM06] [WIL15]. However, the flux weakening current is demanded to weaken the PM excited magnetic field beyond the base speed, which results in low efficiency and power factor at high speed operation.

Some attempts have been made to overcome the drawback of constant magnetic field in PM machines, and a variety of non-PM machines have been investigated for potential alternatives. It has been revealed that the induction machine (IM) exhibits higher efficiency under high speed operation and better overload capability [BUY14] [FIN08]. Therefore, the IM is more promising for EV/HEV with requirement for rapid starting performance and high

speed operation, and has been commercialized in Tesla Model S. Moreover, the stator wound field (WF) and rotor WF synchronous machines have been optimized in comparison with the commercial IPMM in [CHU14] and [LIU14b], respectively. Although the high cost rare-earth PMs are removed in the WF machines, the peak torque and overall efficiency are sacrificed as well.

Hybrid excitation has been proposed as a trade-off between PM excitation and WF excitation, in which high torque density as well as flexible flux weakening control can be inherited together [TAP03]. It has been revealed in [AMA09] that the overall operation efficiency can be enhanced by combining PM excitation and DC excitation appropriately. More recently, hybrid excited machines (HEMs) with slot circumferentially magnetized PM have been investigated to mitigate the uncontrolled generator fault of conventional PM machines in [ZHU19a]. This classification of machines, including the rotor slot PM [FUK08b] [ISH96] and stator slot PM HE machines [AFI15], exhibit high fault tolerant capability under high speed operation and is potentially promising for EV/HEV.

This chapter compares the electromagnetic performances of various HE machines presented in chapters 2-5, with the commercialized IPMM. The Toyota Prius 2010 IPMM, as shown in Fig. 6.1 (a), has been selected as the benchmark, and comparisons have been conducted based on the same frame size and thermal condition. A stator wound field variable flux reluctance machine (VFRM) and stator slot PM fault tolerant hybrid excited machine (FTHEM) are also optimized for comparison as shown in Figs. 6. 1 (b) and (c), respectively. In section 6.2, the design procedure and optimization constraints are presented to achieve a fair comparison. Then, in section 6.3, the electromagnetic performances of these HE machines, i.e. back-EMF, torque density, flux weakening performance, and efficiency along with the driving circle are compared with the IPMM.

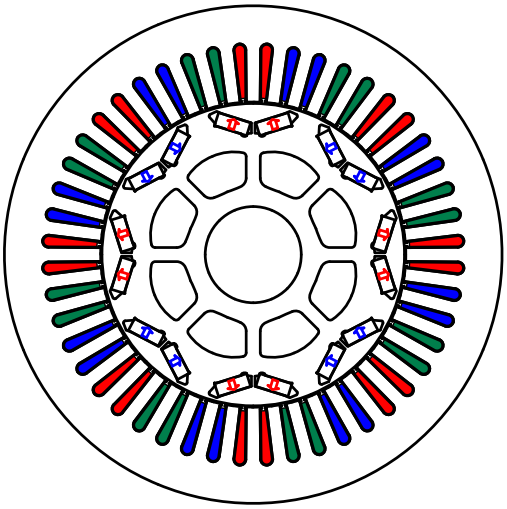

(a) 8p48s Prius 2010 IPMM

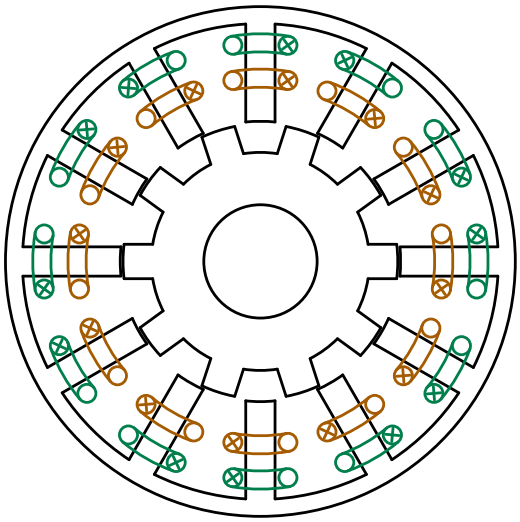

(b) 10r12s VFRM

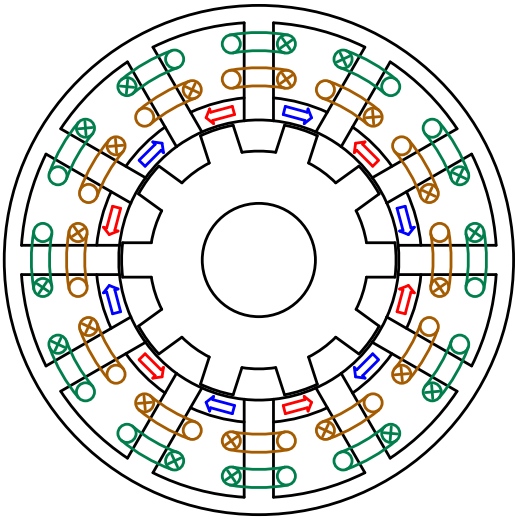

I 10r12s FTHEM

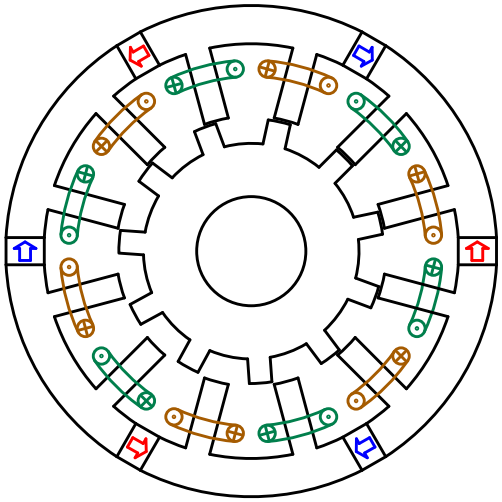

(d) 11r12s PFHEM

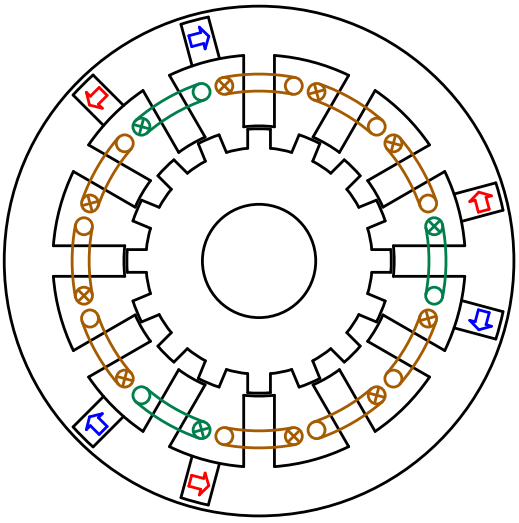

I 16r12s DSHEM

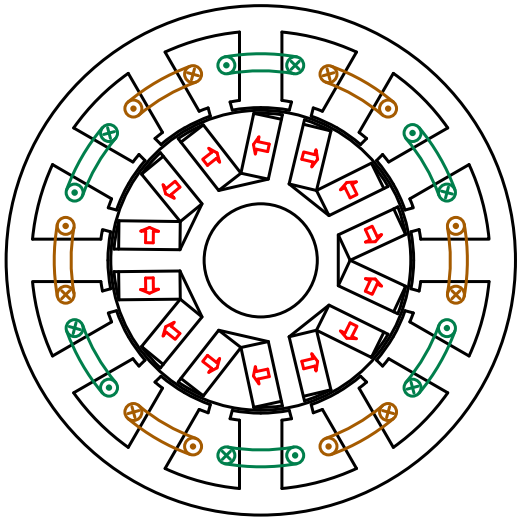

(f) 14p12s CPHEM

Fig. 6.1. Machine topology of the Toyota Prius 2010 IPMM, VFRM and HEMs.

6.2 Design and Optimization

The cross section of the Toyota Prius 2010 IPMM is shown in Fig. 6.1 (a), which has been discussed in detail in [KAM06] and selected as the benchmark. The stator wound field VFRM and fault tolerant hybrid excited machine (FTHEM) are also optimized in comparison with the proposed HE machines, as shown in Figs. 6. 1 (b) and (c), respectively. Moreover, the parallel flux HEM (PFHEM) discussed in chapter 2, doubly salient HEM (DSHEM) discussed in chapter 3, and consequent pole HEM (CPHEM) discussed in chapters 4 and 5, are shown in Figs. 1 (d) I and (f). The consequent pole VIPM rotor utilizes flux-concentrating effect and is selected for comparison in Fig. 1 (f) according to the discussion in chapter 5. To obtain a fair comparison, the optimization of the HEMs is conducted within the same constraint of the IPMM listed in Table 6.1. It should be noted that the electromagnetic performances are evaluated in this chapter. The current densities of field and armature windings are kept the same considering the ideally identical thermal management. The thermal model and mechanical model will be added in the future work.

Table 6.1 Constraints of optimization

Parameter	Value
Stator outer diameter	264mm
Air-gap length	0.73mm
Stack length	50.8mm
Winding packing factor	0.47
Field/armature current density	26.8A/mm^2

Global optimization is conducted with the assistance of commercial software Ansys Maxwell, for maximum average torque under the constraint in Table 6.1. The purpose of this chapter is to evaluate the torque density and efficiency of the HE machine for EV/HEV, and the torque ripple is not concerned during optimization. After global optimization, the main parameters of the HEMs are shown in Table 6.2. The numbers of turns for field and armature windings are determined by the IPMM rated current as well as current density. The comparison between VFRM and the IPMM has been conducted in [LIU14b]. In this chapter, the performances of VFRM are discussed to show the effect of stator PM in the FTHEM, and the parameters of the VFRM are kept the same as the FTHEM except the elimination of PM.

Since the winding in the HEMs are non-overlapped, the end-winding length can be reduced compared with the overlapped winding in the IPMM. The 3D model illustration and basic parameters of the FTHEM are shown in Fig. 6.2. Supposing the end-winding is composed by the arc and line, the length per coil for field and armature windings considering end-winding length can be expressed in (6.1) and (6.2), respectively, where l_{st} is the stack length, w_t, r_1, r_2, r_3, and θ_1 are illustrated in Fig. 6.2 (b). Subsequently, the resistance of the non-overlapped phase armature winding and field winding can be calculated with the consideration of end-winding length, as shown in Table 6.2. Compared with the IPMM phase resistance of 0.077Ω, the armature winding resistances in the HEMs are reduced as the result of non-overlapped winding, albeit with an additional field winding resistance.

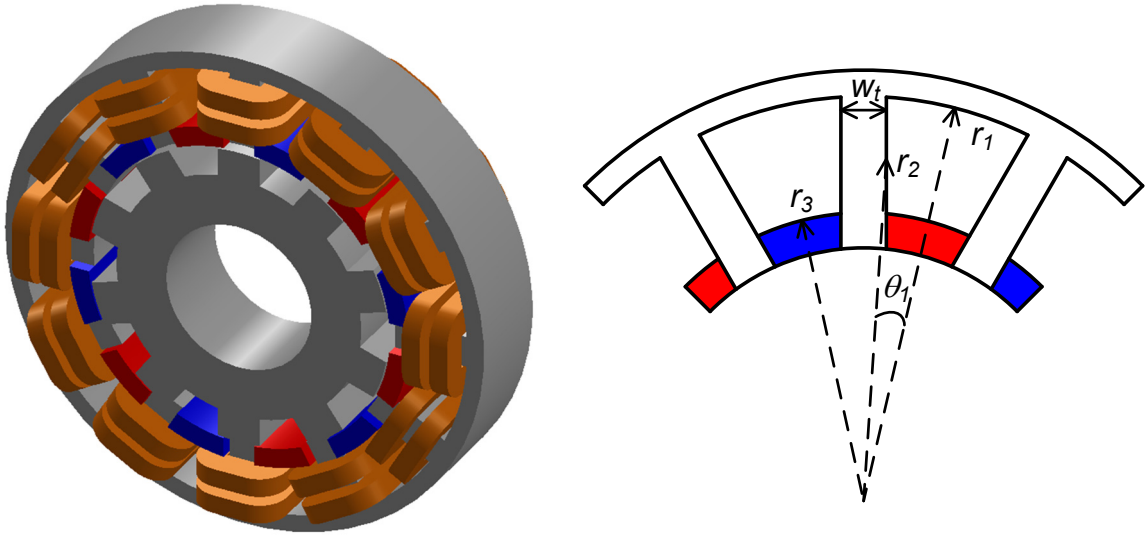

(a) 3D model (b) Basic parameters

Fig. 6.2. Illustration of end-winding length for the non-overlapped winding in the FTHEM.

$$L_{cf} = 2l_{st} + 2\left[w_t + \frac{r_1 + r_2}{2}\pi\theta_1 \right] \tag{6.1}$$

$$L_{ca} = 2l_{st} + 2\left[w_t + \frac{r_2 + r_3}{2}\pi\theta_1 \right] \tag{6.2}$$

Table 6.2 Main parameters of the PM and HE machines after optimization

Parameter	IPMM	VFRM	FTHEM	PFHEM	DSHEM	CPHEM
Stator slot number	48	12	12	12	12	12
Rotor pole number	8	10	10	11	16	14
DC bus voltage	650V					
Rated armature current	167A (RMS)					
Rated field current	N/A	167A				
Rated speed	3000rpm					
Maximum speed	13500rpm					
Stator outer diameter	264mm					
Stack length	50.8mm					
Air-gap length	0.73mm					
Stator inner diameter	161.9mm	171.6mm		179.5mm	187.4mm	176.9mm
Stator yoke thickness	20mm	9.3mm		19.2mm	18.0mm	13.2mm
Stator tooth width	7.55mm	17.5mm		17.5mm	15.3mm	24.7mm
PM height	7.1mm	N/A	10.5mm	13.5mm	11mm	7.5mm
PM width	17.9mm	N/A	30mm	17.5mm	17.5mm	35.9mm
Rotor pole width	N/A	22.9mm		19.0mm	16.6mm	N/A
Winding packing factor	0.47					
Turns per phase	88	80		64	90	60
Turns of field winding	N/A	240		192	90	180
Phase resistance	0.077Ω	0.053Ω		0.041Ω	0.056Ω	0.044Ω
Field winding resistance	N/A	0.163Ω		0.123Ω	0.056Ω	0.132Ω

6.3 Comparison of Electromagnetic Performance

6.3.1 Back-EMF and Torque Density

The open-circuit phase back-EMF waveforms with/without DC excitation at the rated speed of 3000rpm for the HEMs are compared with IPMM and VFRM in Figs. 6.3 and 6.4. Without DC excitation, the back-EMF of the VFRM and FTHEM are negligible due to stator shunted PM flux [AFI15]. The back-EMF waveform of the CPHEM is close to trapezoidal with significant 3rd harmonics, since the optimization is conducted for high torque density and the

harmonics are not concerned. Meanwhile, the PFHEM and DSHEM exhibit lower fundamental phase back-EMFs than the Prius IPMM, whereas the CPHEM possesses a higher back-EMF without DC excitation. With rated field excitation of i_{dc}=167A, the back-EMF of the HEMs can be regulated as shown in Fig. 6.3. It can be observed that the VFRM exhibits the lowest fundamental back-EMF, and the other HEMs exhibit comparable fundamental back-EMF with the Prius IPMM. With rated DC excitation, some harmonics in the phase back-EMF are eliminated for the CPHEM and the waveform is more sinusoidal as shown in Fig. 6.3.

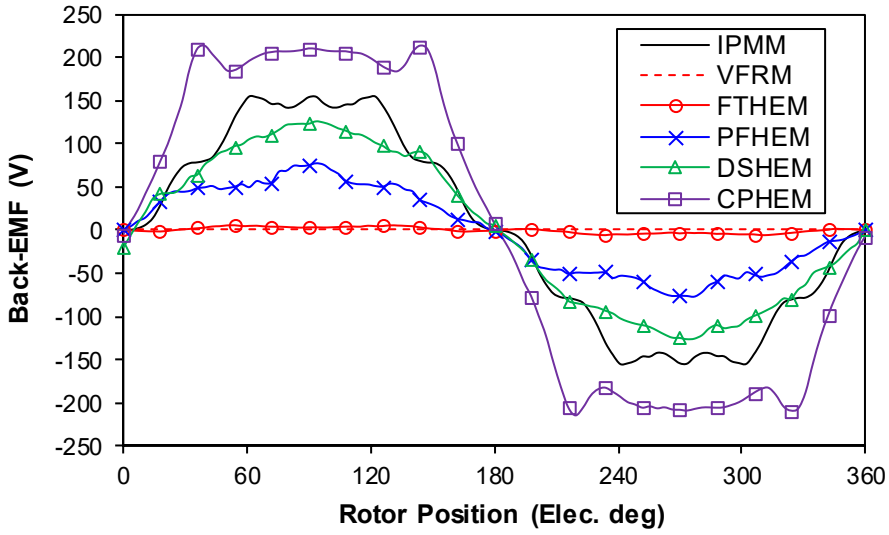

(a) Waveforms

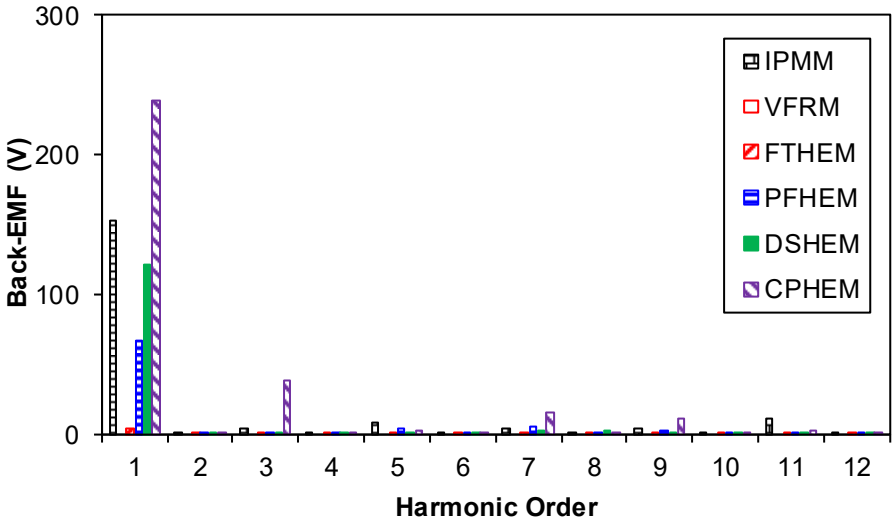

(b) Spectra

Fig. 6.2. Open-circuit phase back-EMF without DC excitation at the rated speed of 3000rpm.

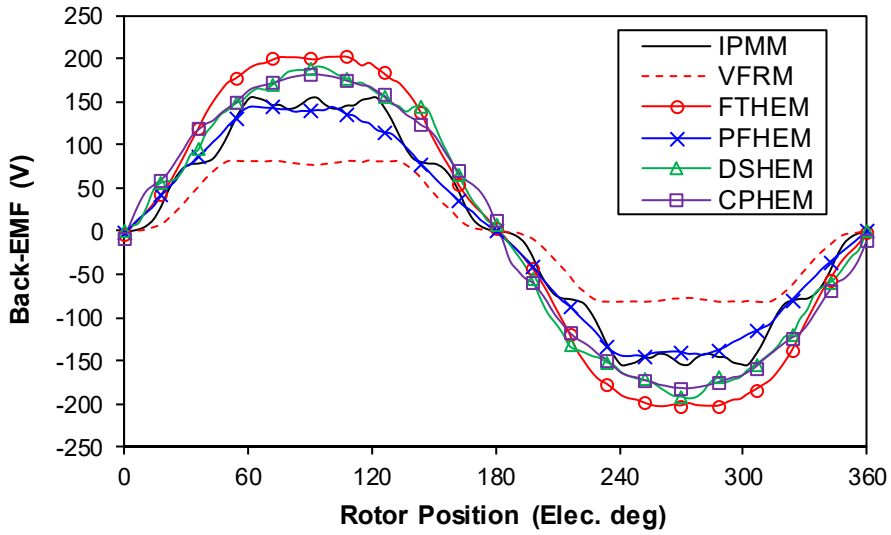

(a) Waveforms

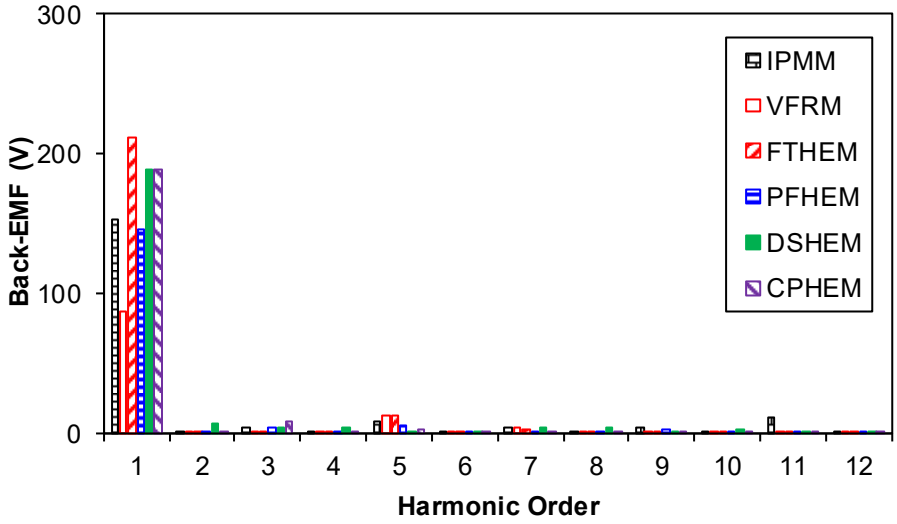

(b) Spectra

Fig. 6.3. Open-circuit phase back-EMF with maximum DC excitation of i_{dc}=+167A at the rated speed of 3000rpm.

Moreover, the variation of fundamental phase back-EMF at rated speed of 3000rpm with the DC excitation current is shown in Fig. 6.4. There is no field winding in the IPMM, and the back-EMF is constant as a benchmark. With the regulation of DC excitation, the back-EMF of the HEMs and VFRM can be regulated flexibly. The CPHEM exhibits the highest peak back-EMF, whereas the VFRM exhibits the lowest peak back-EMF due to absence of PM. With the increase of DC excitation current, the back-EMF of the HEMs even reduces due to the over-saturation effect [ZHA11].

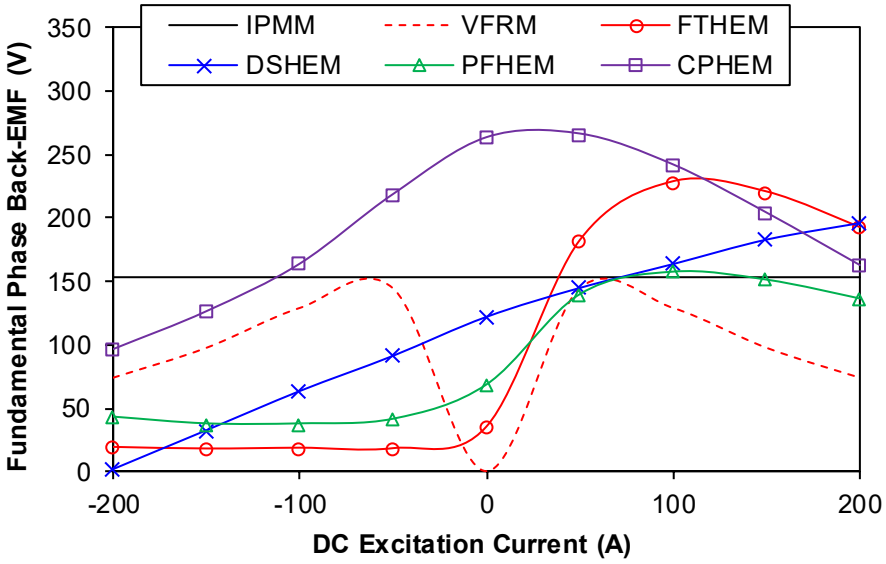

Fig. 6.4. Variation of open-circuit phase back-EMF fundamental with DC excitation current at the rated speed of 3000rpm.

The electromagnetic torque waveforms with MTPA control at rated armature current with different DC excitations are compared in Figs. 6.4 and 6.5, respectively. The DSHEM exhibits significant 3rd pulsating torques due to the even order harmonics in phase back-EMF, which has been illustrated in chapter 3. It should be noted that the purpose of this chapter is to evaluate the torque density of these HEMs with IPMM and VFRM, and the torque ripple is not concerned. The average torques at rated armature current with/without DC excitations are summarized in Table 6.3. With rated DC excitation, the torque density of the HEMs can be enhanced except the CPHEM due to the over-saturation effect as illustrated in Fig. 6.4. The torque density of the CPHEM is the highest whereas that for the VFRM is the lowest due to absence of PM. Moreover, the torque densities of these HEMs are lower than that of the Prius IPMM since additional spaces are spared for the field excitation. Therefore, the HEMs take advantage of magnetic field regulation of DC coil with the sacrifice of torque density.

Table 6.3 Average torques of the PM and HE machines at rated armature current

	IPMM	VFRM	FTHEM	PFHEM	DSHEM	CPHEM
Without DC	220Nm	0	83Nm	27.2Nm	67Nm	200Nm
With DC		84Nm	173Nm	114.1Nm	84Nm	189Nm

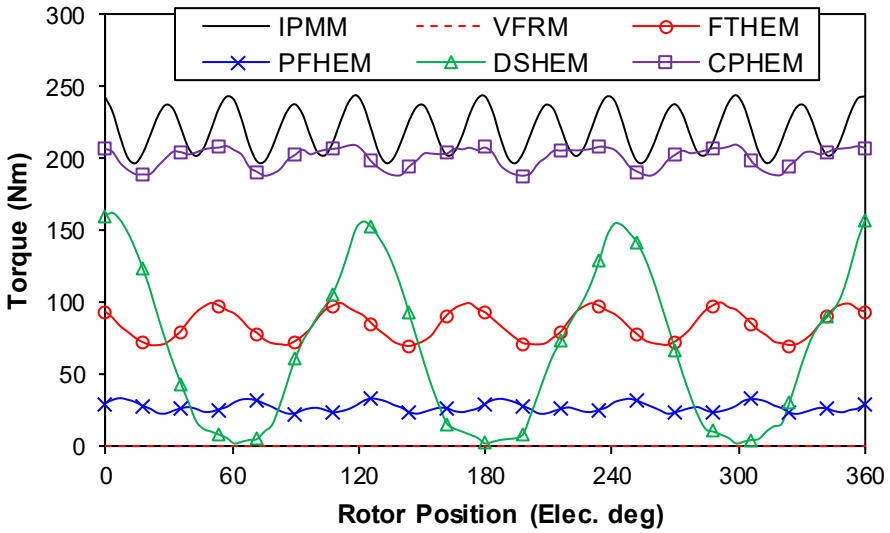

(a) Waveforms

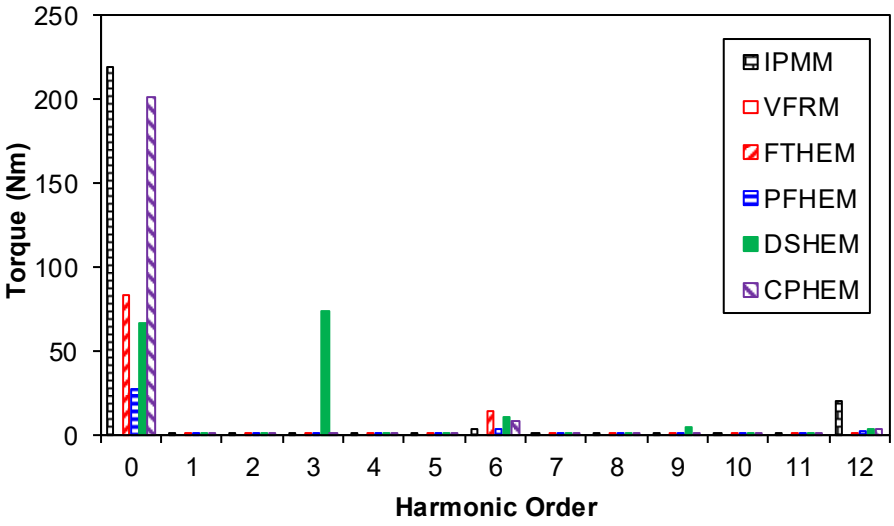

(b) Spectra

Fig. 6.5. Electromagnetic torque at rated armature current with amplitude of i_m=236A without DC excitation under MTPA control.

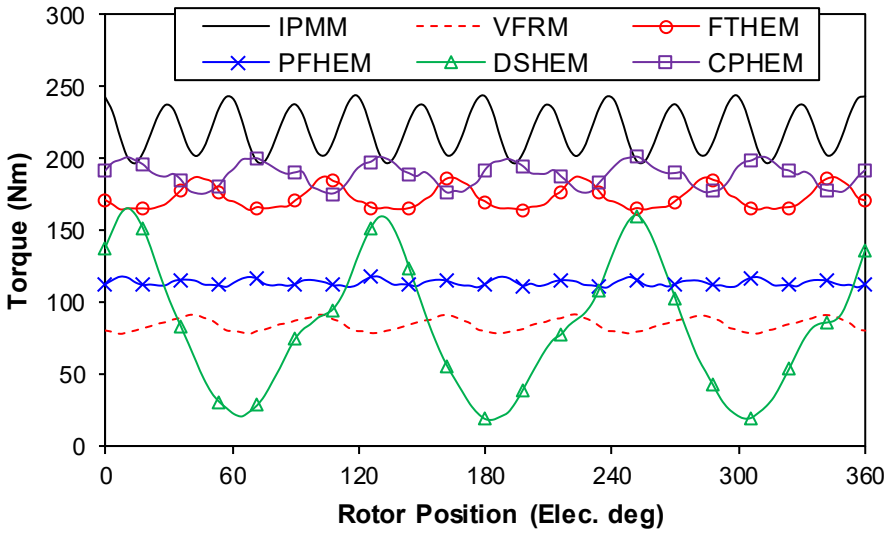

(a) Waveforms

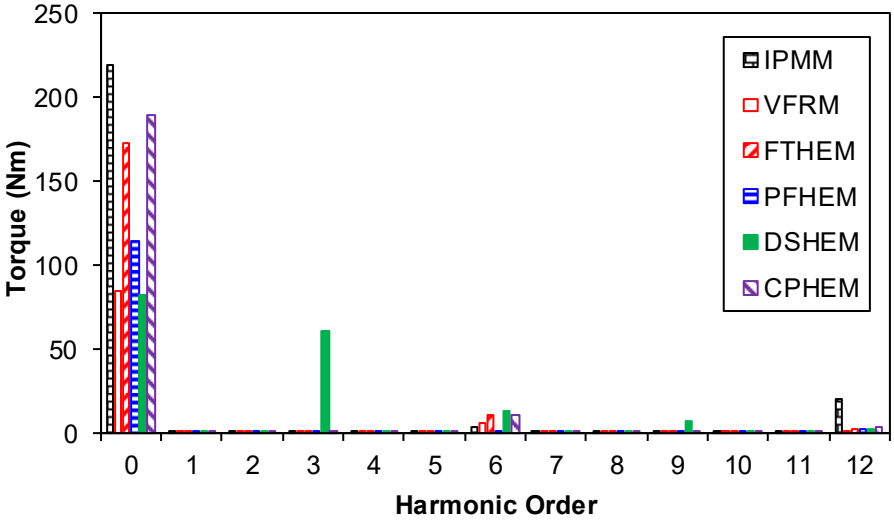

(b) Spectra

Fig. 6.6. Electromagnetic torque at rated armature current with amplitude of i_m=236A and maximum DC excitation of i_{dc}=+167A under MTPA control.

Fig. 6.7 shows the average torque against armature current amplitude under the MTPA control (i_{dc}=0.707I_a to keep constant field/armature current density for the HEM and VFRM). At light load, the torque density of the CPHEM is similar with that of the IPMM and the VFRM exhibits the lowest average torque due to absence of PM. However, the overload capability of the consequent-pole machine is limited and the IPMM exhibits the highest average torque at rated current excitation. Under heavy load, the FTHEM shows similar torque density with the CPHEM since the PMs in the FTHEM are beneficial to suppress the magnetic saturation and

the FTHEM is suitable for overload operation. Besides, it can be identified that the DSHEM is easy to get saturated, and the torque density is the lowest under heavy load.

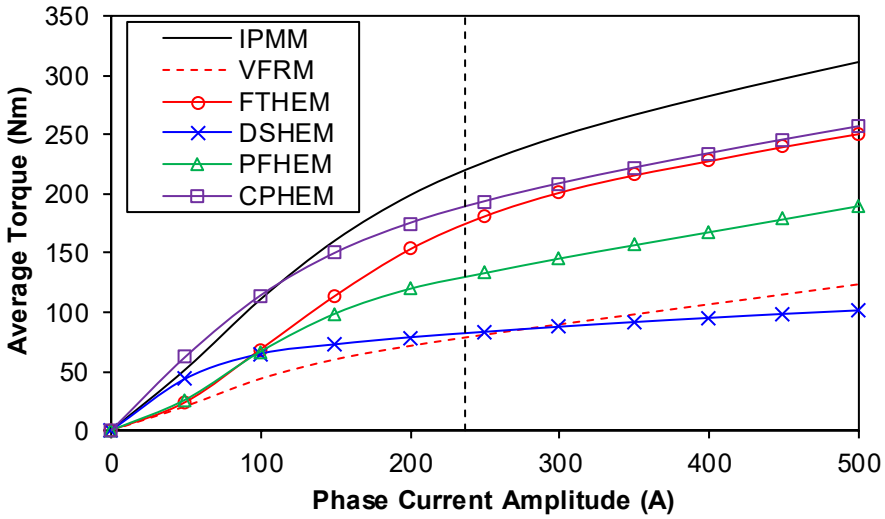

Fig. 6.7. Average torque against armature current amplitude under MTPA control (i_{dc}=0.707I_a to keep constant field/armature current density for the HEM and VFRM).

6.3.2 Flux-Weakening Performance

A significant requirement for the EV/HEV machine is wide operating region and good flux weakening performance. The flux weakening factor is defined in (6.3), to evaluate the flux weakening capability for the PM/HE machines. When the flux weakening factor is lower than 1 (k_{fw}<1), the PM flux cannot be countered by armature current and the flux weakening region is limited. However, when the flux weakening factor is significantly larger than 1 (k_{fw}>>1), the phase current as well as the power will drop at high speed operation. Therefore, the ideal design for the flux weakening operation is k_{fw}~=1.

$$k_{fw} = \frac{L_d I_m}{\psi_{PM\pm DC}} \tag{6.3}$$

The flux linkage, inductance and flux weakening factor for these machines are compared in Table 6.4. With the regulation of field excitation, all these HE machines have ideally infinite flux weakening region since the flux weakening factor can be larger than 1.

Moreover, the torque and power-speed envelopes under the peak current and DC bus voltage are calculated with the flux linkage method [QI09] as shown in Fig. 6.8. In the constant torque region, the average torque of IPMM is the highest as illustrated in section 6.3.1. However, the output power of the IPMM is reduced at flux-weakening region due to high

salient ratio [SOO94]. The base speed of the VFRM is the highest due to the smallest back-EMF shown in Fig. 6.4. At the flux-weakening region, the output torques/powers of the VFRM, FTHEM, PFHEM and CPHEM are all higher than that of the Prius IPMM as the result of additional field regulation. Meanwhile, the CPHEM exhibits the highest output torque/power at the constant power region, which is beneficial for the high speed operation.

Table 6.4 Flux linkage, inductance and flux weakening factor

	IPMM	VFRM	FTHEM	PFHEM	DSHEM	CPHEM
$\psi_{PM\text{-}DC}$	N/A	-27.8mWb	-0.034Wb	-9.2mWb	6.1mWb	48.8mWb
ψ_{PM}	122.3mWb	N/A	N/A	14.8mWb	33.9mWb	109.5mWb
ψ_{PM+DC}	N/A	27.8mWb	0.034Wb	41.9mWb	52.6mWb	80.8mWb
L_d	1.54Mh	0.56Mh	0.78Mh	0.71Mh	1.2Mh	0.88Mh
k_{fw}	3.0	>4.8	>2.7	>4.0	5.4~46.4	1.9~4.3

When the machine is operating above the base speed, the back-EMF can be significantly higher than the DC bus voltage. If the flux weakening control signals are removed occasionally, the winding with high back-EMF can be dangerous and may destroy the power devices, which is denoted as uncontrolled generator fault (UCGF) [JAH99]. The UCGF should be considered carefully for the machines equipped for EV/HEV, since the maximum speed is generally several times of the base speed. The amplitude of line-line back-EMF fundamentals with DC excitation of these machines at maximum operation speed are illustrated in Fig. 6.9. The back-EMF of IPMM cannot be controlled with UCGF, and the line-line back-EMF is higher than the DC bus voltage, which is potentially dangerous. However, the back-EMF of the HEMs can still be regulated by the DC excitation under the UCGF. With the regulation of DC excitation, the line-line back-EMFs of the VFRM, FTHEM, PFHEM and DSHEM can be smaller than the DC bus voltage and the generation fault can be eliminated. Although the CPHEM exhibits higher EMF than the DC bus voltage with the regulation of DC excitation, the voltage can still be reduced with negative DC excitation and fault tolerance is enhanced. Therefore, the system reliability and fault tolerant capability at high speed operation are enhanced for the HEMs and VFRM with the utilization of field excitation.

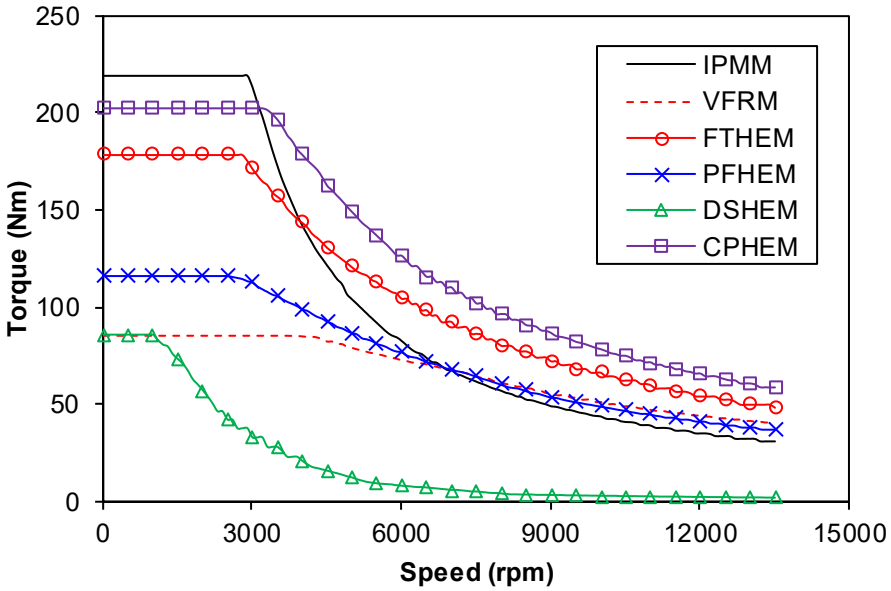

(a) Torque-speed envelopes

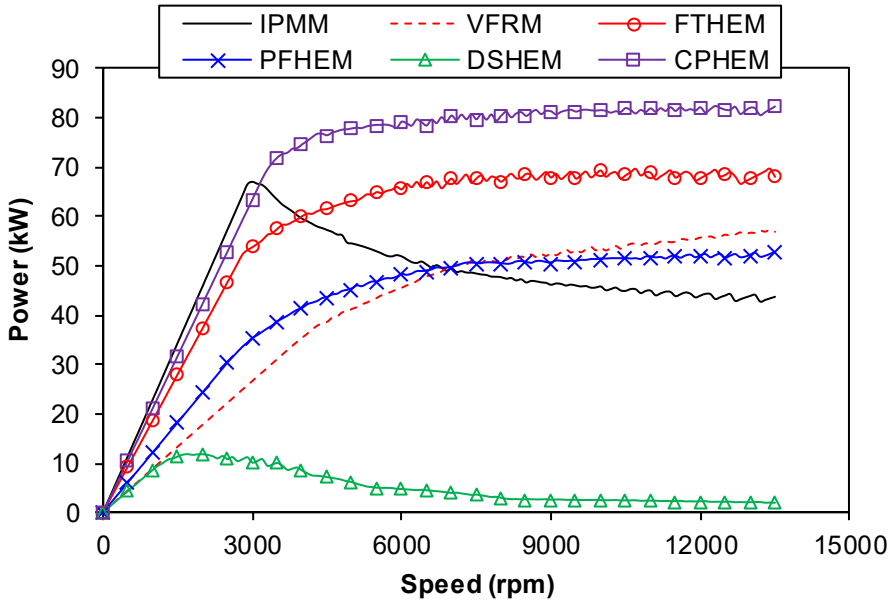

(b) Power-speed envelopes

Fig. 6.8. Torque, power, and power factor-speed envelopes under the whole operating region (0~13500rpm).

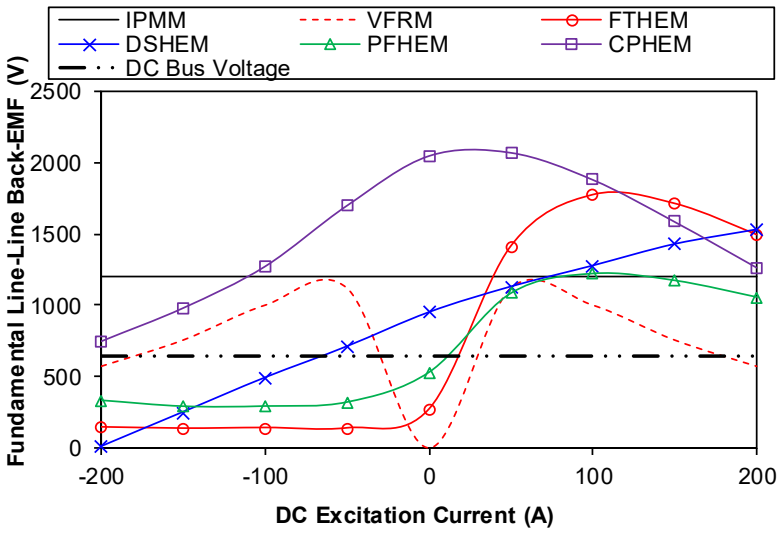

Fig. 6.9. Line-line back-EMF fundamental versus DC excitation current at the maximum operation speed of 13500rpm.

6.3.3 Efficiency Evaluation with Driving Cycle

The efficiency maps considering winding copper loss, core iron loss, magnet loss and mechanical loss of these machines under the same DC bus voltage and peak current are compared in Fig. 6.10. The winding copper loss is obtained from the winding current and resistance listed in Table 6.2. The core iron loss is synthesized from the hysteresis loss and eddy current loss. Since the conductive NdFeB magnet is employed, eddy current is allowed in the magnet and the magnet loss is obtained from the eddy current and conductivity. The mechanical loss is determined from the rotating speed according to (6.4), where Ω_m is rotating speed, k_{m1} and k_{m2} are coefficients.

$$p_m = k_{m1}\Omega_m + k_{m2}\Omega_m^{\ 2} \tag{6.4}$$

Although the torque and power-speed envelopes for HEMs and VFRM are extended at high speed operation, the overall efficiency is lower than the IPMM. This can be accounted for the salient structure in the HEMs and VFRM, and more abundant harmonics in the magnetic field. The maximum efficiency for IPMM is 96%, whereas that for the VFRM is only 88%. The maximum efficiencies of the HEMs are between the IPMM and VFRM, and the introduction of PMs for the HEM is still beneficial for efficiency improvement compared with the VFRM. The CPHEM exhibits the highest efficiency among the HEMs and the maximum efficiency is 94%. It can be identified that although the output torque of the CPHEM at high speed operation is improved than the IPMM with the utilization of field excitation, the efficiency is still limited due to the additional field winding copper loss.

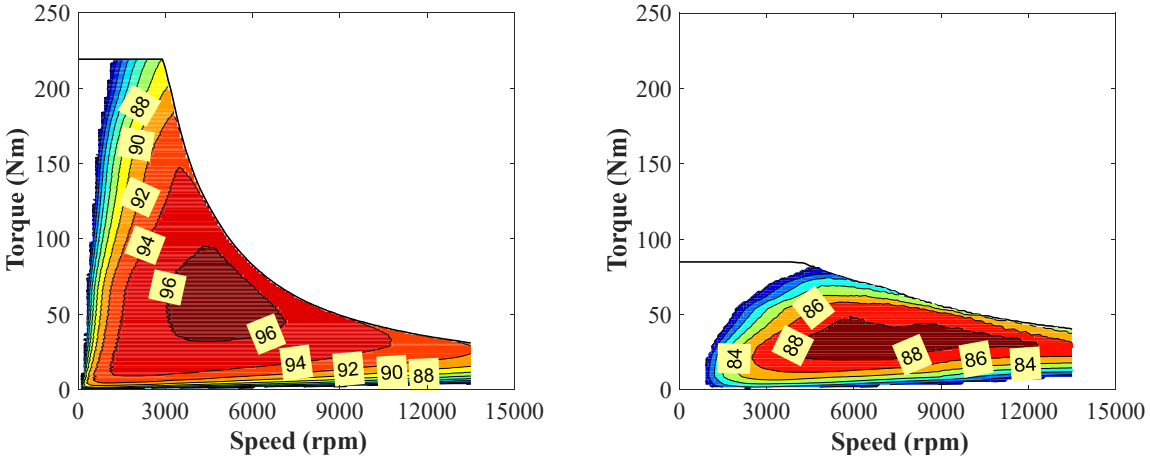

(a) IPMM

(b) VFRM

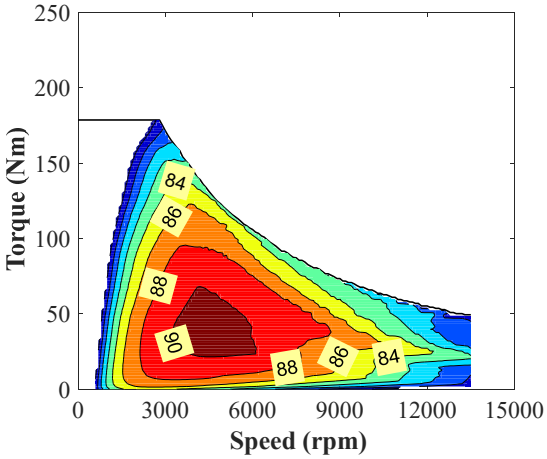

(c) FTHEM

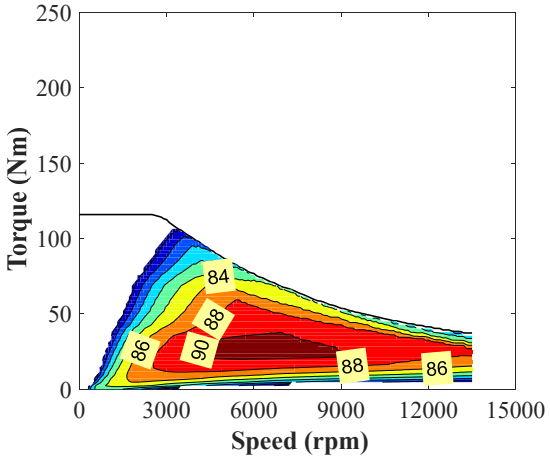

(d) PFHEM

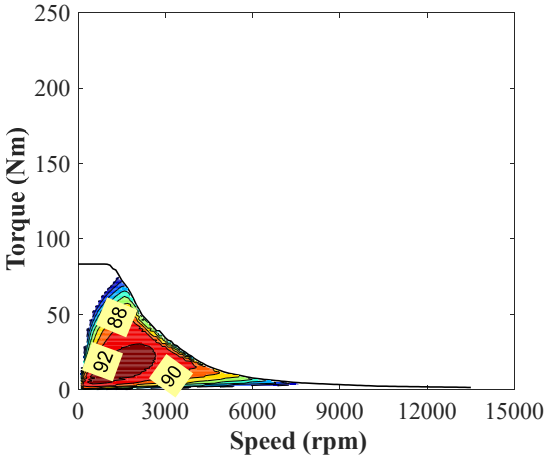

(e) DSHEM

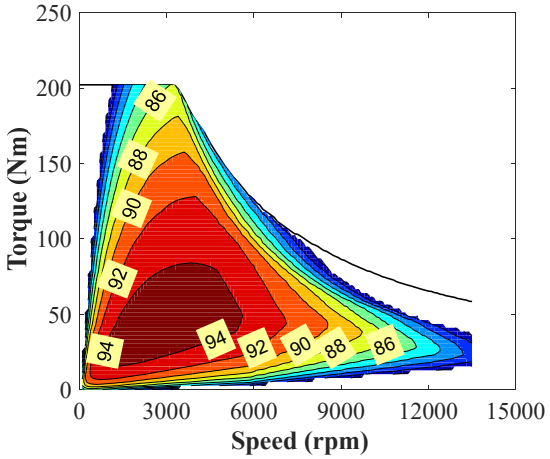

(f) CPHEM

Fig. 6.10. Efficiency maps under the same DC bus voltage (650V), maximum phase current (236A) and field current (167A) (Operating range as 0~13500rpm).

To further evaluate the machine efficiency considering onboard operating range, the vehicle machine operating speed at different time for the New European Drive Cycle (NEDC) is shown at Fig. 6.11. By utilizing the ADVISOR (Advanced Vehicle Simulator) and Toyota Prius vehicle parameters in [KAM06], the IPMM operation points over NEDC is obtained in Fig. 6.12. It can be observed that the machine is mainly operating under low-speed low-torque region for the NEDC.

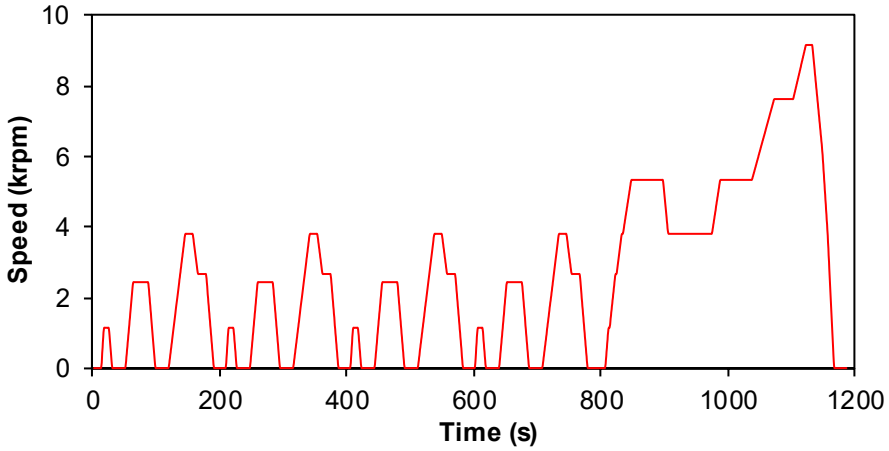

Fig. 6.11. New European Drive Cycle (NEDC).

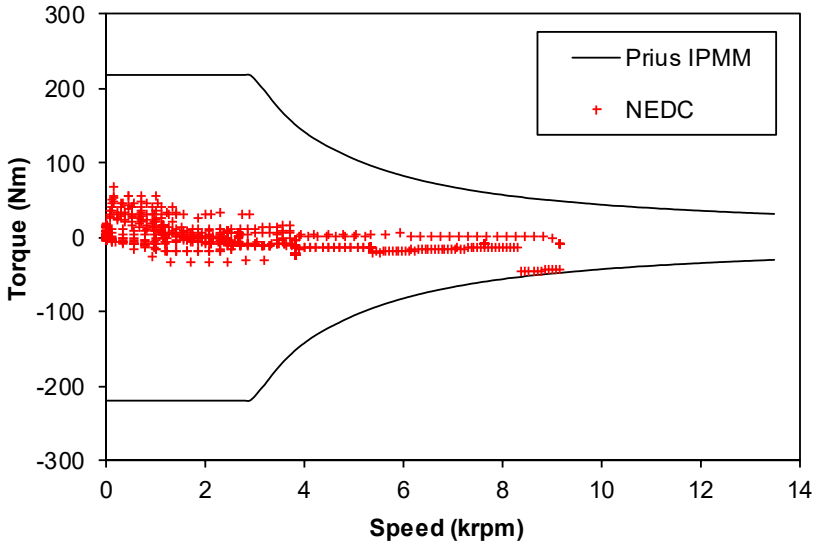

Fig. 6.12. Drive train operation point under NEDC within the Prius IPMM torque-speed envelope.

By replacing the IPMM with VFRM and HEMs and supposing the vehicle parameters are constant, the corresponding operating points and machine efficiency with different machines can be evaluated. The vehicle machine average efficiency under NEDC with alternative machines are compared in Fig. 6.13. All the HEMs and VFRM can satisfy the operation points

in Fig. 6.12, except the DSHEM since the flux-weakening performance of DSHEM is relatively poor as shown in Fig. 6.10. The IPMM exhibits the highest average efficiency, whereas the VFRM possesses the lowest efficiency due to absence of PM. Among the HEMs, the CPHEM has the highest average efficiency and is slightly lower than that of IPMM.

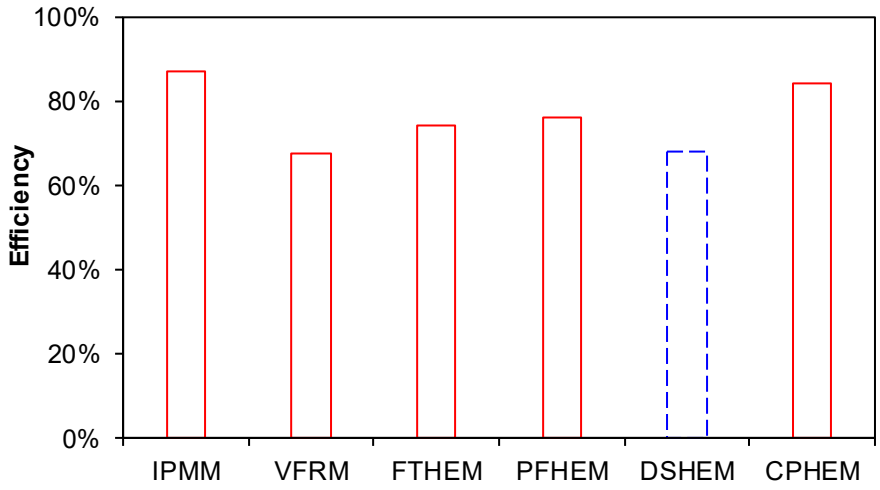

Fig. 6.13. Vehicle machine efficiency under NEDC drive cycle.

To demonstrate the main loss consumption, the machine average losses under NEDC operation are compared in Fig. 6.14. It can be observed that additional field winding loss is introduced in the VFRM and HEMs with the utilization of DC coils. Besides, since doubly salient structure and non-overlapping winding are employed in the HEMs and VFRM, the core hysteresis loss and eddy current loss are increased significantly as the result of more abundant magnetic field harmonics. Moreover, these HEMs have larger PM loss compared with the IPMM due to the abundant field harmonics. Therefore, although the flux weakening performance of the HEM is enhanced compared with IPMM, the operating efficiency is reduced.

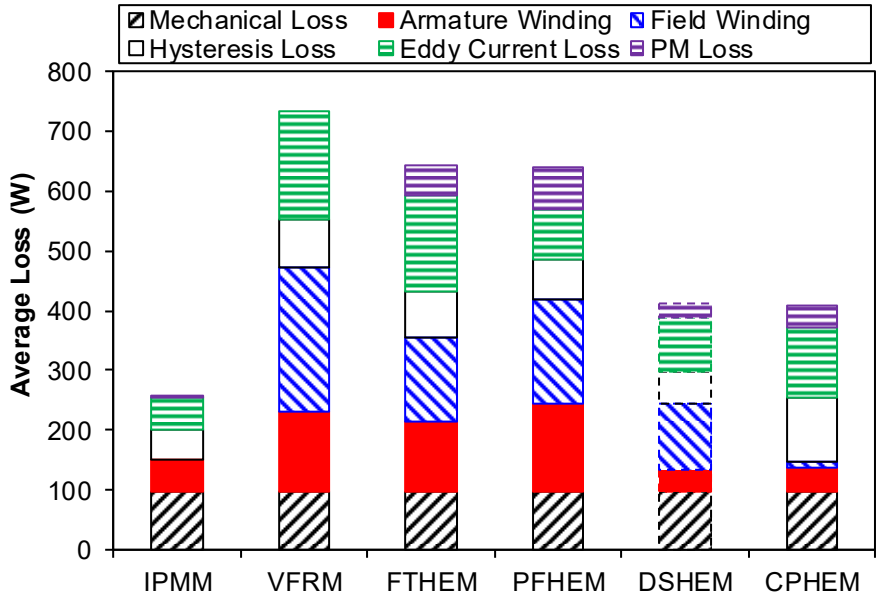

Fig. 6.14. Vehicle motor average loss under NEDC.

6.4 Summary

This chapter compared the electromagnetic performances between the VFRM, FTHEM, PFHEM, DSHEM and CPHEM with IPMM for potential EV/HEV applications. The HEMs are optimized within the same frame and thermal condition of the commercialized Toyota Prius 2010 IPMM to gain a fair comparison.

It is revealed that the HEMs possess controllable back-EMF and output torque with the introduction of field winding, albeit with sacrificed torque density. Moreover, the output torques and powers of the FTHEM and CPHEM at flux weakening region can be higher compared with IPMM due to more flexible flux regulation of DC excitation as well as armature current. Nevertheless, the DC field winding copper loss is introduced and the doubly salient structure with non-overlapping winding results in larger stator and rotor iron losses. Therefore, the overall operating efficiency of the HEMs within the driving cycle is reduced compared with the IPMM.

Chapter 7

General Conclusion and Future Work

The main research topics of this thesis are focused on investigation of novel hybrid excited (HE) machines and evaluation of the corresponding electromagnetic performance. Three novel HE machines have been proposed and investigated in chapters 2, 3, and 4. Various rotor configurations have been extended in chapter 5 based on the proposed machine in chapter 4. Furthermore, the proposed HE machines are compared with the interior PM machine (IPMM) and a fault tolerant HE machine (FTHEM) in chapter 6. This chapter summarizes the investigations in the whole thesis, regarding the proposed machine topologies, main features and performance comparisons. Based on the research work in this thesis, the future work for further investigation is also presented.

7.1 Proposed Machine Topologies

The proposed machine topologies in this thesis are summarized in Fig. 7.1. In chapter 2, a novel parallel flux HE machine (PFHEM) is proposed, as shown in Fig. 7.1 (a). Then, the doubly salient HE machine (DSHEM) proposed in chapter 3 is shown in Fig. 7.1 (b). Furthermore, the novel Inset-PM consequent pole rotor HE machine (Inset-PM CPHEM), proposed in chapter 4, is illustrated in Fig. 7.1 (c). In chapter 5, various IPM consequent pole rotor HE machines (IPM CPHEM) are extended, and one basic topology is shown in Fig. 7.1 (d).

Based on the machine topologies illustration in Fig. 7.1, the configurations of these proposed HE machines are summarized in Table 7.1. All proposed HE machines possess stationary field winding (FW) with elimination of brushes and slip rings. The field and armature windings are compact with non-overlapped wound around the stator teeth. In the proposed PFHEM and DSHEM in chapters 2 and 3, the PMs are located in the stator yoke and the rotor is salient as the switched reluctance machine (SRM). In the proposed CPHEMs in chapters 4 and 5, the PMs are allocated in the rotor and the stator is entire laminated core. Since the field and armature windings are in the same stator slots of the PFHEM and CPHEMs, integrated field and armature winding with open-winding drive circuit can be employed to eliminate the field coils.

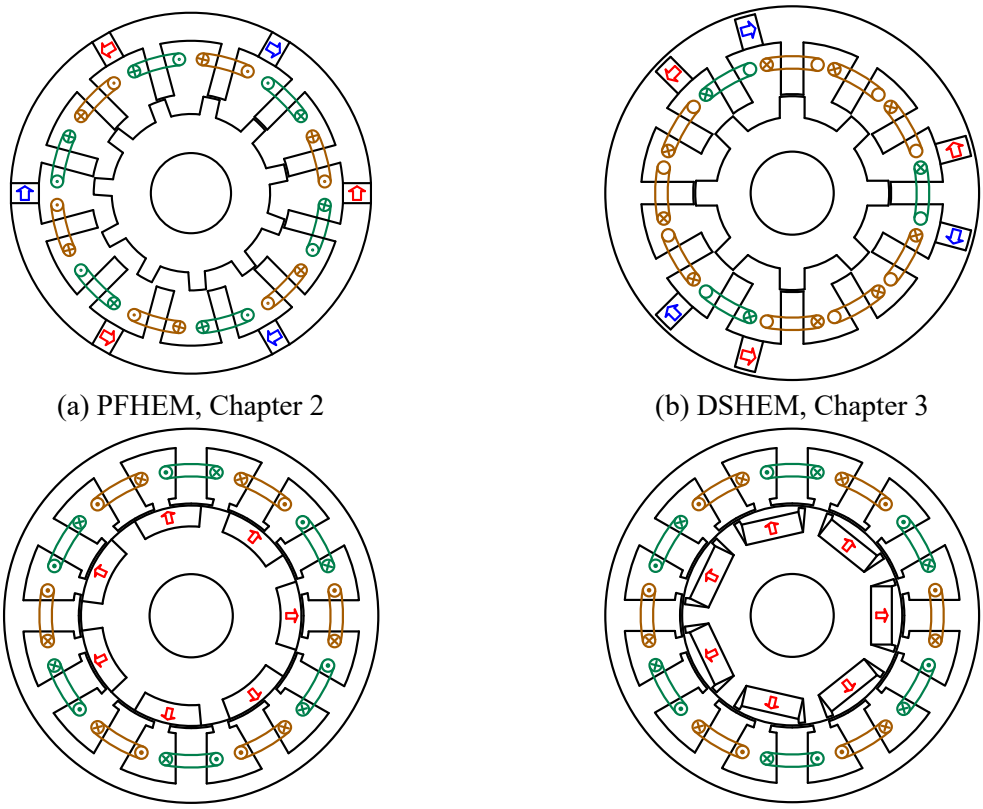

(a) PFHEM, Chapter 2 (b) DSHEM, Chapter 3

(c) Inset-PM CPHEM, Chapter 4 (d) IPM CPHEM, Chapter 5

Fig. 7.1. Configurations of the proposed HE machines in this thesis (Red and blue arrow components indicate PMs, brown and green lines indicate field and armature windings).

Table 7.1 Proposed machine topologies in this thesis

	PFHEM Chapter 2	DSHEM Chapter 3	Inset-PM CPHEM Chapter 4	IPM CPHEM Chapter 5
PM location	Stator yoke	Stator yoke	Rotor surface	Rotor inside
FW location	Stator			
Brushes and slip rings	No			
Winding configuration	Non-overlapped field and armature windings			
Stator core	Π-shape segment	Three-teeth and one-tooth segments alternatively	Entire stator core	
Rotor core	Salient rotor as SRM		Consequent-pole Inset-PM rotor	Consequent-pole IPM rotor
Integrated field/armature windings	Yes	No	Yes	Yes

7.2 Main Features

According to the discussion of the proposed HE machines in each chapter, the main features of these proposed machines are summarized in Table 7.2.

The PFHEM presented in chapter 2 is developed from the biased flux HE machine by separating the PM and WF flux paths. Since the PM and WF excitations are in parallel, the flux regulation capability is enhanced. Different stator and rotor pole combinations are investigated to eliminate the even order harmonics in the back-EMF. It is revealed that the proposed HE machine exhibits higher torque density at flux-enhancing operation, meanwhile with reduced PM usage than the counterpart. Due to low PM excited open-circuit back-EMF, the proposed machine possesses high fault tolerance for high speed uncontrolled generator fault.

The DSHEM discussed in chapter 3 is developed from the doubly salient PM machine by introducing field winding. It inherits the non-overlapped winding configuration and compact structure can be achieved. By properly selecting the stator and rotor pole numbers, the distribution factor of 1 can be obtained for potentially high torque density. Besides, a trade-off of the iron bridge design should be determined for hybridization between PM and WF excitations.

In chapters 4 and 5, the CPHEMs with Inset-PM and various IPM rotor configurations are presented. The abundant spatial harmonics in the MMF of non-overlapped winding are utilized to react with the field excitation through magnetic modulation effect. It is demonstrated that the CPHEMs exhibit comparable torque density with the surface mounted PM (SPM) machine, whereas the operation region is extended with field regulation. Nevertheless, the overload capability is sacrificed due to the consequent pole rotor structure. By utilizing flux-concentrating effect in the VIPM and UIPM rotors, the torque density of the HE machine can be enhanced, albeit with more severe magnetic saturation and limited flux regulation capability. Furthermore, the copper loss can be reduced and the operation efficiency can be enhanced with the open-winding drive circuit to eliminate the field winding.

Table 7.2 Main features of proposed machines in this thesis

Proposed HEM	Main Features
PFHEM Chapter 2	• Developed from the biased flux HE machine • Parallel flux paths of PM and WF excitations • Enhanced flux regulation capability with the original counterpart • Proper stator and rotor pole combination to eliminate the even order harmonics in the flux linkage and back-EMF • Higher torque density at flux-enhancing operation, with reduced PM consumption than the counterpart • High fault tolerance for high speed uncontrolled generator fault
DSHEM Chapter 3	• Developed from the doubly salient PM machine • Inherited the non-overlapped winding and compact structure • Distribution factor of 1 for proper stator and rotor pole combination • Iron bridge thickness trade-off design for the hybridization of PM and FW excitations
Inset-PM CPHEM Chapter 4	• Abundant harmonics in the MMF of non-overlapped armature winding utilization with FW excitation • Comparable torque density with the SPM machine at rated excitation • Extended operation region compared with the pure PM machine • Sacrificed overload capability due to consequent-pole rotor
IPM CPHEM Chapter 5	• Abundant harmonics in the MMF of non-overlapped armature winding utilization with FW excitation • Utilization of flux-concentrating effect with VIPM and UIPM rotors to enhance the output capability • Over-saturation effect caused by flux-concentrating effect • Improved efficiency with open-winding technique to eliminate FW

7.3 Performance Comparison

To demonstrate the feasibility of these HE machines for variable operation in EV/HEV, these developed HE machines are optimized and compared with the pure PM excitation (IPMM)

and the existing FTHEM. Since the Inset-PM CPHEM possesses rotor surface PM and is not suitable for high speed operation, the VIPM CPHEM is selected for optimization and comparison. According to the investigation in chapter 6, the comparison of the electromagnetic performances is summarized from the perspective of torque density, power density, flux regulation capability, efficiency, and fault tolerance at high speed operation. Table 7.3 shows the performance comparison under the same optimization constraint of Toyota Prius 2010, and the comparison results are summarized in Fig. 7.2. The IPMM exhibits superior torque density and average efficiency under drive cycle, with sacrificed fault tolerance for high speed operation. The FTHEM and PFHEM possess wide flux regulation range, and high fault tolerant capability. Nevertheless, the torque density and operation efficiency are not comparable with the pure PM machine. The CPHEM exhibits slightly sacrificed torque density and efficiency than the IPMM, whereas the flux regulation ratio is also lower than the other HE machines. The DSHEM possesses the lowest torque and power density over the other machines, and it cannot satisfy the NEDC drive cycle operation points.

Table 7.3 Performance comparison under the same optimization constraint of Toyota Prius 2010

	IPMM	FTHEM	PFHEM Chapter 2	DSHEM Chapter 3	CPHEM Chapter 5
Average torque (Constant torque region)	219.3Nm	178.7Nm	115.8Nm	85.2Nm	202.2Nm
Maximum power	67.1kW	69.8kW	52.7kW	11.9kW	82.5kW
Back-EMF regulation ratio (Negative FW excitation)	N/A	-49.7%	-45.1%	-98.8%	-63.2%
Back-EMF regulation ratio (Positive FW excitation)	N/A	+555.2%	+131.2%	+60.8%	+2.1%
Average efficiency (Under DEDC drive cycle)	87.0%	74.0%	76.1%	N/A	84.0%
Minimum line-line back-EMF @ rotor speed of 13500rpm	1197V	136.4V	290.7V	252.5V	844.4V
DC bus voltage			650V		

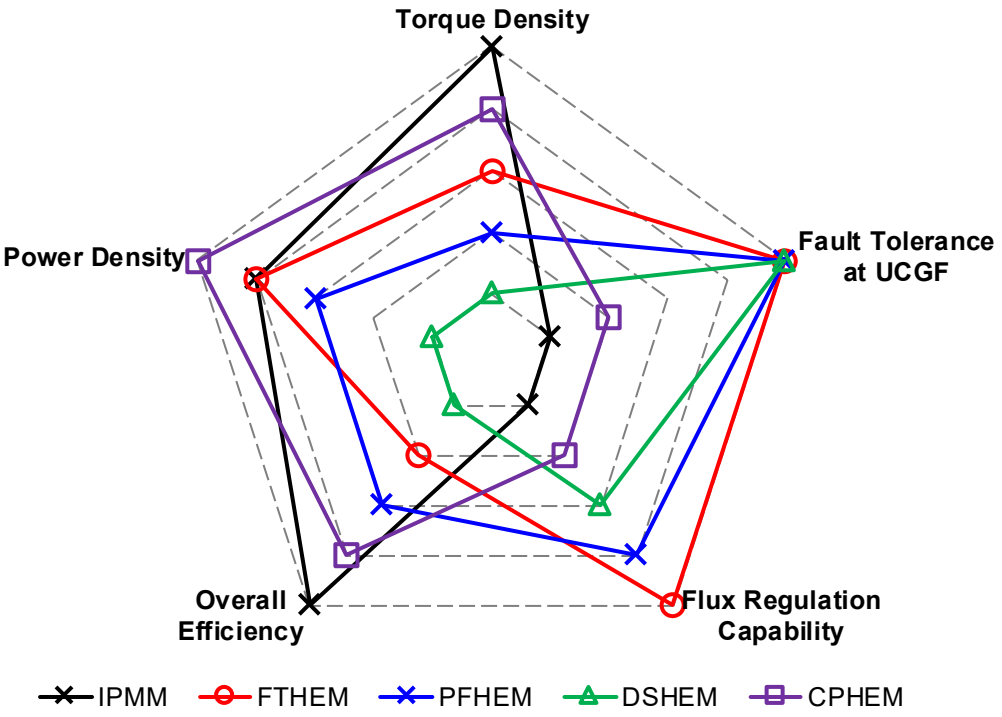

Fig. 7.2. Comparison of electromagnetic characteristics of proposed HE machines with IPMM and FTHEM.

According to the above discussion, each of the proposed HE machines has its unique characteristics compared with the IPMM. The CPHEM has the closest torque density and efficiency with the Toyota Prius 2010 IPMM, whereas the flux regulation capability is limited. The PFHEM exhibits wide flux regulation ratio and high fault tolerance for high speed operation, with sacrificed torque/power density and efficiency. Therefore, the selection of a proper machine should be based on the operation requirements as the trade-off of different performances.

7.4 Future Work

Following the research work in this thesis, the future work can be carried out for further investigations.

7.4.1 Machine Optimization

The purpose of this thesis is to propose novel HE machines and evaluate the electromagnetic performance characteristics. Therefore, the optimization goal in this thesis is maximum torque density under flux concentrating effect. However, the machine parameters can be quite different considering the different PM and FW excitation portions. The future

work can be conducted for maximum efficiency during machine optimization by considering the most frequently operation point in the driving cycle.

7.4.2 Parasitic Effect

This thesis mainly focuses on the torque density and flux regulation capability of proposed HE machines, and the parasitic effect is not concerned. It has been demonstrated that the cogging torque, torque ripple, iron loss, and magnet loss are significant due to doubly salient structure. Further investigation can be focused on the suppression of the parasitic effect of the HE machines.

7.4.3 Control Strategies with Optimal Field and Armature Current Ratio

In HE machines, the field and armature winding currents can be combined flexibly to achieve both flux-enhancing and flux-weakening. In chapter 5, the optimal current ratio between field and armature current is derived for maximum average torque under fixed winding copper loss. However, this is the simplified scenario supposing the copper loss is dominant at low speed operation. Other control strategies with optimal current ratio require to be discussed for high speed operation, with the consideration of fixed voltage/current limit and significant iron loss.

7.4.4 Investigation of Thermal Model

This thesis mainly focuses on the electromagnetic performance analysis of the HE machines. Since additional field winding copper loss is produced compared with pure PM machines, the thermal model should be established to evaluate the thermal management of the HE machines with the consideration of more severe losses.

7.4.5 Investigation of Noise, Vibration and Harshness (NVH)

This thesis proposes and evaluates several novel HE machines. The optimization and discussion are mainly focused on the torque density and field regulation capability. The torque ripple and the unbalanced magnetic pull are only mentioned but not discussed in detail. The correspondingly noise, vibration and harshness (NVH) are rather significant for smooth operation of the machines. The future work should be conducted within the NVH analysis and design techniques to further suppress the NVH.

References

[AFI15] I. A. A. Afinowi, Z. Q. Zhu, Y. Guan, J. C. Mipo and P. Farah, "Hybrid-excited doubly salient synchronous machine with permanent magnets between adjacent salient stator poles," *IEEE Trans. Magn.*, vol. 51, no. 10, pp. 1-9, Oct. 2015.

[AFI16] I. A. A. Afinowi, Z. Q. Zhu, Y. Guan, J. Mipo and P. Farah, "A novel brushless AC doubly salient stator slot permanent magnet machine," *IEEE Trans. Energy Convers.*, vol. 31, no. 1, pp. 283-292, March 2016.

[AKE00] A. D. Akemakou and S. K. Phounsombat, "Electrical machine with double excitation, especially a motor vehicle alternator," U.S. Patent 6 147 429, Nov. 14, 2000.

[AKI03] H. Akita, Y. Nakahara, N. Miyake and T. Oikawa, "New core structure and manufacturing method for high efficiency of permanent magnet motors," *38th IAS Annual Meeting on Conference Record of the Industry Applications Conference, 2003.*, Salt Lake City, UT, USA, 2003, pp. 367-372 vol.1.

[ALI15a] Q. Ali, T. A. Lipo and B. Kwon, "Design and analysis of a novel brushless wound rotor synchronous machine," *IEEE Trans. Magn.*, vol. 51, no. 11, pp. 1-4, Nov. 2015.

[ALI15b] H. Ali, E. bin Sulaiman, M. Jenal and M. F. Omar, "Three phase segmental rotor hybrid excitation flux switching motors for various applications," *2015 IEEE Student Conference on Research and Development (SCOReD)*, Kuala Lumpur, 2015, pp. 373-377.

[ALI16] Q. Ali, S. Atiq, T. A. Lipo, and B. I. Kwon, "PM assisted, brushless wound rotor synchronous machine," *J. Magn.*, vol. 21, no. 3, pp. 399–404, Nov. 2016.

[AMA09] Y. Amara, L. Vido, M. Gabsi, E. Hoang, A. H. Ben Ahmed and M. Lecrivain, "Hybrid excitation synchronous machines: energy-efficient solution for vehicles propulsion," *IEEE Trans. Veh. Technol.*, vol. 58, no. 5, pp. 2137-2149, Jun 2009

[AMA11] Y. Amara, S. Hlioui, R. Belfkira, G. Barakat and M. Gabsi, "Comparison of open circuit flux control capability of a series double excitation machine and a parallel double excitation machine," *IEEE Trans. Veh. Technol.*, vol. 60, no. 9, pp. 4194-4207, Nov. 2011.

[AYD02] M. Aydin, Surong Huang and T. A. Lipo, "A new axial flux surface mounted permanent magnet machine capable of field control," *Conference Record of the 2002 IEEE Industry Applications Conference. 37th IAS Annual Meeting (Cat. No.02CH37344)*, Pittsburgh, PA, USA, 2002, pp. 1250-1257 vol.2.

[BAN06] J. F. Bangura, "Design of high-power density and relatively high-efficiency flux-switching motor," *IEEE Trans. Energy Convers.*, vol. 21, no. 2, pp. 416-425, June 2006.

[BAR14] M. Barcaro and N. Bianchi, "Interior PM machines using ferrite to replace rare-earth surface PM machines," *IEEE Trans. Ind. Appl.*, vol. 50, no. 2, pp. 979-985, March-April 2014.

[BIA06a] N. Bianchi, S. Bolognani and P. Frare, "Design criteria for high-efficiency SPM synchronous motors," *IEEE Trans. Energy Convers.*, vol. 21, no. 2, pp. 396-404, June 2006.

[BIA06b] N. Bianchi and M. Dai Prè, "Use of the star of slots in designing fractional-slot single-layer synchronous motors," *Proc. IEE-Electr. Power Appl.,* vol. 153, pp. 459-466, 2006.

[BIA16] N. Bianchi, S. Bolognani, E. Carraro, M. Castiello and E. Fornasiero, "Electric vehicle traction based on synchronous reluctance motors," *IEEE Trans. Ind. Appl.*, vol. 52, no. 6, pp. 4762-4769, Nov.-Dec. 2016.

[BOL14] I. Boldea, L. N. Tutelea, L. Parsa and D. Dorrell, "Automotive electric propulsion systems with reduced or no permanent magnets: an overview," *IEEE Trans. Ind. Electron.*, vol. 61, no. 10, pp. 5696-5711, Oct. 2014.

[BUY14] V. T. Buyukdegirmenci, A. M. Bazzi and P. T. Krein, "Evaluation of induction and permanent-magnet synchronous machines using drive-cycle energy and loss minimization in traction applications," *IEEE Trans. Ind. Appl.*, vol. 50, no. 1, pp. 395-403, Jan.-Feb. 2014.

[CAI19a] S. Cai, Z. Q. Zhu, J. Mipo and S. Personnaz, "A novel parallel hybrid excited machine with enhanced flux regulation capability," *IEEE Trans. Energy Convers.*, vol. 34, no. 4, pp. 1938-1949, Dec. 2019.

[CAI19b] S. Cai, Z. Q. Zhu, S. Mallampalli, J. Mipo and S. Personnaz, "Comparative analysis of novel fractional slot non-overlapping winding hybrid excited machines having different consequent pole rotor topologies," *2019 IEEE Energy Conversion Congress and Exposition (ECCE)*, Baltimore, MD, USA, 2019, pp. 6508-6515.

[CAI20a] S. Cai, Z. Q. Zhu, C. Wang, J. C. Mipo and S. Personnaz, "A novel fractional slot non-overlapping winding hybrid excited machine with consequent-pole PM rotor," *IEEE Trans. Energy Convers.*, accepted.

[CAI20b] S. Cai, Z. Q. Zhu, J. C. Mipo, and S. Personnaz, "Investigation of novel doubly salient hybrid excited machine with non-overlapped field winding," *IEEE Trans. Energy Convers.,* to be submitted.

[CAO12a] R. Cao, C. Mi and M. Cheng, "Quantitative comparison of flux-switching permanent-magnet motors with interior permanent magnet motor for EV, HEV, and PHEV applications," *IEEE Trans. Magn.*, vol. 48, no. 8, pp. 2374-2384, Aug. 2012.

[CAO12b] W. P. Cao, B. C. Mecrow, G. J. Atkinson, J. W. Bennett and D. J. Atkinson, "Overview of electric motor technologies used for more electric aircraft (MEA)," *IEEE Trans. Ind. Electron.*, vol. 59, no. 9, pp. 3523-3531, Sept. 2012.

[CHA02] K. T. Chau, Ming Cheng and C. C. Chan, "Nonlinear magnetic circuit analysis for a novel stator doubly fed doubly salient machine," *IEEE Trans. Magn.*, vol. 38, no. 5, pp. 2382-2384, Sept. 2002.

[CHA03] K. T. Chau, J. Z. Jiang and Y. Wang, "A novel stator doubly fed doubly salient permanent magnet brushless machine," *IEEE Trans. Magn.*, vol. 39, no. 5, pp. 3001-3003, Sept. 2003.

[CHA07] C. C. Chan, "The state of the art of electric, hybrid, and fuel cell vehicles," in *Proceedings of the IEEE*, vol. 95, no. 4, pp. 704-718, April 2007.

[CHA08] K. T. Chau, C. C. Chan and C. Liu, "Overview of permanent-magnet brushless drives for electric and hybrid electric vehicles," *IEEE Trans. Ind. Electron.*, vol. 55, no. 6, pp. 2246-2257, June 2008.

[CHA96] C. C. Chan, K. T. Chau, J. Z. Jiang, W. Xia, M. Zhu and R. Zhang, "Novel permanent magnet motor drives for electric vehicles," *IEEE Trans. Ind. Electron.*, vol. 43, no. 2, pp. 331-339, April 1996.

[CHA97] C. C. Chan, R. Zhang, K. T. Chau and J. Z. Jiang, "Optimal efficiency control of PM hybrid motor drives for electrical vehicles," *PESC97. Record 28th Annual IEEE Power Electronics Specialists Conference. Formerly Power Conditioning Specialists Conference 1970-71. Power Processing and Electronic Specialists Conference 1972*, Saint Louis, MO, USA, 1997, pp. 363-368 vol.1.

[CHE01] M. Cheng, K. T. Chau and C. C. Chan, "Static characteristics of a new doubly salient permanent magnet motor," *IEEE Trans. Energy Convers.*, vol. 16, no. 1, pp. 20-25, March 2001.

[CHE08] Z. H. Chen, N. Zhou and X. L. Meng, "Analysis on a novel doubly salient machine," *2008 International Conference on Electrical Machines and Systems*, Wuhan, 2008, pp. 3522-3525.

[CHE10] J. T. Chen, Z. Q. Zhu, S. Iwasaki and R. Deodhar, "Low cost flux-switching brushless AC machines," *2010 IEEE Vehicle Power and Propulsion Conference*, Lille, 2010, pp. 1-6.

[CHE11a] M. Cheng, W. Hua, J. Zhang and W. Zhao, "Overview of stator-permanent magnet brushless machines," *IEEE Trans. Ind. Electron.*, vol. 58, no. 11, pp. 5087-5101, Nov. 2011.

[CHE11b] J. T. Chen, Z. Q. Zhu, S. Iwasaki and R. P. Deodhar, "A novel hybrid-excited switched-flux brushless ac machine for EV/HEV applications," *IEEE Trans. Veh. Technol.*, vol. 60, no. 4, pp. 1365-1373, May 2011.

[CHE14] Z. Chen, B. Wang, Z. Chen and Y. Yan, "Comparison of flux regulation ability of the hybrid excitation doubly salient machines," *IEEE Trans. Ind. Electron.*, vol. 61, no. 7, pp. 3155-3166, July 2014.

[CHE20] H. Chen, A. El-Refaie and N. Demerdash, "Flux-switching permanent magnet machines: A review of opportunities and challenges – Part I: fundamentals and topologies," *IEEE Trans. Energy Convers.*, early access.

[CHI15] A. Chiba, K. Kiyota, N. Hoshi, M. Takemoto and S. Ogasawara, "Development of a rare-earth-free SR motor with high torque density for hybrid vehicles," *IEEE Trans. Energy Convers.*, vol. 30, no. 1, pp. 175-182, March 2015.

[CHU14] W. Q. Chu, Z. Q. Zhu, J. Zhang, X. Ge, X. Liu, D. Stone, and M. Foster, "Comparison of electrically excited and interior permanent magnet machines for hybrid electric vehicle application," *2014 17th International Conference on Electrical Machines and Systems (ICEMS)*, Hangzhou, 2014, pp. 401-407.

[CHU15] W. Q. Chu, Z. Q. Zhu, J. Zhang, X. Liu, D. A. Stone and M. P. Foster, "Investigation on operational envelops and efficiency maps of electrically excited machines for electrical vehicle applications," *IEEE Trans. Magn.*, vol. 51, no. 4, pp. 1-10, April 2015.

[CHU16] S. Chung, S. Moon, D. Kim and J. Kim, "Development of a 20-pole–24-slot SPMSM with consequent pole rotor for in-wheel direct drive," *IEEE Trans. Ind. Electron.*, vol. 63, no. 1, pp. 302-309, Jan. 2016.

[CIS10] M. V. Cistelecan, F. J. T. E. Ferreira and M. Popescu, "Three phase tooth-concentrated multiple-layer fractional windings with low space harmonic content," *Proc. IEEE ECCE*, Atlanta, GA, 2010, pp. 1399-1405.

[COL99] F. Colamartino, C. Marchand and A. Razek, "Torque ripple minimization in permanent magnet synchronous servodrive," *IEEE Trans. Energy Convers.*, vol. 14, no. 3, pp. 616-621, Sept. 1999.

[CRO02] J. Cros and P. Viarouge, "Synthesis of high performance PM motors with concentrated windings," *IEEE Trans. Energy Convers.*, vol. 17, no. 2, pp. 248-253, June 2002.

[DAJ11] G. Dajaku and D. Gerling, "Eddy current loss minimization in rotor magnets of PM machines using high-efficiency 12-teeth/10-slots winding topology," *Proc. ICEMS*, Beijing, China, 2011, pp. 1-6.

[DAJ14] G. Dajaku, W. Xie and D. Gerling, "Reduction of low space harmonics for the fractional slot concentrated windings using a novel stator design," *IEEE Trans. Magn.*, vol. 50, no. 5, pp. 1-12, May 2014.

[DEO97] R. P. Deodhar, S. Andersson, I. Boldea and T. J. E. Miller, "The flux-reversal machine: a new brushless doubly-salient permanent-magnet machine," *IEEE Trans. Ind. Appl.*, vol. 33, no. 4, pp. 925-934, July-Aug. 1997.

[DIN19] W. Ding and S. Li, "Maximum ratio of torque to copper loss control for hybrid excited flux-switching machine in whole speed range," *IEEE Trans. Ind. Electron.*, vol. 66, no. 2, pp. 932-943, Feb. 2019.

[DRU17] J. Druant, H. Vansompel, F. De Belie and P. Sergeant, "Optimal control for a hybrid excited dual mechanical port electric machine," *IEEE Trans. Energy Convers.*, vol. 32, no. 2, pp. 599-607, June 2017.

[DU18] Y. Du, C. Zhang, X. Y. Zhu, F. Xiao. Y. D. Sun, Y. F. Z, and L. Quan, "Principle and analysis of doubly salient PM motor with π-shaped stator iron core segments," *IEEE Trans. Ind. Electron., 2018*.

[FAN06a] Y. Fan, K. T. Chau and S. Niu, “Development of a new brushless doubly fed doubly salient machine for wind power generation,” *IEEE Trans. Magn.*, vol. 42, no. 10, pp. 3455-3457, Oct. 2006.

[FAN06b] Y. Fan, K. T. Chau and M. Cheng, “A new three-phase doubly salient permanent magnet machine for wind power generation,” *IEEE Trans. Ind. Appl.*, vol. 42, no. 1, pp. 53-60, Jan.-Feb. 2006.

[FAS14] A. Fasolo, L. Alberti and N. Bianchi, “Performance comparison between switching-flux and IPM machines with rare-earth and ferrite PMs,” *IEEE Trans. Ind. Appl.*, vol. 50, no. 6, pp. 3708-3716, Nov.-Dec. 2014.

[FIN08] T. Finken, M. Felden and K. Hameyer, “Comparison and design of different electrical machine types regarding their applicability in hybrid electrical vehicles,” *2008 18th International Conference on Electrical Machines*, Vilamoura, 2008, pp. 1-5.

[FOD07] D. Fodorean, A. Djerdir, I. Viorel and A. Miraoui, “A double excited synchronous machine for direct drive application—design and prototype tests,” *IEEE Trans. Energy Convers.*, vol. 22, no. 3, pp. 656-665, Sept. 2007.

[FRE87] B. Frederick, “Hybrid excited generator with flux control of consequent pole rotor,” U.S. Patent 4 656 379, Apr. 7, 1987.

[FUK08a] T. Fukami, Yasuhiro Matsui, Takahito Hayamizu, K. Shima, R. Hanaoka and S. Takata, “Steady-state analysis of a permanent-magnet-assisted salient-pole synchronous generator,” *2008 18th International Conference on Electrical Machines*, Vilamoura, 2008, pp. 1-6.

[FUK08b] T. Fukami, M. Momiyama, K. Shima, R. Hanaoka and S. Takata, “Steady-state analysis of a dual-winding reluctance generator with a multiple-barrier rotor,” *IEEE Trans. Energy Convers.*, vol. 23, no. 2, pp. 492-498, June 2008.

[GAO18] Y. Gao, D. Li, R. Qu, X. Fan, J. Li and H. Ding, “A novel hybrid excitation flux reversal machine for electric vehicle propulsion,” *IEEE Trans. Veh. Technol.*, vol. 67, no. 1, pp. 171-182, Jan. 2018.

[GAU14] B. Gaussens, E. Hoang, M. Lécrivain, P. Manfe and M. Gabsi, “A hybrid-excited flux-switching machine for high-speed DC-alternator applications,” *IEEE Trans. Ind. Electron.*, vol. 61, no. 6, pp. 2976-2989, June 2014.

[GEN15] W. Geng, Z. Zhang, K. Jiang and Y. Yan, “A new parallel hybrid excitation machine: permanent-magnet/variable-reluctance machine with bidirectional field-regulating capability,” *IEEE Trans. Ind. Electron.*, vol. 62, no. 3, pp. 1372-1381, March 2015.

[GIE12] J. F. Gieras, “PM synchronous generators with hybrid excitation systems and voltage control Capabilities: A review,” *2012 XXth International Conference on Electrical Machines*, Marseille, 2012, pp. 2573-2579.

[GIU15] F. Giulii Capponi, G. Borocci, G. De Donato and F. Caricchi, “Flux regulation strategies for hybrid excitation synchronous machines,” *IEEE Trans. Ind. Appl.*, vol. 51, no. 5, pp. 3838-3847, Sept.-Oct. 2015.

[HAN11] J. Han, Z. Zhang and S. M. Jiangsu, “Investigation of field regulation performance of a new hybrid excitation synchronous machine with dual-direction magnetic shunt rotor,” *2011 International Conference on Electrical Machines and Systems*, Beijing, 2011, pp. 1-5.

[HE18] M. J. He, W. Xu, C. Y. Ye, and W. Hua, “Design of hybrid excited asymmetric stator pole doubly salient machine,” *The XIX International Conference on Electrical Machines – ICEM 2018*, Greece, 2018.

[HEN94a] G. Henneberger, J. R. Hadji-Minaglou, and R. C. Ciorba, “Design and test of permanent magnet synchronous motor with auxiliary excitation winding for electric vehicle application,” in *Proc. Eur. Power Electron. Symp.*, Oct. 1994, pp. 645–649.

[HEN94b] G. Henneberger and S. Küppers, “Improvement of the output performance of claw-pole alternators by additional permanent-magnets,” *in Proc. ICEM*, Paris, France, 1994, pp. 472–476.

[HLI08] S. Hlioui, L. Vido, Y. Amara, M. Gabsi, M. Lecrivain and A. Miraoui, “PM and hybrid excitation synchronous machines: performances comparison,” *2008 18th International Conference on Electrical Machines*, Vilamoura, 2008, pp. 1-6.

[HLI13] S. Hlioui, Y. Amara, E. Hoang, M. Lecrivain and M. Gabsi, “Overview of hybrid excitation synchronous machines technology,” *2013 International Conference on Electrical Engineering and Software Applications*, Hammamet, 2013, pp. 1-10.

[HOA07] E. Hoang, M. Lecrivain and M. Gabsi, “A new structure of a switching flux synchronous polyphased machine with hybrid excitation,” *2007 European Conference on Power Electronics and Applications*, Aalborg, 2007, pp. 1-8.

[HOA97] E. Hoang, A. Ben Ahmed, and J. Lucidarme, “Switching flux permanent magnet polyphased synchronous machines,” in *European Conference on Power Electronics and Applications*, 1997, pp. 3.903-3.908.

[HUA08] W. Hua, M. Cheng, Z. Q. Zhu and D. Howe, “Analysis and optimization of back EMF waveform of a flux-switching permanent magnet motor,” *IEEE Trans. Energy Convers.*, vol. 23, no. 3, pp. 727-733, Sept. 2008.

[HUA09] W. Hua, M. Cheng and G. Zhang, “A novel hybrid excitation flux-switching motor for hybrid vehicles,” *IEEE Trans. Magn.*, vol. 45, no. 10, pp. 4728-4731, Oct. 2009.

[HUA14] J. Huang, X. J. Wang and Z. C. Sun, “Variable flux memory motors: A review,” *2014 IEEE Conference and Expo Transportation Electrification Asia-Pacific (ITEC Asia-Pacific)*, Beijing, 2014, pp. 1-6.

[HUA15] W. Hua, G. Zhang and M. Cheng, “Flux-regulation theories and principles of hybrid-excited flux-switching machines,” *IEEE Trans. Ind. Electron.*, vol. 62, no. 9, pp. 5359-5369, Sept. 2015.

[HUA16a] L. R. Huang, Z. Q. Zhu, and W. Q. Chu, “Optimization of electrically excited synchronous machine for electrical vehicle applications,” in *Power*

Electronics, Machines and Drives (PEMD 2016), 8th IET International Conference on, 2016, pp. 1-6.

[HUA16b] H. Hua and Z. Q. Zhu, "Novel hybrid-excited switched-flux machine having separate field winding stator," *IEEE Trans. Magn.*, vol. 52, no. 7, pp. 1-4, July 2016.

[HUA16c] H. Hua, Z. Q. Zhu and H. L. Zhan, "Novel consequent-pole hybrid excited machine with separated excitation stator," *IEEE Trans. Ind. Electron.*, vol. 63, no. 8, pp. 4718-4728, Aug. 2016.

[HUA16d] H. Hua and Z. Q. Zhu, "Novel parallel hybrid excited machines with separate stators," *IEEE Trans. Energy Convers.*, vol. 31, no. 3, pp. 1212-1220, Sept. 2016.

[HUA17a] H. Hua and Z. Q. Zhu, "Novel partitioned stator hybrid excited switched flux machines," *IEEE Trans. Energy Convers.*, vol. 32, no. 2, pp. 495-504, June 2017.

[HUA17b] L. R. Huang, J. H. Feng, S. Y. Guo, J. X. Shi, W. Q. Chu and Z. Q. Zhu, "Analysis of torque production in variable flux reluctance machines," *IEEE Trans. Energy Convers.*, vol. 32, no. 4, pp. 1297-1308, Dec. 2017.

[HUA18a] H. Hua and Z. Q. Zhu, 'Novel partitioned stator hybrid excited machines with magnets on slot-openings'. *Int. Conf. Power Electric Machines and Drives (PEMD)*, Liverpool, UK, April 2018.

[HUA18b] W. Hua, X. Zhu and Z. Z. Wu, "Influence of coil pitch and stator-slot/rotor-pole combination on back EMF harmonics in flux-reversal permanent magnet machines," *IEEE Trans. Energy Convers.*, vol. 33, no. 3, pp. 1330-1341, Sept. 2018.

[HUS17] A. Hussain and B.-I. Kwon, "A new brushless wound rotor synchronous machine using a special stator winding arrangement," *Elect. Eng.*, pp. 1–8, Nov. 2017.

[HUS18] A. Hussain, S. Atiq and B. Kwon, "Consequent-pole hybrid brushless wound-rotor synchronous machine," *IEEE Trans. Magn.*, vol. 54, no. 11, pp. 1-5, Nov. 2018.

[HWA18] S. Hwang, J. Sim, J. Hong and J. Lee, "Torque improvement of wound field synchronous motor for electric vehicle by PM-assist," *IEEE Trans. Ind. Appl.*, vol. 54, no. 4, pp. 3252-3259, July-Aug. 2018.

[ISH96] H. Ishikawa, "AC generator for vehicle having combined structure of field coil and permanent magnet," U.S. Patent 5 825 116, Oct. 31, 1996.

[JAC00] A. G. Jack, B. C. Mecrow, P. G. Dickinson, D. Stephenson, J. S. Burdess, N. Fawcett, and J. T. Evans, "Permanent magnet machines with powdered iron cores and pressed windings," *IEEE Trans. Ind. Appl*., vol. 36, no. 4, pp. 1077–1084, Jul./Aug. 2000.

[JAH99] T. M. Jahns and V. Caliskan, "Uncontrolled generator operation of interior PM synchronous machines following high-speed inverter shutdown," *IEEE Trans. Ind. Appl.*, vol. 35, no. 6, pp. 1347-1357, Nov.-Dec. 1999.

[JAW16] G. Jawad, Q. Ali, T. A. Lipo and B. Kwon, "Novel brushless wound rotor synchronous machine with zero-sequence third-harmonic field excitation," *IEEE Trans. Magn.*, vol. 52, no. 7, pp. 1-4, July 2016.

[JIA15] S. Jia, R. Qu and J. Li, "Analysis of the power factor of stator dc-excited 217ernier reluctance machines," *IEEE Trans. Magn.*, vol. 51, no. 11, pp. 1-4, Nov. 2015, Art no. 8207704.

[JIA16] S. Jia, R. Qu, J. Li, D. Li and H. Fang, "Hybrid excited Vernier PM machines with novel DC-biased sinusoidal armature current," *2016 IEEE Energy Conversion Congress and Exposition (ECCE)*, Milwaukee, WI, 2016, pp. 1-8.

[JIA17a] S. Jia, R. Qu, D. Li, J. Li and W. Kong, "Improved torque capacity for flux modulated machines by injecting DC currents into the armature windings," *IEEE Trans. Magn.*, vol. 53, no. 6, pp. 1-5, June 2017.

[JIA17b] S. Jia, R. Qu, J. Li, D. Li and W. Kong, "A stator-PM consequent-pole Vernier machine with hybrid excitation and DC-biased sinusoidal current," *IEEE Trans. Magn.*, vol. 53, no. 6, pp. 1-4, June 2017, Art no. 8105404.

[JIN10] M. J. Jin, Y. Wang, J. X. Shen, P. C. K. Luk, W. Z. Fei, and C. Wang, "Cogging torque suppression in a permanent magnet flux-switching integrated-starter-generator," *IET Electric Power Applications,* vol. 4, pp. 647-656, 2010.

[JUN18] Y. Jung, M. Lim, M. Yoon, J. Jeong and J. Hong, "Torque ripple reduction of IPMSM applying asymmetric rotor shape under certain load condition," *IEEE Trans. Energy Convers.*, vol. 33, no. 1, pp. 333-340, March 2018.

[KAM06] M. Kamiya, "Development of traction drive motors for the Toyota hybrid system," *IEEJ Trans. On Ind. Appl.,* vol. 126, pp. 473-479, 2006.

[KAM12] K. Kamiev, J. Nerg, J. Pyrhönen, V. Zaboin, V. Hrabovcová, and P. Rafajdus, "Hybrid excitation synchronous generators for island operation," IET Electric Power Applications, vol. 6, pp. 1-11, 2012.

[KEF10] L. Kefsi, Y. Touzani and M. Gabsi, "Hybrid excitation synchronous motor control with a new flux weakening strategy," *2010 IEEE Vehicle Power and Propulsion Conference*, Lille, 2010, pp. 1-5.

[KOS05] T. Kosaka, Y. Kano, N. Matsui and C. Pollock, "A novel multi-pole permanent magnet synchronous machine with SMC bypass core for magnet flux and SMC field-pole core with toroidal coil for independent field strengthening/weakening," *2005 European Conference on Power Electronics and Applications*, Dresden, 2005, pp. 10 pp.-P.10.

[KOS10] T. Kosaka, M. Sridharbabu, M. Yamamoto and N. Matsui, "Design studies on hybrid excitation motor for main spindle drive in machine tools," *IEEE Trans. Ind. Electron.*, vol. 57, no. 11, pp. 3807-3813, Nov. 2010.

[LEE13] J. Lee and B. Kwon, "Optimal rotor shape design of a concentrated flux IPM-type motor for improving efficiency and operation range," *IEEE Trans. Magn.*, vol. 49, no. 5, pp. 2205-2208, May 2013.

[LEE15] C. H. T. Lee, K. T. Chau and C. Liu, "Design and analysis of a cost-effective magnetless multiphase flux-reversal dc-field machine for wind power

generation," *IEEE Trans. Energy Convers.*, vol. 30, no. 4, pp. 1565-1573, Dec. 2015.

[LI08] H. Li and Z. Chen, "Overview of different wind generator systems and their comparisons," *IET Renew. Power Gen.*, vol. 2, pp. 123–138, 2008.

[LI14] G. J. Li, Z. Q. Zhu, W. Q. Chu, M. P. Foster and D. A. Stone, "Influence of flux gaps on electromagnetic performance of novel modular pm machines," *IEEE Trans. Energy Convers.*, vol. 29, no. 3, pp. 716-726, Sept. 2014.

[LI17] W. Li, T. W. Ching and K. T. Chau, "A new high-temperature superconducting Vernier permanent-magnet machine for wind turbines," *IEEE Trans. Appl. Supercond.*, vol. 27, no. 4, pp. 1-5, June 2017.

[LI18] J. Li, K. Wang and C. Liu, "Torque improvement and cost reduction of permanent magnet machines with a dovetailed consequent-pole rotor," *IEEE Trans. Energy Convers.*, vol. 33, no. 4, pp. 1628-1640, Dec. 2018.

[LI19] Y. Li, H. Yang, H. Lin, S. Lyu and Z. Pan, "Comparative study of stator-consequent-pole permanent magnet machines with different stator-slot configurations," *IEEE Trans. Magn.*, vol. 55, no. 7, pp. 1-8, July 2019, Art no. 8106308.

[LI95] Y. Li and T. A. Lipo, "A doubly salient permanent magnet motor capable of field weakening," *Proceedings of PESC '95. Power Electronics Specialist Conference*, Atlanta, GA, USA, 1995, pp. 565-571 vol.1.

[LIA05] C. Z. Liaw, W. L. Soong, B. A. Welchko and N. Ertugrul, "Uncontrolled generation in interior permanent-magnet Machines," *IEEE Trans. Ind. Appl.*, vol. 41, no. 4, pp. 945-954, July-Aug. 2005.

[LIA95] Y. F. Liao, F. Liang and T. A. Lipo, "A novel permanent magnet motor with doubly salient structure," *IEEE Trans. Ind. Appl.*, vol. 31, no. 5, pp. 1069-1078, Sept.-Oct. 1995.

[LIB06] F. Libert and J. Soulard, "Manufacturing methods of stator cores with concentrated windings," *2006 3rd IET International Conference on Power Electronics, Machines and Drives – PEMD 2006*, The Contarf Castle, Dublin, Ireland, 2006, pp. 676-680.

[LIN14] N. Lin, D. Wang, Y. Shen and K. Wei, "Investigation on hybrid ratio between PM and current excitation sources for high-speed synchronous generator," *2014 17th International Conference on Electrical Machines and Systems (ICEMS)*, Hangzhou, 2014, pp. 505-508.

[LIU07] X. Liu, H. Lin, Z. Q. Zhu, C. Yang, S. Fang and J. Guo, "A novel dual-stator hybrid excited synchronous wind generator," *IEEE Trans. Ind. Appl.*, vol. 45, no. 3, pp. 947-953, May-June 2009.

[LIU09] X. Liu, H. Lin, C. Yang, S. Fang, and J. Guo, "Static characteristic of a novel dual-stator hybrid excited synchronous generator based on 3D finite element method," in *Electrical Machines and Systems, 2007. ICEMS. International Conference on*, 2007, pp. 1539-1543.

[LIU10a] C. Liu, K. T. Chau and J. Z. Jiang, "A permanent-magnet hybrid brushless integrated starter–generator for hybrid electric vehicles," *IEEE Trans. Ind. Electron.*, vol. 57, no. 12, pp. 4055-4064, Dec. 2010.

[LIU10b] C. Liu, K. T. Chau, and W. Li, "Comparison of fault-tolerant operations for permanent-magnet hybrid brushless motor drive," *IEEE Trans. Magn*., vol. 46, no. 6, pp. 1378–1381, Jun. 2010.

[LIU13] X. Liu and Z. Q. Zhu, "Electromagnetic performance of novel variable flux reluctance machines with dc-field coil in stator," *IEEE Trans. Magn.*, vol. 49, no. 6, pp. 3020-3028, June 2013.

[LIU14a] H. Liu, Y. Wang, Z. Deng and L. Song, "Comparative study of the parallel hybrid excited flux-switching machine topology for aerospace generator system," *2014 IEEE Conference and Expo Transportation Electrification Asia-Pacific (ITEC Asia-Pacific)*, Beijing, 2014, pp. 1-6.

[LIU14b] X. Liu, Z. Q. Zhu and D. Wu, "Evaluation of efficiency optimized variable flux reluctance machine for Evs/HEVs by comparing with interior PM machine," *2014 17th International Conference on Electrical Machines and Systems (ICEMS)*, Hangzhou, 2014, pp. 2648-2654.

[LIU17a] Y. Liu, Z. Zhang and X. Zhang, "Design and optimization of hybrid excitation synchronous machines with magnetic shunting rotor for electric vehicle traction applications," *IEEE Trans. Ind. Appl.*, vol. 53, no. 6, pp. 5252-5261, Nov.-Dec. 2017.

[LIU17b] Y. Liu and Z. Q. Zhu, "Comparative study of magnetic gearing effect in integral slot, fractional slot winding and Vernier PM machines," *2017 20th International Conference on Electrical Machines and Systems (ICEMS)*, Sydney, NSW, 2017, pp. 1-6.

[LIU19] X. Liu, Z. W. Yuan, S. H. Li and Z. Q. Zhu, "Field excitation optimization in hybrid excited switched flux permanent magnet machine for maximum output power," *2019 22th International Conference on Electrical Machines and Systems (ICEMS)*, Harbin, 2019, pp. 1-6.

[LUO00] X. Luo and T. A. Lipo, "A synchronous/permanent magnet hybrid AC machine," *IEEE Trans. Energy Convers.*, vol. 15, no. 2, pp. 203–210, Jun. 2000.

[MCC87] F. B. McCarty, "Hybrid excited generator with flux control of consequent-pole rotor," U.S. Patent No. 4656379, Apr. 04, 1987.

[NAO01] N. Naoe and T. Fukami, "Trial production of a hybrid excitation type synchronous machine," *IEMDC 2001. IEEE International Electric Machines and Drives Conference (Cat. No.01EX485)*, Cambridge, MA, USA, 2001, pp. 545-547.

[NED11] B. Nedjar, S. Hlioui, Y. Amara, L. Vido, M. Gabsi and M. Lecrivain, "A new parallel double excitation synchronous machine," *IEEE Trans. Magn.*, vol. 47, no. 9, pp. 2252-2260, Sept. 2011.

[OWE09] R. L. Owen, Z. Q. Zhu and G. W. Jewell, "Hybrid excited flux-switching permanent magnet machines," *2009 13th European Conference on Power Electronics and Applications*, Barcelona, 2009, pp. 1-10.

[OWE10] R. L. Owen, Z. Q. Zhu and G. W. Jewell, "Hybrid-excited flux-switching permanent-magnet machines with iron flux bridges," *IEEE Trans. Magn.*, vol. 46, no. 6, pp. 1726-1729, June 2010.

[OWE11] R. Owen, Z. Q. Zhu, J. B. Wang, D. A. Stone and I. Urquhart, "Review of variable-flux permanent magnet machines," *2011 International Conference on Electrical Machines and Systems*, Beijing, 2011, pp. 1-6.

[PEL11] G. Pellegrino, A. Vagati, and P. Guglielmi, "Design tradeoffs between constant power speed range, uncontrolled generator operation, and rated current of IPM motor drives," *IEEE Trans. Ind. Appl*., vol. 47, no. 5, pp. 1995–2003, Sep./Oct. 2011.

[POT19] N. Pothi, Z.Q. Zhu, and Yuan Ren, "Comparison of flux-weakening control strategies of novel hybrid-excited permanent magnet machines," *IEEE Trans. Ind. Appl.*, vol.55, no.4, pp. 3589-3597, 2019.

[QI09] G. Qi, J. T. Chen, Z. Q. Zhu, D. Howe, L. B. Zhou and C. L. Gu, "Influence of skew and cross-coupling on flux-weakening performance of permanent-magnet brushless AC machines," *IEEE Trans. Magn.*, vol. 45, no. 5, pp. 2110-2117, May 2009.

[QU19] G. Qu, Y. Fan and Z. Wu, "Design and analysis of a new hybrid-excited permanent magnet machine with unequal teeth," *IEEE Trans. Magn.*, vol. 55, no. 7, pp. 1-5, July 2019, Art no. 8105805.

[RAF10] A. M. EL-Refaie, "Fractional-slot concentrated-windings synchronous permanent magnet machines: opportunities and challenges," *IEEE Trans. Ind. Electron.*, vol. 57, no. 1, pp. 107-121, Jan. 2010.

[RAM11] T. Raminosoa, C. Gerada and M. Galea, "Design Considerations for a Fault-Tolerant Flux-Switching Permanent-Magnet Machine," *IEEE Trans. Ind. Electron.*, vol. 58, no. 7, pp. 2818-2825, July 2011.

[RAU55] S. E. Rauch and L. J. Johnson, "Design principles of flux-switching alternators," *AIEE Trans.*, vol. 74III, pp. 1261–1268, 1955.

[REB11] R. Rebhi, A. Ibala and A. Masmoudi, "An attempt to improve the generating capabilities of a hybrid claw pole machine," *2011 International Conference on Electrical Machines and Systems*, Beijing, 2011, pp. 1-5.

[REB14] R. Rebhi, A. Ibala and A. Masmoudi, "Hybrid excited claw pole alternators: Attempt to satisfy the increasing power need on board," *2014 17th International Conference on Electrical Machines and Systems (ICEMS)*, Hangzhou, 2014, pp. 3510-3514.

[RED12] P. B. Reddy, A. M. El-Refaie, K. Huh, J. K. Tangudu and T. M. Jahns, "Comparison of interior and surface PM machines equipped with fractional-slot concentrated windings for hybrid traction applications," *IEEE Trans. Energy Convers.*, vol. 27, no. 3, pp. 593-602, Sept. 2012.

[REF05] A. M. EL-Refaie and T. M. Jahns, “Optimal flux weakening in surface PM machines using fractional-slot concentrated windings,” *IEEE Trans. Ind. Appl.*, vol. 41, no. 3, pp. 790-800, May-June 2005.

[REF10] A. M. EL-Refaie, “Fractional-slot concentrated-windings synchronous permanent magnet machines: Opportunities and challenges,” *IEEE Trans. Ind. Electron.*, vol. 57, no. 1, pp. 107–121, Jan. 2010.

[REF13] A. M. El-Refaie, “Motors/generators for traction/propulsion applications: A review,” in *IEEE Veh. Technol. Mag.*, vol. 8, no. 1, pp. 90-99, March 2013.

[SAT11] Y. Sato, S. Ishikawa, T. Okubo, M. Abe, and K. Tamai, “Development of high response motor and inverter system for the Nissan LEAF electric vehicle,” *SAE Technical Paper*, 0148-7191, 2011.

[SHI07] S. Shinnaka and T. Sagawa, “New optimal current control methods for energy-efficient and wide speed-range operation of hybrid-field synchronous motor,” *IEEE Trans. Ind. Electron.*, vol. 54, no. 5, pp. 2443-2450, Oct. 2007.

[SOO02] W. L. Soong and N. Ertugrul, “Field-weakening performance of interior permanent-magnet motors,” *IEEE Trans. Ind. Appl.*, vol. 38, no. 5, pp. 1251-1258, Sept.-Oct. 2002.

[SPO89] E. Spooner, S. A. W. Khatab and N. G. Nicolaou, “Hybrid excitation of AC and DC machines,” *1989 Fourth International Conference on Electrical Machines and Drives Conf.*, London, UK, 1989, pp. 48-52.

[STU03] B. Stumberger, G. Stumberger, D. Dolinar, A. Hamler and M. Trlep, “Evaluation of saturation and cross-magnetization effects in interior permanent-magnet synchronous motor,” *IEEE Trans. Ind. Appl.*, vol. 39, no. 5, pp. 1264-1271, Sept.-Oct. 2003.

[SYV95] C. Syverson, “Hybrid alternator,” U.S. Patent No. US005397975A, Mar. 14, 1995.

[SYV98] C. Syverson, and W. Francis, “Hybrid alternator”, US Patent 5747909 B1/5 may 1998.

[TAN12] Y. Tang, J. J. H. Paulides, T. E. Motoasca and E. A. Lomonova, “Flux-switching machine with dc excitation,” *IEEE Trans. Magn.*, vol. 48, no. 11, pp. 3583-3586, Nov. 2012.

[TAP03] J. A. Tapia, F. Leonardi and T. A. Lipo, “Consequent-pole permanent-magnet machine with extended field-weakening capability,” *IEEE Trans. Ind. Appl.*, vol. 39, no. 6, pp. 1704-1709, Nov.-Dec. 2003.

[UND10] S. J. Underwood and I. Husain, “Online parameter estimation and adaptive control of permanent-magnet synchronous machines,” *IEEE Trans. Ind. Electron.*, vol. 57, no. 7, pp. 2435-2443, July 2010.

[VID05a] L. Vido, M. Gabsi, M. Lecrivain, Y. Amara and F. Chabot, “Homopolar and bipolar hybrid excitation synchronous machines,” *IEEE International Conference on Electric Machines and Drives, 2005.*, San Antonio, TX, 2005, pp. 1212-1218.

[VID05b] L. Vido, Y. Amara, M. Gabsi, M. Lecrivain and F. Chabot, "Compared performances of homopolar and bipolar hybrid excitation synchronous machines," *Fourtieth IAS Annual Meeting. Conference Record of the 2005 Industry Applications Conference, 2005*, Kowloon, Hong Kong, 2005, pp. 1555-1560 vol. 3.

[WAL05] J. A. Walker, D. G. Dorrell and C. Cossar, "Flux-linkage calculation in permanent-magnet motors using the frozen permeabilities method," *IEEE Trans. Magn.*, vol. 41, no. 10, pp. 3946-3948, Oct. 2005.

[WAN01] C. X. Wang, I. Boldea and S. A. Nasar, "Characterization of three phase flux reversal machine as an automotive generator," *IEEE Trans. Energy Convers.*, vol. 16, no. 1, pp. 74-80, March 2001.

[WAN05] H. Wang, Z. An, R. Tang and Y. Niu, "Design of a hybrid excitation permanent magnet synchronous with low voltage regulation," *2005 International Conference on Electrical Machines and Systems*, Nanjing, 2005, pp. 480-483 Vol. 1.

[WAN12a] Y. Wang and Z. Deng, "Hybrid excitation topologies and control strategies of stator permanent magnet machines for DC power system," *IEEE Trans. Ind. Electron.*, vol. 59, no. 12, pp. 4601-4616, Dec. 2012.

[WAN12b] Y. Wang and Z. Deng, "Comparison of hybrid excitation topologies for flux-switching machines," *IEEE Trans. Magn.*, vol. 48, no. 9, pp. 2518-2527, Sept. 2012.

[WAN13] W. J. Wang and Z. Zhang, "Maximum torque control of hybrid excitation synchronous machine drives based on field current self-optimizing method," *IECON 2013 – 39th Annual Conference of the IEEE Industrial Electronics Society*, Vienna, 2013, pp. 2977-2982.

[WAN14] K. Wang, Z. Q. Zhu and G. Ombach, "Synthesis of high performance fractional-slot permanent-magnet machines with coil-pitch of two slot-pitches," *IEEE Trans. Energy Convers.*, vol. 29, no. 3, pp. 758-770, Sept. 2014.

[WAN17a] Q. Wang and S. Niu, "Overview of flux-controllable machines: Electrically excited machines, hybrid excited machines and memory machines," *Renewable and Sustainable Energy Reviews,* vol. 68, pp. 475-491, 2017.

[WAN17b] Q. Wang and S. Niu, "A novel hybrid-excited dual-PM machine with bidirectional flux modulation," *IEEE Trans. Energy Convers.*, vol. 32, no. 2, pp. 424-435, June 2017.

[WAN17c] Q. Wang, S. Niu and X. Luo, "A novel hybrid dual-PM machine excited by AC with DC bias for electric vehicle propulsion," *IEEE Trans. Ind. Electron.*, vol. 64, no. 9, pp. 6908-6919, Sept. 2017.

[WAN17d] Y. Wang and Z. Deng, "A controllable power distribution strategy for open winding hybrid excitation generator system," *IEEE Trans Energy Convers.*, vol. 32, no. 1, pp. 122-136, March 2017.

[WAN18] Q. Wang and S. Niu, "A novel DC-coil-free hybrid-excited machine with consequent-pole PM rotor," *Energies*, vol. 11, p. 700, 2018.

[WAN19] Q. Wang, X. Zhang and S. Niu, “Design of dual-electrical-port DC-coil-free hybrid-excited machines,” *IEEE Trans. Energy Convers.*, vol. 34, no. 3, pp. 1328-1336, Sept. 2019.

[WEL04] B. A. Welchko, T. A. Lipo, T. M. Jahn, and S. E. Schulz, “Fault tolerant three-phase AC motor drive topologies: A comparison of features, cost, and limitations,” *IEEE Trans. Power Electron*., vol. 19 no. 4, pp. 1108-1116, Jul. 2004.

[WIL15] R. Wilden and S. P. Gudergan, “The impact of dynamic capabilities on operational marketing and technological capabilities: investigating the role of environmental turbulence,” *Journal of the Academy of Marketing Science*, vol. 43, pp. 181-199, 2015.

[WU17] Z. Z. Wu and Z. Q. Zhu, ‘Design and analysis of a novel partitioned stator hybrid excitation machine’, *Proc. Chin. Soc. Electr. Eng.*, 2017, 37, (22), pp. 6543–6556.

[WU18] Y. Wu, L. Sun, Z. Zhang, Z. Miao and C. Liu, “Analysis of torque characteristics of parallel hybrid excitation machine drives with sinusoidal and rectangular current excitations,” *IEEE Trans. Magn.*, vol. 54, no. 11, pp. 1-5, Nov. 2018, Art no. 8207205.

[XU16] W. Xu and M. He, “Novel 6/7 stator/rotor hybrid excitation doubly salient permanent magnet machine,” *IEEE Trans. Magn.*, vol. 52, no. 7, pp. 1-5, July 2016.

[YAM11] K. Yamazaki, S. Tamiya, K. Shima, T. Fukami, and K. Shirai, “Modeling of salient-pole synchronous machines assisted by permanent magnets,” *IEEE Trans. Magn.*, vol. 47, no. 10, pp. 3028–3031, Oct. 2011.

[YAN08] C. Yang, H. Lin, J. Guo and Z. Q. Zhu, “Design and analysis of a novel hybrid excitation synchronous machine with asymmetrically stagger permanent magnet,” *IEEE Trans. Magn.*, vol. 44, no. 11, pp. 4353-4356, Nov. 2008.

[YAO15] F. Yao, Q. An, X. Gao, L. Sun and T. A. Lipo, “Principle of operation and performance of a synchronous machine employing a new harmonic excitation scheme,” *IEEE Trans. Ind. Appl.*, vol. 51, no. 5, pp. 3890-3898, Sept.-Oct. 2015.

[YU11] C. Yu and K. T. Chau, “Design, analysis, and control of DC-excited memory motors,” *IEEE Trans. Energy Convers.*, vol. 26, no. 2, pp. 479-489, June 2011.

[YU18] J. Yu and C. Liu, “Design of a Double-Stator Magnetless Vernier Machine for Direct-Drive Robotics,” in *IEEE Transactions on Magnetics*, vol. 54, no. 11, pp. 1-5, Nov. 2018, Art no. 8105805.

[ZE18] Q. Ze, D. Liang, P. Kou and Z. Liang, “Reduction of torque and voltage ripple in a doubly salient permanent magnet generator,” *IEEE Trans. Energy Convers.*, vol. 33, no. 2, pp. 702-715, June 2018.

[ZHA05] C. H. Zhao and Y. G. Yan, “A review of development of hybrid excitation synchronous machine,” *Proceedings of the IEEE International Symposium on*

Industrial Electronics, 2005. ISIE 2005, Dubrovnik, Croatia, 2005, pp. 857-862 vol. 2.

[ZHA08] Z. Zhang, Y. Yan, S. Yang and Z. Bo, “Principle of operation and feature investigation of a new topology of hybrid excitation synchronous machine,” *IEEE Trans. Magn.*, vol. 44, no. 9, pp. 2174-2180, Sept. 2008.

[ZHA11] G. Zhang, M. Cheng, W. Hua and J. Dong, "Analysis of the oversaturated effect in hybrid excited flux-switching machines," *IEEE Trans. Magn.*, vol. 47, no. 10, pp. 2827-2830, Oct. 2011.

[ZHA12] Z. Zhang, Y. Tao and Y. Yan, "Investigation of a new topology of hybrid excitation doubly salient brushless DC generator," *IEEE Trans. Ind. Electron.*, vol. 59, no. 6, pp. 2550-2556, June 2012.

[ZHA15a] G. Zhang, W. Hua, M. Cheng, J. Liao, K. Wang and J. Zhang, "Investigation of an improved hybrid-excitation flux-switching brushless machine for HEV/EV applications," *IEEE Trans. Ind. Appl.*, vol. 51, no. 5, pp. 3791-3799, Sept.-Oct. 2015.

[ZHA15b] J. Zhao, M. Lin, D. Xu, L. Hao and W. Zhang, "Vector control of a hybrid axial field flux-switching permanent magnet machine based on particle swarm optimization," *IEEE Trans. Magn.*, vol. 51, no. 11, pp. 1-4, Nov. 2015, Art no. 8204004.

[ZHA16] W. Zhang, X. Liang, M. Lin, L. Hao and N. Li, "Design and analysis of novel hybrid-excited axial field flux-switching permanent magnet machines," *IEEE Trans. Appl. Supercond.*, vol. 26, no. 4, pp. 1-5, June 2016.

[ZHA18] X. Zhao, S. Niu and W. Fu, "Design of a novel parallel-hybrid-excited dual-PM machine based on armature harmonics diversity for electric vehicle propulsion," *IEEE Trans. Ind. Electron*., 2018.

[ZHE19] M. Zheng, Z. Q. Zhu, S. Cai and S. S. Xue, "A novel modular stator hybrid-excited doubly salient synchronous machine with stator slot permanent magnets," *IEEE Trans. Magn.*, vol. 55, no. 7, pp. 1-9, July 2019, Art no. 8104409.

[ZHU05] X. Y. Zhu and M. Cheng, "A novel stator hybrid excited doubly salient permanent magnet brushless machine for electric vehicles," *2005 International Conference on Electrical Machines and Systems*, Nanjing, 2005, pp. 412-415 vol. 1.

[ZHU06] X. Zhu, M. Cheng, W. Hua, J. Zhang and W. Zhao, "Design and analysis of a new hybrid excited doubly salient machine capable of field control," *Conference Record of the 2006 IEEE Industry Applications Conference Forty-First IAS Annual Meeting*, Tampa, FL, 2006, pp. 2382-2389.

[ZHU07] Z. Q. Zhu and D. Howe, "Electrical machines and drives for electric, hybrid, and fuel cell vehicles," in *Proceedings of the IEEE*, vol. 95, no. 4, pp. 746-765, April 2007.

[ZHU08a] X. Y. Zhu, M. Cheng, W. X. Zhao, J. Z. Zhang and W. Hua, "An overview of hybrid excited electric machine capable of field control," *Transactions of China Electrotechnical Society,* vol. 23, pp. 30-39, 2008.

[ZHU08b] Z. Q. Zhu *et al*., "Analysis and reduction of magnet eddy current loss in flux-switching permanent magnet machines," *2008 4th IET Conference on Power Electronics, Machines and Drives*, York, 2008, pp. 120-124.

[ZHU09] Z. Q. Zhu, "A simple method for measuring cogging torque in permanent magnet machines," *2009 IEEE Power & Energy Society General Meeting*, Calgary, AB, 2009, pp. 1-4.

[ZHU11a] Z. Q. Zhu, "Switched flux permanent magnet machines — Innovation continues," *2011 International Conference on Electrical Machines and Systems*, Beijing, 2011, pp. 1-10.

[ZHU11b] Z. Q. Zhu, "Fractional slot permanent magnet brushless machines and drives for electric and hybrid propulsion systems," *COMPEL-Int. J. Comput. Math. Elect. Electron. Eng.,* vol. 30, pp. 9-31, 2011.

[ZHU15] Z. Q. Zhu, Y. J. Zhou, J. T. Chen and J. E. Green, "Investigation of nonoverlapping stator wound-field synchronous machines," *IEEE Trans. Energy Convers.*, vol. 30, no. 4, pp. 1420-1427, Dec. 2015.

[ZHU16] Z. Q. Zhu, B. Lee and X. Liu, "Integrated field and armature current control strategy for variable flux reluctance machine using open winding," *IEEE Trans. Ind. Appl.*, vol. 52, no. 2, pp. 1519-1529, March-April 2016.

[ZHU17a] X. Zhu, Z. Xiang, C. Zhang, L. Quan, Y. Du and W. Gu, "Co-reduction of torque ripple for outer rotor flux-switching PM motor using systematic multi-level design and control schemes," *IEEE Trans. Ind. Electron.*, vol. 64, no. 2, pp. 1102-1112, Feb. 2017.

[ZHU17b] Z. Q. Zhu and B. Lee, "Integrated field and armature current control for dual three-phase variable flux reluctance machine drives," *IEEE Trans. Energy Convers.*, vol. 32, no. 2, pp. 447-457, June 2017.

[ZHU18] Z. Q. Zhu, H. Yang, S. Cai, H. Y. Li, Y. Liu, J. C. Mipo, S. Personnaz, "Hybrid excited stator slot PM machines with overlapping windings," *2018 XIII International Conference on Electrical Machines (ICEM)*, Alexandroupoli, 2018, pp. 2185-2191.

[ZHU19a] Z. Q. Zhu, N. Pothi, P. L. Xu, Y. Ren, “Uncontrolled generator fault protection of novel hybrid-excited permanent magnet machines utilizing field excitation current control,” *IEEE Trans. Ind. Appl.*, vol.55, no.4, pp. 3598-3606, 2019.

[ZHU19b] Z. Q. Zhu and S. Cai, "Overview of hybrid excited machines for electric vehicles," *Keynote Speech at 2019 Eleventh International Conference on Ecological Vehicles and Renewable Energies (EVER)*, Monte Carlo, 2019.

[ZHU19c] Z. Q. Zhu and S. Cai, "Hybrid excited permanent magnet machines for electric and hybrid electric vehicles," in *CES Transactions on Electrical Machines and Systems*, vol. 3, no. 3, pp. 233-247, Sept. 2019.

[ZHU19d] X. Zhu, W. Hua and G. Zhang, "Analysis and reduction of cogging torque for flux-switching permanent magnet machines," *IEEE Trans. Ind. Appl.*, vol. 55, no. 6, pp. 5854-5864, Nov.-Dec. 2019.

[ZUL10] A. Zulu, B. C. Mecrow and M. Armstrong, "A wound-field three-phase flux-switching synchronous motor with all excitation sources on the stator," *IEEE Trans. Ind. Appl.*, vol. 46, no. 6, pp. 2363-2371, Nov.-Dec. 2010.

Publications

Journal papers:

[J1] **S. Cai**, Z. Q. Zhu, C. Wang. J. C. Mipo, and S. Personnaz, “A novel fractional slot non-overlapping winding hybrid excited synchronous machine with consequent-pole PM rotor," *IEEE Trans. Energy Convers.*, early access.

[J2] **S. Cai**, Z. Q. Zhu, J. Mipo and S. Personnaz, "A novel parallel hybrid excited machine with enhanced flux regulation capability," *IEEE Trans. Energy Convers.*, vol. 34, no. 4, pp. 1938-1949, Dec. 2019.

[J3] **S. Cai**, Z. Q. Zhu, J. C. Mipo, and S. Personnaz, “Investigation of novel fractional slot non-overlapping winding hybrid excited machines with different consequent-pole rotor topologies,” *IEEE Trans. Ind. Appl.,* revised.

[J4] **S. Cai**, Z. Q. Zhu, J. C. Mipo, and S. Personnaz, “Investigation of novel doubly salient hybrid excited machine with non-overlapped field winding,” submitted to *IEEE Trans. Energy Convers.*

[J5] M. Zheng, **S. Cai**, and Z. Q. Zhu, “Investigation of a hybrid excited doubly salient machine with permanent magnets located on stator slot openings,” *IET EPA,* accepted.

[J6] Z. Q. Zhu and **S. Cai**, "Hybrid excited permanent magnet machines for electric and hybrid electric vehicles," *CES Transactions on Electrical Machines and Systems*, vol. 3, no. 3, pp. 233-247, Sept. 2019.

[J7] M. Zheng, Z. Q. Zhu, **S. Cai** and S. S. Xue, "A novel modular stator hybrid-excited doubly salient synchronous machine with stator slot permanent magnets," *IEEE Trans. Magn.*, vol. 55, no. 7, pp. 1-9, July 2019, Art no. 8104409.

[J8] M. Zheng, Z. Q. Zhu, **S. Cai**, H. Y. Li and Y. Liu, "Influence of magnetic saturation and rotor eccentricity on back EMF of novel hybrid-excited stator slot opening permanent magnet machine," *IEEE Trans. Magn.*, vol. 54, no. 11, pp. 1-5, Nov. 2018, Art no. 8105905.

[J9] M. Zheng, Z. Q. Zhu, **S. Cai**, H. Y. Li and Y. Liu, "Influence of stator and rotor pole number combinations on the electromagnetic performance of stator slot-opening PM hybrid-excited machine," *IEEE Trans. Magn.*, vol. 55, no. 5, pp. 1-10, May 2019, Art no. 8101210.

[J10] Y. F. Zhang, Z. Q. Zhu, **S. Cai**, D. W. Liang, S. Mallampalli, J. C. Mipo, and S. Personnaz, “One-dimensional lumped parameter thermal model of electrical machines,” IET Science, Measurement & Technology, accepted subject to revision.

Conference papers:

[C1] **S. Cai**, Z. Q. Zhu, S. Mallampalli, J. Mipo and S. Personnaz, "Comparative analysis of novel fractional slot non-overlapping winding hybrid excited machines having different consequent pole rotor topologies," *2019 IEEE Energy Conversion Congress and Exposition (ECCE)*, Baltimore, MD, USA, 2019, pp. 6508-6515.

[C2] **S. Cai,** Z.Q. Zhu, L.R. Huang, and H. Qu, “Comparison of stator slot permanent magnet hybrid excited machine with rotor interior permanent magnet machine for EV/HEV,” *PEMD 2020 – 10th International Conference on Power Electronics, Machines and Drives,* Nottingham, UK, 2020.

[C3] Z. Q. Zhu and **S. Cai**, "Overview of hybrid excited machines for electric vehicles," *2019 Fourteenth International Conference on Ecological Vehicles and Renewable Energies (EVER)*, Monte-Carlo, Monaco, 2019, pp. 1-14.

[C4] H. Yang, Z. Q. Zhu, **S. Cai**, H. Y. Li, Y. Liu, J. C. Mipo and S. Personnaz, “Performance comparison of stator slot permanent magnet machines with non-overlapping and overlapping windings,” *2018 XIII International Conference on Electrical Machines (ICEM)*, Alexandroupoli, 2018, pp. 2283-2289.

[C5] Z. Q. Zhu, H. Yang, **S. Cai**, H. Y. Li, J. C. Mipo, S. Personnaz, "Hybrid excited stator slot PM machines with overlapping windings," *2018 XIII International Conference on Electrical Machines (ICEM)*, Alexandroupoli, 2018, pp. 2185-2191.

[C6] H. Qu, Z.Q. Zhu, **S. Cai**, L.R. Huang, “Analysis and mitigation of demagnetization issue in stator slot PM machines,” *PEMD 2020 – 10th International Conference on Power Electronics, Machines and Drives,* Nottingham, UK, 2020.